AEDC-TR-80-8

ARENDT

An Evaluation of Wind Tunnel Test Techniques for Aircraft Nozzle Aferbody Testing at Transonic Mach Number

T. L. Kennedy
ARO, Inc.

November 1980

Final Report for Period October 1, 1977 — January 1, 1979

Approved for public release; distribution unlimited.

ARNOLD ENGINEERING DEVELOPMENT CENTER
ARNOLD AIR FORCE STATION, TENNESSEE
AIR FORCE SYSTEMS COMMAND
UNITED STATES AIR FORCE

This report has been reviewed by the Office of Public Affairs (PA) and is releasable to the National Technical Information Service (NTIS). At NTIS, it will be available to the general public, including foreign nations.
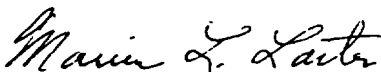
APPROVAL STATEMENT

This report has been reviewed and approved.

ELTON R. THOMPSON
Project Manager
Directorate of Technology

Approved for publication:

FOR THE COMMANDER

MARION L. LASTER
Director of Technology
Deputy for Operations

REPORT DOCUMENTATION PAGE		READ INSTRUCTIONS BEFORE COMPLETING FORM
1. REPORT NUMBER AEDC-TR-80-8	2. GOVT ACCESSION NO.	3. RECIPIENT'S CATALOG NUMBER
4. TITLE (and Subtitle) AN EVALUATION OF WIND TUNNEL TEST TECHNIQUES FOR AIRCRAFT NOZZLE AFTERBODY TESTING AT TRANSONIC MACH NUMBERS		5. TYPE OF REPORT & PERIOD COVERED Final Report - October 1977 - January 1979
		6. PERFORMING ORG. REPORT NUMBER
7. AUTHOR(s) T. L. Kennedy, ARO, Inc., a Sverdrup Corporation Company		8. CONTRACT OR GRANT NUMBER(s)
9. PERFORMING ORGANIZATION NAME AND ADDRESS Arnold Engineering Development Center/DOT Air Force Systems Command Arnold Air Force Station, Tennessee 37389		10. PROGRAM ELEMENT, PROJECT, TASK AREA & WORK UNIT NUMBERS Program Element 65807F
11. CONTROLLING OFFICE NAME AND ADDRESS Arnold Engineering Development Center/DOS Air Force Systems Command Arnold Air Force Station, Tennessee 37389		12. REPORT DATE November 1980
		13. NUMBER OF PAGES 182
14. MONITORING AGENCY NAME & ADDRESS(if different from Controlling Office)		15. SECURITY CLASS. (of this report) UNCLASSIFIED
		15a. DECLASSIFICATION DOWNGRADING SCHEDULE N/A

16. DISTRIBUTION STATEMENT (of this Report)

Approved for public release; distribution unlimited.

17. DISTRIBUTION STATEMENT (of the abstract entered in Block 20, if different from Report)

18. SUPPLEMENTARY NOTES

Available in Defense Technical Information Center (DTIC).

19. KEY WORDS (Continue on reverse side if necessary and identify by block number)

nozzles	wind tunnel tests	aerodynamic characteristics
afterbodies	transonic flow	measurement
models	jet mixing flow	
supports	simulation	

20. ABSTRACT (Continue on reverse side if necessary and identify by block number)

The results of many experiments to develop and verify wind tunnel test techniques for determining engine exhaust effects on aircraft performance at transonic Mach numbers are summarized. The influence of model support interference, exhaust jet simulation techniques, wind tunnel calibration-flow quality and operating conditions, model geometric effects, and measurement techniques on afterbody aerodynamic forces are discussed. Recommendations are given for reducing or eliminating adverse interference effects on wind tunnel test data.

DD FORM 1473 EDITION OF 1 NOV 65 IS OBSOLETE
1 JAN 73

PREFACE

The work reported herein was conducted by the Arnold Engineering Development Center (AEDC), Air Force Systems Command (AFSC), for the Directorate of Technology (AEDC/DOT). The work was done by ARO, Inc., AEDC Group (a Sverdrup Corporation Company), operating contractor for the AEDC, AFSC, Arnold Air Force Station, Tennessee, under Project No. P32P-R3A. The Air Force project manager for this program was Mr. Elton R. Thompson, AEDC/DOT. The manuscript was submitted for publication on January 14, 1980.

CONTENTS

Page

ILLUSTRATIONS

Figure   Page

Figure   Page

1.0 INTRODUCTION

In recent years problems have been encountered in achieving the predicted performance of high-performance aircraft. The source of the difficulty has often been the inability to predict airframe propulsion system interaction effects, even though a large portion of the total aircraft system testing is used to determine the effect of propulsion system operation on the aircraft performance. A major portion of the testing is required to determine the throttle-dependent afterbody drag. The future use of the engine exhaust to favorably influence the afterbody flow field, optimization of nozzle integration into the airframe, and thrust vectoring will require a more extensive jet-effects testing effort to determine system performance.

For several years AEDC research and technology efforts have been directed toward the development and verification of wind tunnel test techniques to determine engine exhaust effects on aircraft performance. The selection of the best support system, jet simulation technique, model size and exactness, measurement techniques, and allowance for wind tunnel interference are interrelated and often lead to conflicting requirements. The information from the research and technology efforts combined with information obtained from routine development or systems tests provide guidance for the selection of compromises needed to obtain useful data. The purpose of this report is to compile and evaluate the available data that will provide guidance during the early test planning phase of system development programs to increase selection of optimum test techniques compatible with the objectives of proposed experiments.

2.0 SUPPORT INTERFERENCE

The most significant problem normally encountered in designing an experiment to determine airframe configuration performance is the selection of the support system. For afterbody testing, most models have been strut supported; however, the resulting interference at supersonic Mach numbers has precipitated a trend toward the use of wing-tip and annular-jet sting supports for recent testing. There are many compromises possible in the selection of a support system depending on the test objectives, model configuration, Mach number range of interest, and the required Reynolds numbers. The support system must have adequate strength and rigidity to withstand the aerodynamic loads and provide space for instrumentation and high-pressure air or fuel lines. Since a minimum-sized support system represents minimum interference, compromises to allow the usually desired testing at high Reynolds numbers are required for every installation. In configuration optimization studies, the assumption is often made that increments measured between configurations are valid because the interference, although present, is assumed to be a constant for all

9

configurations. This is a very poor assumption as will be shown. In most instances, some method must be chosen to determine the support interference in order to assure the validity of the data whether the test objective is to determine the incremental or absolute values of the test parameters.

2.1 STRUT SUPPORT INTERFERENCE

In the past the most common method of supporting an afterbody model has been with a strut attached to the model fuselage either with the model upright or inverted. Three examples of strut supports are shown in Fig. 1. In many tests, the strut blockage (typically 0.75 percent) is about the same or larger than the model blockage and can result in a significant amount of tunnel wall interference at transonic Mach numbers.

The flow-field disturbance created by a strut is very large and is unfortunately in proximity to the area of interest on the model. The disturbances are illustrated by data obtained during a recent tunnel calibration, a portion of which was dedicated to calibration of two probes. The probes were strut mounted from the floor and ceiling centerline as shown in Fig. 2. The blockage of both probe struts is 0.44 percent compared to the usual model support blockage of about 0.8 percent. The changes in the wall and centerline pressure coefficient distributions caused by the struts and probes are shown in Fig. 3. The disturbances on the tunnel centerline at subsonic speeds are relatively small but still measurable at all Mach numbers. As would be expected large shock disturbances are evident downstream of the struts at supersonic Mach numbers, and the magnitude is greater near Mach 1.0. The disturbance on the floor ahead of the strut is typical of interference observed at transonic speeds from both stings and struts, extends far forward of the support, and increases in magnitude as Mach 1.0 is approached. Measurable disturbances were also recorded on the floor downstream of the strut at subsonic Mach numbers. When the disturbances are related to pressure drag, the difficulty in obtaining interference-free data when using a strut support is obvious. For a typical fighter aircraft, a 0.01 change in pressure coefficient over an afterbody results in a 100-drag-count change based on body area and approximately an 8-drag-count change based on wing area.

2.1.1 Effect of Strut Design Parameters

Many investigations have been conducted at AEDC in an attempt to obtain strut configurations that will minimize support interference. The approach generally consisted of testing a simple sting-supported model to obtain baseline data and then testing with various struts to evaluate their effect on the model pressure distributions. Some typical configurations investigated in the AEDC 1-foot, transonic Aerodynamic Wind Tunnel (1T) are shown in Fig. 4 (Ref. 1). The model blockage was 0.55 percent, and the strut blockage

ranged from 0.6 to 0.9 percent, depending on strut thickness. The effect of strut location on the base pressure coefficient is shown in Fig. 5. At supersonic Mach numbers, large deviations from the sting-alone data are evident. The effect of one of the struts on the body surface pressures along the 0-, 90-, and 180-deg rays is shown in Fig. 6. The data are typical for all of the struts shown in Fig. 4. As with base pressure, the effects are relatively small at subsonic Mach numbers, but at supersonic Mach numbers very large effects cause significant errors in pitching moment and lift as well as drag. Typically, boattail drag coefficients at supersonic Mach numbers for such bodies are approximately 0.2. A bias error in pressure coefficient of 0.05 over the body would produce an error in drag of about 25 percent. Since the strut interference shown in Fig. 6, at supersonic Mach numbers, is a function of axial location, it is obvious that the error in boattail drag would be dependent on boattail geometry. For unsymmetrical models the interference effects in all coefficients are configuration dependent because of the large radial gradients in the interference pressure. Large errors would also be expected in the variation of the aerodynamic coefficients with Mach number. Thus, to attempt to determine an optimum strut configuration for a general class of models is useless.

The interference effects of struts having different chords, thicknesses, and locations with respect to the model are shown in Fig. 7 for the 0- and 180-deg rays. At Mach number 0.9, which is typical of subsonic Mach numbers, the interference increased when strut thickness was increased (compare struts C-1 to F and D to E). Although there is an apparent increase in interference with increasing chord at subsonic speeds, the effect is caused primarily by trailing-edge location. The shorter chord strut, C-2, had essentially the same effect as the longer chord strut, D.

At Mach 1.2 all of the strut configurations produce severe interference. The only significant change in the interference occurred with the minimum chord, minimum thickness strut mounted in the aft position, C-2. Measurements along the 0-deg ray on a body of revolution are assumed by many investigators to be interference-free; they obviously are not. The data at Mach 1.2 show this row to be far from interference-free and in fact to have greater interference than the 180-deg row located in the wake of the strut. For some strut-model configurations, the complex shock structure caused by the strut results in a shock standing on the top of the model, the location of which is a function of Mach number, blockage, and model-strut-shock interactions. When present this shock has a more adverse effect along the 0-deg ray than on the 180-deg position, which is subjected primarily to the effects of the strut shock and expansion waves. At Mach number 1.4, the interference is much lower for all struts and tends to follow the data obtained at subsonic speeds for which lower drag struts caused the least interference. The interference at 0 and 180 deg is nearly equal in magnitude but opposite in sign and could cause significant effects on normal force and pitching moment.

Previously unpublished data taken in Tunnel 1T (Fig. 8) indicate that base pressure interference at supersonic Mach numbers can be reduced by increasing the distance from the model base to the strut trailing edge. This alternative may not be practical for an aircraft model. Extension of the model nose to an upstream strut using a cylindrical section similar to a sting is a possible alternative, but the model shock structure and viscous flow field may be unrealistic with such an arrangement.

An investigation reported in Ref. 2 measured the support interference effects on a boattail configuration as a function of strut sweep angle. As shown in Fig. 9, the base and boattail interference were greatly reduced at supersonic Mach numbers with the 45-deg swept strut. However, sweeping the strut while holding chord and thickness constant results in reduced strut cross section in the strut axis and a decrease in the strength of the strut. For a given load, the lateral deflection of the model with the 45-deg sweep angle strut of Ref. 2 would be four times greater than with the 0-deg sweep angle strut. To achieve the same rigidity, the strut thickness should be increased by approximately 60 percent. Unpublished data indicate that significant reduction in base pressure interference was not achieved by sweeping a strut of constant cross section (chord increased with sweep angle); the lateral rigidity was also reduced by 40 percent. To determine if sweep angle can actually be used to reduce interference, further investigation would be required using strut configurations having similar strength. Since increased thickness or chord increases the subsonic interference, a practical swept strut configuration may not be suitable for subsonic Mach numbers.

2.1.2 Strut-Supported Aircraft Configurations

To determine the interference for various afterbody configurations, a model was tested both sting mounted and strut mounted with dummy stings as shown in Fig. 10 (Ref. 3). The afterbody forces were measured with a balance. Thus, the force differences measured between the two support systems included skin friction as well as pressure drag. Significant interference in drag was observed as shown in Fig. 11. Comparison of the interference for the different afterbody configurations indicates a configuration sensitivity to interference and, thus, emphasizes the difficulty of obtaining valid effects of configuration changes with a strut-mounted model.

A comprehensive study of strut, sting, and wing-tip support systems is reported in Ref. 4. A photograph of the strut-supported model with a dummy sting is shown in Fig. 12. The model was extensively instrumented with pressure orifices to determine afterbody drag. The strut interference on axial-force coefficient is shown in Fig. 13 for angles of attack of 0 and 7 deg. The strut caused large changes in axial-force coefficient at both angles of attack. At transonic Mach numbers the interference was as high as 50 percent of the afterbody axial-force coefficient.

The effect of strut interference on the normal-force coefficient is shown in Fig. 14. As would be expected, based on the axisymmetric studies, the interference is significant even at 0-deg angle of attack. The magnitude of interference in normal-force coefficient (approximately 0.01) represents an error of about 12 drag counts when resolved into the drag axis at 7-deg angle of attack.

The change in pressure distribution caused by the strut is shown in Fig. 15 for various rows of orifices. Examination of the pressure distribution changes at Mach 0.9 shows that the strut caused large changes in the flow field particularly over the top of the model, which is in the wake of the strut. At 7-deg angle of attack very large changes in the pressure coefficients were evident particularly in the area of the nozzle. Similar strut interference effects were observed at Mach 1.2, where the strut caused shocks and expansions to move relative to their location on the sting-mounted model. Large changes in the pressure occur in the region of the nozzle where the projected areas in the axial direction are large, thus producing a large effect on axial-force coefficient. With such large changes in the afterbody flow field resulting from strut interference, the results of configuration studies with a strut-mounted model would have a large uncertainty since the interference is expected to be configuration dependent.

Strut interference is caused by a combination of increased tunnel blockage and wave interference. The strut interference relative to a sting-mounted model was determined for both 1/9-scale and 1/4-scale F-16 afterbody models. The model struts had scaled thicknesses; but, the chord relative to fuselage length was longer for the 1/9-scale installation as shown in Fig. 16. The trailing edge of the strut was at the same axial station for both models. The interference in axial-force coefficient shown in Fig. 17 was obtained by taking the difference between the data obtained with the strut-mounted model and a dummy sting and that with the sting-mounted model. At subsonic Mach numbers the strut interference for each of the models was similar, but at Mach numbers from 1.0 through 1.2 there were large differences in both the magnitude and sign of the interference at both angles of attack. These data illustrate the uncertainty introduced by strut interference and the changes in strut interference that can occur with changes in tunnel blockage and strut geometry.

2.2 STING SUPPORT INTERFERENCE

The accounting system usually used to determine aircraft forces from wind tunnel data involves the application of throttle-dependent force increments obtained from afterbody model tests to the basic force model aerodynamics. The force model sting interference and alteration of aft fuselage lines to accommodate the sting can result in large changes in the aerodynamics and must be properly accounted for. To supply proper afterbody force

13

measurements the force model afterbody and support configuration must be tested during the afterbody testing phase to allow application of the afterbody increments to force model data. The current trend toward high thrust-to-weight aircraft has resulted in engine sizes that permit a model to be supported through the nozzle without aft fuselage line alteration. Actual nozzle configurations should be used when possible on the force model to obtain better drag increments between the force model and afterbody model.

2.2.1 Effect of Sting Diameter

In the investigation reported in Ref. 5 various sting diameters were tested without any downstream support, as shown in Fig. 18. The effect of sting diameter on afterbody drag coefficient is shown in Fig. 19. Considerable interference at subsonic Mach numbers was observed for even the smallest sting used in the investigation. The sting-to-nozzle diameter ratios investigated are representative of those needed to support a typical single engine fighter model, with the larger diameter ratios being applicable to dry power settings and the smaller ratios being appropriate for nozzles for afterburning power settings. The nozzle exit diameter changes with power settings and the interference of a constant diameter sting would be expected to change. If a true "jet-off" drag coefficient is desired an interference investigation would be required for each nozzle configuration.

2.2.2 Effect of Sting Support Structure

A sting-supported model must be held by some structure downstream of the model. The sting should be long enough to prevent interference from the supporting structure on the model flow field. The effect of the downstream structure is to decrease the axial force in addition to that caused by the presence of the sting. The installation shown in Fig. 20 was used to study probe design and in addition to provide information on the influence of a strut on the flow field ahead of it. Combined strut and probe blockage was 1.2 percent, which is considerably higher than normally used in transonic wind tunnel testing. However, the example is instructive in that it demonstrates that support interference must be given adequate consideration during the initial phase of system programs that include wind tunnel testing. The influence of a strut spanning Tunnel 1T propagates forward as far as thirty strut thicknesses at subsonic Mach numbers (Fig. 21). If interference-free data are to be obtained the model base should be forward of this location.

During calibration of Tunnel 16T the centerline pipe was supported at the downstream end by the main pitch mechanism, as shown in Fig. 22. The extent of the complete support system interference may be inferred from the location of the deviation of the centerline pressure distribution from the established free-stream Mach number. The strut blockage interference is alleviated by bulges in the tunnel sidewalls; these bulges compensate for the

strut blockage. With the data from Ref. 6, the extent of the detectable upstream interference is shown in Fig. 23 as a function of free-stream Mach number. At Mach numbers above M_∞ = 1.1, the interference was downstream of the closest orifice located two diameters from the roll mechanism. For interference-free afterbody data, a model base should not be located closer than approximately 6.5 roll mechanism diameters from the roll mechanism. This location for interference-free data is closer by approximately 10 strut thicknesses to the strut than the data of Fig. 21 would predict, thus indicating the effectiveness of the bulge region in reducing the blockage effect of the support strut.

The effect of some sting configurations on model base pressure was reported in Refs. 1 and 2. Details of the configurations tested are shown in Fig. 24. Base pressure coefficients measured with the various sting configurations are shown in Fig. 25. Each of the configurations deviated significantly from the baseline configuration (most aft location of the taper) at subsonic Mach numbers, and two of the configurations had significant interference at supersonic Mach numbers. The variation of base pressure coefficient with Mach number indicates that interference is present for the baseline configuraion at 0.9 Mach number. Based on the data in Fig. 23 none of the configurations should have had an effect on the base pressure at 0.6 Mach number or at Mach numbers above 1.1, indicating that the model wake allows propagation of the disturbance much further upstream than the boundary layer on the centerline pipe. The interference is probably configuration sensitive, with separated afterbodies expected to be the most sensitive. The error in base pressure as a function of the proximity of the sting taper to the model base for Mach number 0.9 is shown in Fig. 26. For the data shown, the maximum sting diameter is 50 percent larger than the model diameter and causes a larger effect than expected with typical model/sting configurations. Nevertheless, it is obvious that large errors in afterbody drag could occur when the sting is not long enough.

Since the interference is a function of the afterbody base-to-sting diameter ratio and afterbody configuration, it is not possible to develop sting selection criteria that will be valid for all configurations. Sting configurations are normally dictated by strength requirements. When sting interference is expected to have an unacceptable influence on the data, a study is recommended to determine the interference caused by sting taper and the feasibility of correcting the data. A tapered dummy sting can be mounted at various distances ahead of the actual tapered sting to determine if the actual tapered portion of the sting is far enough away from the model.

2.3 STING SUPPORT WITH AN ANNULAR JET

One of the most promising methods of supporting a jet-effects model is to sting mount the model and simulate the jet exhaust with an annular jet around the sting. Air is supplied

to the model through the sting and exhausted from an annular nozzle having the correct area ratio and nozzle divergence angle. A parametric study of the simulation of a full jet with an annular jet is reported in Ref. 5. The model (Fig. 18) was tested with both an annular and a full jet. The annular-jet configuration consisted of a dummy sting installed through the nozzle, simulating a real sting as far aft as the maximum sting diameter. The difference in drag coefficient between the conventional jet and the annular jet for various combinations of sting-to-nozzle diameter ratios is shown in Fig. 27 as a function of nozzle area ratio at the nozzle design pressure ratio. The most significant differences occurred with the largest diameter ratio and with the nozzle having an area ratio of 1.134. The differences in drag coefficient between a full jet and an annular jet for an area ratio of 1.134 are shown in Fig. 28 as a function of sting-to-exit diameter ratio along with the jet-off sting interference from Fig. 19. At subsonic Mach numbers the differences in the jet-on data were much less than the jet-off sting interference. The jet-on interference is less than one percent of the drag coefficient even with large stings. At Mach number 1.2 the interference is comparable to the jet-off sting interference and varied from 2 to 7.5 percent of the afterbody drag coefficient. Compared to the usual support system interference the differences in axial-force coefficient between an annular jet and a full jet are small.

Valid data can be obtained with the annular-jet technique over a wide range of nozzle pressure ratios; however, the use of very large stings makes simulation of high-pressure ratios difficult and causes large errors for pressure ratios below the nozzle design pressure ratio (Ref. 5). The technique of simulation at other than design pressure ratio presented in Ref. 5 has been found to be satisfactory.

2.3.1 Aircraft Configurations with Annular-Jet Simulation

Two aircraft configurations have been tested using the annular-jet technique. For both configurations, a study was made to determine the adequacy of the annular jet in simulating a full jet. The 1/9-scale F-16 model shown in Fig. 29 was tested using a wing-tip mount with a full jet and using dummy stings with an annular jet (Ref. 4). The sting geometry was duplicated as far aft as the maximum model sting diameter. As shown in Fig. 30 both normal-and axial-force coefficients are in good agreement for the two techniques. The nozzle configurations and angles of attack shown encompass the range normally needed for performance evaluation. The errors are minimal when compared to those introduced by strut interference for the same configuration. As shown in Figs. 13 and 14, the strut mounting introduced errors as high as 75 drag counts and caused interference in normal force at all Mach numbers.

A 0.2-scale YF-17 model was also tested using a wing-tip mount with jet simulation both with and without stings. The model is shown with dummy stings in Fig. 31. Shown in Fig. 32 are the differences between the annular-jet and conventional-jet pressure-integrated force coefficient for two nozzles. Negligible normal-force coefficient differences were obtained for the limited angle-of-attack range of the test. The largest axial-force coefficient difference was 0.0008 for the smallest nozzle, which had a very small annular-jet clearance.

The model was also tested sting mounted (Ref. 7) using the annular-jet technique (Fig. 33). A comparison of the axial-force coefficients for the afterbody and nozzle with those obtained from flight test data (Ref. 8) are shown in Fig. 34 for a fully closed nozzle position. At each Mach number, nozzle pressure ratio variations were minimal for the flight data. Excellent agreement was obtained between the flight data and wind tunnel data, indicating that a sting-supported annular-jet model properly simulates the jet and has minimal support interference. Significant nozzle pressure ratio variations were obtained during the flight test at Mach 1.2 for a relatively small angle-of-attack range, $\alpha = 1$ to 4 deg. A comparison between the wind tunnel and flight data is shown in Fig. 35 as a function of NPR at Mach 1.2. The flight axial-force coefficients on the nozzle are slightly less than those obtained for the wind tunnel model. As will be shown in Section 3.0 the differences are compatible with the differences between a hot and cold jet when the actual jet temperature is significant. At Mach number 1.2 the flight data were obtained with an afterburning power setting; the exhaust gas temperature was significantly higher than at subsonic Mach numbers.

For configurations that can be tested using the annular-jet technique (axisymmetric nozzle), jet-on afterbody data can be obtained with proper cold-jet simulation and minimal support interference at all transonic Mach numbers. The data presented in Refs. 4 and 7 indicate that this technique is valid for off-design pressure ratios at angle of attack, with various nozzles representing a range of power settings.

2.4 WING-TIP SUPPORT

Initial evaluation of the interference of wing-tip support systems (Ref. 9) indicated that the support interference was not as configuration sensitive or as severe as strut interference at supersonic Mach numbers. The model was tested sting mounted and with wing-tip support simulation as shown in Fig. 36. The wing-tip support interference drag increments for three nozzle configurations are shown in Fig. 37 to be less than and more consistent than strut interference and similar for various nozzles except at Mach numbers 0.9 and 1.2.

A 20-percent-scale YF-17 model was subsequently tested (Ref. 7), and an evaluation of the support interference was made. Since this model was about as large as could be tested in Tunnel 16T, interference from support system blockage would be as significant as could be expected for any test. The model was sting supported and annular-jet simulation was used. The wing-tip support was simulated with dummy components as shown in Fig. 38. The interference contribution of the wing-tip stings and the horizontal strut in two positions is shown in Fig. 39. In comparison to the interference attributable to strut supports the wing-tip support interference is minimal but larger than that for an annular-jet-supported model. The data indicate that at subsonic speeds care should be taken to locate the horizontal support strut far enough downstream of the model, particularly if data at Mach numbers near unity are desired. The effects of the downstream strut are consistent with the data in Fig. 21 and indicate that the data can be used to select the strut location, depending upon the Mach numbers for which data are desired. Installation of the wing-tip support included alteration of the wing planform; this alteration caused normal-force coefficient changes at angle of attack that became more severe at higher subsonic Mach numbers. Although the wing-tip support interference was not significant for the relatively low angles of attack of the investigation, the interference should be re-evaluated for investigations at high angles of attack and transonic Mach numbers where changes in the downwash could cause large interference effects.

Similar investigations were also conducted with the F-16 model (Ref. 4). As shown in Fig. 29, the model was tested using a wing-tip mount with dummy stings and sting mounted to determine the wing-tip support interference. The support interference in axial- and normal-force coefficients at 0-deg angle of attack is shown in Fig. 40. In the Mach number range from 0.8 to 1.05, throttle-dependent data obtained with the support system would be highly questionable because of the large values of interference. At 7-deg angle of attack the interference in axial-force coefficient is similar to that at 0-deg angle of attack, but large normal-force coefficient increments were measured at Mach numbers above 0.9. At the supersonic Mach numbers the interference was as much as 17 percent of the total afterbody normal-force coefficient. The interference in axial-force coefficient would be acceptable for determination of throttle-dependent corrections at supersonic Mach numbers, but careful consideration should be given to the normal-force coefficient interference if the objectives of a test were to determine performance with a thrust vectoring nozzle. Parametric studies of the effects of the aft support strut axial position indicated that a significant portion of the wing-tip support system interference at subsonic Mach numbers could be eliminated by proper strut placement. For minimum interference at supersonic Mach numbers, the nose of the wing-tip sting should be located such that neither shock nor expansion waves from the nose intersect the portion of the model of interest. For design of a wing-tip support system, Ref. 4 should be consulted for the effects of altering the wing planform, the wing-tip sting spacing and geometry, and the aft strut location.

2.5 SUPPORT SYSTEM COMPARISON

A comparison of the afterbody axial- and normal-force coefficients from a strut, wing-tip, and sting support system are shown in Fig. 42 for the F-16 model. Since the sting is common to all configurations, the effect of each support system can be interpreted by the variation relative to the sting data. At subsonic speeds, both the wing-tip and strut supports caused reduced axial-force coefficients compared to those obtained with the sting support and a delayed drag rise. The strut support interference on axial- and normal-force coefficients was very large at supersonic Mach numbers below Mach 1.5. The strut support also resulted in large interference on normal-force coefficients at subsonic Mach numbers. At 7-deg angle of attack the wing-tip support system caused reduced axial-force coefficients at the subsonic Mach numbers and increased normal-force coefficients at supersonic Mach numbers, which resulted in the drag coefficient differences shown. The reduced normal-force coefficients caused by the strut at nearly all Mach numbers caused increased disagreement for the strut-supported configuration when drag coefficient was the parameter of interest. In addition, the effect of the strut on normal-force coefficient would make it difficult to evaluate nozzle configurations that provide lift augmentation.

3.0 JET SIMULATION

The accepted method of testing for jet effects has been to simulate the jet exhaust with ambient temperature air and to neglect corrections to the measured aerodynamics because of jet temperature effects. The usual practice has been to scale the nozzle internal geometry and test at nozzle total to free-stream static pressure ratios (NPR) corresponding to the hot jet being simulated. During experiments to determine the differences in afterbody drag obtained with a hot and a cold jet (Ref. 10), the cold jet produced higher drag. The differences not only were significant, but they were configuration and Mach number dependent. Using an estimated drag higher than the actual drag results in a heavier, more costly aircraft that is no longer acceptable. The current emphasis is on design of minimum cost aircraft tailored to a specific mission.

During the past several years, systematic experiments (Refs. 11 and 12) have been conducted to determine the parameters that must be matched to simulate a hot exhaust or to develop a method that could be used to correct the data for the effects of temperature. In these experiments two boattail configurations were used to assure that the results were not configuration peculiar and were valid if the boattail flow was attached or separated. The tests were conducted in the AEDC Tunnel 16T and Tunnel 1T with similar strut-mounted models of appropriate size for each of the wind tunnels. The model geometry used in each tunnel is shown in Fig. 42. Details of the boattails are given in Fig. 43. Although interference-free data to aid in the analysis would be desirable, the strut-mounted

19

configuration was considered acceptable because the jet itself was the only variable. Further, any jet simulation technique must be applicable in the flow field of the aircraft wings and tail surfaces that produce flow-field perturbations similar to the strut. The aerodynamic effects of the jet have been judged by comparing the afterbody pressure drag obtained by integration of measured pressures over appropriate areas.

3.1 HOT-JET EFFECTS

An experiment to determine the effect of a typical turbojet exhaust on afterbody pressure drag was conducted with the Tunnel 16T model and is reported in Ref. 10. The results for typical subsonic and supersonic Mach numbers and each of the boattails are shown in Figs. 44 and 45. In terms of the currently desired precision for predicting aircraft performance, the effects shown are considered to be significant. Typically the higher temperature exhaust produces a lower drag when compared at the same NPR. The effect is largest for the separated boattail (25-deg) at subsonic Mach numbers. As shown in Ref. 10, some improvement in the drag coefficient correlation for different temperatures can be achieved for the 15-deg boattail if the data are considered to be a function of jet-shape-related parameters. At subsonic Mach numbers little, if any, improvement in the drag correlation was obtained for the 25-deg boattail using any shape-related parameter. The differences between the hot- and cold-jet data for the 25-deg boattail are presumed to be primarily a result of changes in jet entrainment as a function of exhaust temperature.

Many investigators have suggested (e.g., Refs. 13 and 14) that for proper simulation both a jet-shape parameter and a mixing parameter must be matched. In order to determine a method of correction or simulation, the effects of shape parameters and entrainment parameters must be isolated since they are often interrelated. Entrainment of the external flow by the jet exhaust produces results associated with a smaller jet without entrainment; however, for purposes of this discussion matching of jet shape implies matching of the shape of an inviscid jet in a quiescent environment. Inviscid quiescent jet-plume-shape parameters that have often been used include initial jet inclination angle, nozzle static-to-free-stream static pressure ratio, and jet diameter-to-nozzle exit diameter. For a fixed nozzle geometry these parameters are a function of specific heat ratio and jet total-to-free-stream static pressure ratio. Parameters often associated with entrainment include jet exhaust velocity, mass flux, momentum, and kinetic energy.

3.2 EFFECT OF JET SPECIFIC HEAT RATIO

Changes in exhaust temperature result in a change in specific heat ratio. To isolate the effect of specific heat ratio on afterbody drag, an experiment was conducted in the AEDC

Tunnel 1T using gases having the same total temperature and molecular weight (nitrogen and ethylene) but different specific heat ratios. A comparison of the resulting afterbody drag coefficient as a function of NPR for each of the boattails is shown in Fig. 46. The changes in drag coefficient are measurable, but not large, as shown in Fig. 47. The specific heat ratio for ethylene is lower than that for typical turbojet exhausts, but the afterbody drag can be correlated with that for nitrogen by any of the shape parameters. The remaining difference in the drag measured in hot exhausts and ambient air, after correlation with a shape parameter, must be the result of the mixing of the jet and free-stream flows. However, since relatively good data correlation for the nitrogen and ethylene jets can be achieved through the use of shape parameters, then the jet and free-stream mixing must be similar for the two gases. The exit velocity of nitrogen is less than one percent greater than that of ethylene, but the mass flow, exit momentum, and kinetic energy for the same exit static pressures are approximately 25-percent higher than those for ethylene. Thus, the mixing phenomena may be dependent upon exit velocity but apparently are not very sensitive to mass flow, momentum, or kinetic energy.

3.3 EFFECT OF JET GAS CONSTANT

An investigation to determine jet-entrainment effects on afterbody drag was conducted in the AEDC Tunnel 1T using hydrogen, nitrogen, and mixtures of the two gases (Ref. 12). Since the two gases have the same specific heat ratio but differing gas constant, parameters such as jet velocity, mass flux, and kinetic energy, which may relate to the jet-entrainment process, could be varied over a wide range at a constant nozzle pressure ratio representing a fixed inviscid jet plume shape. Afterbody drag coefficient as a function of nozzle total pressure ratio is shown in Fig. 48 with gas constant as a parameter. Although the absolute drag value varies widely as a function of pressure ratio for each of the gas constants, the effect of gas constant does not change the variations resulting in essentially parallel curves. Using nitrogen as a reference, the incremental change in drag as a function of gas constant is shown in Fig. 49 for various pressure ratios. Since the drag coefficient increments do not vary with pressure ratio, the data indicate that incremental entrainment effects are not a function of the absolute value of parameters that are a function of pressure, such as mass flow, kinetic energy, exit momentum, and velocity at the plume boundary. With gas constant as a variable at a constant pressure ratio and temperature, the jet momentum is constant but velocity, density, and kinetic energy vary as $R^{1/2}$, R^{-1}, and $R^{3/2}$, respectively. One would expect that the entrainment would increase with increasing velocity (R) and result in increased drag. One explanation of the phenomenon might be that the density decreases at a more rapid rate than the velocity increases; thus, the exhaust is capable of entraining less of the stream flow. A method of correcting for temperature effects developed in Ref. 15 indicates that this is the case.

21

A subsequent experiment was conducted with the 25-deg boattail model with several additional nozzle area ratios. The results (Fig. 50) for each area ratio were similar to those shown in Fig. 49; however, the jet-on absolute drag was changed appreciably as a function of area ratio. Within the scatter of the data the three curves are linear and parallel, indicating that the effect of gas constant on incremental drag coefficient is not a function of nozzle area ratio. The changes in drag coefficient as a function of area ratio are proportional to the change in momentum; however, further data or analyses are required to determine if a relationship exists that relates the change in drag as a function of both area ratio and gas constant. As shown in Fig. 51 the exit velocity to free-stream velocity ratio does not collapse the data into a single function. A correlation using a combination of several parameters is possible, but insufficient information is presently available to determine if such multiple parameters are universally applicable to hot-jet data.

A comparison of the effect of varying temperature and gas constant is shown in Fig. 52. Since the correct parameter is not currently known the data are shown as a function of the product of gas constant and total temperature. Similar variations for the two variables indicate that temperature effects could be evaluated by varying gas constant. Exact agreement of the two data sets would not be expected because there are large temperature profile gradients in the hot jet, and the support interference and the area ratios are different between the two sets of data. However, the data suggest that it is possible to compensate for the effect of temperature when using ambient temperature gas by also testing at another temperature or with a gas having a different gas constant (molecular weight). Since the jet entrainment effect on drag is not a function of NPR, data obtained at a single pressure ratio for each configuration and test condition would allow extrapolation to be made to any other temperature for a range of pressure ratios. If a relationship between the effects of area ratio, gas constant, and temperature can be determined, it may be possible to determine corrections for temperature by varying area ratio.

3.4 EFFECTS OF INTERNAL NOZZLE GEOMETRY

Large changes in the nozzle exhaust exit conditions can be accomplished by altering the internal nozzle geometry. Although the engine nozzle geometry can be duplicated, it may be desirable to alter the internal nozzle geometry when testing an aircraft model in a wind tunnel.

3.4.1 Nozzle Divergence Half Angle

The parameter most often matched to simulate the exhaust plume for rockets and missiles has been the initial jet inclination angle (δ_j) at quiescent conditions defined in the sketch on the following page.
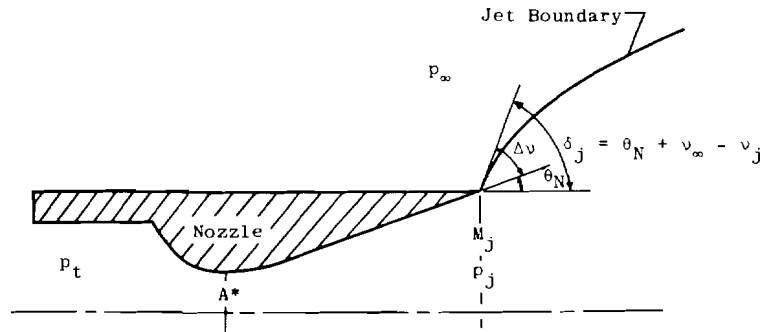
To determine if this parameter is important for simulating turbojet and turbofan exhausts, the internal nozzle geometry of the 15-deg boattail model tested in Tunnel 16T was modified to investigate the effect of nozzle divergence half angle. The pressure drag coefficient as a function of nozzle pressure ratio is shown in Fig. 53 with nozzle divergence angle as a parameter ($\nu_\infty - \nu_j$ is constant at a given NPR and A_e/A^*). Near design pressure ratio (NPR = 4) there was a slight effect of divergence angle on pressure drag, but at higher pressure ratios the effect was within the repeatability of the data. (Matching of nozzle pressure ratio for any divergence angle results in matching of all shape-related parameters except jet inclination angle.) At nozzle pressure ratios from 2 to 16 and nozzle divergence angles from 2-1/2 to 10 deg, afterbody drag is only slightly a function of initial jet inclination angle. The data are not collapsed by jet inclination angle, and therefore jet inclination angle is not a correlation parameter. If jet inclination angle were matched as a simulation parameter, an error in drag coefficient as high as 0.03 would result for the data shown. To illustrate further that initial jet inclination angle is not a correlation parameter, afterbody drag coefficient is shown as a function of jet inclination angle in Fig. 54.

3.4.2 Nozzle Area Ratio Effects

As shown previously there are large effects of varying nozzle area ratio on afterbody drag at design pressure ratio. Since all shape-related parameters were matched at the nozzle design pressure ratio, the only effects of area ratio shown previously were due to entrainment. Selection of the correct shape parameter is necessary when pressure ratio is varied in order to compare afterbody drag for various area ratio nozzles. Area ratio variations in the normal turbojet and turbofan operating regime were investigated with the 15-deg boattail model (Ref. 5). Afterbody drag coefficient as a function of nozzle pressure ratio is shown in Fig. 55 for various area ratios. When compared on this basis there are large effects of area ratio, particularly at the higher pressure ratios.

As shown in Fig. 56 some improvement in the correlation is realized when the data are compared as a function of incremental Prandtl-Meyer angle, an often used shape parameter.

23

Note, however, that at the higher $\Delta\nu$'s the drag coefficient decreases with increasing area ratio, which is opposite the effect observed with large area ratio changes at design pressure ratio, as shown in Fig. 50. The remaining difference in drag coefficient therefore cannot be attributed to the entrainment effect caused by varying area ratio.

A shape-related parameter that yields consistent results for all variables has been the ratio of the quiescent inviscid plume diameter — when expanded isentropically to free-stream static pressure — to the nozzle exit diameter. The same results are also observed if the diameter is determined by a method-of-characteristics solution for the plume diameter as shown in Ref. 5. The drag coefficients for various area ratios are shown as a function of plume diameter ratio in Fig. 57. The remaining differences in drag are consistent with the previously shown entrainment effects, and the differences between the data obtained with the solid plumes (stings) and real plumes are believed to be a measure of the absolute entrainment effects. The annular-jet data previously discussed in Section 2.0 also compared well using diameter ratio as the correlating parameter despite very large changes in the initial jet inclination angle as a result of the sting. In general, afterbody drag appears to be more sensitive to the blockage imposed by the jet than to the near field shape of the plume.

4.0 WIND TUNNEL CALIBRATION

Shown in Fig. 58 is the error in Mach number computed from the isentropic relations that will result in an error of ±0.01 in the quantity p_∞/q_∞. A ±0.01 error in p_∞/q_∞ causes an error of 100 counts in afterbody drag based on afterbody projected area and approximately 10 drag counts based on wing area for typical fighter aircraft. Such uncertainties in wind tunnel Mach number calibration can be reasonably expected at subsonic Mach numbers. Force coefficients for a portion of a body such as an afterbody are very sensitive to errors in free-stream static pressure. If pressures are integrated to determine the force coefficient on a body or a portion thereof, the error in the force coefficient caused by an error in free-stream pressure is equal to the product of the error in free-stream static pressure and the projected area divided by the reference area. For example, the error in afterbody drag coefficient is $\Delta C_D = E_{p\infty}A_p/q_\infty S$. If the force is determined by a shell balance, the error is equal to but opposite in sign to the integrated pressure error as a result of the cavity pressure correction ($\Delta C_D = -E_{p\infty}A_p/q_\infty S$). As a result of the uncertainty in pressure measurements during testing and wind tunnel calibrations, the minimum uncertainty in free-stream Mach number is typically ±0.003 in transonic wind tunnels.

Systematic variations in the Mach number calibration with Reynolds number that are within the uncertainty of Mach number have been observed during calibration of Tunnel 16T as reported in Ref. 6. Shown in Fig. 59 is the pressure drag obtained by integration of pressure distributions for a body of revolution at $M_\infty = 0.6$. The effect of the error in free-

stream static pressure was relatively small for the total drag coefficient (equal to ΔP_∞ times the base area) but very large for the forebody and afterbody when considered separately. The error in total drag would be zero if the pressure integration included the model base (closed body). If the systematic variation in the tunnel calibration with Reynolds number is considered ($\Delta M_\infty = 0.006$ at $M_\infty = 0.6$ for the Reynolds number range of the tunnel), the pressure drag of the forebody, afterbody, and total body drag are nearly invariant with Reynolds number as would be expected. Thus, normally acceptable small errors in Mach number that affect p_∞ can cause erroneous conclusions concerning the effects of Reynolds number on drag.

The data shown in Fig. 60 were calculated considering the Reynolds number effects on the tunnel calibration. Apparent Reynolds number effects on forebody and afterbody pressure drag coefficient still exist. The Mach number deviation required to force the data at lower Reynolds number to be equal to the coefficient at the highest Reynolds number (least uncertain data) is also shown. The required increment in Mach number is within the uncertainty in Mach number at the lower Reynolds numbers.

Configuration studies would be valid at a constant Reynolds number with small errors in Mach number if the afterbody closure does not vary. However, for studies such as throttle-dependent drag where the nozzle closure varies, errors proportional to the error in free-stream static pressure and change in afterbody projected area are introduced between configurations. A similar error is present during force model testing as a result of cavity pressure and internal duct drag corrections.

For performance predictions the afterbody testing and force model testing uncertainty should be considered together since it is possible to minimize the effect of free-stream static pressure bias errors by giving proper consideration to the method of measurement of forces (pressure integration or balance) and testing at the same tunnel pressure level. Since the uncertainty in Mach number is present in all facilities, larger uncertainties in performance are introduced if all of the testing is not accomplished in the same facility. For performance prediction it is highly recommended that all testing be accomplished in a single facility, with the tests designed to minimize the effect of free-stream static pressure errors by making measurements that will minimize systematic free-stream static pressure errors by considering the impact of p_∞ on each test.

4.1 TUNNEL NOISE

The location of the transition from laminar to turbulent flow has been shown to be highly influenced by wind tunnel noise. Measurable effects on afterbody pressure drag have not been observed when either the tunnel Reynolds number is varied or the boundary layer is

artificially tripped except in some few cases at supersonic Mach numbers in which shock boundary-layer interactions have caused Reynolds number effects (see Ref. 16). For afterbodies for which a Reynolds number effect is observed, a realistic flight boundary layer must be simulated to predict accurately the pressure drag at flight Reynolds numbers. Except for very large or full-scale models, an artifically tripped boundary layer cannot produce a properly scaled boundary layer over the complete model even in a low-noise tunnel. Thus, if Reynolds number effects on pressure drag are observed, extrapolation of the data to full-scale Reynolds numbers must be done with caution.

4.2 FLOW ANGULARITY

Typical afterbody forces are shown as a function of angle of attack in Fig.61. Even though the forces on lifting surfaces are not involved, the normal-force component from lift carryover on the fuselage contributes significantly to the afterbody drag at angle of attack and thus an error in angle could cause a large change in drag. Near zero angle of attack small errors in angle do not cause a significant error in drag coefficient. Since flow angularity and model size for each afterbody configuration would be the same, configuration studies and throttle-dependent increments should be valid for small values of flow angularity. In general, flow angularity does not contribute to an uncertainty that would compromise the objectives of most tests, but this should be a consideration for each test program. Typical force model techniques of using upright and inverted testing can be used to determine the influence of flow angularity on the test data.

4.3 MACH NUMBER GRADIENTS

A longitudinal Mach number gradient in the wind tunnel results in the requirement for a "bouyancy" correction. The longitudinal Mach number gradient as measured during Tunnel 16T calibrations is within the uncertainty of the individual centerline pressure measurements. A tunnel centerline pressure distribution for Mach number 0.8, which is the subsonic Mach number with the largest pressure gradient, is shown in Fig. 62. Also shown is a least-squares linear curve fit that was used to define the gradient. The gradient thus defined is shown in Fig. 63 for the Mach number range of Tunnel 16T. The area distribution for a typical fighter is shown in Fig. 64. Assuming a 10-ft-long model, integration of the pressure gradient at 0.8 Mach number over the fuselage area as bouyancy corrections are normally applied results in a forebody drag coefficient increment of -0.00011 and an afterbody drag coefficient increment of -0.00011 for a total aircraft correction of 2.2 drag counts. The bouyancy correction would be smaller in proportion to the model length for shorter models, since the pressure gradient over the model is less. Since the pressure gradients are within the uncertainty of the tunnel calibration data and the corrections are well within the uncertainty of usual model data, a bouyancy correction is not required for tests in Tunnel 16T.

26

4.4 TUNNEL WALL ANGLE

The effective porosity of Tunnel 16T may be varied by varying tunnel sidewall angle. The "optimum" wall angle schedule as a function of Mach number for best wave cancellation at supersonic Mach numbers was determined using a long cone-cylinder model (Ref. 17). Since the afterbody is highly subject to reflected shocks and expansions in the flow, one would expect the most accurate results to be obtained with the optimum wall angle schedule. For small models, differences in afterbody drag between zero wall angle and optimum wall angle have been small. For larger sting-mounted models at Mach numbers where reflected wave interference would be expected, better agreement between different sizes of the same configuration has been obtained when testing was accomplished using the optimum wall angle schedule. The effect of wall angle on axial-force coefficient at Mach numbers 1.05, 1.1, and 1.2 is shown in Fig. 65 for a large-scale model. Although the variation in axial-force coefficient at optimum wall angle indicates wall interference at Mach 1.1, the interference is obviously greater with zero wall angle. In addition, the optimum wall angle data are in better agreement with the small-scale model.

The effect of wall angle on afterbody drag coefficient was also determined for the large-scale model with the model strut mounted as shown in Fig. 66. The strut interference is so large and varies so widely between the two sizes of models that a comparison is difficult. The largest effect of wall angle was at Mach number 1.1, where zero wall angle data are in better agreement with those from the sting-mounted configuration than those obtained with optimum wall angle. A portion of the interference is the result of increased blockage caused by the strut. Since optimum wall angle requires converged walls in the flow direction at Mach numbers 1.05 through 1.2, optimum wall angle would be expected to aggravate blockage interference and does not appear to be applicable for strut-mounted models. Strut interference studies have shown that strut interference can be reduced by varying wall angle; however, the wall angle schedule was found to be model configuration dependent.

5.0 MODEL GEOMETRIC EFFECTS

5.1 MODEL SIZE SELECTION

Large models can provide near full-scale Reynolds numbers in wind tunnels such as the AEDC Tunnel 16T and thus provide realistic viscous flow effects. They can also be constructed to reproduce more accurately the full-scale geometry features since protuberances and other small variations can be fabricated with reasonable tolerances. Instrumentation can be more readily installed and clearances for balances can be more accurately controlled. The major disadvantages are cost and inability to test large-scale

models in smaller facilities. Utilization of wind tunnels at high power conditions with small models is no longer cost effective with the rising cost of energy. The additional cost of a large model for testing at the same characteristic Reynolds number as a smaller model can be recovered in a few hours of testing as a result of reduced power cost at lower unit Reynolds numbers.

Afterbody drag is very sensitive to model size at Mach numbers near 1.0. If data near M = 1.0 are important then a small model size is required. The effect of model scale was investigated with the three models shown in Fig. 67 (Ref. 18). Shown in Fig. 68 is the integrated afterbody pressure drag based on aircraft wing area for these models. At Mach numbers above 0.95 and below 1.2, large differences in afterbody pressure drag coefficient were observed between the three scale models. The data were obtained at the same characteristic Reynolds number and wall angle. Approximately 50 percent of the aircraft drag rise at M = 1.0 occurred on the afterbody. A delayed aircraft drag rise for the larger model, a characteristic often observed for high blockage models, is entirely attributable to the afterbody drag rise being delayed by blockage interference effects. If data for Mach numbers in this range are important, then a small model should be used. Even the small model exhibits a variation other than would be expected between Mach 1.0 and 1.1. However, with the exception of Mach numbers between 0.95 and 1.2, excellent agreement was obtained in the data from the three models. The smallest model size is typical of models built to be used in 4-ft wind tunnels. In a 4-ft tunnel, the blockage would be 0.8 percent and span 52 percent of tunnel width, thus meeting usual aerodynamic testing criteria. Data in the smaller wind tunnel would be expected to be similar to those for the largest model tested in Tunnel 16T, i.e., the data at Mach numbers 1.0 should be used with caution.

The 1/9-scale and 1/4-scale F-16 models were tested using a sting mount with an annular jet as previously discussed. The afterbody axial-force coefficient for the two models at the same characteristic Reynolds number is shown in Fig. 69 as a function of Mach number. At 0-deg angle of attack the large differences observed near Mach 1.0 with the bodies of revolution (Fig. 68) were not observed. The afterbody projected area was much smaller for the aircraft configurations and thus reduces the effect of changes in the flow over the aft portion of the model. Reflected wave interference would be expected in the Mach number range from 1.0 to 1.2 for the largest model and is evident in the data. At 7-deg angle of attack (Fig. 70) the expected delayed drag rise occurs for the largest model.

Although the differences in drag coefficient near Mach 1.0 can be attributed to both blockage and wave interference, the effects of model length and blockage are difficult to separate and are very attitude and configuration dependent. Usually the drag near Mach 1.0 has very little impact on performance predictions because typical missions require negligible time at Mach 1.0. Therefore, data are seldom obtained at these Mach numbers when tests

are being conducted to optimize a configuration. A larger model size will allow testing at or very near flight Reynolds numbers, thus reducing errors if a configuration is sensitive to Reynolds number. When selecting a model size caution must be used when considering the mounting system and its contribution to the tunnel blockage. Typical struts for afterbody models have a blockage similar to that for the models. As shown previously, the strut interference is a function of its size. If Mach numbers very near Mach 1.0 are not necessary to achieve the objectives of a particular program, selection of a large scale model is recommended for the following reasons:

1. If a given characteristic Reynolds number is required, it can be achieved at lower tunnel power, thus reducing test costs.

2. For the same characteristic Reynolds number the support system size relative to model size can be reduced, thus reducing the effects of support interference.

3. The model can be constructed more accurately, and instrumentation space is increased.

5.2 EFFECT OF AFTERBODY GEOMETRY

Some experimenters (Ref. 19) have concluded that in all cases the complete model should be on a balance because afterbody geometry changes can influence the drag of the forward portion of the model. The effect of afterbody changes on forebody drag was investigated in the experiment reported in Ref. 16. The model and the boattails used are shown in Fig. 71. The afterbody pressure drag obtained by integrating pressure distributions on each of the boattails was significantly different as shown in Fig. 72. The forebody drag, shown in Fig. 73, was within the data repeatability for all three configurations despite large changes in the afterbody drag. The data indicate that in the Mach number range from 0.6 to 1.4 even large afterbody changes do not have a measurable effect on the pressure drag of the portion of the body ahead of the maximum body diameter. Thus, measurement of only afterbody drag for afterbody configuration studies is a valid test technique for jet effects testing in transonic wind tunnels.

5.3 EFFECT OF FOREBODY GEOMETRY

A similar investigation was conducted to determine the effect of a change in forebody geometry on afterbody drag. Shown in Fig. 74 is the pressure drag obtained by integration of pressures on the forebodies shown in the sketch. The blunt forebody had more than twice as much drag as the streamlined forebody at all Mach numbers. The afterbody drag for the two configurations is shown to be nearly the same at all Mach numbers in Fig. 75. In

addition, the afterbody pressure distributions were the same with either forebody configuration. Thus afterbody drag for this type of model configuration at 0-deg angle of attack appears to be insensitive to changes in forebody drag at Mach numbers from 0.6 to 1.4.

5.4 NOZZLE EXTERNAL GEOMETRY

Small changes in nozzle external geometry can result in significant changes in afterbody drag even when the projected area does not change. The boattail geometries shown in Fig. 76 were used during the investigation reported in Ref. 10. The jet-on pressure drag for each of the boattails is shown in Fig. 77. Even though the contour changes between the 10- and 15-deg boattails are small, significant differences in drag were observed at transonic and supersonic Mach numbers. The 25-deg boattail, which has a large separated area, has much greater drag than the other boattails at all Mach numbers. Thus, scale models should duplicate full-scale contours to avoid obtaining test data that may lead to incorrect conclusions.

5.5 BASE EFFECTS

One compromise often required for a scale model is an unrealistic base area at the nozzle exit. Very sharp full-scale nozzle exits cannot be scaled for small models, and clearance for balance deflections or pressure lines near the nozzle exit often result in a non-scale base. The boattail configurations shown in Fig. 76 were also tested with a smaller jet exit diameter. As shown in Fig. 78, the jet effect on afterbody pressure drag produced different results for the small change in jet diameter. Using the jet diameter, when expanded to ambient pressure, as a correlating parameter will provide better agreement between the sets of data; but, significant disagreements will still exist as a result of the local discontinuity at the base. To obtain the proper jet effect, every effort should be made to maintain a scaled base area at the nozzle exit.

5.6 INLET FAIRING

One would surmise that the entire flow field around an aircraft should be faithfully simulated to achieve satisfactory afterbody drag measurements. Without some type of engine simulator the jet cannot be simulated while simultaneously taking the inlet air on board. In the usual jet-effects test, there is, by necessity, a fairing over the inlet. There have been numerous investigations to determine the effect of a fairing over the inlet. The results of Refs. 3 and 20 show that there are measurable effects but that the effects on the integrated

forces are small. The model shown in Fig. 79 was tested with a full flowing inlet, an inlet mass flow ratio of approximately 50 percent, and inlet fairings as shown. As reported in Ref. 20 and shown in Fig. 80, except at Mach 1.0, there was very little effect on the afterbody force coefficients. The effect of the inlet fairing on pressure distributions was determined by subtracting pressures measured with the flow-through configurations from those for each of the other configurations. At Mach 0.9 and above, measurable differences in afterbody pressure coefficients were observed as shown in Fig. 81. (All of the data shown were for an angle of attack of 7 deg. The pressure coefficient differences were less at angles of attack of 0 deg.) The nozzle had very low closure to allow full inlet flow, and the changes in pressure coefficient and drag could be larger for a nozzle having a larger closure. Fairing of the inlet will cause local disagreement between pressure coefficients obtained in a wind tunnel and flight; however, for this configuration the afterbody axial-force coefficient was not a function of inlet configuration or spillage. Since large changes in forebody drag, as shown in Figs. 74 and 75, had no effect on afterbody drag or pressure distributions, the changes in pressure distributions as a result of inlet fairing may be attributed to the introduction of an unsymmetrical disturbance.

5.7 EFFECT OF EMPENNAGE

Since the aircraft horizontal and vertical tails are in close proximity to the afterbody and can have a significant influence on the flow field of the afterbody, they must be faithfully reproduced. A comprehensive study of the effects of the wing and empennage and reduced span empennage on fuselage afterbody drag at 0-deg angle of attack is reported in Ref. 3. As would be expected significant effects were observed, and configuration increments obtained without the lifting surfaces were found to be invalid. Larger effects would be expected with the lifting surfaces when the model angle of attack is other than 0 deg.

The performance accounting systems currently in use apply corrections for throttle-dependent drag (which are independent of aircraft attitude). The flow field over the afterbody is changed extensively at angle of attack or with horizontal tail deflection as a result of the lift distribution imposed by the horizontal tail. The data shown in Fig. 82 illustrate that the increment to correct the force data from the altered afterbody to the real afterbody configuration would be approximately 10 aircraft drag counts too large at $\alpha = 6$ deg if the 0-deg angle-of-attack data were used. These data indicate the importance of investigating afterbody aerodynamics with realistic empennage configurations and at conditions representative of flight attitudes. A performance accounting system that includes angle of attack and horizontal tail setting variations in throttle-dependent drag should be used to prevent large errors that can be introduced by using a nonlifting accounting system.

5.8 CONFIGURATION DETAILS

Many seemingly minor full-scale details are often overlooked or neglected. Although seldom simulated, bleed flows for cooling or environmental control systems have the potential for causing large changes in drag, particularly if the exits are normal to the local flow or in areas where flow separation is likely to occur.

The engine bay purge system for the YF-17 aircraft was simulated as shown in Fig. 83. The engine bay had screened openings at the top and bottom of each bay. Flow was provided by a bleed in the inlet. This exhaust system appeared to have the potential of causing large disturbances because it allowed flow from the higher pressure region on the bottom of the fuselage to the lower pressure region on top of the fuselage. Small changes in the pressure distributions were observed at subsonic Mach numbers, but the largest effects were at supersonic Mach numbers. The changes in the local pressure coefficients at Mach 1.2 are shown in Fig. 84. These pressure distributions illustrate that measurable effects of the bay purge exits, located at $x/L = 0.94$, $\theta = 0$, and 180 deg, were observed in areas removed from the exit location. Thus, consideration should be given to simulation of bleed flows and vents if their location is such that the flow could be expected to disturb the flow field around the afterbody.

6.0 MEASUREMENT TECHNIQUES

Depending on the objectives of an experiment there are many methods of measuring the desired aerodynamic forces and coefficients. Since the measurement techniques selected influence the accounting system used to define aircraft performance, careful consideration must be given very early in a program to the data uncertainty associated with each of the wind tunnel tests and its contribution to the overall performance estimate. As mentioned in Section 4.0, it is possible to reduce the effect of fixed facility-related errors by conducting all of the tests in the same wind tunnel.

6.1 UNCERTAINTY ANALYSIS

During the design of an experiment and selection of measurement techniques, a thorough uncertainty analysis will provide guidance in the selection of the measurements and test procedure that will produce the best chance of attaining the desired uncertainty for a single test or for all of the tests required to determine total aircraft performance. The uncertainty of a given measurement is composed of two quantities, bias and precision (illustrated on the following page), that are propagated through the data reduction system of equations and appear in the final test data. The magnitude of the uncertainty in the final

data is dependent not only on the measurement techniques but also upon how the measurements are combined to obtain the final data, i.e., the data reduction equations. A complete discussion of the uncertainty analysis and propagation of error is beyond the scope of this report but may be found in Ref. 21.
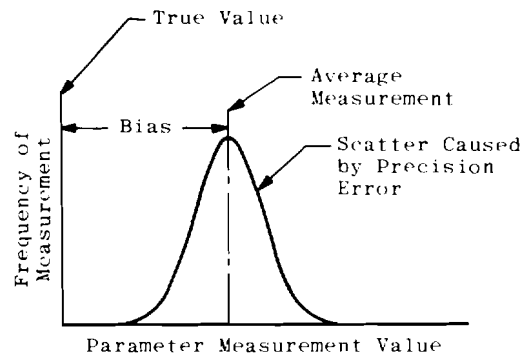
Careful consideration should be given to the bias and the precision independently, since the bias errors can often be eliminated by taking incremental differences between configurations when the bias errors do not change. For instance, the bias error in free-stream static pressure would drop out of the difference in drag between two configurations if the afterbody projected area is the same. Although some sacrifice in productivity would result, the average of repeated measurements can be used to obtain better precision, if done properly. Comparison of the uncertainty between various measurement techniques is the only way to evaluate one technique against another. Careful consideration must be given as to how an instrument will be used in evaluating uncertainty. For instance, bare balance precision is not the total uncertainty when the balance is used with metric breaks and seals. The uncertainty of a pressure integration is subject to errors produced by pressure dynamics and insufficient measurements to determine the required pressure distribution. These effects are often difficult to quantify in an uncertainty analysis but must be considered when comparing one measurement technique to another.

6.2 METRIC BREAK CHOICES

The uncertainty in drag of a portion of a body is highly influenced by the choice of the portion of the body to be considered. For example, the portion of the body on which the forces are measured (metric) is selected during the model design and cannot be arbitrarily changed during testing. A large portion of the uncertainty for force and moment tests results from poor metric break selections. When the force is defined by integrating pressures the portion of the body that is included in the integration can be changed at will, provided sufficient pressure orifices are installed to define the pressure distribution on the portion of the body that is of interest.

33

When a cavity pressure correction to balance data is required, the uncertainty in the difference between free-stream static pressure and the cavity pressure can be a significant contribution to the uncertainty of drag measurements. In addition, pressure differences across the metric seal can introduce significant forces. Shown in Fig. 85 is a typical nacelle balance arrangement to measure throttle-dependent drag using a "shell"-type balance with a metric break at the location of the maximum cross section. The total axial force and the contribution of each of the corrections are shown in Fig. 86 for a subsonic and supersonic Mach number. The cavity and base pressure correction are opposite in sign for the two test conditions. Note the magnitude of the metric seal correction that is often not completely accounted for. The metric split seal correction must be determined with the balance by establishing the proper pressure differences between the internal and external portions of the nacelle, which results in a change in cavity area and tension in the seal. The effective cavity area can also best be determined during these calibrations. An uncertainty that cannot be determined for such a seal is the effect of an external nonuniform pressure distribution around the seal as would exist during testing. For this reason it is desirable to minimize the seal correction. For supersonic Mach numbers, Fig. 86b, the pressure differential around the seal varied from zero to six times the average pressure differential. For a seal at the top of a strut, the pressure distribution around the seal is generally more uniform than around a seal normal to the body axis. The uncertainty introduced by the contribution of the seal and cavity corrections could be essentially eliminated with a metric break parallel to the axial-force axis such that total nacelle axial force would be measured by the balance, e.g., along the top of the nacelle in Fig. 85. The uncertainty would be introduced into normal force, but, for small angles of attack, would have a small contribution to drag.

If a metric break is not sealed, flow from high-pressure regions to lower pressure regions can cause separation of the flow over a major portion of the body in addition to spurious internal force. Since the metric break deflects as the balance deflects, a mismatch in the body contour with rearward- and forward-facing steps results. Large discontinuities in pressure distribution have been observed for a model having multimetric breaks. (The model was capable of vectored thrust, which added to the balance deflections.) During a portion of the test, the aft balance was locked and the aft metric break taped to determine the effect of metric break deflection. Shown in Fig. 87 is the change in pressure coefficient along the top and bottom centerline between the locked and free aft balance configurations at the same test condition. The forward balance was not loaded in normal force at $\alpha = 0$ and therefore did not deflect. The same pressure differences are shown in Fig. 86b, $\alpha = 12$ deg, which did cause the forward balance to deflect. The positive and negative pressure changes tend to offset each other in the axial-force integration; however, large changes in lift would be expected over that for a nondeflecting metric break. In addition, the discontinuity could cause separation of the flow. Similar discontinuities in pressure distributions were observed for the forward metric break but are not evident in the pressure differences shown in Fig. 86.

However, they were not resolved by eliminating the deflection. Note that the model was strut mounted. Had the whole model been metric, the cavity corrections could have been minimized and model discontinuity at metric breaks would have been eliminated. To effect a seal, some type of restraint is required. Each metric break adds an uncertainty to balance readings that is a function of balance deflections. When the deflections of two balances become involved, it becomes impossible to arrive at a loading matrix to correct for the seal contribution to each of the balance loads. When the seal is between two balances, often the only meaningful force is the sum of the two balance readings.

Repeatability of data is of prime importance for configuration studies. Friction in a balance system causes the nonrepeatability to be equal to twice the seal friction force. A friction type of seal is to be avoided at all costs. Although they may appear frictionless without a pressure differential, many slot-type seals contribute large friction forces when a differential pressure is applied to the seal. If this type of seal must be used, repeatability should be evaluated by applying loads to the model with a pressure differential across the seal. The most effective positive seal appears to be a loosely formed seal, shown below, which is fastened at both edges because it allows for balance deflections and differential temperature expansion without providing friction or significant restraint to the balance.
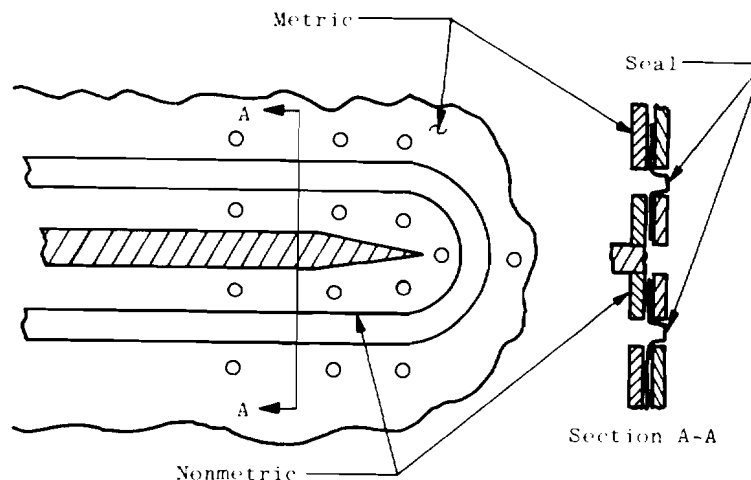
6.3 EFFECT OF BELLOWS

Thrust is a function of the interaction of the jet flow and free-stream flow for nozzles having external expansion surfaces. To evaluate performance when this type of nozzle is used, thrust must be measured. The largest contribution to the uncertainty of the thrust measurement is that associated with bridging the balance with the jet flow.

Current methods of bridging the balance with the high-pressure air involve the use of bellows assemblies to provide a repeatable and minimal effect on the balance. Shown in Fig. 88 is a typical bellows assembly. Design criteria to provide minimum uncertainty in the thrust measurement are a low spring constant for the bellows, minimum axial momentum where the internal flow duct becomes metric, minimum pressure differential across the bellows, and placement of the bellows relative to the balance to minimize bellows deflection. Low spring constant for the bellows minimizes the effect of movement of the bellows relative to the balance caused by pinned joints or temperature gradients between the balance and the bellows assembly. Extensive balance calibrations are required to account for the effect of bellows pressure differential on the balance. When testing is to be conducted at various free-stream static pressures, pressure differential and momentum corrections must be determined independently. These corrections are as high as 5 percent of the balance capacity and cannot be neglected. The momentum correction is required to correct for the momentum of the air crossing the bellows and is determined by static testing of sonic nozzles at test altitude pressures. The momentum correction is only a function of the bellows chamber pressure as long as the bellows sonic nozzles remain choked. Thrust data obtained for such a system have been found to be repeatable to $\pm 1/2$ percent of thrust for a wide range of nozzle areas at thrust values as low as 20 percent of the balance capacity. At balance capacity the data repeatability is approximately ± 0.1 percent of thrust. If drag is to be obtained by subtracting static thrust from wind-on thrust minus drag, then the magnitude of the repeatability would be $\sqrt{2}$ greater than the balance because the precision of the balance would enter into both the wind-on value and the static value.

6.4 MULTIPLE BALANCE INSTALLATIONS

Multiple balance installations are often used for analysis of the contribution of various components to performance. If overall performance is the primary goal such installations are detrimental to the performance uncertainty. The uncertainty contribution of multiple metric breaks greatly increases the overall uncertainty of even piggyback balance installations designed to measure thrust and thrust minus drag. When the sum of two balances must be used, such as thrust and drag, the uncertainty of the sum includes the uncertainty of each of the balances in addition to the uncertainties introduced by multiple metric breaks. Performance advantages of configurations are often within the uncertainty of a well-designed experiment. If multiple balance configurations are used, then a careful uncertainty analysis must be made to determine if the measurement uncertainties will allow the test objectives to be realized.

6.5 PRESSURE MEASUREMENTS

The use of pressure measurements to determine pressure drag is often discounted by many experimenters based on experiences in which sufficient pressures were not used to define adequately the distribution in areas of high-pressure gradient or high rates of area change. There are many experiments for which the uncertainty would be much less if pressures were used in place of balances such as for experiments in which the skin friction is very large compared to the pressure drag, or where metric breaks will disturb the flow in the region of interest. If it is desired to define the force on a portion of a model that cannot be instrumented with a balance, the use of pressure instrumentation should be considered. Nacelle drag previously shown in Fig. 86 as measured by a balance was also measured by integrated pressures on the opposite wing. A comparison of the forces measured by the two methods is shown in Fig. 89, and a comparison of the drag coefficient as a function of Mach number is shown in Fig. 90. Excellent agreement was obtained at subsonic Mach numbers; but, beyond Mach number 0.9 a difference greater than the uncertainty of the measurements was observed. An error in free-stream static pressure would essentially cause equal and opposite errors in the balance measured and pressure integrated forces, but an error an order of magnitude greater than the uncertainty in free-stream static pressure would be required to make drag coefficients equal. As mentioned previously the pressure differential across the seal varied greatly around the nacelle at supersonic Mach numbers. The seal correction for the lowest pressure differential would be zero and for the highest difference the correction would be 52 lb or more than twice the total load. The large difference between the balance and pressure forces is probably attributable to an incorrect seal correction.

Careful selection of the location of pressure orifices is essential to achieve a minimum uncertainty. Many computer codes are now available that will predict the pressure distribution for complex model configurations. Although the codes may not predict the pressure level accurately, the pressure gradients generally agree well with experimental data. Experimental data on similar configurations can also be used to provide engineering judgement in the selection of orifice locations. The usual solution to achieve highly repeatable data is to overinstrument an afterbody; this method is acceptable as long as the instrumentation does not become so dense that a large number of erroneous pressures result from pinched tubing. A typical example of the use of previous data to select orifice locations is shown in Fig. 91 from Ref. 8. The orifice locations for seventy orifices were selected based on the pressure distributions obtained from two hundred orifice locations. The pressure distributions obtained with two hundred orifices were compared for variations in test parameters such as angle of attack, nozzle position, nozzle pressure ratio, horizontal tail setting, and Mach number. Areas were then assigned to the orifices and the data were recalculated using only 70 orifices. The differences shown in Fig. 91 are the differences between integrating the pressures for the same data point with seventy orifices and two

hundred orifices. The differences in general are as small as the basic repeatability for two hundred orifice locations over a wide range of test conditions, attitudes, and for two nozzle configurations. Although such a limited number of orifices is not recommended, it is obvious if critical areas are adequately covered, the integration will be valid despite large gradients.

There are several methods available to measure the local pressure on a model. One method is to use individual transducers to measure each pressure. In normal transonic wind tunnels these transducers are located outside the test section. Another is to use a Scanivalve® and one transducer to measure up to 48 pressures. The individual transducer precision is approximately a factor of two better than the Scanivalve transducers. But, for pressure drag derived from the sum of pressure area terms, the transducer precision becomes an insignficant factor because the precision of pressure drag for equal areas is less than that for the transducer by one over the square root of the number of pressures for either multiple transducers or multiple measurements with individual transducers. Differences in the two methods are difficult to define but are primarily attributable to pneumatic lag in the long lines for the facility transducers and changes in the reference pressure during the time required to scan the Scanivalve. For most installations the Scanivalve seems to produce more repeatable pressure drag, but the pressure locations must be selected to minimize pressure changes as the valve steps to each port to achieve the shortest possible measurement time.

7.0 CONCLUSIONS

7.1 SUPPORT SYSTEMS

A strut support is the least desirable support system and produces significant errors in performance estimates and configuration studies, particularly at supersonic Mach numbers.

A wing-tip support system can contribute significant error in afterbody drag at subsonic Mach numbers near Mach 1.0. Careful attention must be paid to the downstream support structure if data at Mach numbers near unity are considered important.

A sting support appears to have the least interference on afterbody drag but large sting diameters and the close proximity of a downstream support structure can significantly reduce afterbody drag.

Simulation of a full jet with an annular jet around a sting has been demonstrated to provide minimal error in afterbody drag for aircraft configurations.

7.2 JET SIMULATION

Large differences in afterbody drag have been measured when jet temperature is varied. The magnitude of the effect of jet exhaust temperature on afterbody drag coefficient is a function of configuration and free-stream conditions.

Changes in the jet exhaust specific heat ratio do not cause significant changes in the afterbody drag coefficient.

Changes in the jet gas constant produce incremental changes in drag coefficient proportional to the change in gas constant and are similar to the effect of varying temperature. The drag coefficient increments are believed to be a result of changes in entrainment and are not a function of jet pressure ratio, suggesting that a correction for temperature effects could be obtained by using ambient gas exhausts with different gas constants.

Large changes in nozzle area ratio produce changes in drag coefficient similar to changing gas constant, and if the relationship between gas constant, area ratio, and temperature can be established, corrections for temperature effects could be determined by testing with several area ratios with an ambient temperature gas. Further work is required to determine methods for correcting for temperature effects.

7.3 WIND TUNNEL CALIBRATION

Drag coefficient for a portion of a body is very sensitive to an error in wind tunnel Mach number. An error in Mach number results in an error in afterbody drag coefficient proportional to the afterbody projected area.

Small systematic errors in tunnel calibration as a function of Reynolds number must be accounted for to determine the effect of Reynolds number. The effect of Reynolds number on afterbody pressure drag coefficient at subsonic Mach numbers has been found to be generally within the Mach number uncertainty.

The effect of tunnel noise on the scale boundary layer should be considered when Reynolds number effects on afterbody drag coefficient are attributable to shock boundary-layer interactions.

The Tunnel 16T optimum wall angle schedule reduces the effect of reflected wave interference for sting-mounted models but can aggravate interference for strut-mounted models.

7.4 MODEL GEOMETRIC EFFECTS

Large-scale models may be tested in Tunnel 16T, but some errors caused by reflected wave interference can be expected in the Mach number range in which the reflections would be expected to impinge on the afterbody. However, the wave interference is significantly less than would be experienced in a solid wall tunnel.

Large afterbody changes do not have a measurable effect on the portion of the body ahead of the maximum cross section. Measurement of only afterbody drag increments is a valid technique for afterbody configuration studies over the Mach number range of Tunnel 16T.

Nozzle external contours, base area, empennage, and bleed flows can have a significant effect on afterbody aerodynamics and should be duplicated as faithfully as possible.

Fairing of a fighter aircraft inlet produced measurable effects on pressure distributions, but the disturbances tend to cancel and produce only small effects in the aerodynamic force coefficients of the afterbody.

7.5 MEASUREMENT TECHNIQUES

Selection of measurement techniques should be made on the basis of an uncertainty analysis in which the effect of fixed and random errors is properly considered.

Balance metric breaks, bellows assembly seals, pressure dynamics, and pressure lag time all add an uncertainty to aerodynamic force measurements in addition to the uncertainty of the instruments.

8.0 RECOMMENDATIONS

When an afterbody experiment is planned, the impact of the many compromises required to achieve the objectives must be considered.

The largest errors at transonic and supersonic Mach numbers are often introduced by the support system. If at all possible a sting support with an annular jet should be used, even for the twin engine aircraft. If a low-interference support system cannot be used, the support interference should be evaluated to ensure that the objectives of the test can be achieved with the proposed support system.

Exhaust gas temperatures of typical afterburning turbojets will result in lower afterbody drag than that measured using ambient temperature air. The incremental effect of jet exhaust temperature on drag coefficient varies with boattail configuration and may affect the results of tests conducted to optimize an afterbody configuration. Further work is required to determine a method of correcting drag coefficient obtained with one exhaust temperature to that which would be obtained at any desired temperature.

Although current jet simulation knowledge does not allow exact simulation of a hot jet, the error in drag coefficient can be reduced by matching a jet shape parameter, such as the ratio of jet diameter when expanded to free-stream static pressure to jet exit diameter.

Drag coefficients for a complete model are more accurate; however, if drag coefficients must be determined for a portion of a body, they will be very sensitive to an error in Mach number. To obtain data having the required accuracy, every effort should be made to minimize the Mach number uncertainty. When attempting to determine the effect of Reynolds number on afterbody pressure drag, the effect of Reynolds number variation on the tunnel calibration must be accounted for.

Large-scale models are expensive, but it may be more cost effective to build a large model and reduce power consumption to achieve a desired characteristic Reynolds number. The model length should be limited to avoid reflected wave interference on the afterbody for the Mach numbers of interest.

Although inviscid incompressible theory predicts that changes in afterbody drag change forebody drag, large afterbody configuration changes have not resulted in measurable changes in forebody drag coefficient for transonic Mach numbers. Measurement of forces on only the afterbody is a valid method of determining a minimum drag configuration provided careful consideration is given to placement of the metric break.

The aircraft afterbody configuration should be as exact as possible to achieve the correct afterbody pressure distributions; however, effects such as fairing of an inlet do not produce significant changes in afterbody drag coefficient because of a tendency for negative and positive changes in local pressures to cancel one another.

Selection of the parameters to be measured and the method to achieve a test objective should be based on a thorough uncertainty analysis with proper consideration of bias and precision separately since bias errors often do not influence configuration studies.

41

Metric breaks cause flow disturbances as a result of balance deflections and introduce an uncertainty in force measurements that cannot be completely accounted for. Therefore, metric breaks should be eliminated, if possible, or carefully placed if they must be used.

Measurement of surface pressures and integration with the appropriate projected areas is a valid method of measuring afterbody forces and provides local flow characteristics that can effectively be used to optimize configurations.

REFERENCES

1. Reichenau, D. E. "Sting and Strut Support Interference Effects on a Cylindrical Model with an Ogive Nose at Mach Numbers from 0.7 to 1.4." AEDC-TR-72-175 (AD-905771L), November 1972.

2. German, R. C. "Strut Support Interference on a Cylindrical Model with Boattail at Mach Numbers from 0.6 to 1.4." AEDC-TR-76-40 (AD-A024473), May 1976.

3. Galigher, L. L. "Integrated Airframe Nozzle Performance Characteristics of a Generalized Twin-Jet, Air Superiority Fighter Aircraft Model at Mach Numbers from 0.6 to 1.6." AEDC-TR-73-125 (AD-912073L), July 1973.

4. Price, E. A., Jr. "An Investigation of F-16 Nozzle-Afterbody Forces at Transonic Mach Numbers with Emphasis on Support System Interference." AEDC-TR-79-56 (AFAPL-TR-79-2099), December 1979.

5. Price, E. A., Jr. "A Parametric Investigation of the Annular Jet Concept for Obtaining Afterbody Drag Data at Transonic Mach Numbers." AEDC-TR-77-104 (AD-050891), February 1978.

6. Jackson, F. M. "Calibration of the AEDC-PWT 16-Ft Transonic Tunnel with the Propulsion Test Section at Various Reynolds Numbers." AEDC-TR-77-121 (AD-A057877), August 1978.

7. Lucas, E. J. "Wind Tunnel Results from a Nozzle Afterbody Test of a 0.2-Scale Fighter Aircraft in the Mach Number Regime of 0.6 to 1.5. Vol. I — Test Technique Evaluation." AEDC-TR-79-10 (AD-B036406L), April 1979.

8. Lucas, E. J. "Evaluation of Wind Tunnel Nozzle Afterbody Test Techniques Utilizing a Modern Twin-Engine Fighter Geometry at Mach Numbers from 0.6 to 1.2." AEDC-TR-79-63, 1980.

9. Lucas, E. J. "Wind Tunnel Results from a Nozzle Afterbody Test of a 0.1-Scale Fighter Aircraft in the Mach Number Regime of 0.6 to 1.6." AEDC-TR-78-25 (AD-B028240L), June 1978.

10. Galigher, L. L., Yaros, S. F., and Bauer, R. C. "Evaluation of Boattail Geometry and Exhaust Plume Temperature Effects on Nozzle Afterbody Drag at Transonic Mach Numbers." AEDC-TR-76-102 (AD-A030852), October 1976.

11. Peters, W. L. "An Evaluation of Jet Simulation Parameters for Nozzle Afterbody Testing at Transonic Mach Numbers." AEDC-TR-76-109 (AD-A031525), October 1976.

12. Peters, W. L. "Jet Simulation Techniques: Simulation of Temperature Effects by Altering Gas Composition." AEDC-TR-78-43 (AD-A067084), March 1979.

13. Bergman, D. "Effects of Engine Exhaust Flow on Boattail Drag." *Journal of Aircraft*, Vol. 8, No. 6, June 1971, pp. 434-439.

14. Compton, W. B. "An Experimental Study of Jet Exhaust Simulation." NASA TM X-71975, June 1974.

15. Bauer, R. C. "A Method for Estimating Jet Entrainment Effects on Nozzle-Afterbody Drag." AEDC-TR-79-85, 1980.

16. Spratley, A. V. "An Investigation of Boattail Geometry and Reynolds Number Effects on Forebody and Afterbody Drag at Transonic Mach Numbers." AEDC-TR-76-161 (AD-A035872), February 1977.

17. Nichols, James H. "Determination of Optimum Operating Parameters for the PWT 16-Ft Transonic Circuit Utilizing One-Percent Bodies of Revolution." AEDC-TN-59-100 (AD-225362), September 1959.

18. Reichenau, David E. A. "An Investigation of Model Scaling Effects at Mach Numbers from 0.60 to 1.40." AEDC-TR-73-202 (AD-915551L), December 1973.

19. Aulehla, F. and Besigk, G. "Reynolds Number Effects on Fore- and Aftbody Pressure Drag." AGARD-CP-150 (Paper No. 12), March 1975.

20. Lowry, Randolph L. "Effects of Inlet Fairing and Spillage on Nozzle/Afterbody Pressure Forces of a 1/9-Scale Fighter Aircraft at Transonic Mach Numbers." AEDC-TR-79-37 (AD-B039607L), July 1979.

21. Abernethy, R. B. and Thompson, J. W., Jr. "Handbook — Uncertainty in Gas Turbine Measurements." AEDC-TR-73-5 (AD-755356), February 1973.
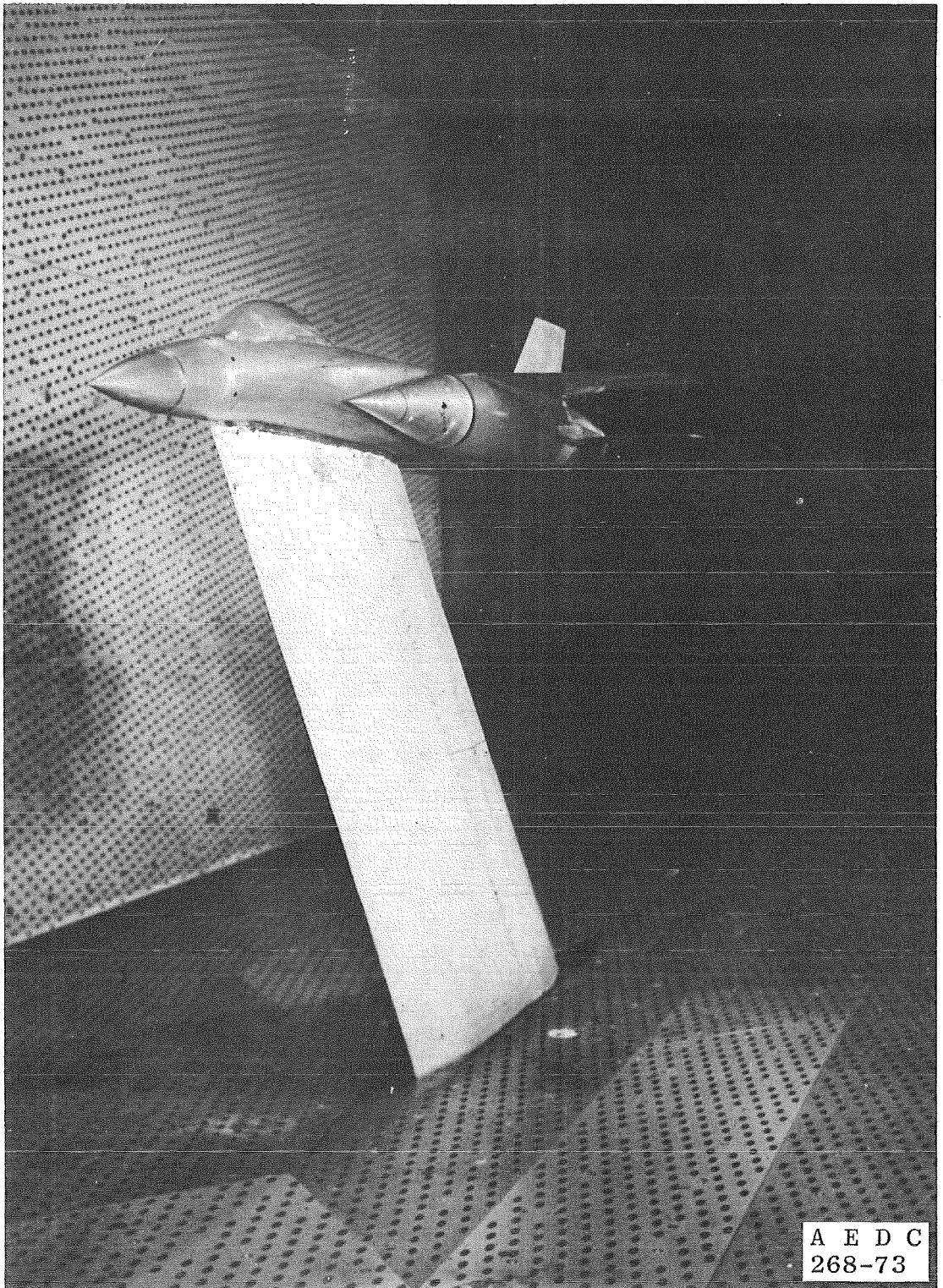
a. Research model
Figure 1. Typical strut-supported model installation.

AEDC
1705-75

b. B-1 afterbody model
Figure 1. Continued.
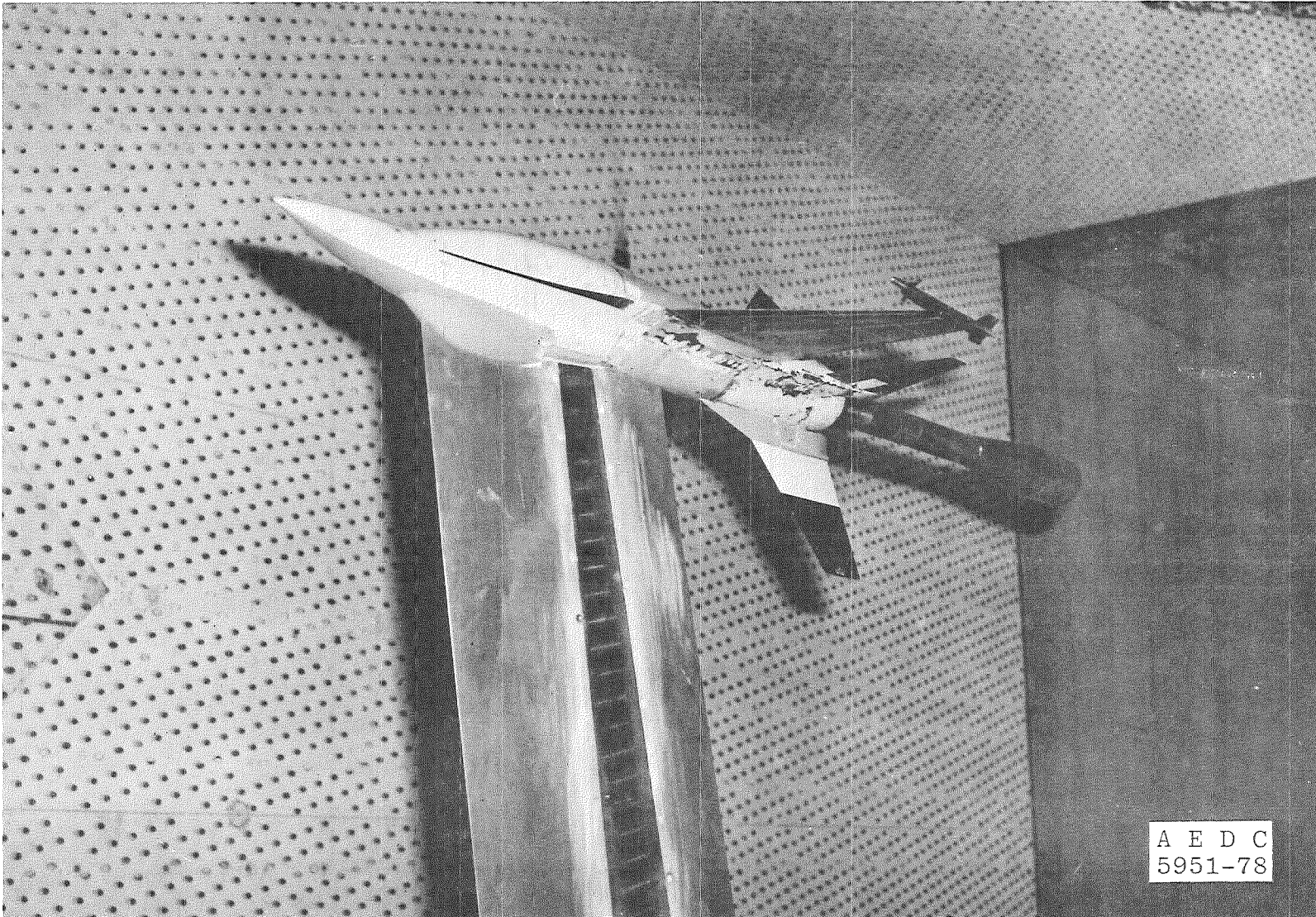
c. 1/9-scale F-16 model
Figure 1. Concluded.
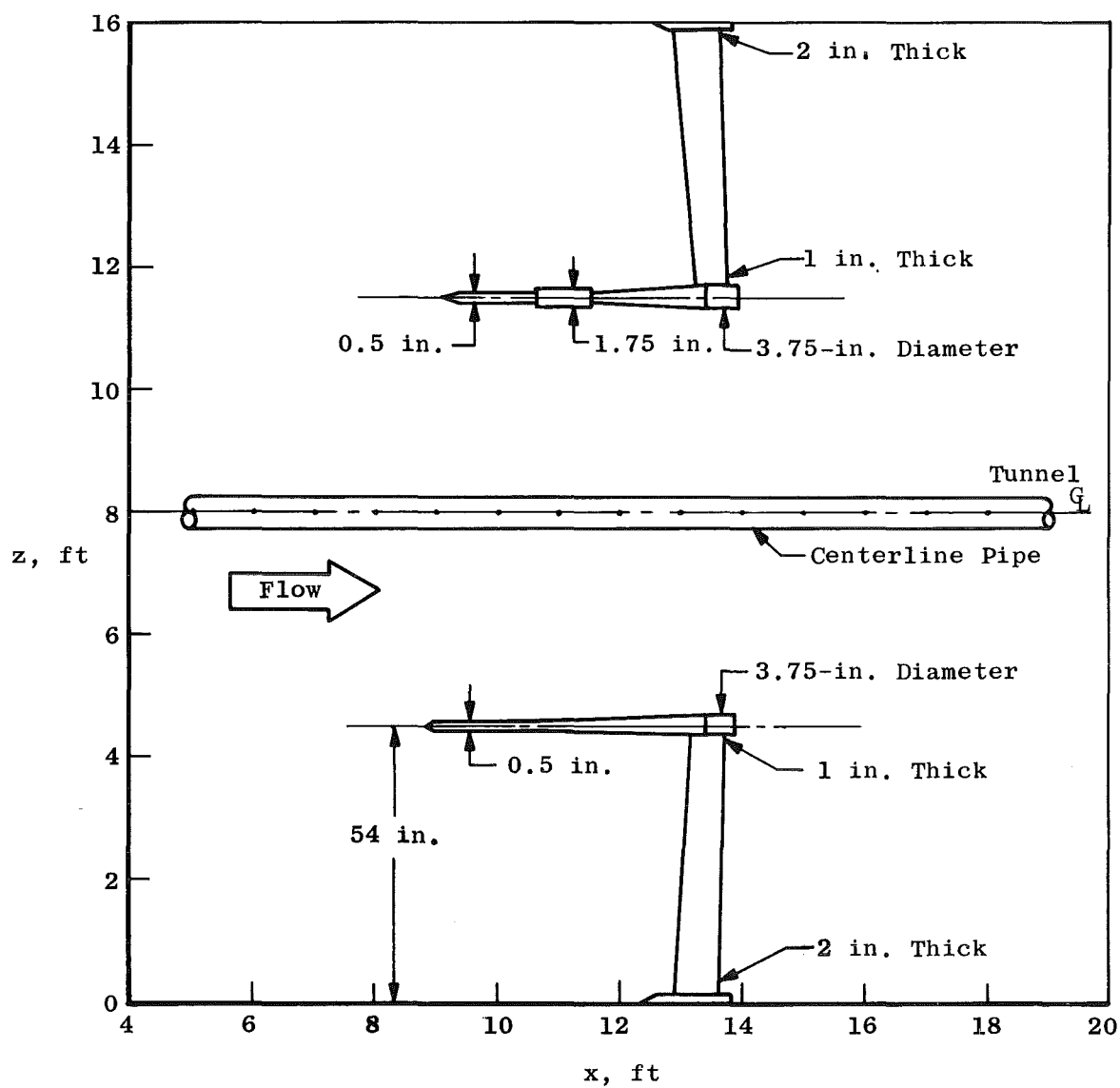
Figure 2. Probe installation in Tunnel 16T.

$$\Delta C_p = C_{p_{\text{with probes}}} - C_{p_{\text{no probes}}}$$

Centerline Pressure Distribution
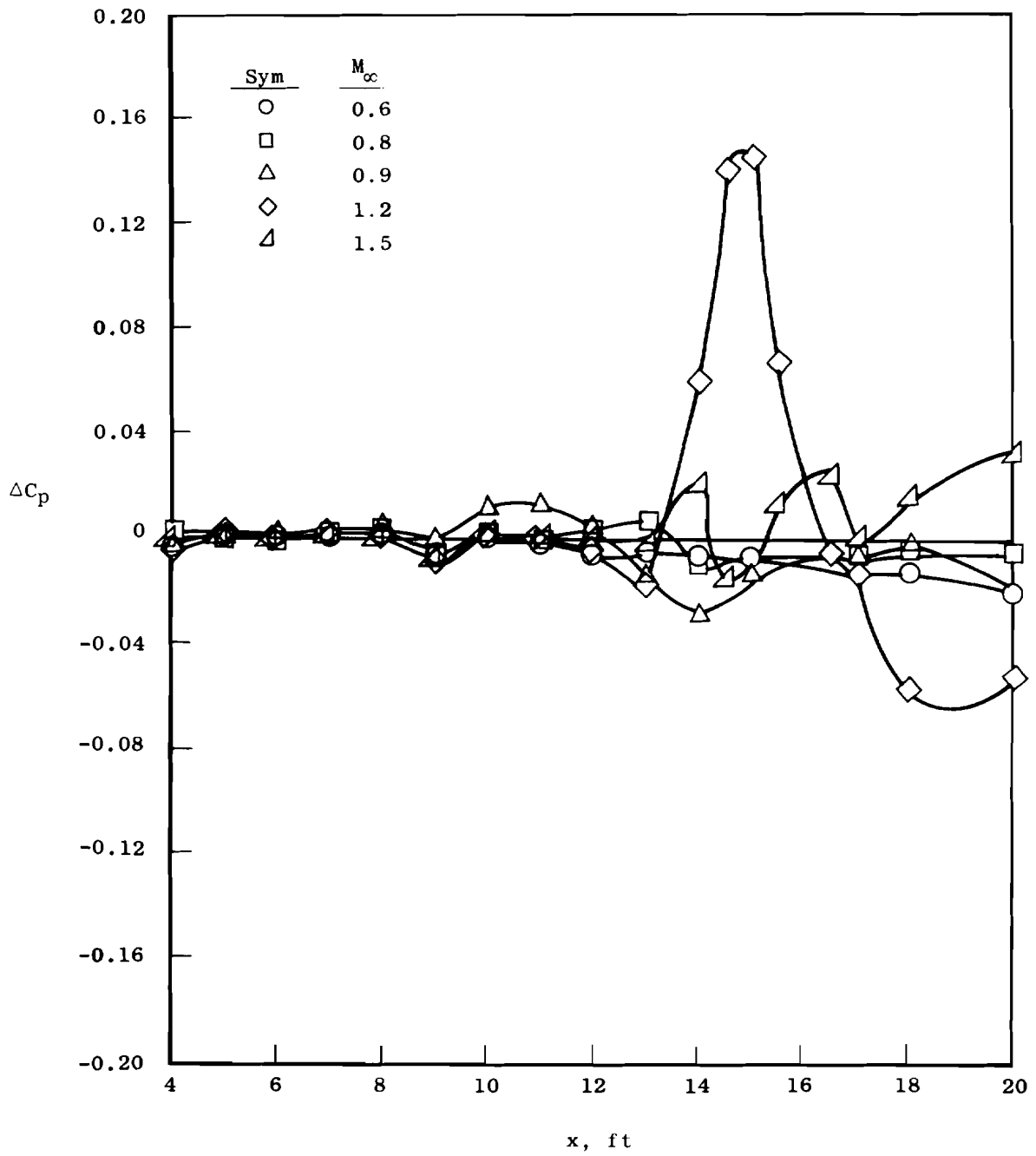
a. Tunnel centerline
Figure 3. Effect of probe installation on tunnel pressure distribution.

$$\Delta C_p = C_{p_{\text{with probes}}} - C_{p_{\text{no probes}}}$$

Floor Pressure Distribution

Sym	M_∞
○	0.6
□	0.8
△	0.9
◇	1.2
◿	1.5

Orifices Located
1 ft Off Centerline
of Bottom Wall

ΔC_p

x, ft
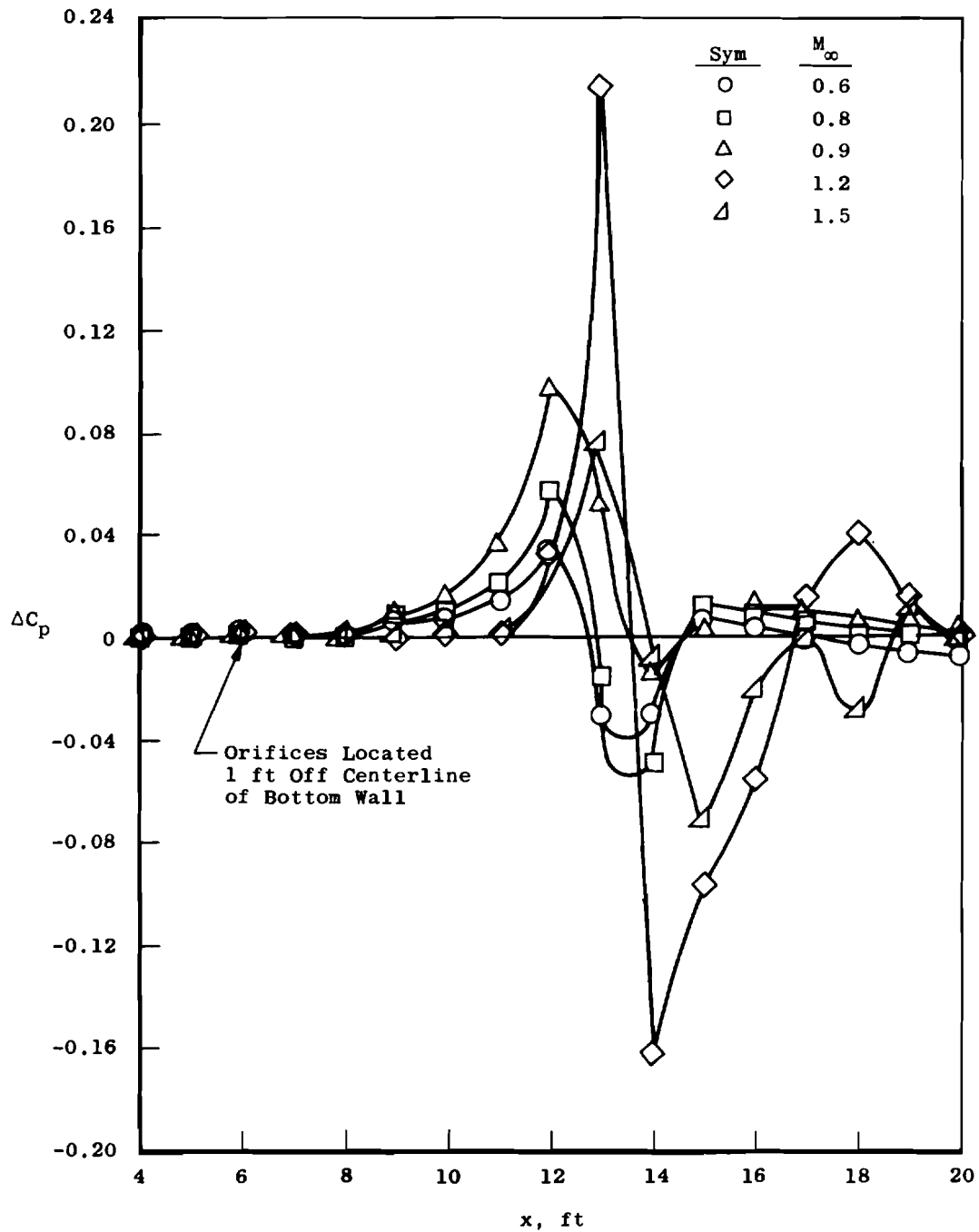
b. Tunnel floor
Figure 3. Concluded.
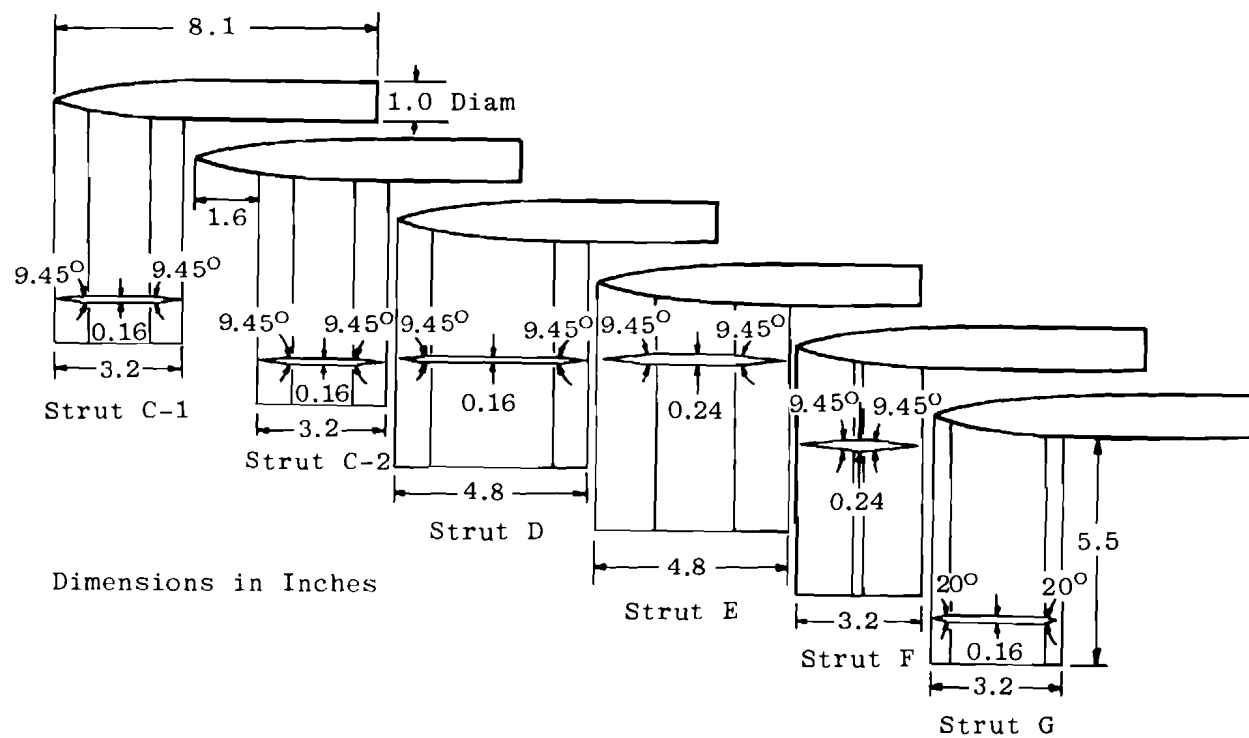
Figure 4. Typical strut configuration.

Sym	Strut	t/c	c, in.
⭘	C-1	0.05	3.2
△	C-2	0.05	3.2
---	Sting	---	---

M_∞
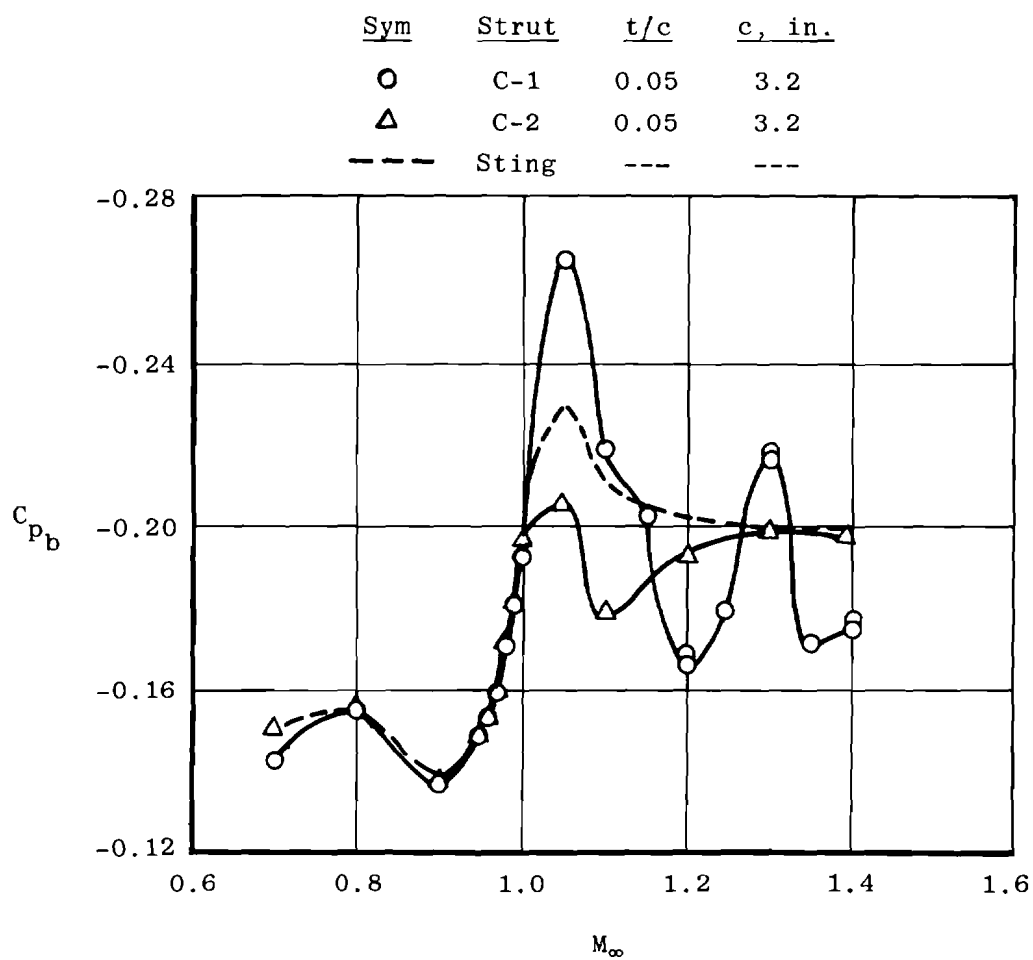
Figure 5. Effect of strut location on base pressure coefficient.
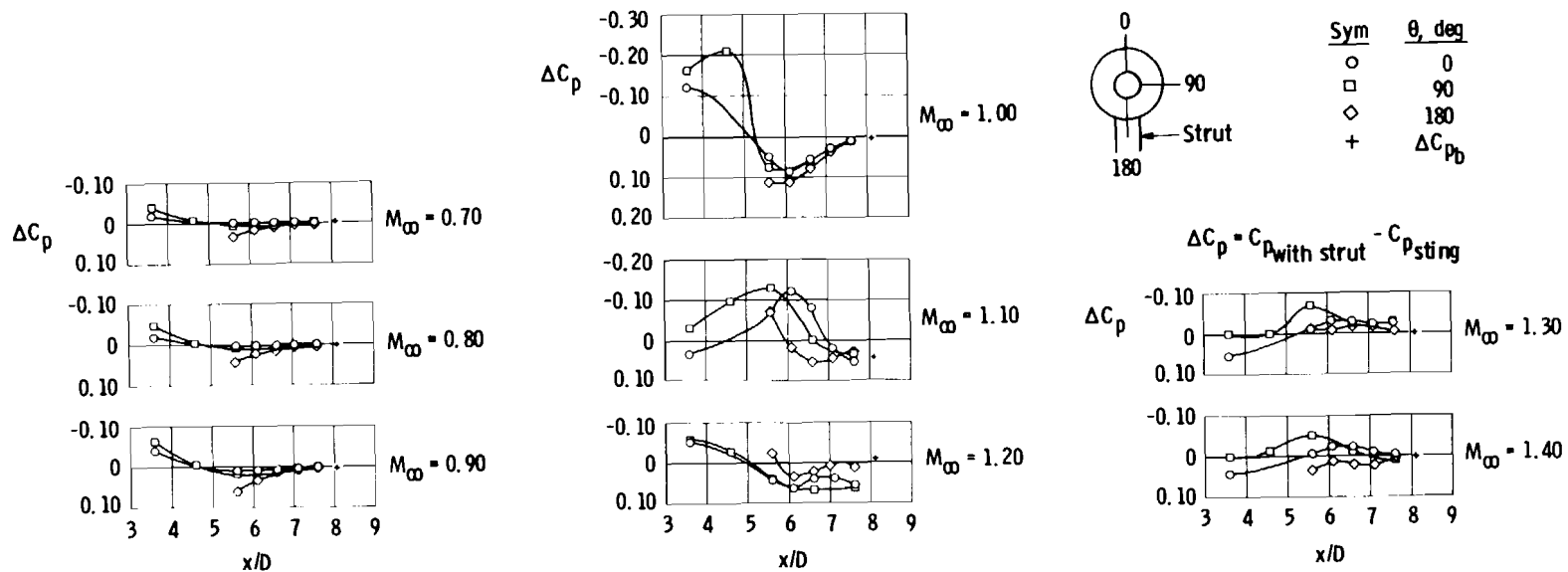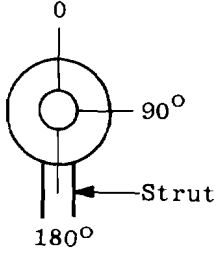
Figure 6. Incremental effect of a strut on model local pressure
coefficients (strut C-2).

Sym	Strut	t/c	c/D	Location of Strut Leading Edge
○	C-1	0.050	3.2	$x/D = 0$
□	C-2	0.075	3.2	$x/D = 0$
△	D	0.033	4.8	$x/D = 0$
◇	E	0.050	4.8	$x/D = 0$
◇	F	0.050	3.2	$x/D = 1.6$

$$\Delta C_p = C_{p_{\text{with strut}}} - C_{p_{\text{sting}}}$$
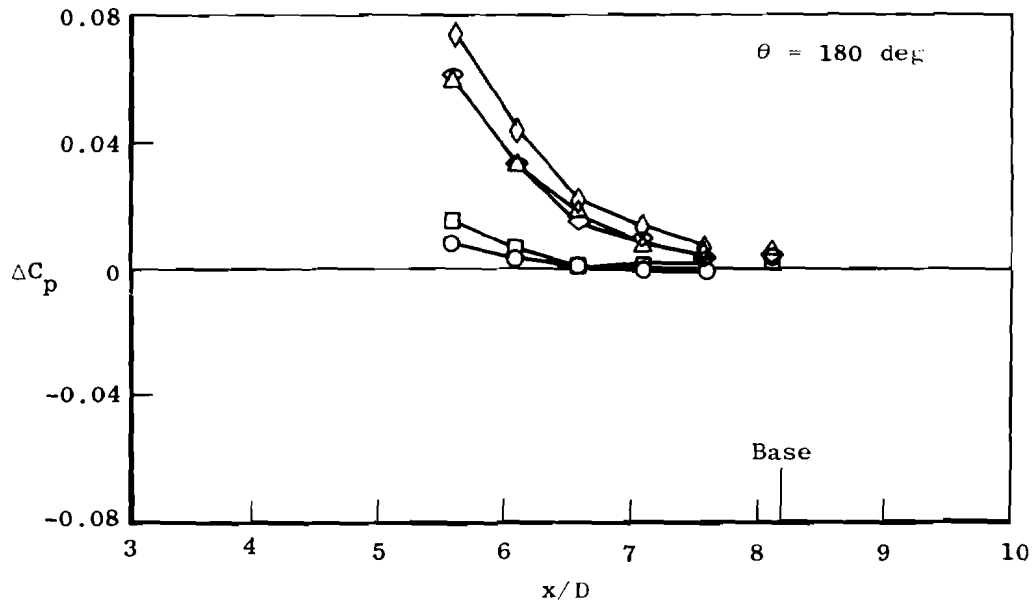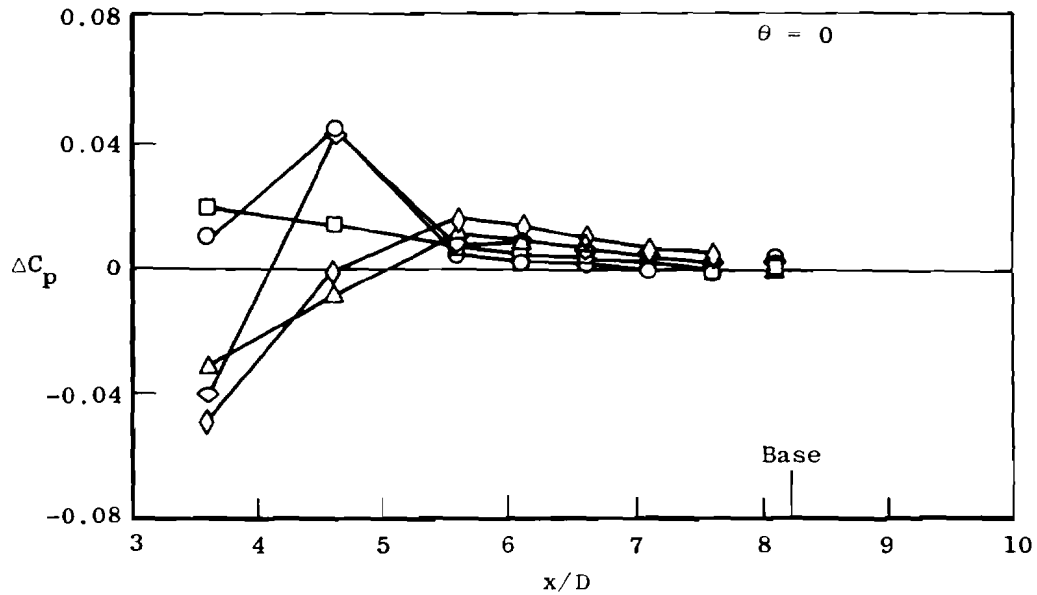
a. $M_\infty = 0.9$

Figure 7. Effect of model strut geometry on local model pressure coefficients.

Sym	Strut	t/c	c/D	Location of Strut Leading Edge
O	C-1	0.050	3.2	x/D = 0
□	C-2	0.075	3.2	x/D = 0
△	D	0.033	4.8	x/D = 0
◇	E	0.050	4.8	x/D = 0
⬡	F	0.050	3.2	x/D = 1.6
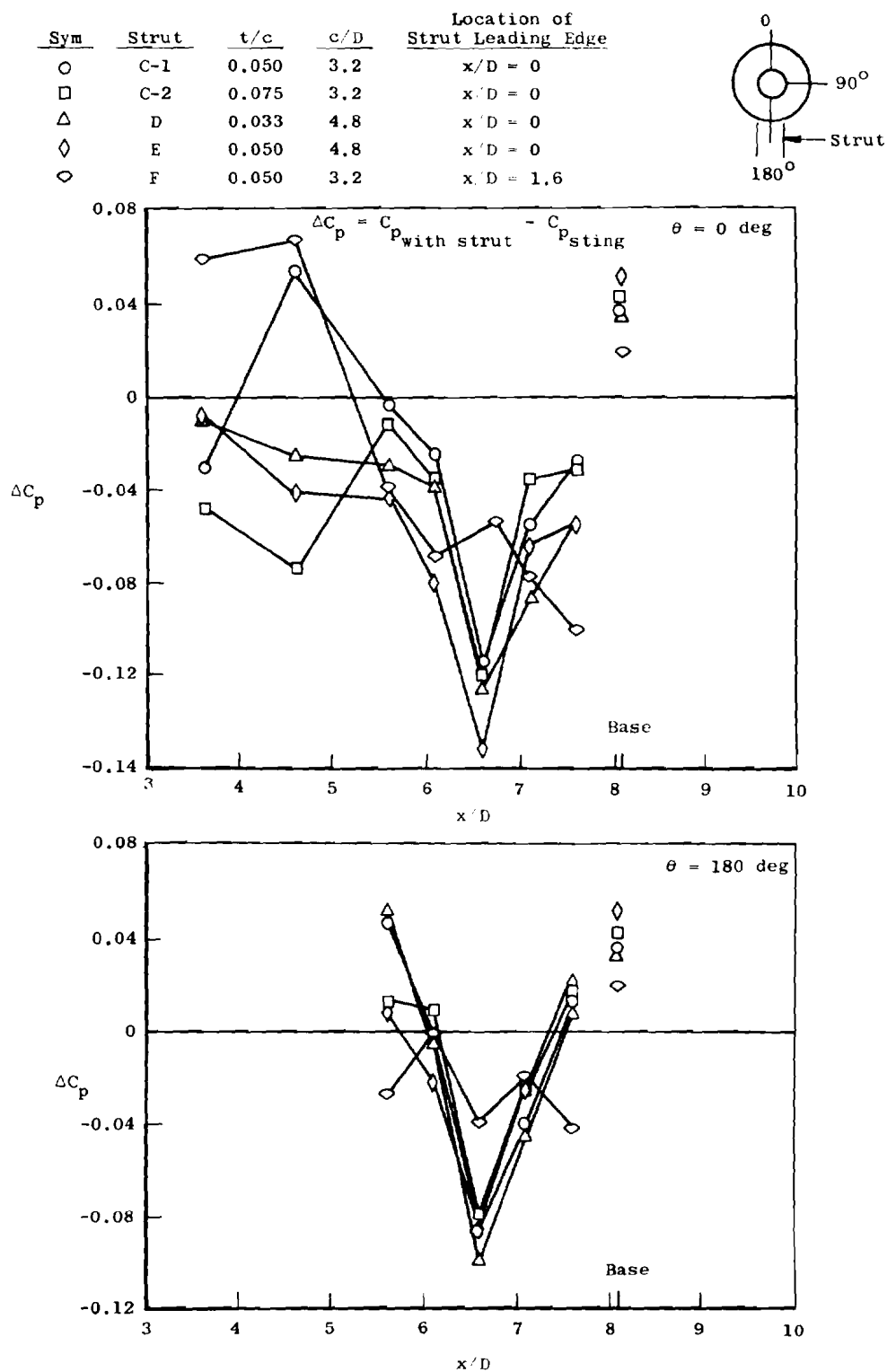
b. $M_\infty = 1.2$
Figure 7.   Continued.

Sym	Strut	t/c	c/D	Location of Strut Leading Edge
○	C-1	0.050	3.2	$x/D = 0$
□	C-2	0.075	3.2	$x/D = 0$
△	D	0.033	4.8	$x/D = 0$
◇	E	0.050	4.8	$x/D = 0$
⬦	F	0.050	3.2	$x/D = 1.6$

$$\Delta C_p = C_{p_{\text{with strut}}} - C_{p_{\text{sting}}} \qquad \theta = 0 \ \text{deg}$$

$\theta = 180 \ \text{deg}$
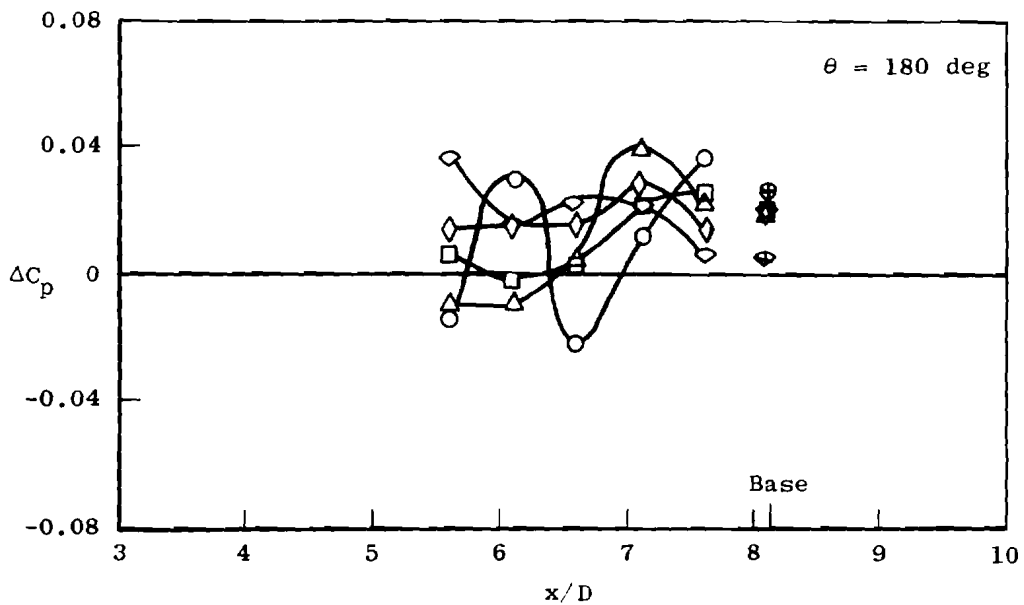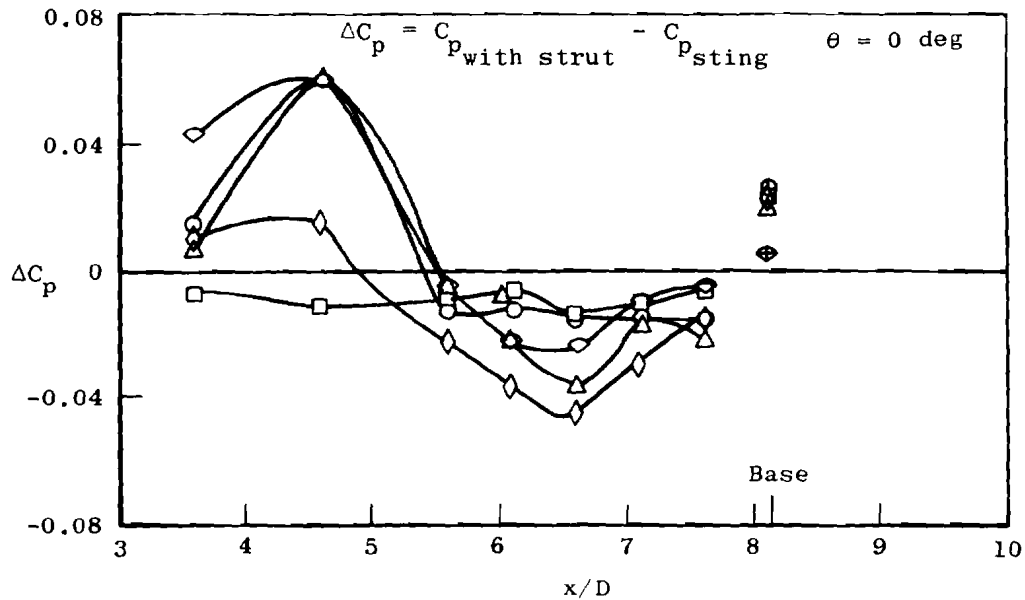
c. $M_\infty = 1.4$

Figure 7. Concluded.
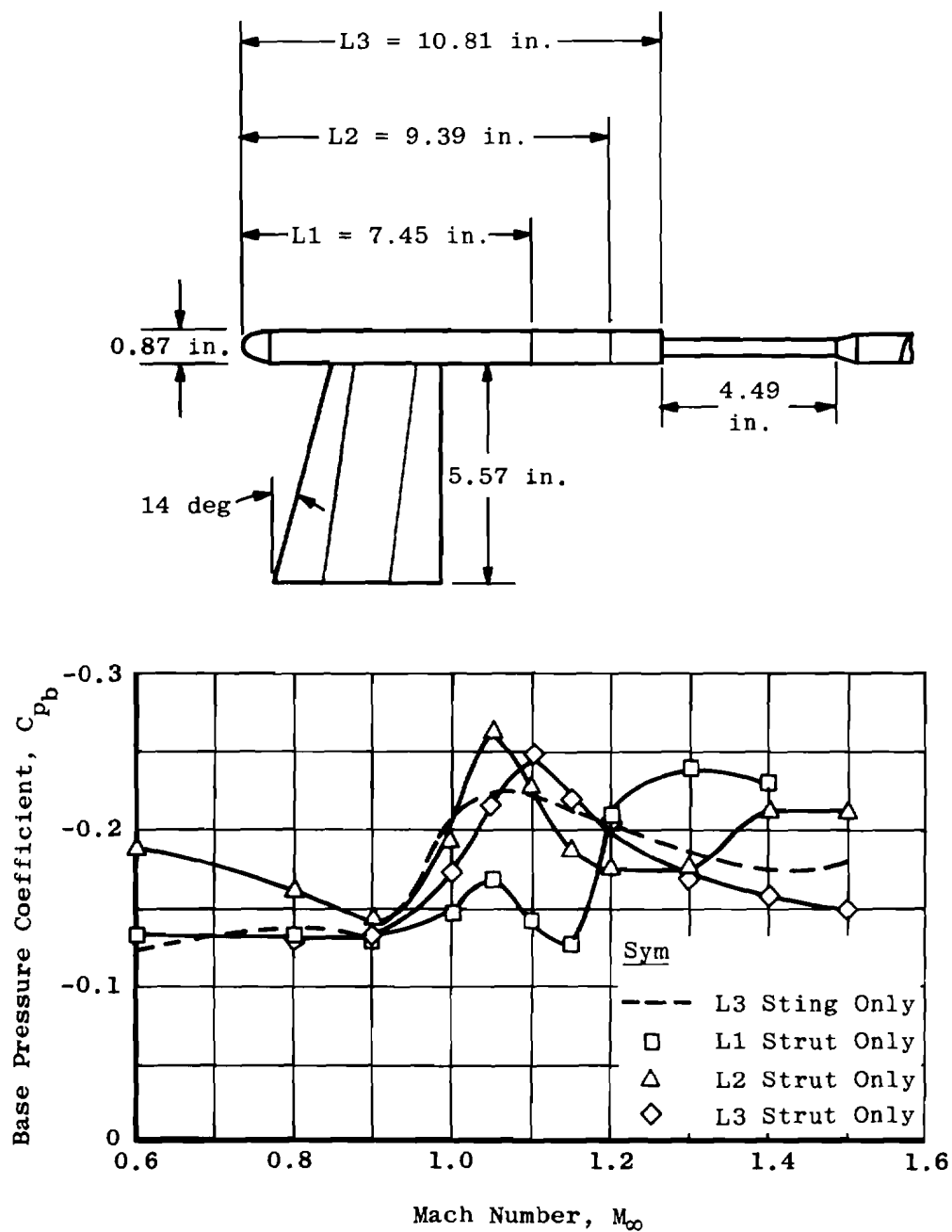
Figure 8. Effect of model length on base pressure coefficient.

Sym	Config	Λ, deg
O	S2	0
□	S5	30
△	S3	45

$$C_{p_b} = C_{p_{b(\text{with strut})}} - C_{p_{b(\text{sting})}}$$
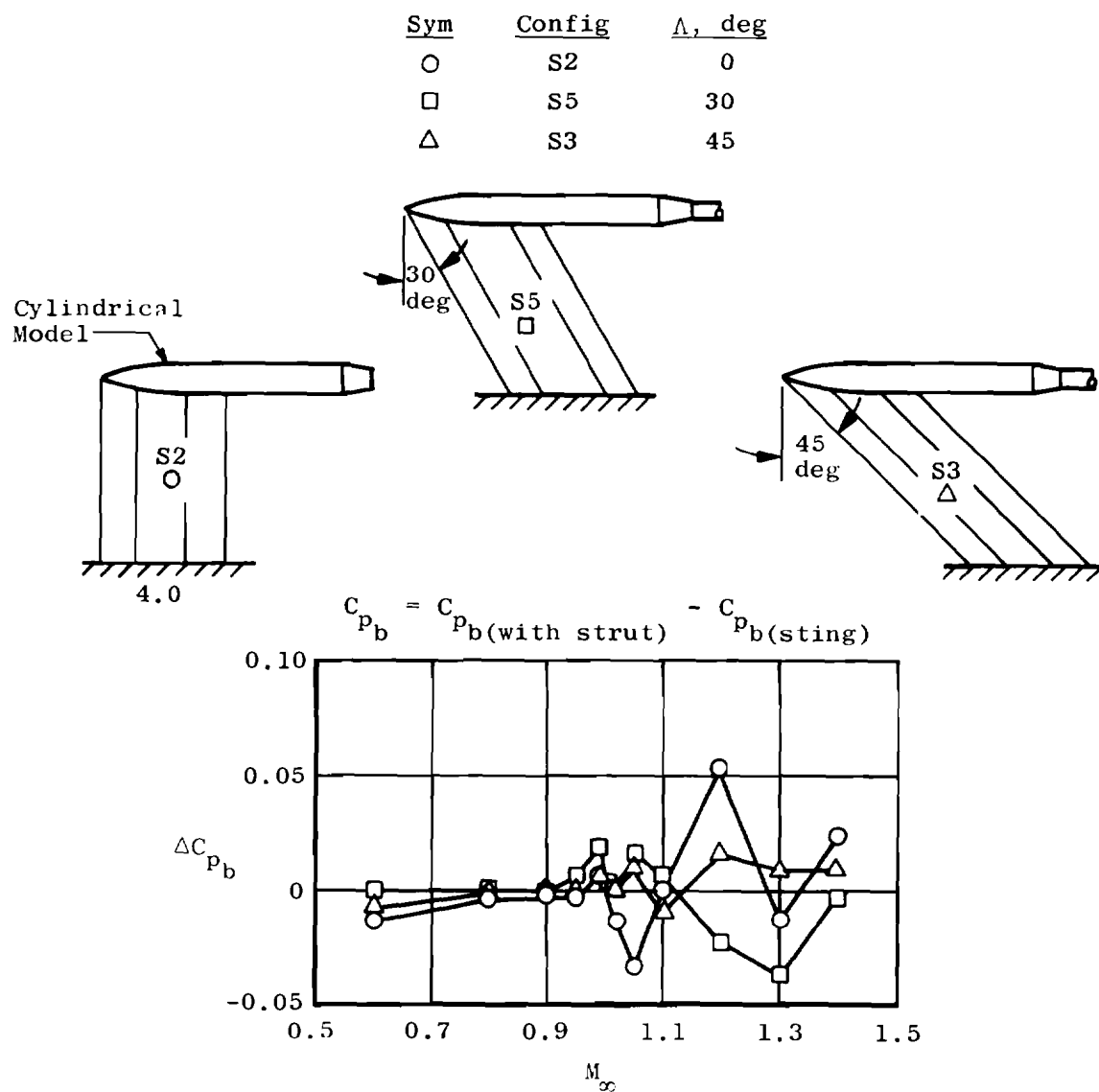
a. Base pressure coefficient increments

Figure 9. Interference pressure coefficient for struts having various sweep angles.

Sym	Config	Λ, deg
O	S2	0
□	S5	30
△	S3	45

$M_\infty = 1.10$

$M_\infty = 1.20$
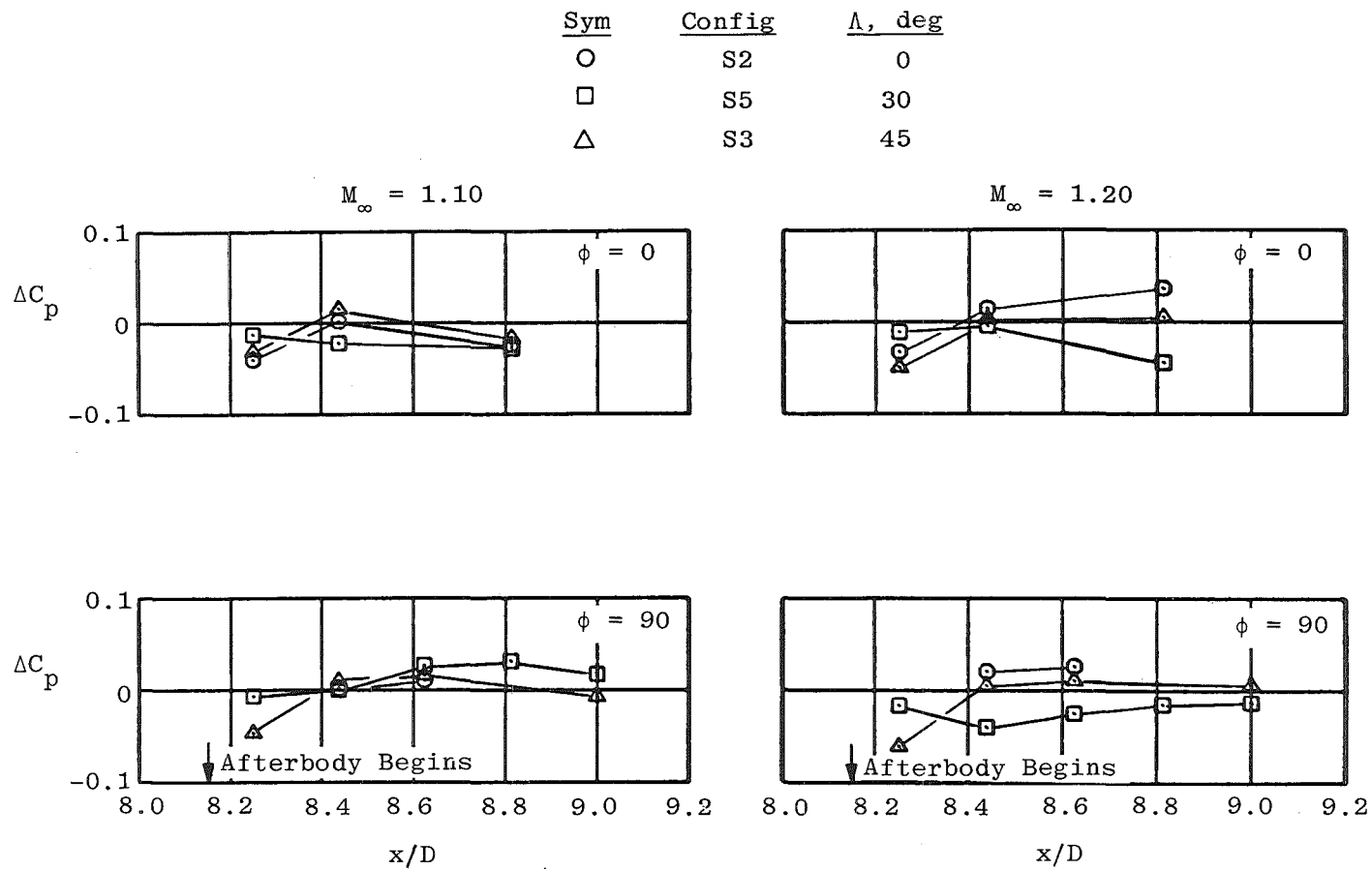
b. Body surface pressure coefficient increments
Figure 9. Concluded.

Wedge
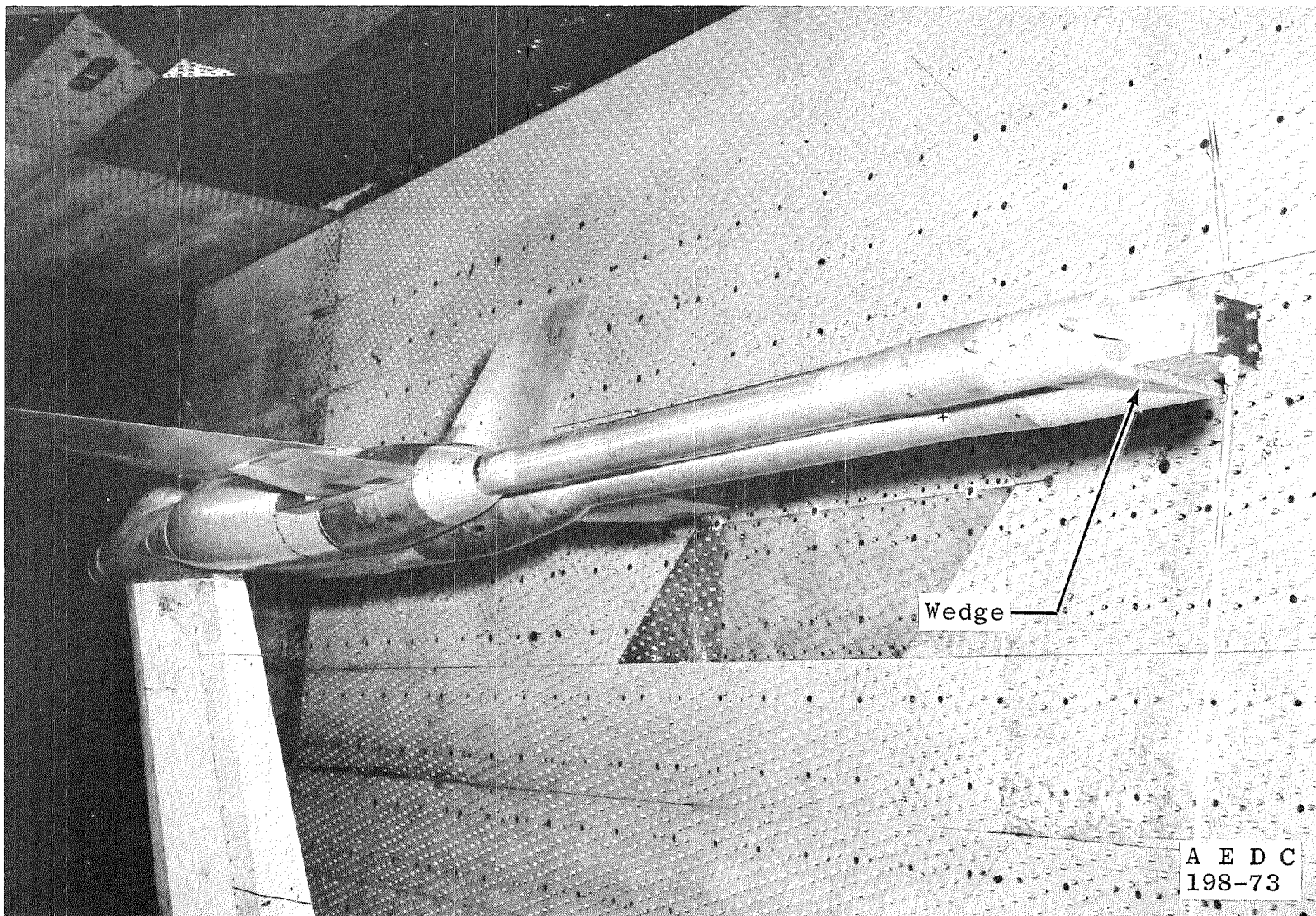
A E D C
198-73

a. Strut mounted with dummy stings
Figure 10. Configurations used to determine strut interference.
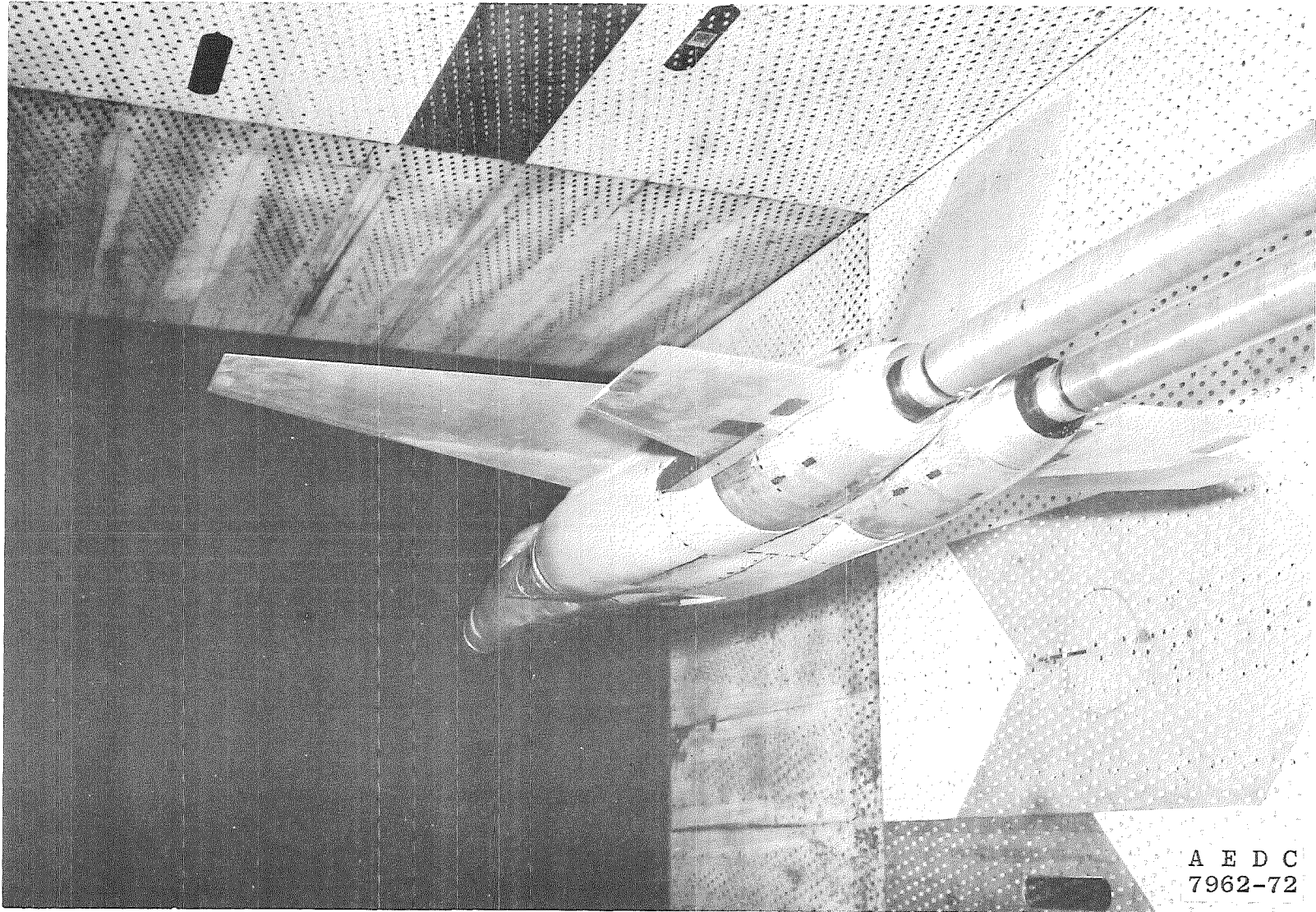
AEDC
7962-72

b. Sting mounted
Figure 10. Concluded.

$$\Delta C_D = \frac{\Delta C_{D_{\text{with strut}}} - C_{D_{\text{without strut}}}}{C_{D_{\text{without strut}}}} \times 100$$
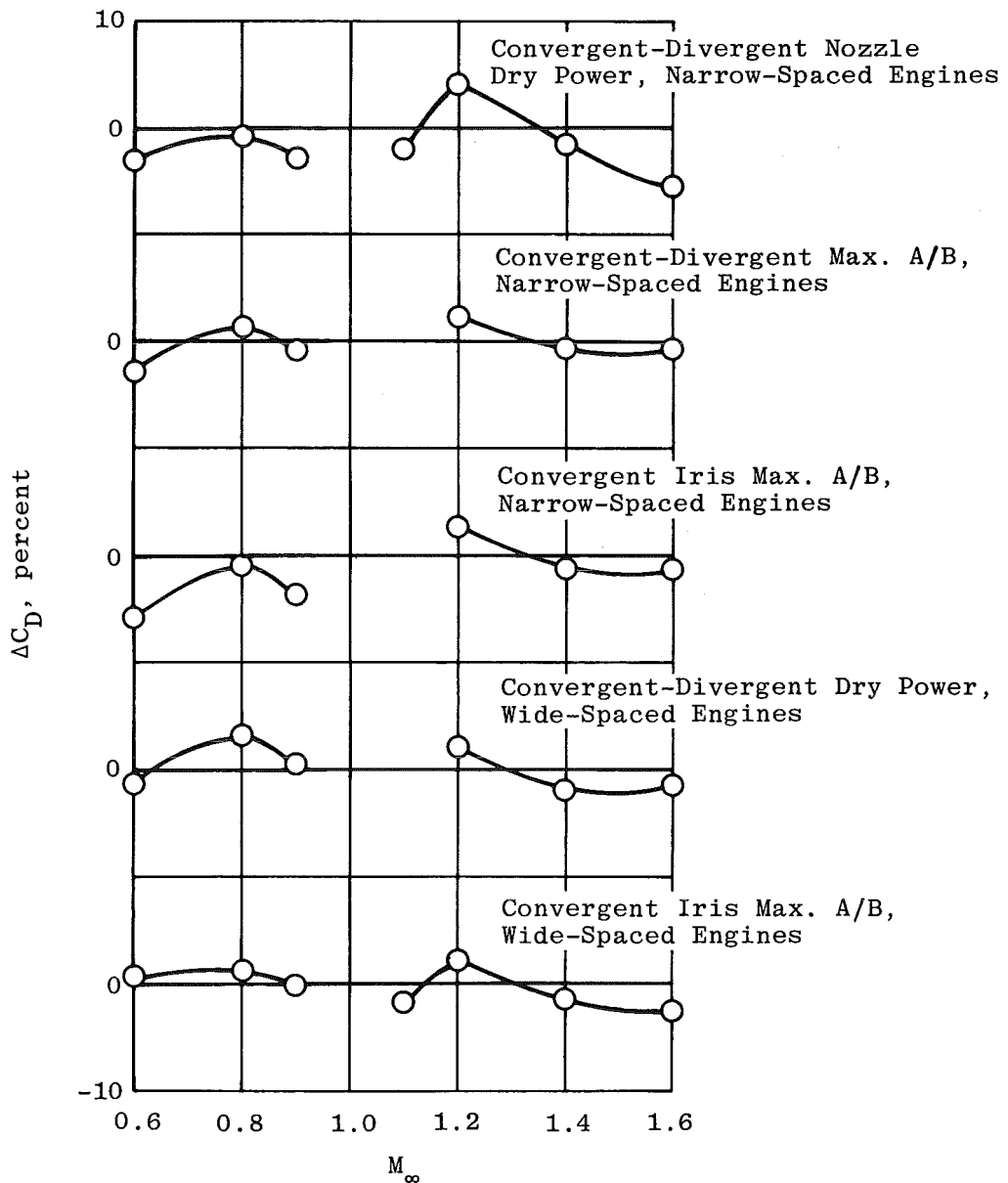
Figure 11. Effect of strut interference on afterbody drag in percent of aircraft drag.
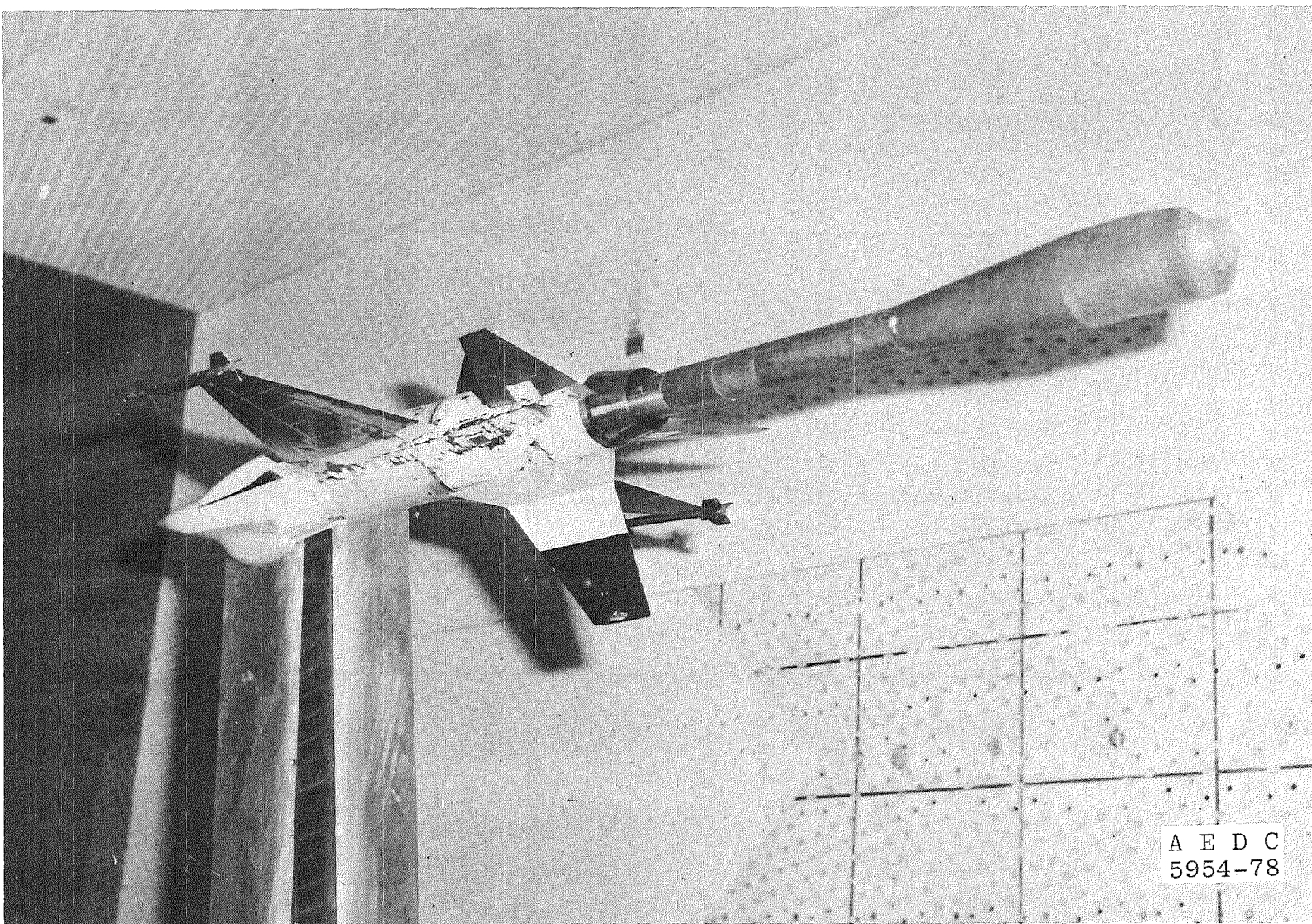
Figure 12. Strut-supported F-16 model with dummy sting.
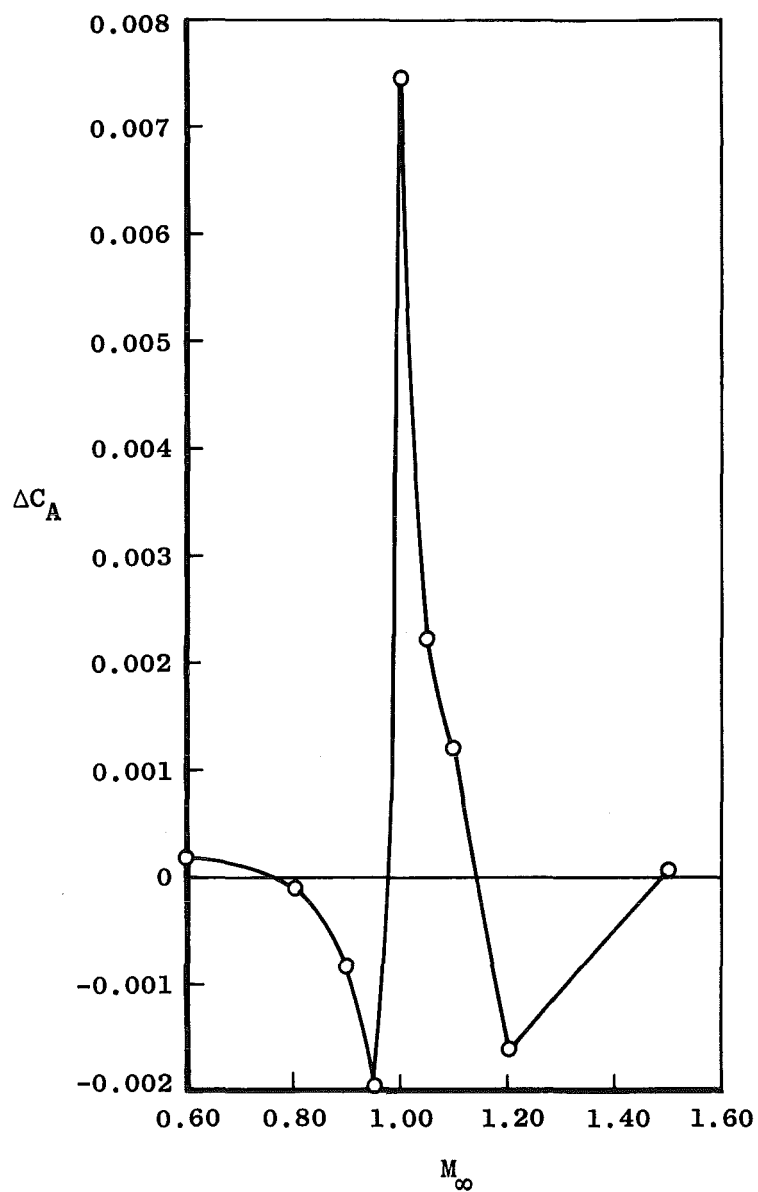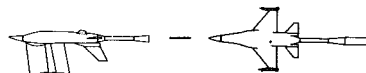
a. $a = 0$

Figure 13. Effect of strut interference on afterbody axial-force coefficient.
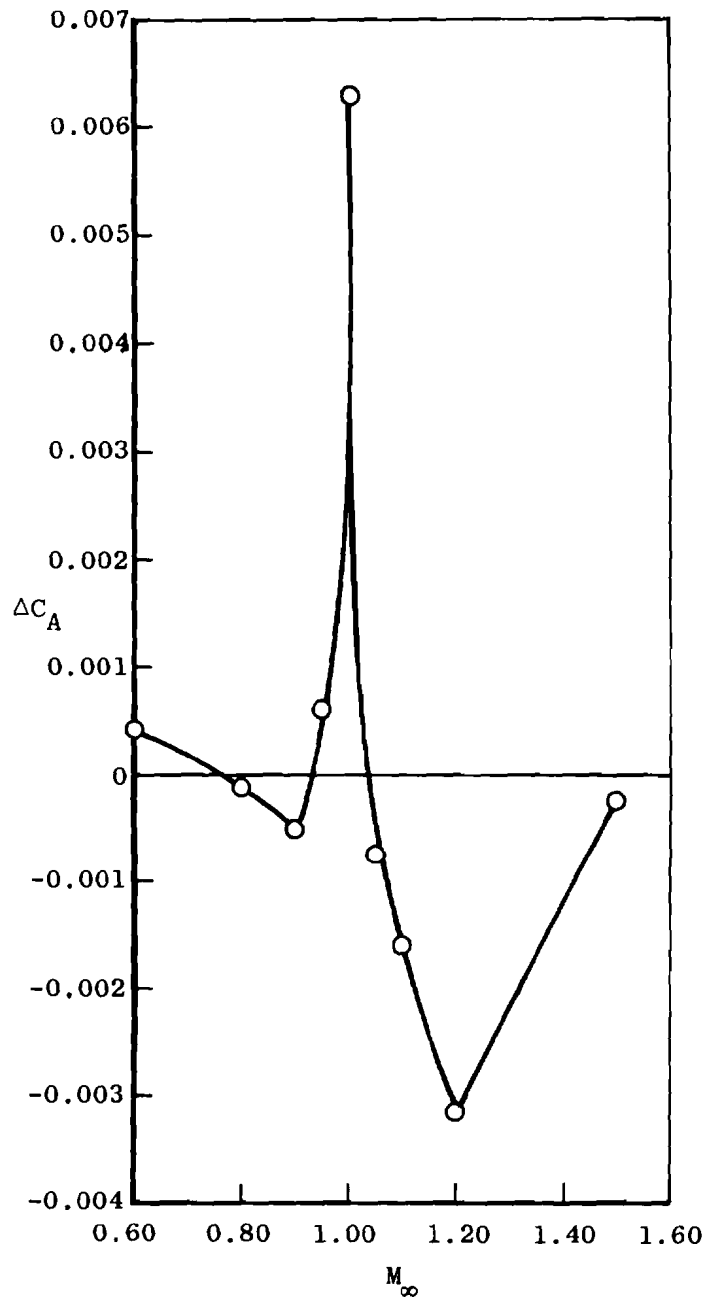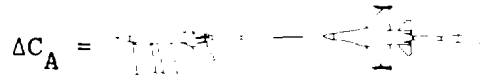
b. $a = 7$ deg
Figure 13. Concluded.
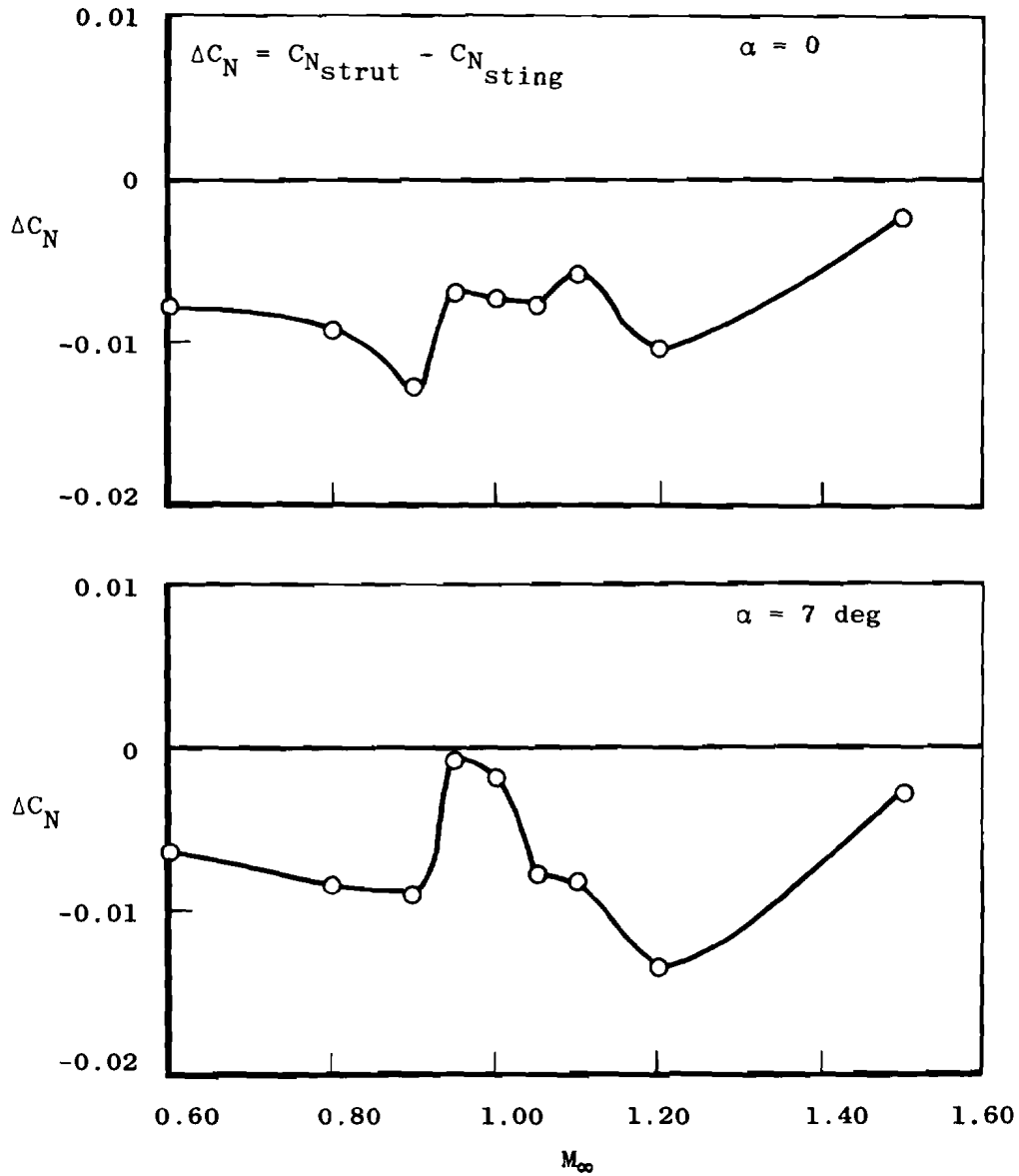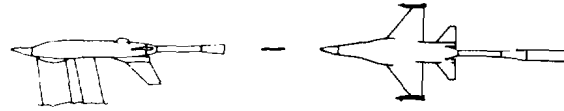
Figure 14. Effect of strut interference on afterbody
normal-force coefficient.
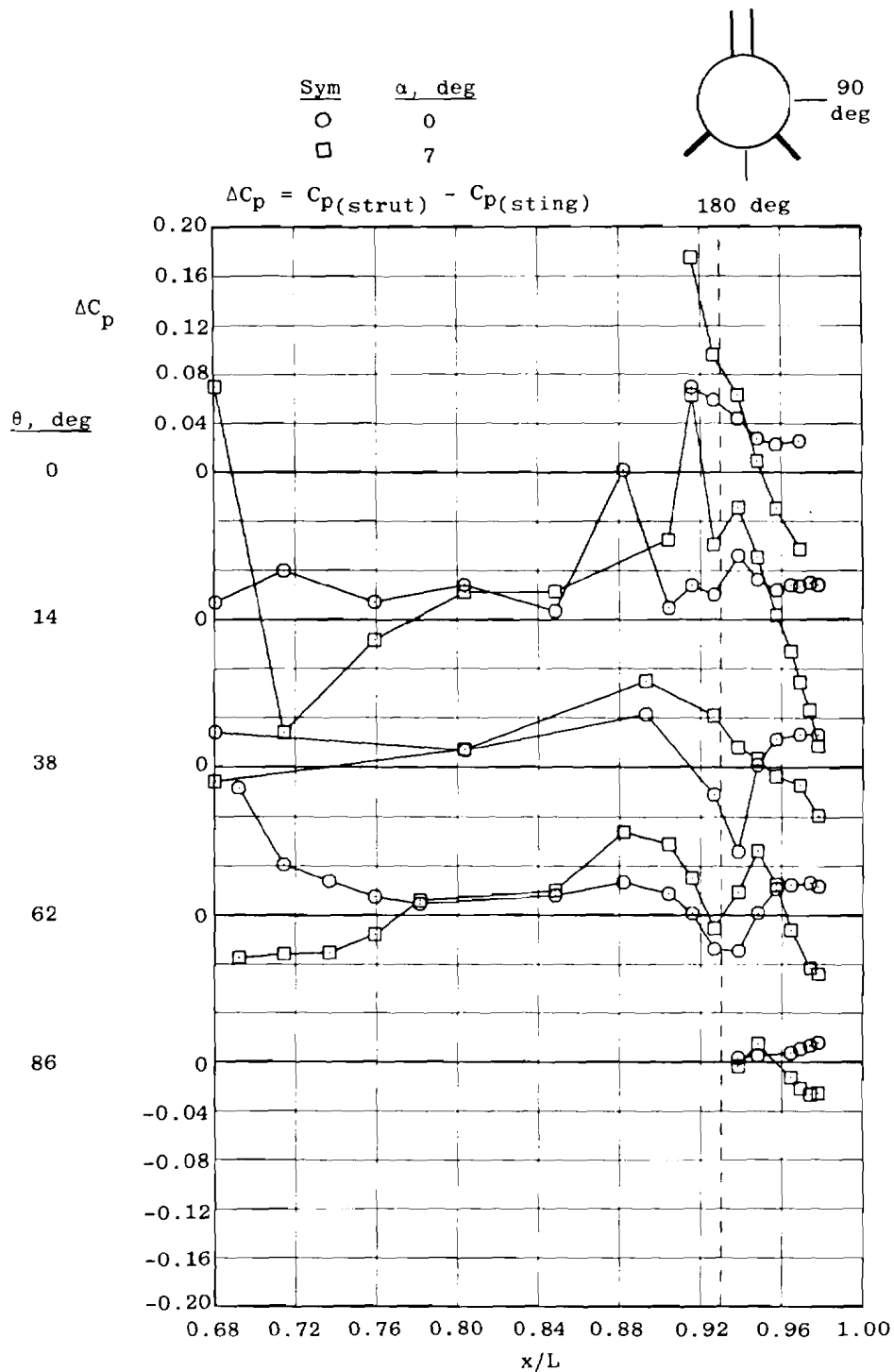
a. $M_\infty = 0.9$

Figure 15. Change in fuselage pressure distribution caused by the strut.
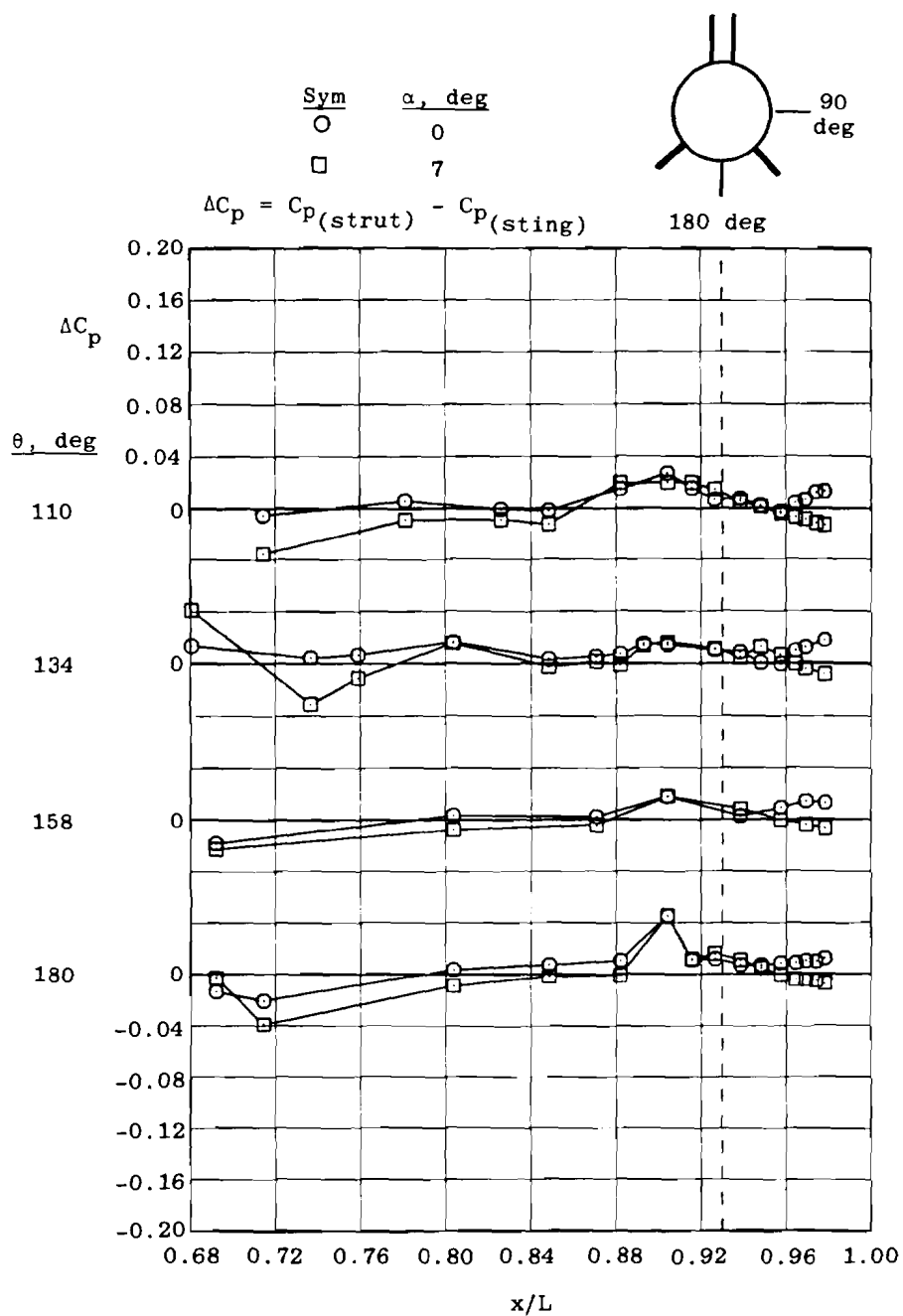
a. Concluded
Figure 15. Continued.
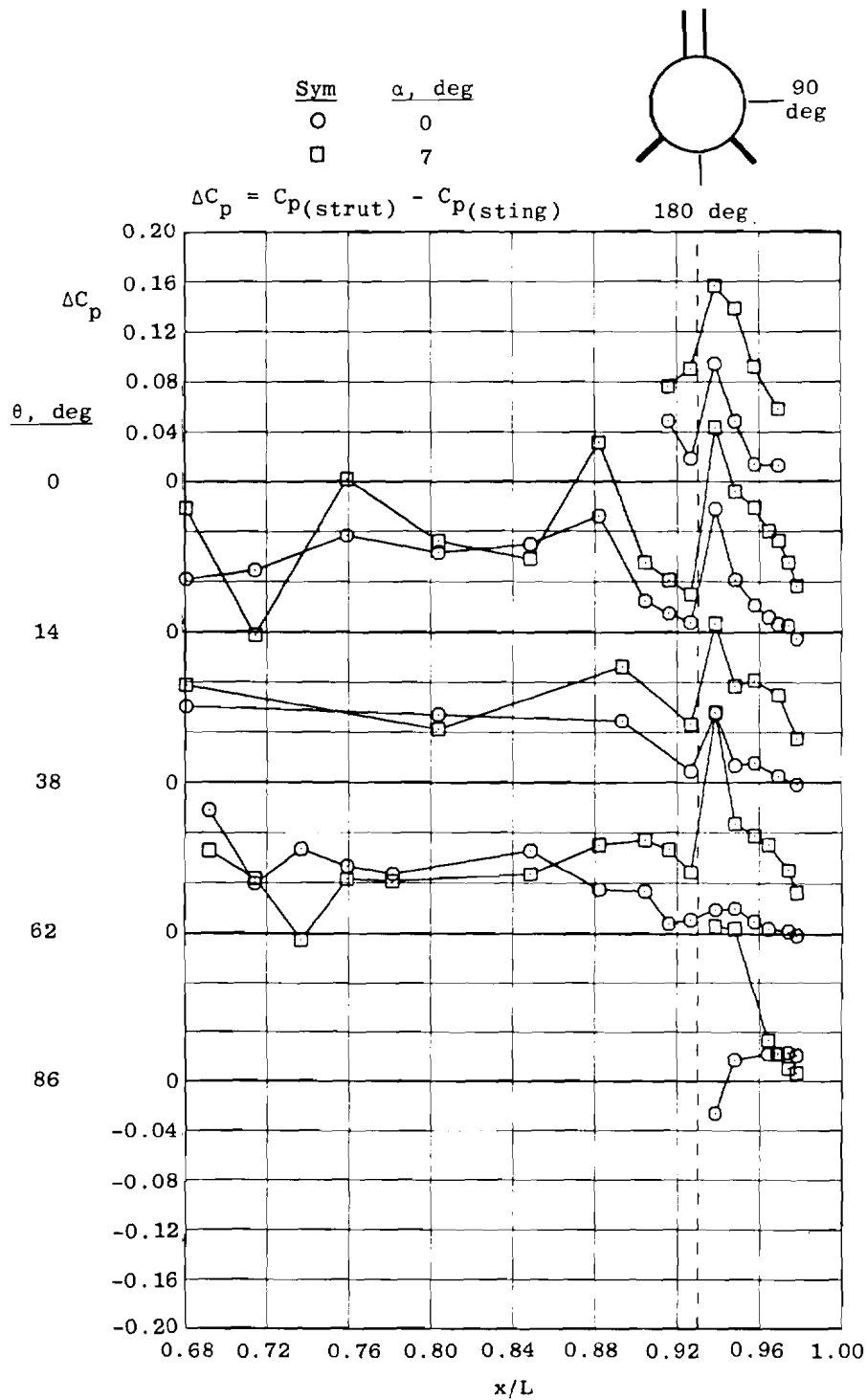
b. $M_\infty = 1.2$
Figure 15. Continued.
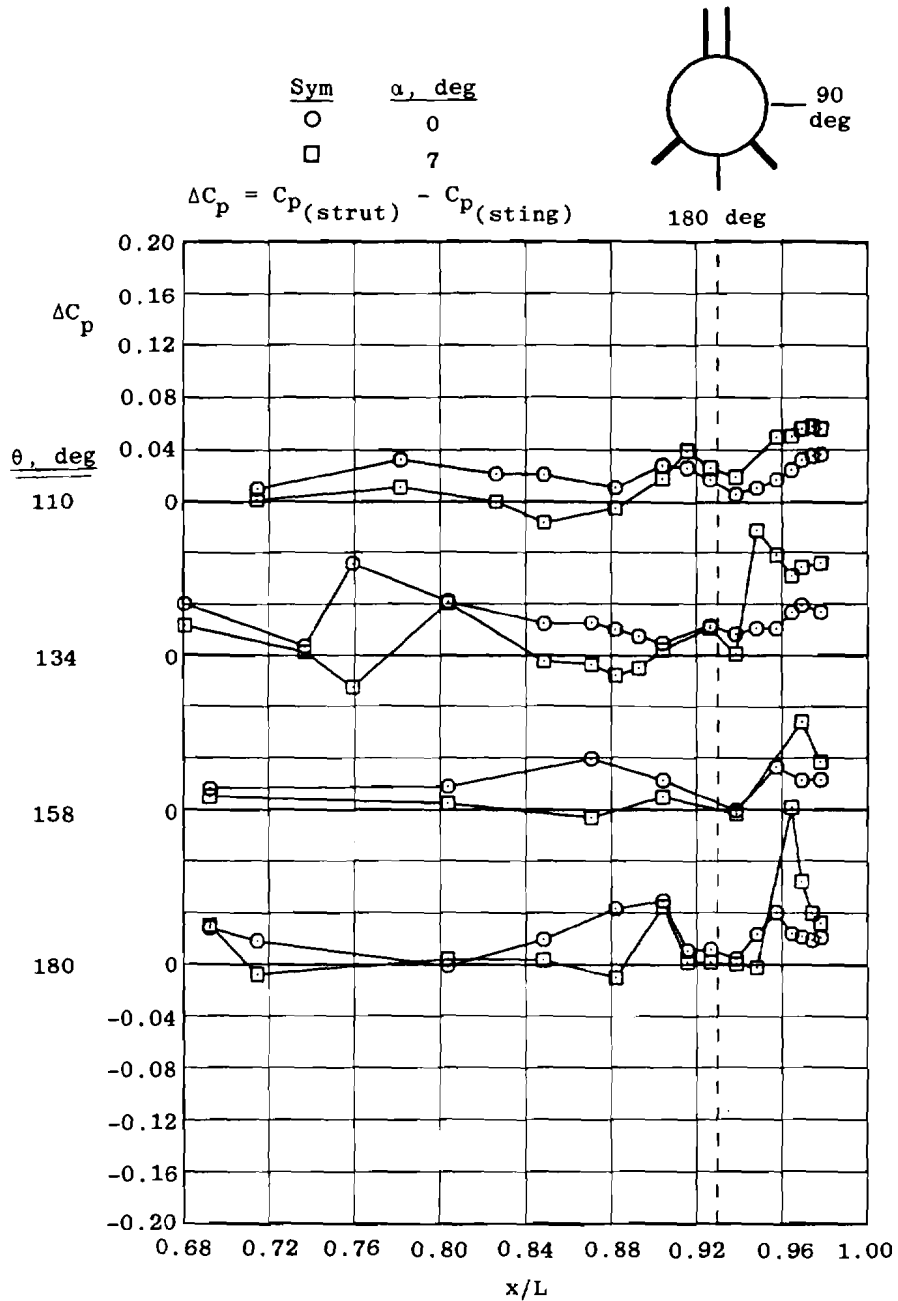
b. Concluded
Figure 15. Concluded.
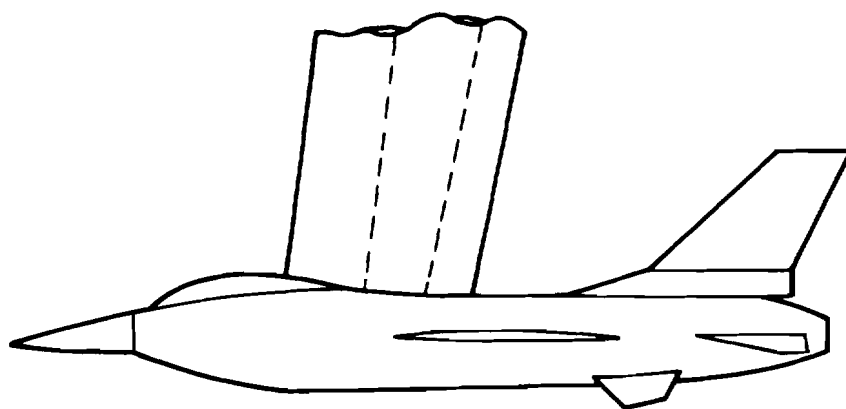
1/4-Scale F-16
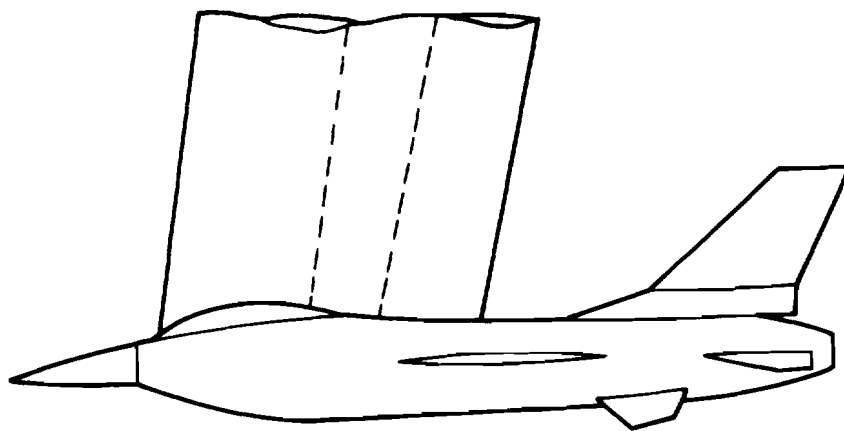
1/9-Scale F-16

Figure 16. Comparison of strut configurations for the 1/9- and 1/4-scale F-16 models.

		Blockage, percent		
Sym	Model	Model	Strut	Total
O	1/9-Scale	0.14	0.39	0.53
□	1/4-Scale	0.71	0.73	1.44

$$\Delta C_A = C_{A_{strut}} - C_{A_{sting}}$$
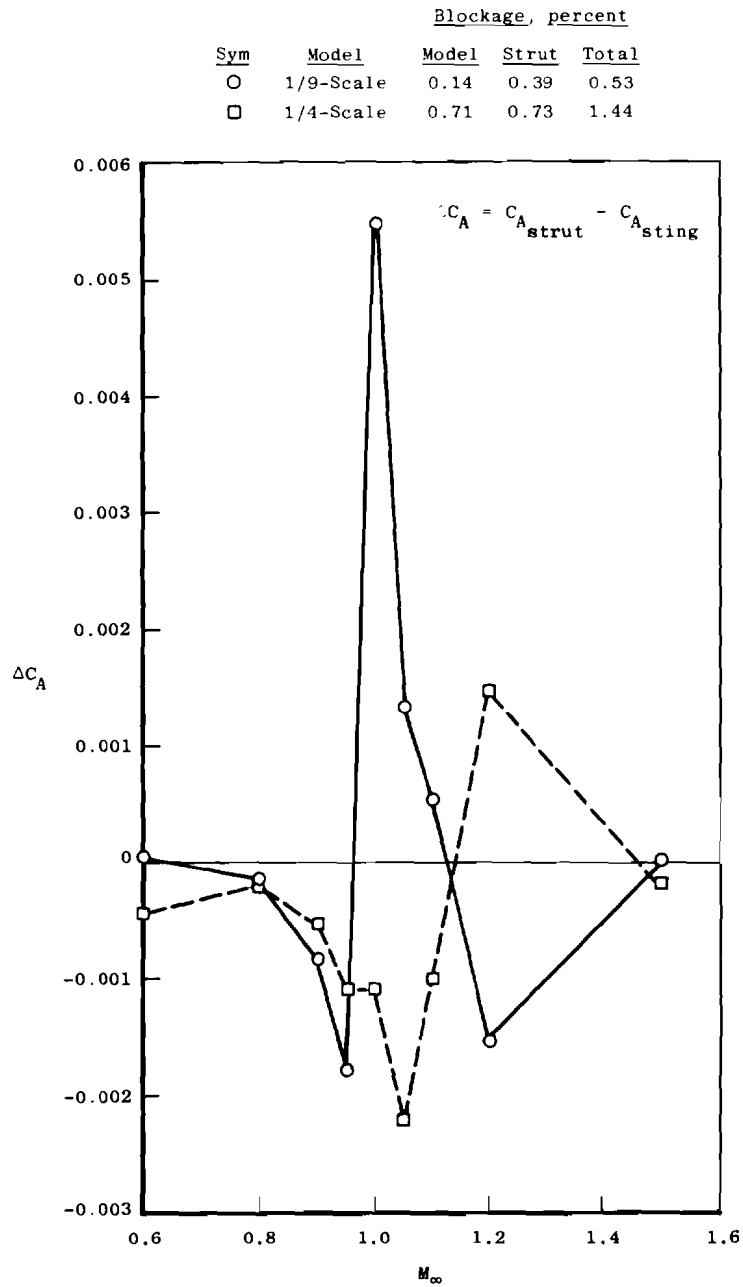
a. $\alpha = 0$ deg

Figure 17. Effect of strut interference on axial-force coefficient for models having different scale.
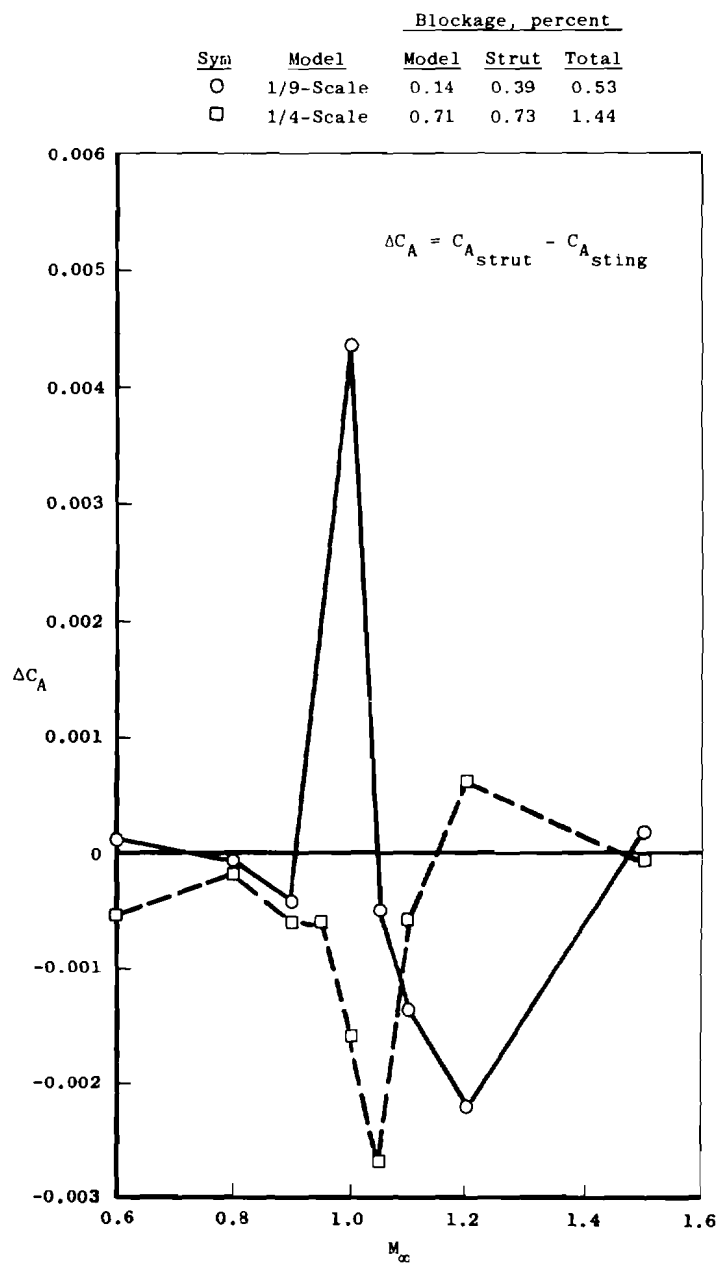
b. a = 7 deg
Figure 17. Concluded.
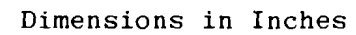
Figure 18. Model used for sting interference studies.
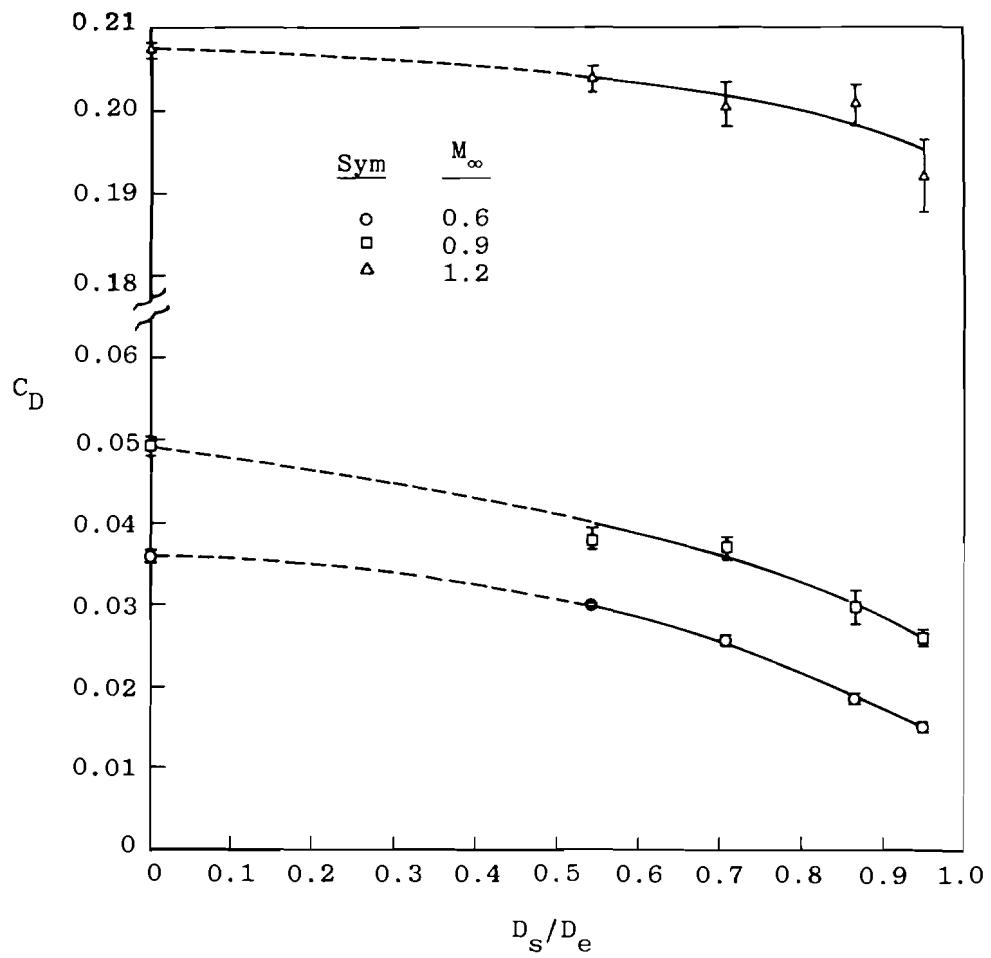
Figure 19. Variation of jet-off afterbody drag with sting size.

Supporting Channel

Sliding Strut   Fixed Strut

13
12
11
10
9
8
7
6
5
4
3
2
1

0.375 x 0.016
Sidewall Strip

1   3   4   5

2   Sliding Strut Positions

18.260°   0.141

0.437   0.625   0.437
Airfoil for
Sliding Strut

15-deg Cone Orifice
0.0135 D
0.042 D   0.062 D
0.50   1.25   0.15
Detail of Static Pressure Probe
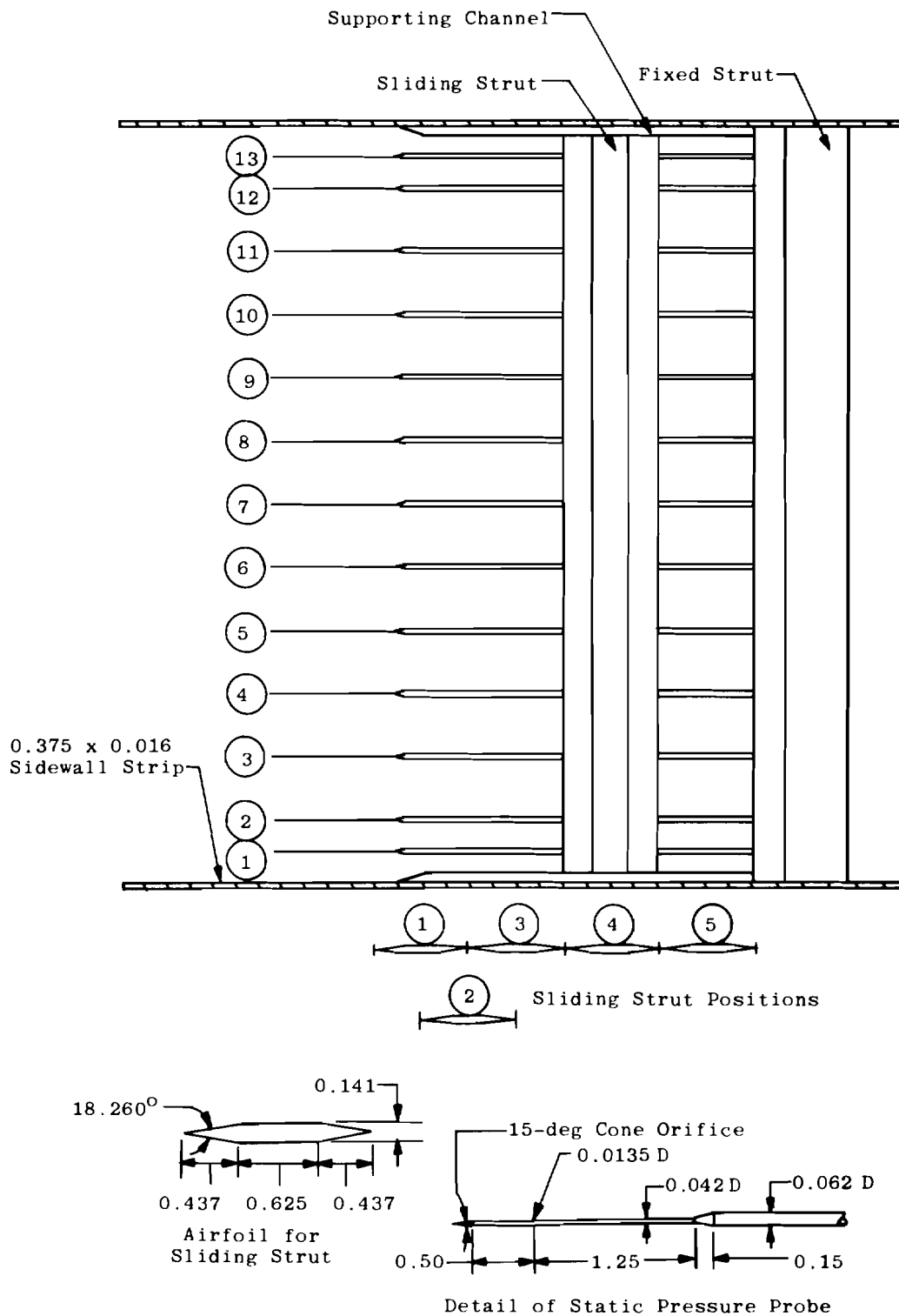
Figure 20. Details of configuration used to study the effect of a strut on the flow field in Tunnel 1T.
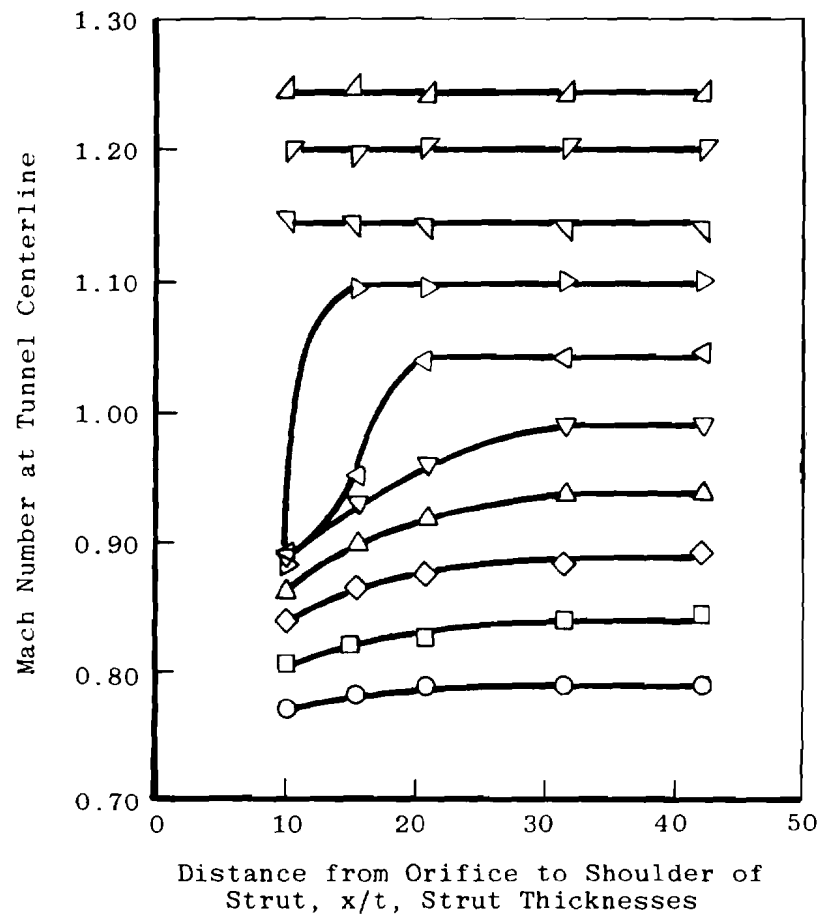
Figure 21. Effect of a strut spanning the tunnel on the local Mach number ahead of the strut.
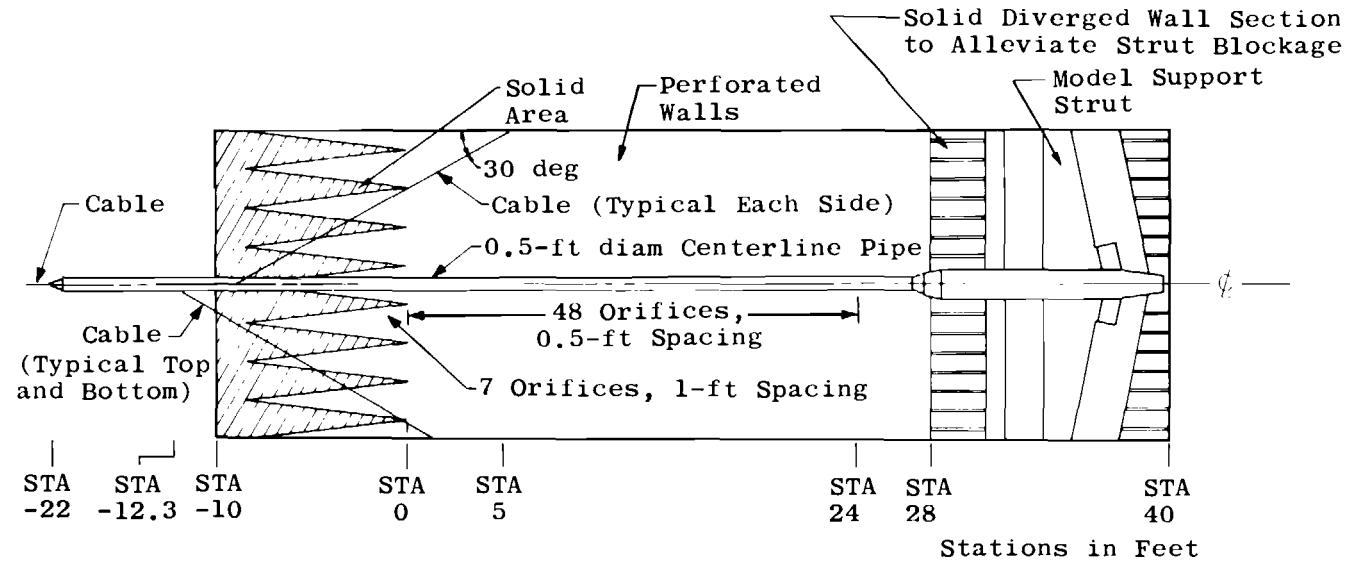
Figure 22. Installation of the centerline pipe for Tunnel 16T calibration.
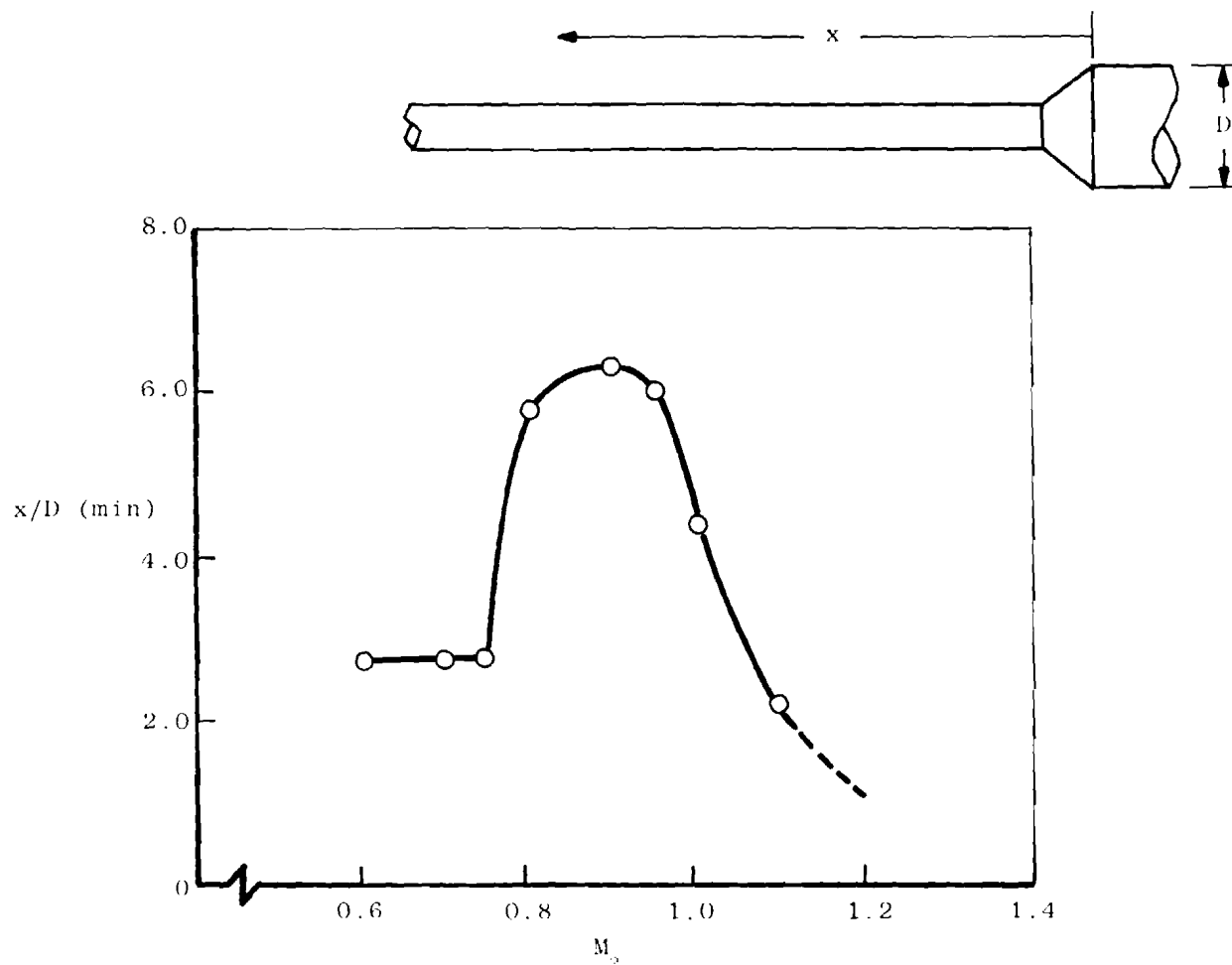
Figure 23. Location relative to the Tunnel 16T pitch system for interference-free data.
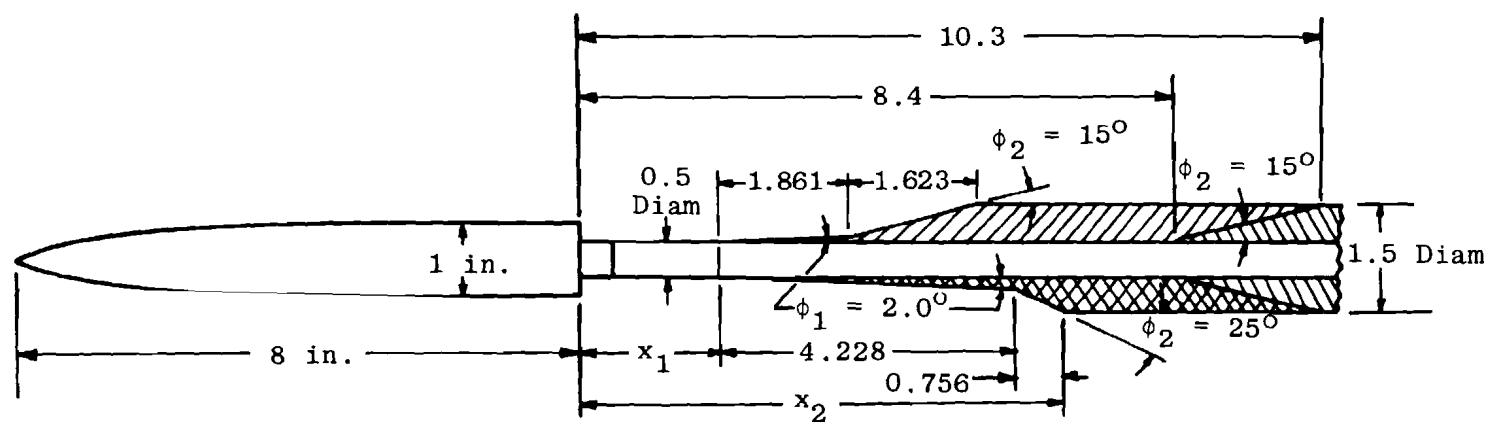
Dimensions in Inches

Figure 24. Configurations investigated to determine the effect of sting
configuration on model surface pressures.

Sym	x_1/D	x_2/D	x_2/D_S	ϕ_1, deg	ϕ_2, deg
○	8.4	10.3	6.9	0	15
□	0.5	4.0	2.7	2.0	15
△	2.0	5.5	3.7	2.0	15
◇	0.5	5.5	3.7	2.0	25
◊	2.0	7.0	4.7	2.0	25

D = 1.0-in. Model Diameter

D_S = Maximum Sting Diameter, 1.5 in.
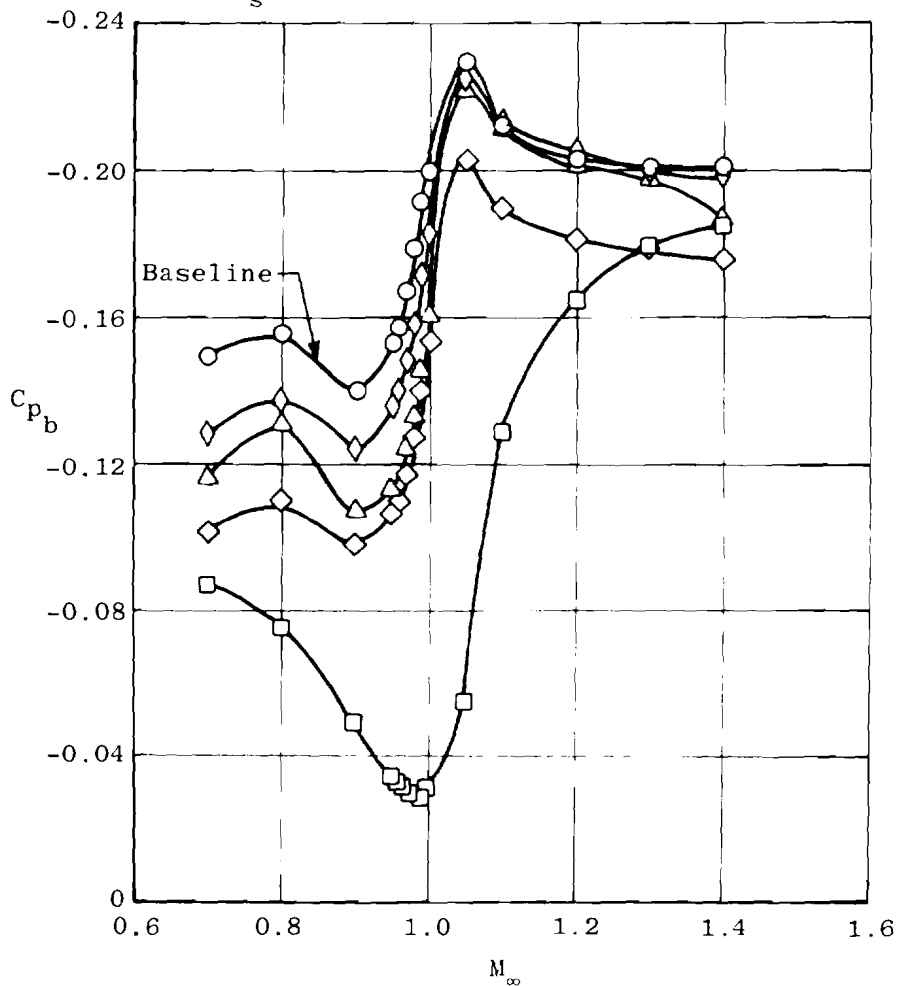
Figure 25. Model base pressure coefficients for various sting configurations.
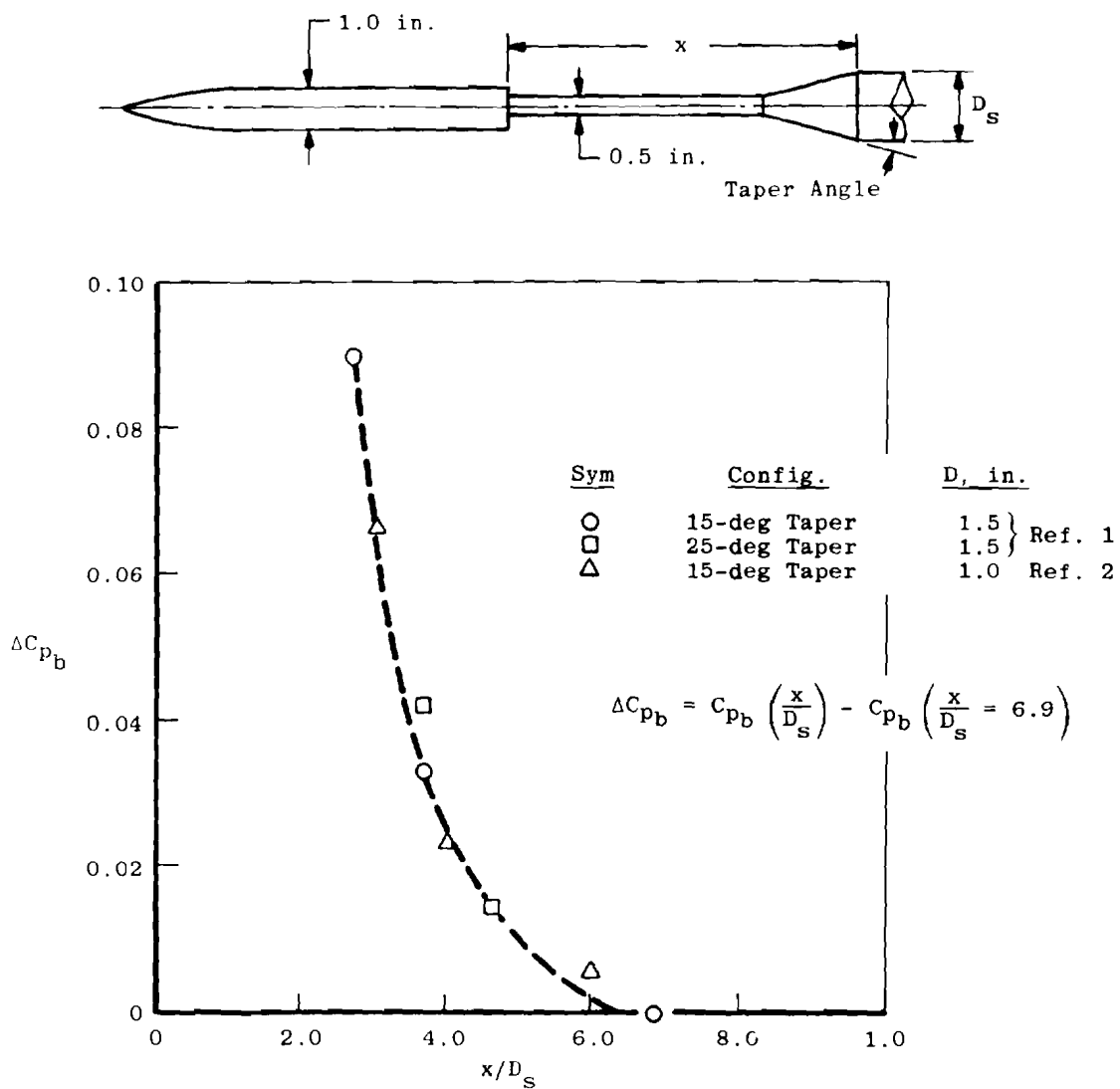
Figure 26. Effect of sting location on model base pressure coefficient at Mach 0.9.

$$\Delta C_D = (C_{D_{ann \ jet}} - C_{D_{con \ jet}})$$

Sym	D_s/D_e
□	0.543
△	0.707
◇	0.866
X	0.950
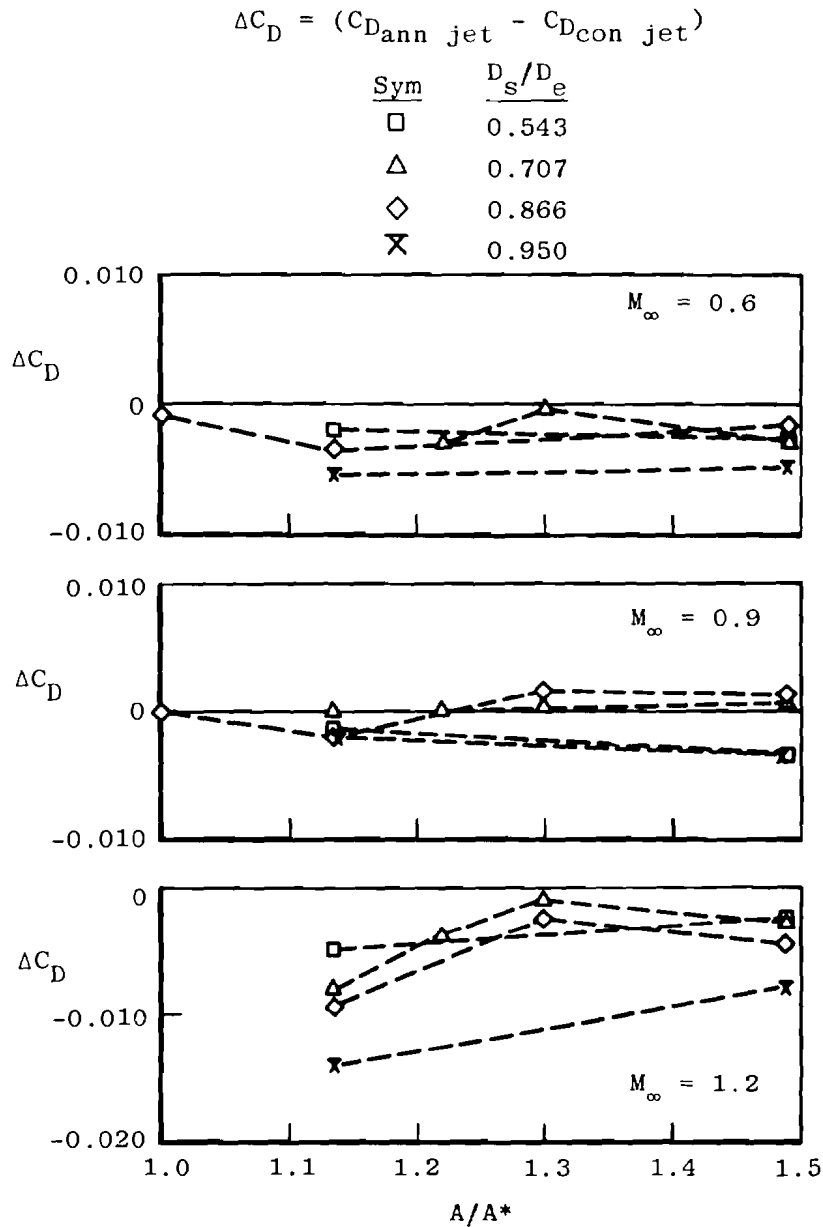
Figure 27. Difference in afterbody drag between annular and conventional jets.

83
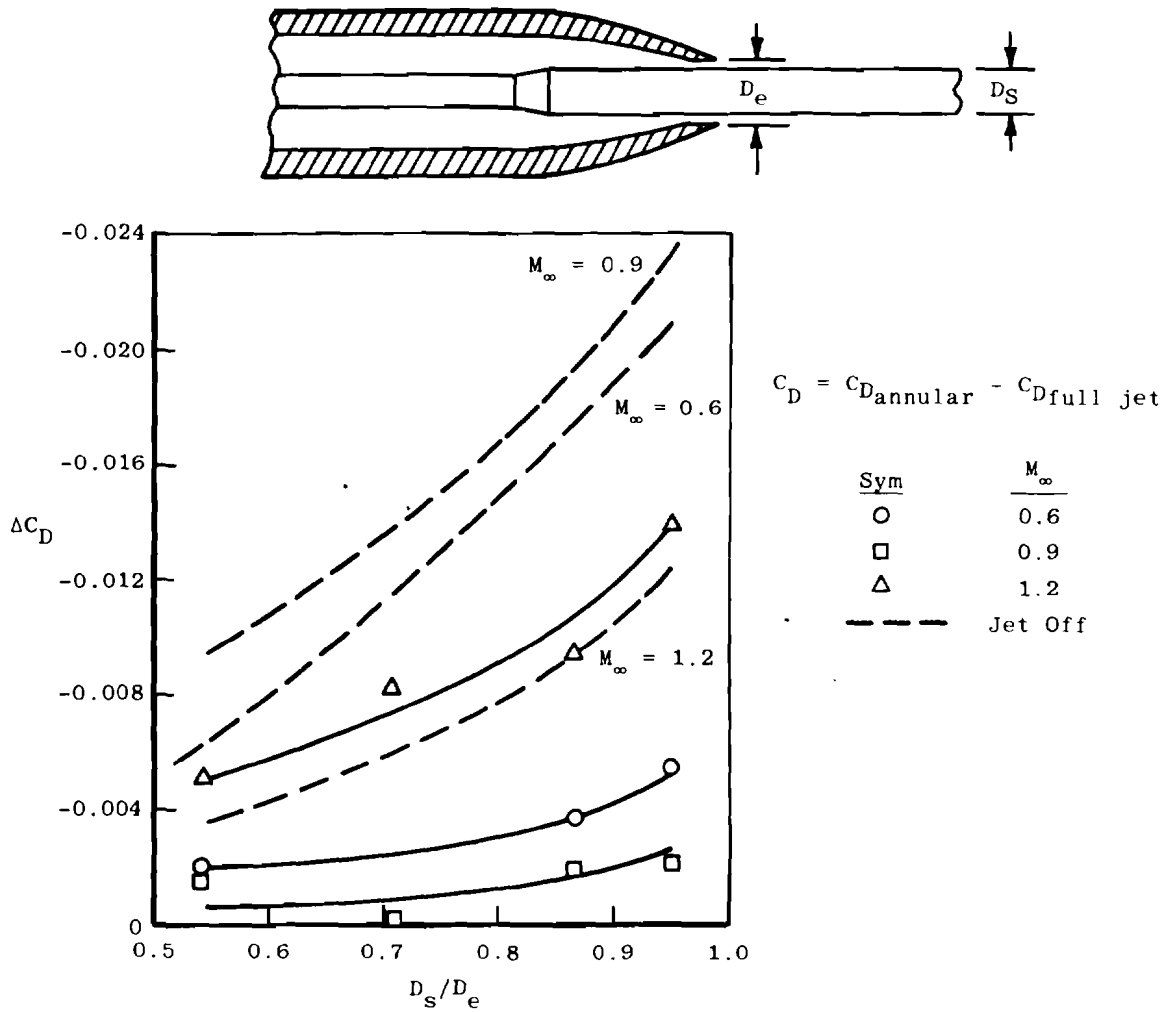
Figure 28. Effect of sting size on the increment in drag between annular and full jets (NPR = design).
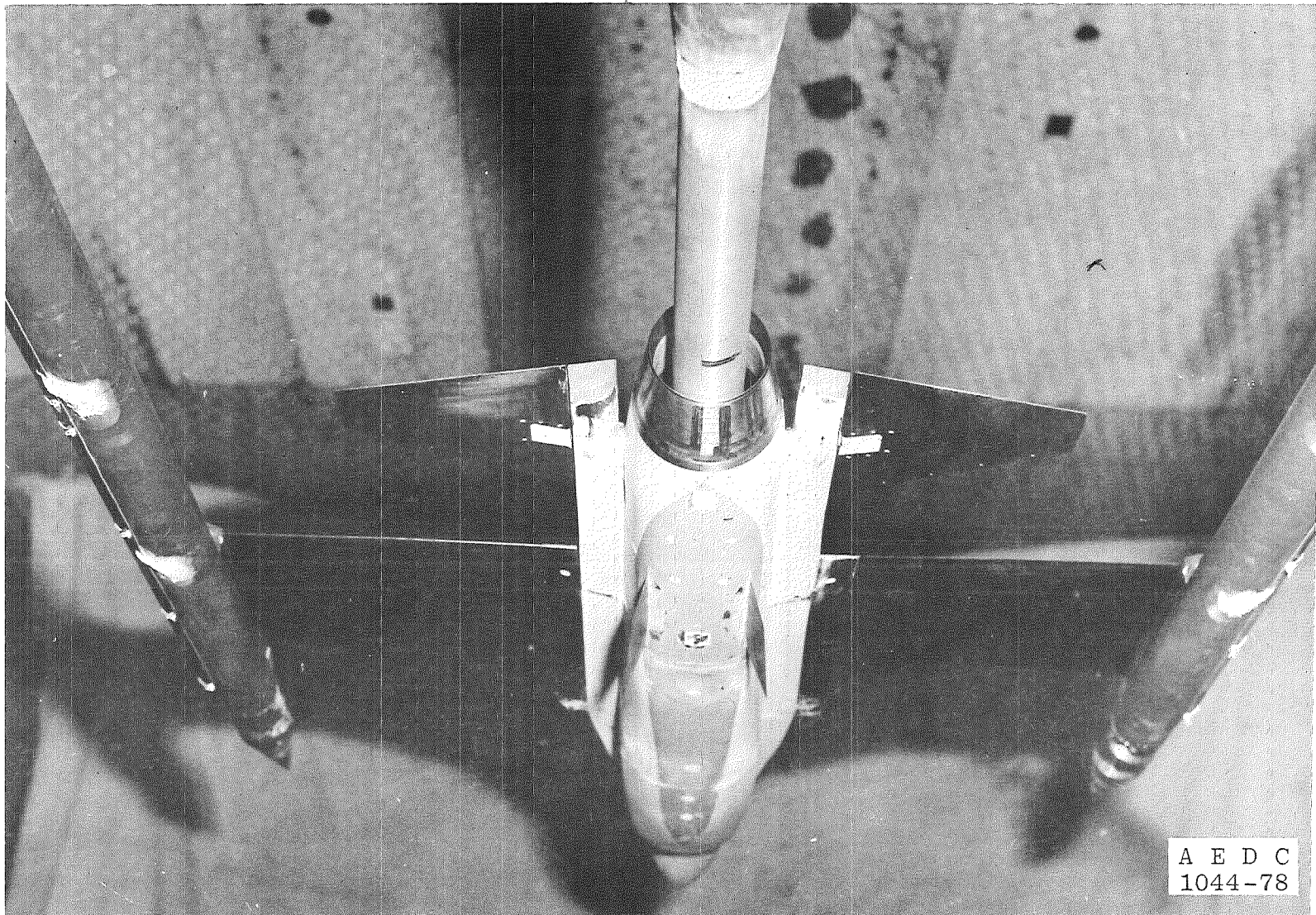
Figure 29. Configuration used to evaluate the annular-jet technique
for the 1/9-scale F-16 model.

AEDC-TR-80-8

Sym	Nozzle	D_s/D_e
O	Cruise	0.865
□	Max. A/B	0.710
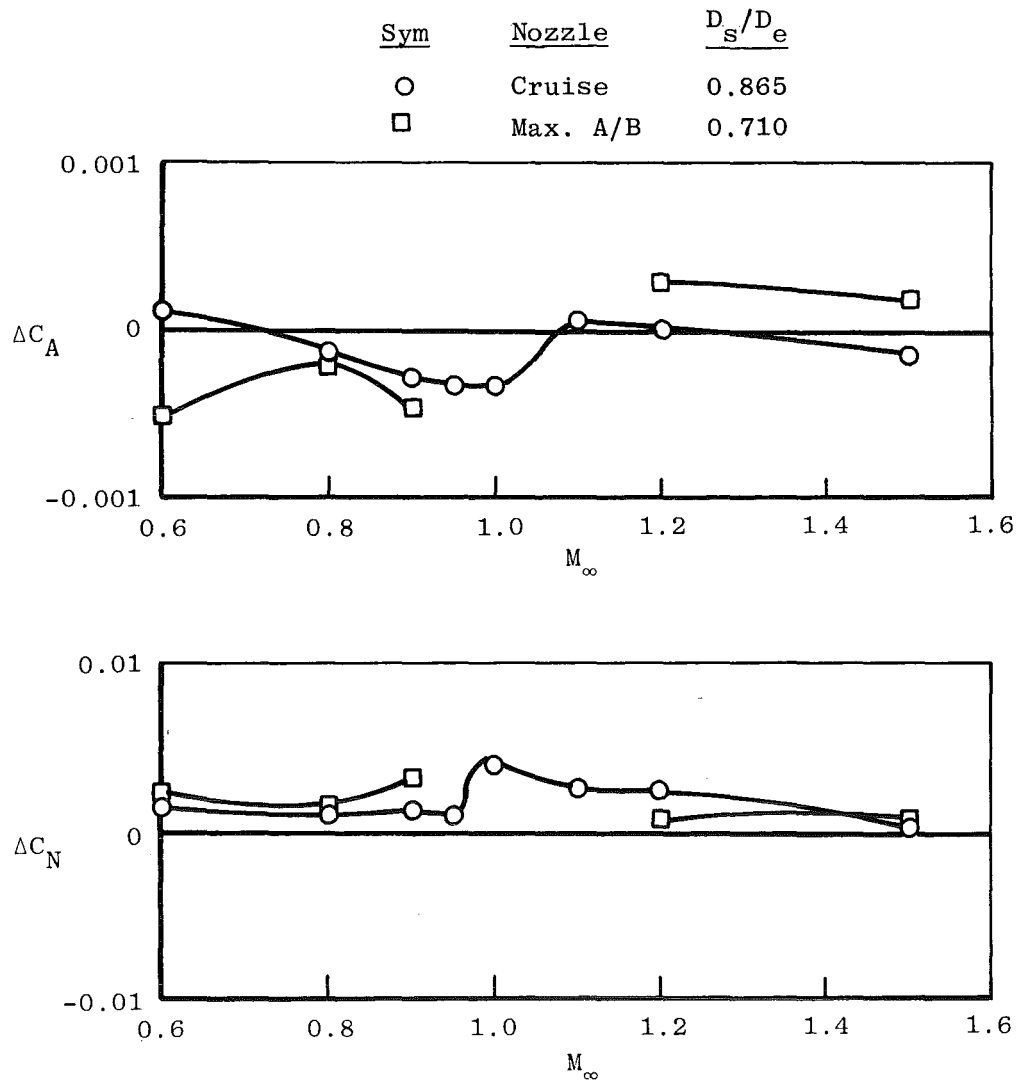
a. $a = 0$

Figure 30. Differences in afterbody force coefficients between annular- and full-jet configurations (NPR = design).

Sym	Nozzle	D_s/D_e
O	Cruise	0.865
□	Max. A/B	0.710
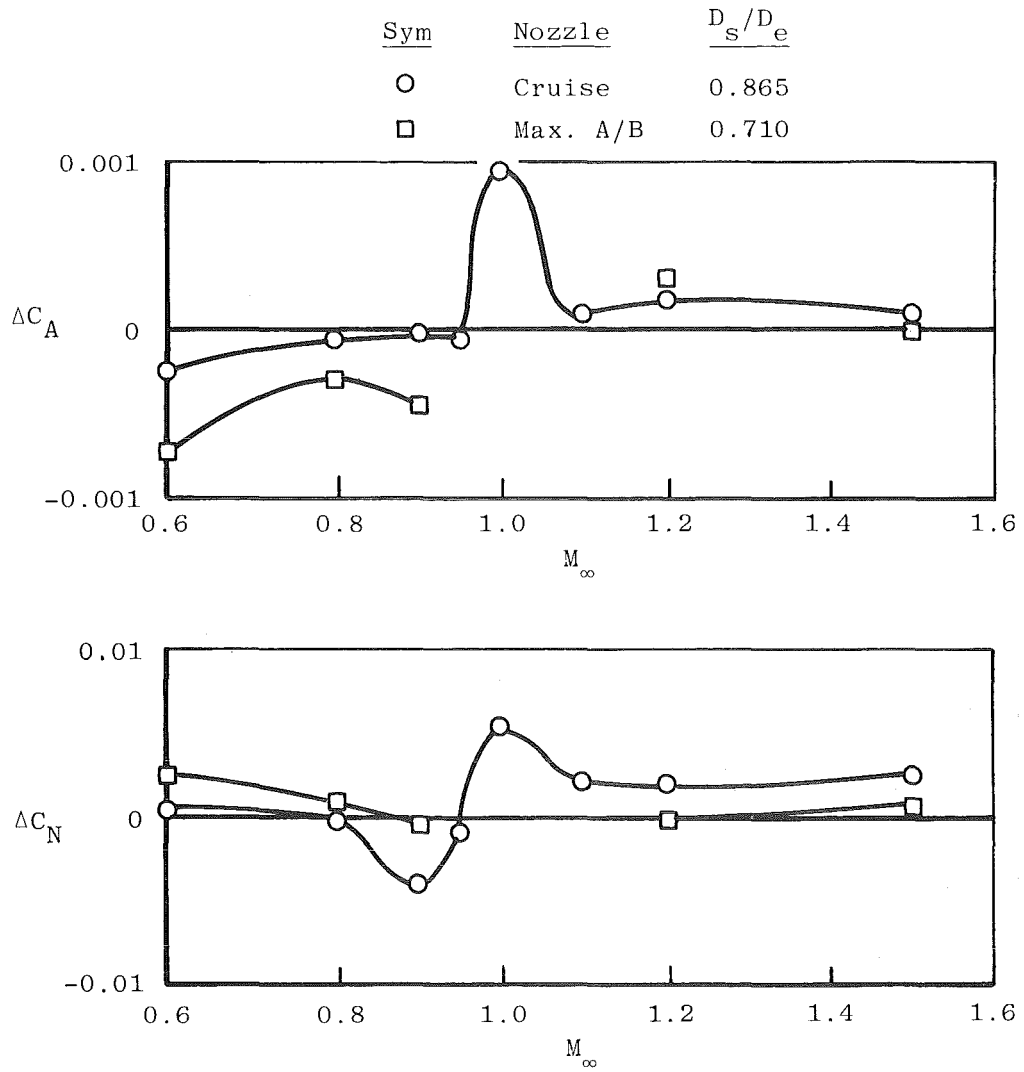
b. a = 7 deg

Figure 30. Concluded.

87
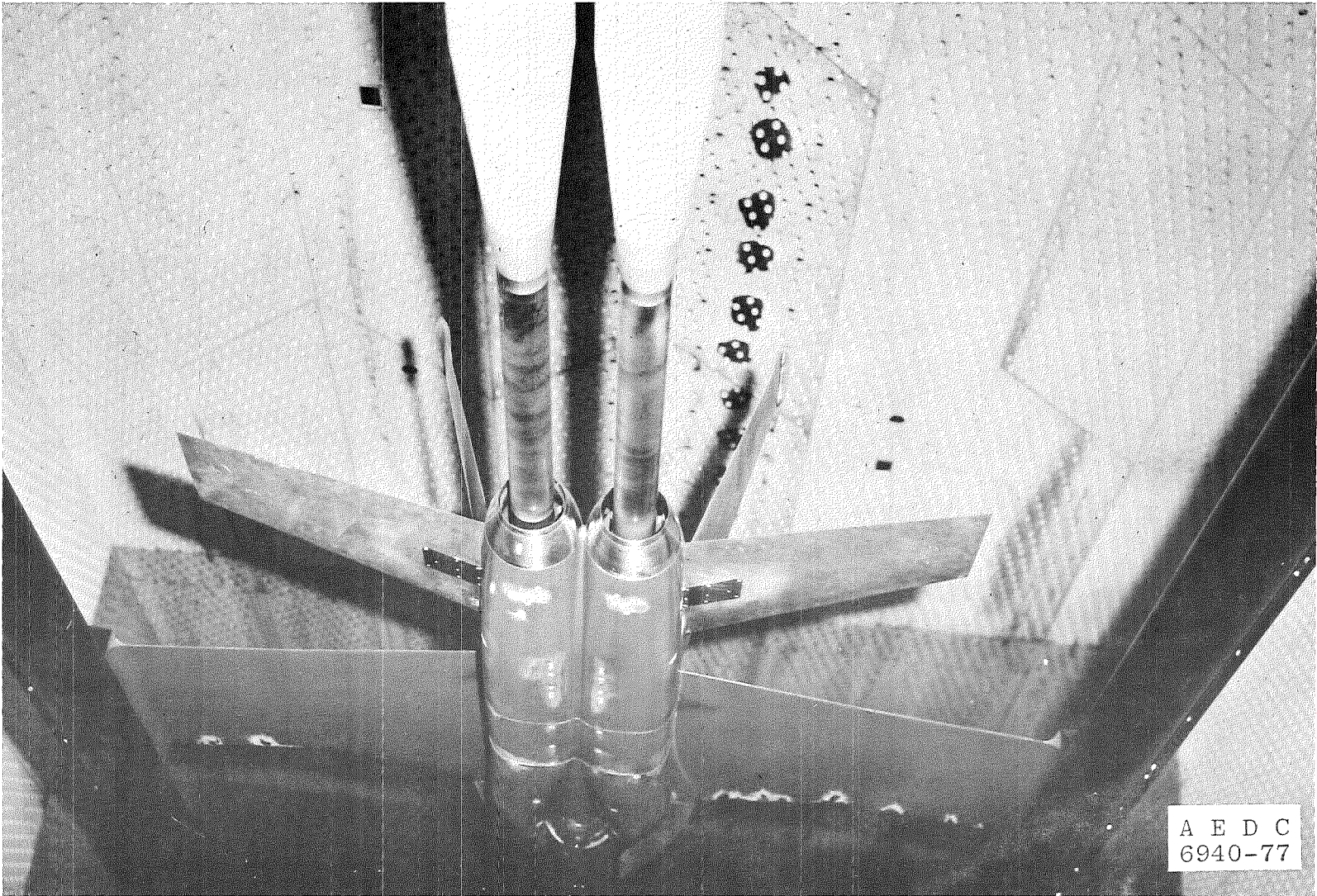
Figure 31. Configuration used to evaluate the annular-jet technique for
a 0.2-scale YF-17 model.

$$\Delta = (A.J. - Conv.)$$

Sym	Nozzle	NPR	D_s/D_e
O	Cruise	3.4	0.87
□	Part A/B	5.0	0.66
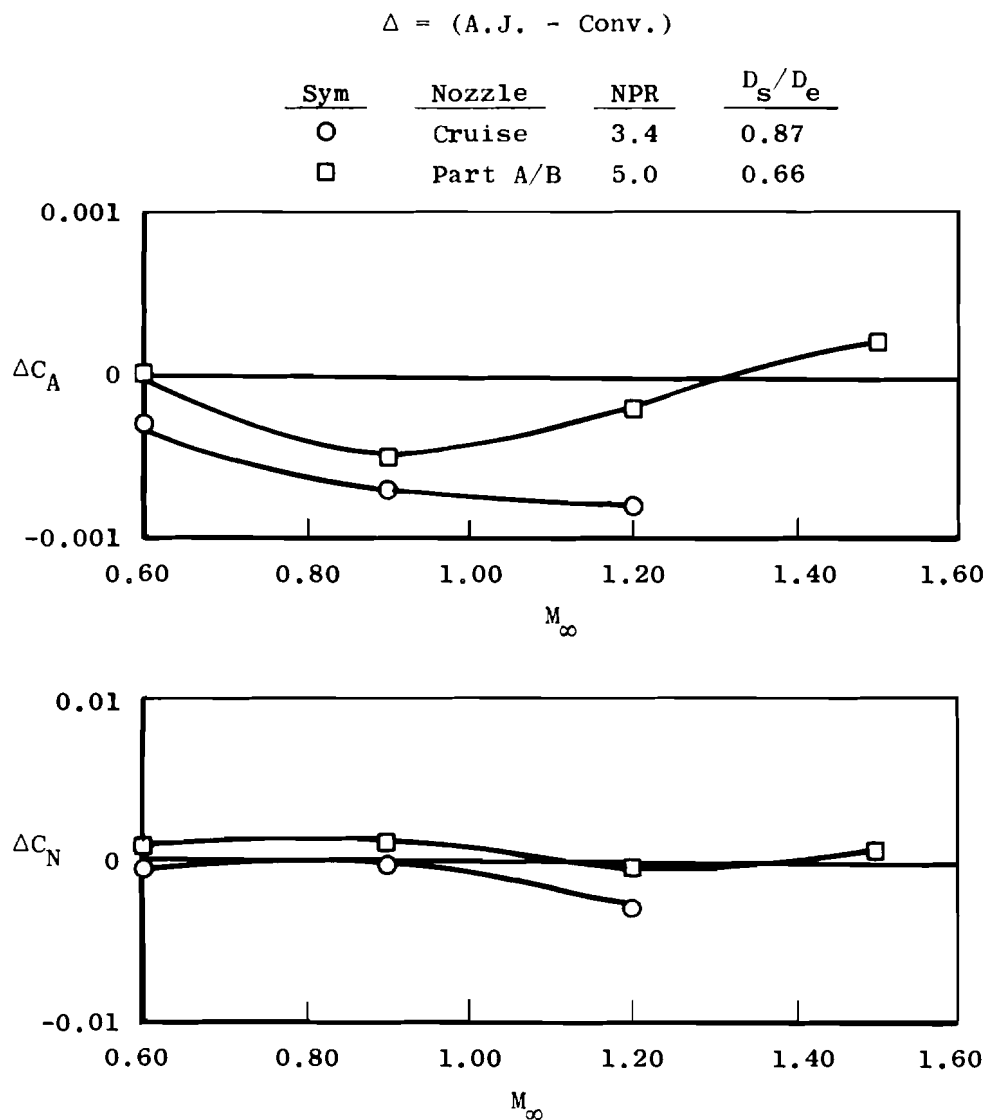
a. $a = 7$ deg

Figure 32. Difference in afterbody force coefficients between an annular and full jet for the 0.2-scale YF-17 model.

$$\triangle = (A.J. - Conv.)$$

Sym	Nozzle	NPR	D_s/D_e
O	Cruise	3.4	0.87
□	Part A/B	5.0	0.66
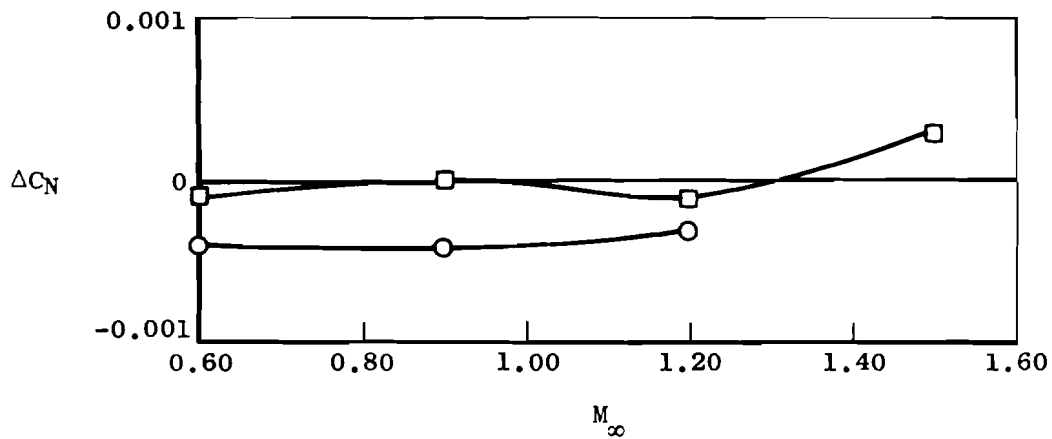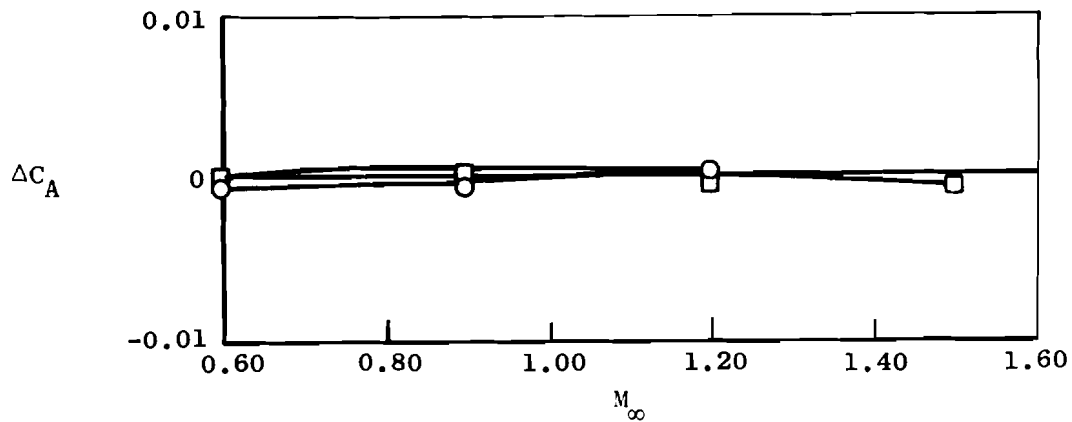
b. a = 4.0 deg
Figure 32. Concluded.
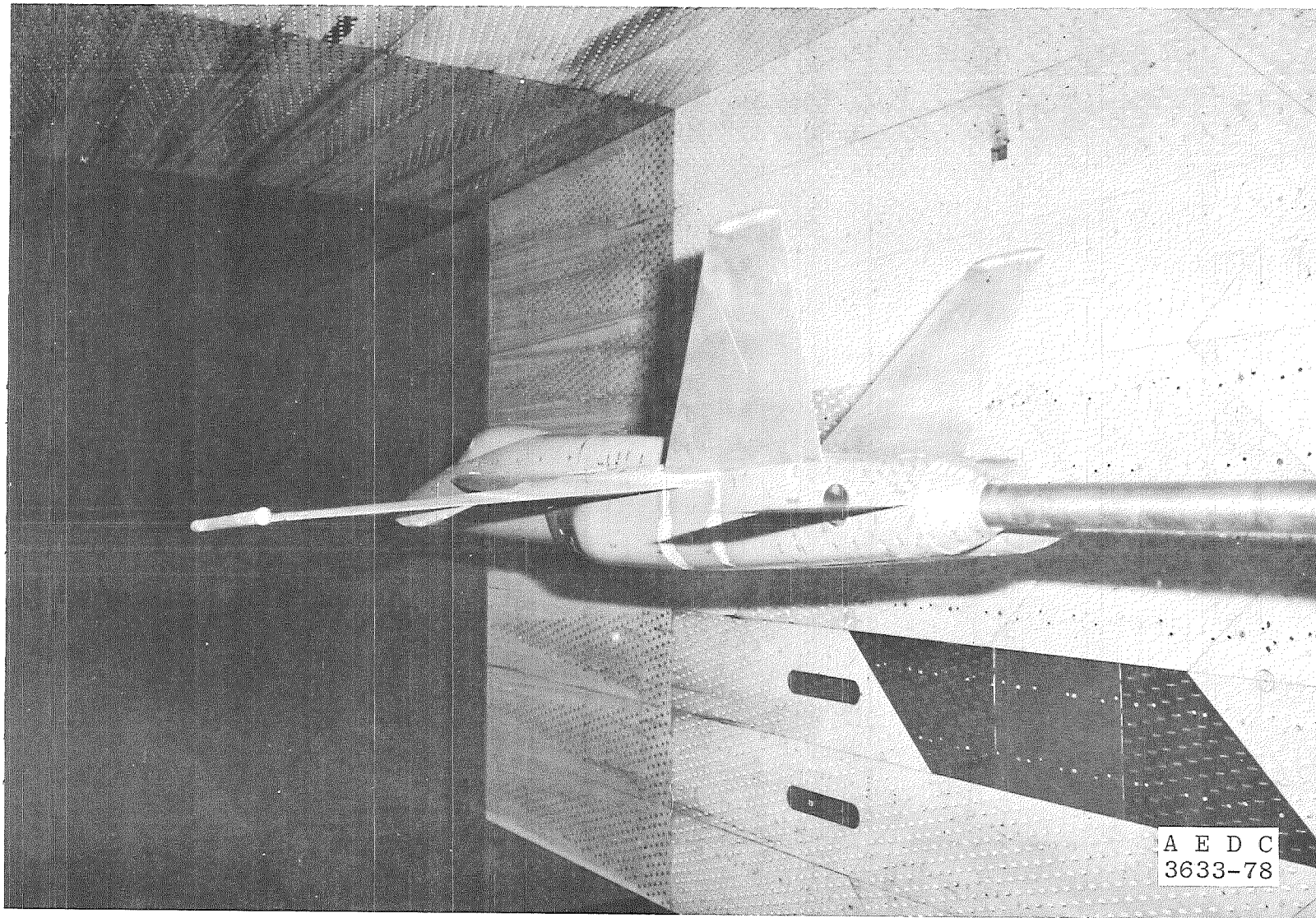
Figure 33. Annular-jet support YF-17 model installation in Tunnel 16T.

AEDC
3633-78
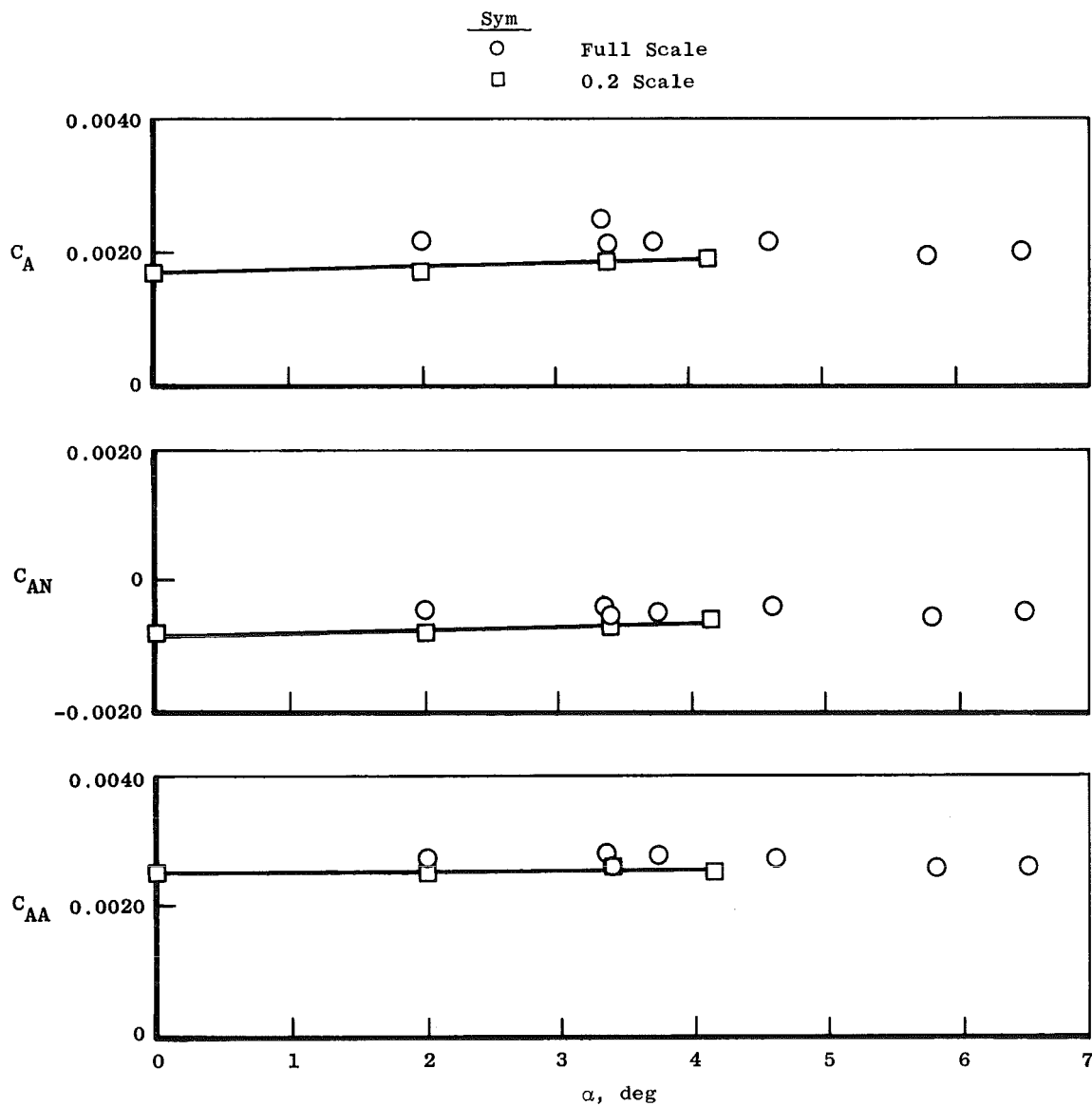
a. $M_\infty = 0.6$, NPR 2.0
Figure 34. Comparison of annular-jet model and flight axial-force
coefficient as a function of angle of attack,
cruise nozzle.
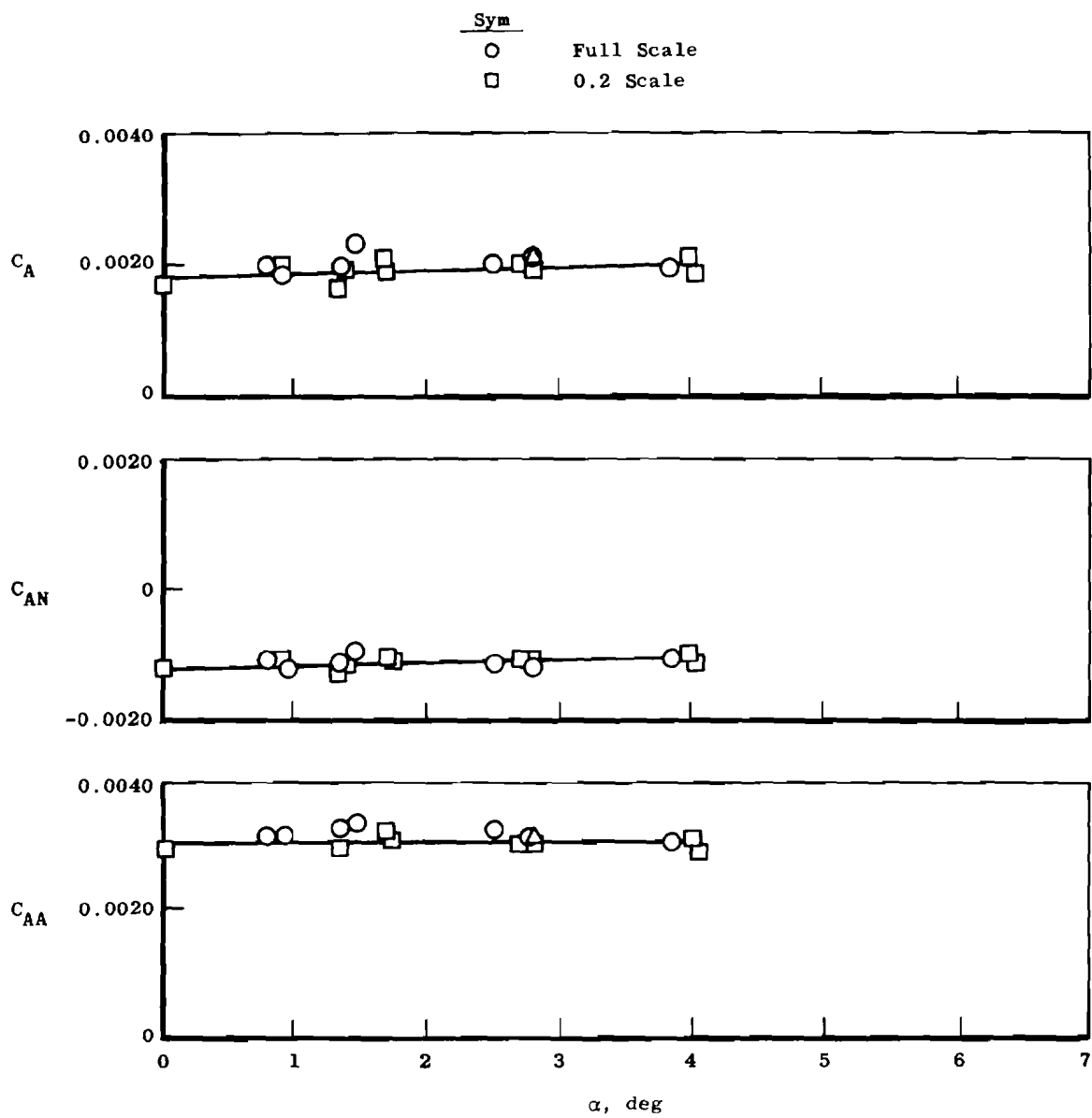
b. $M_\infty = 0.9$, NPR 3.4
Figure 34. Concluded.
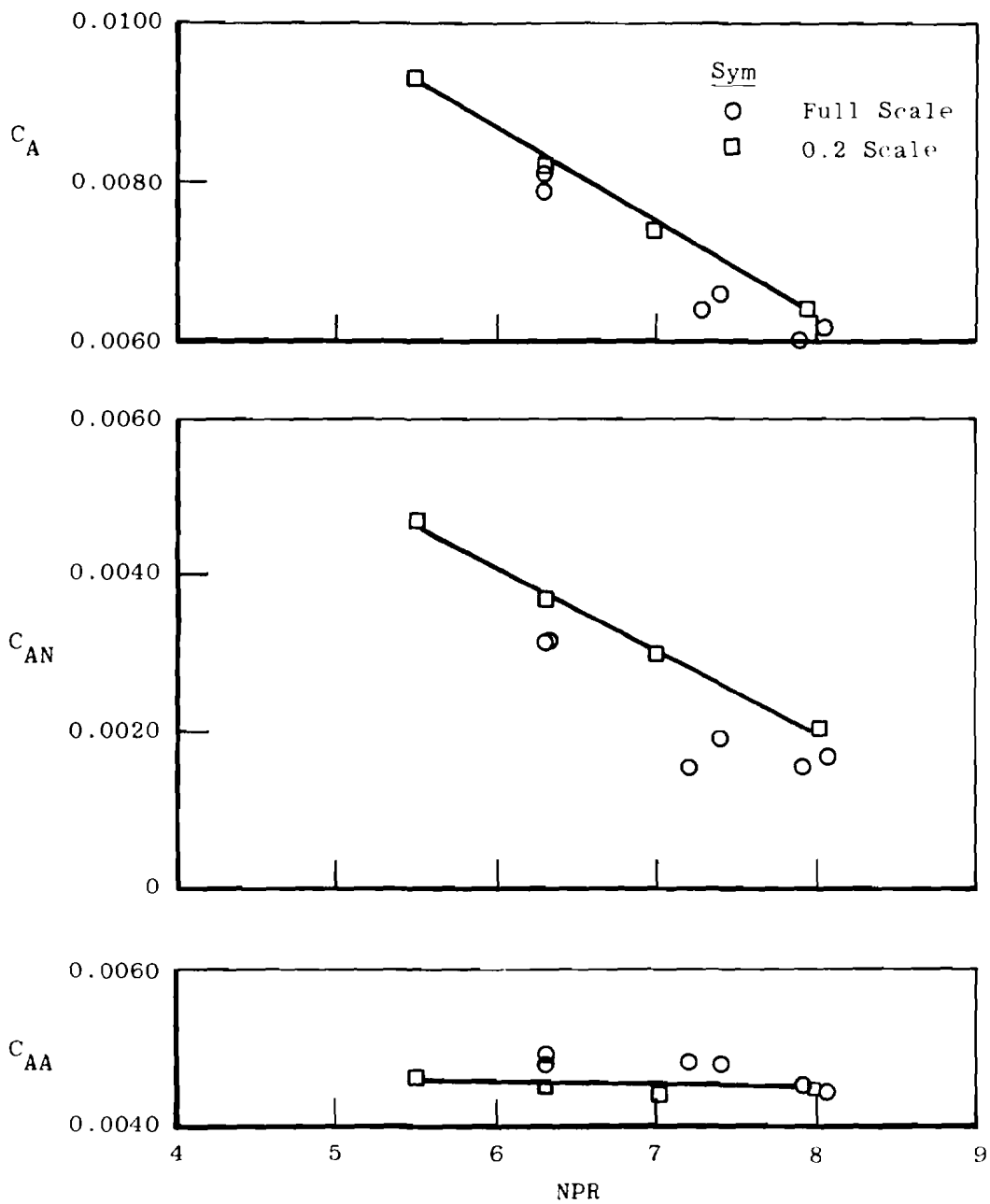
Figure 35. Comparison of annular-jet model and flight axial-force coefficient as a function of nozzle pressure ratio, part a/b nozzle, $a = 3$ deg.
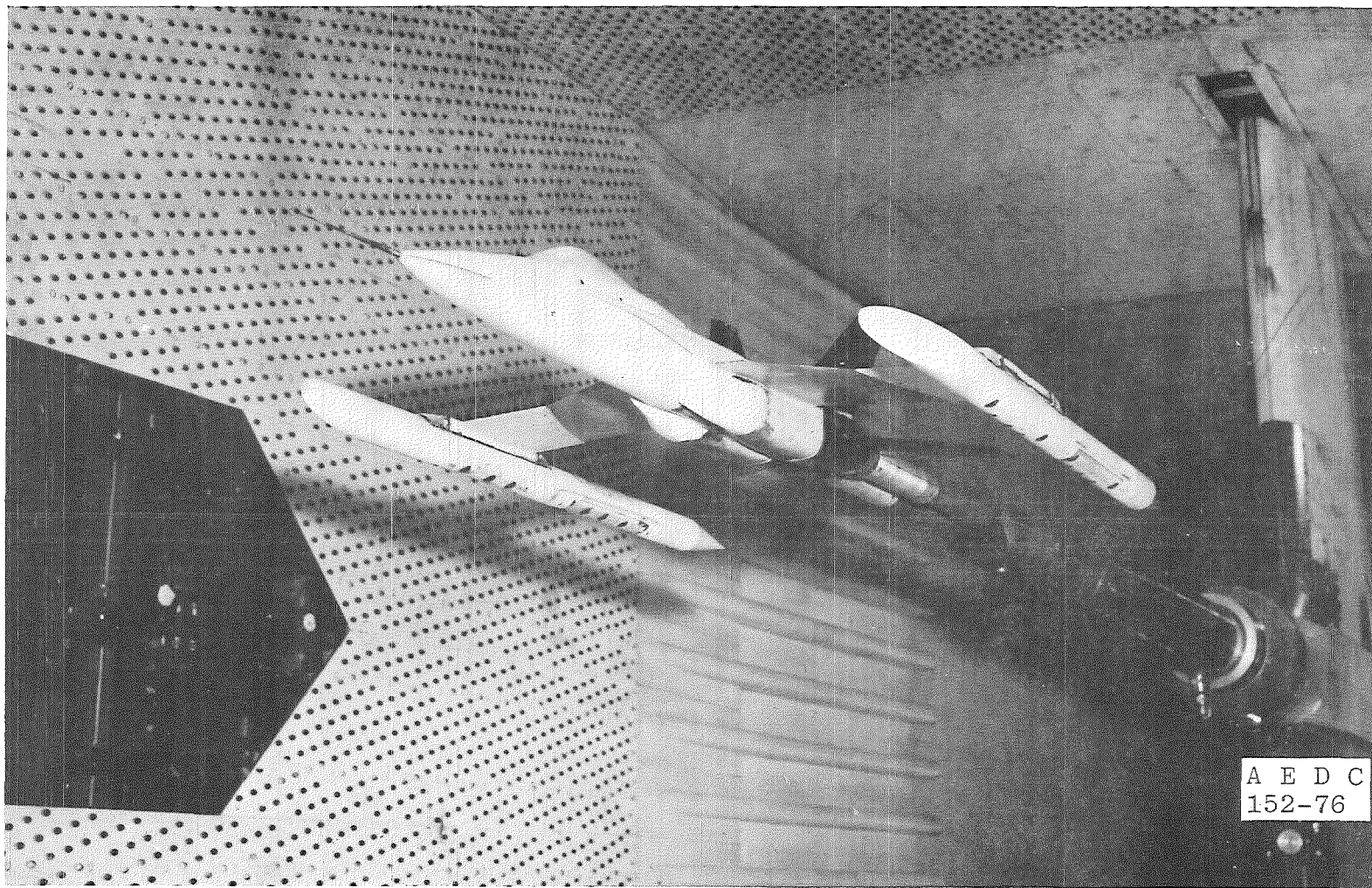
Figure 36. Configuration used to study wing-tip support interference.
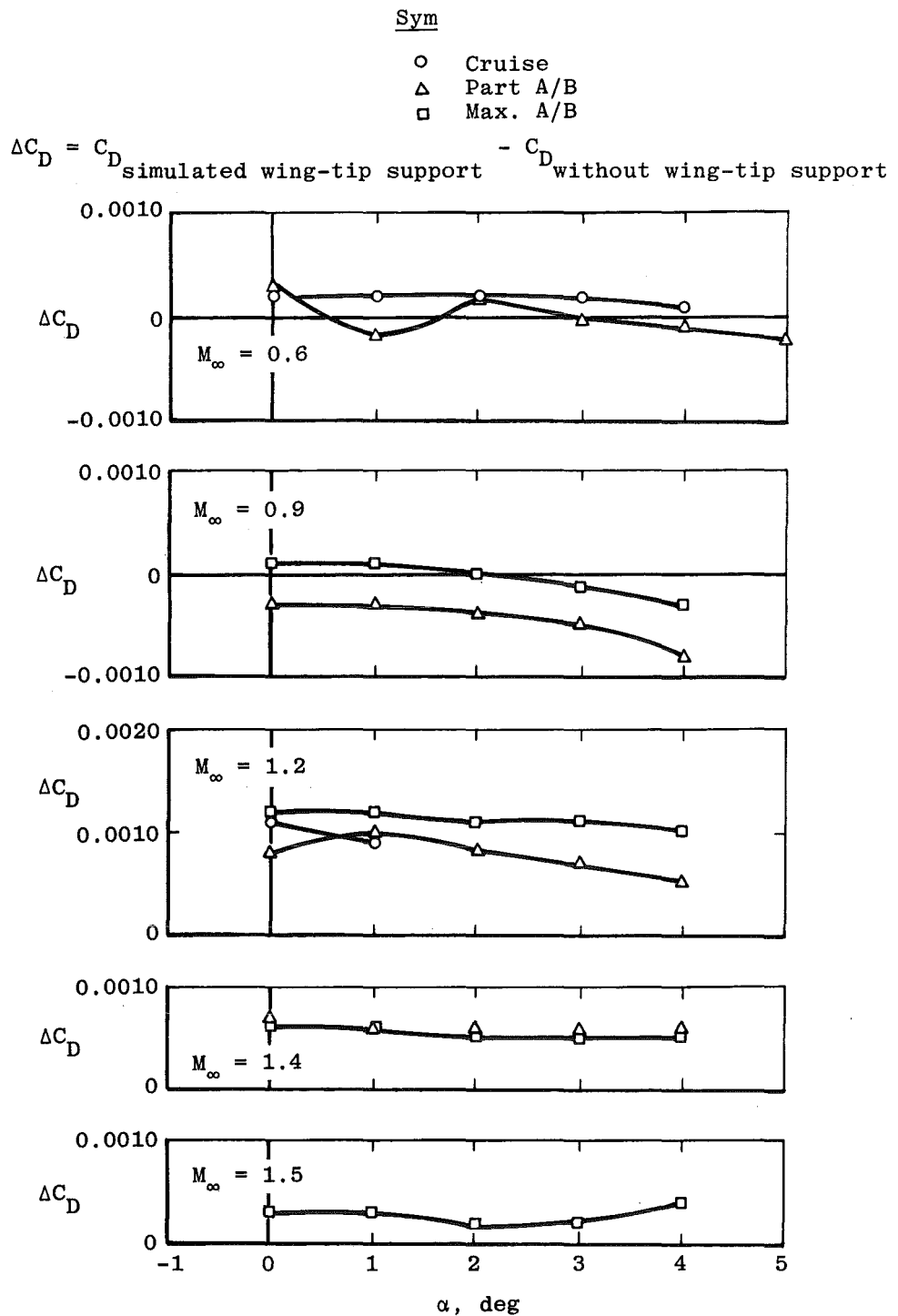
Figure 37. Effect of wing-tip support system interference on the drag coefficient of several nozzles.

96
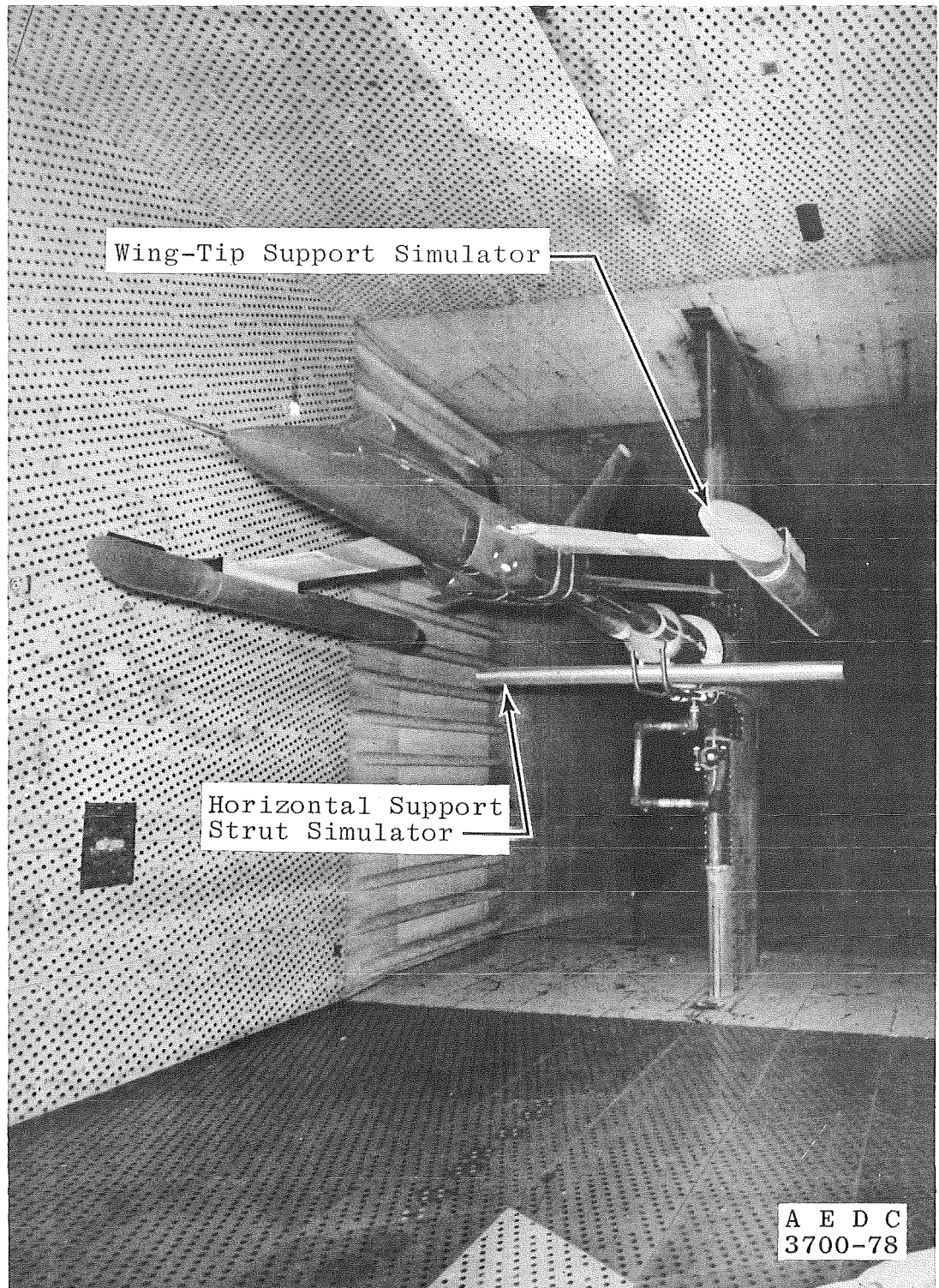
Figure 38. Configuration used to evaluate the interference contribution of various components of a wing-tip support system.

a. $a = 0$
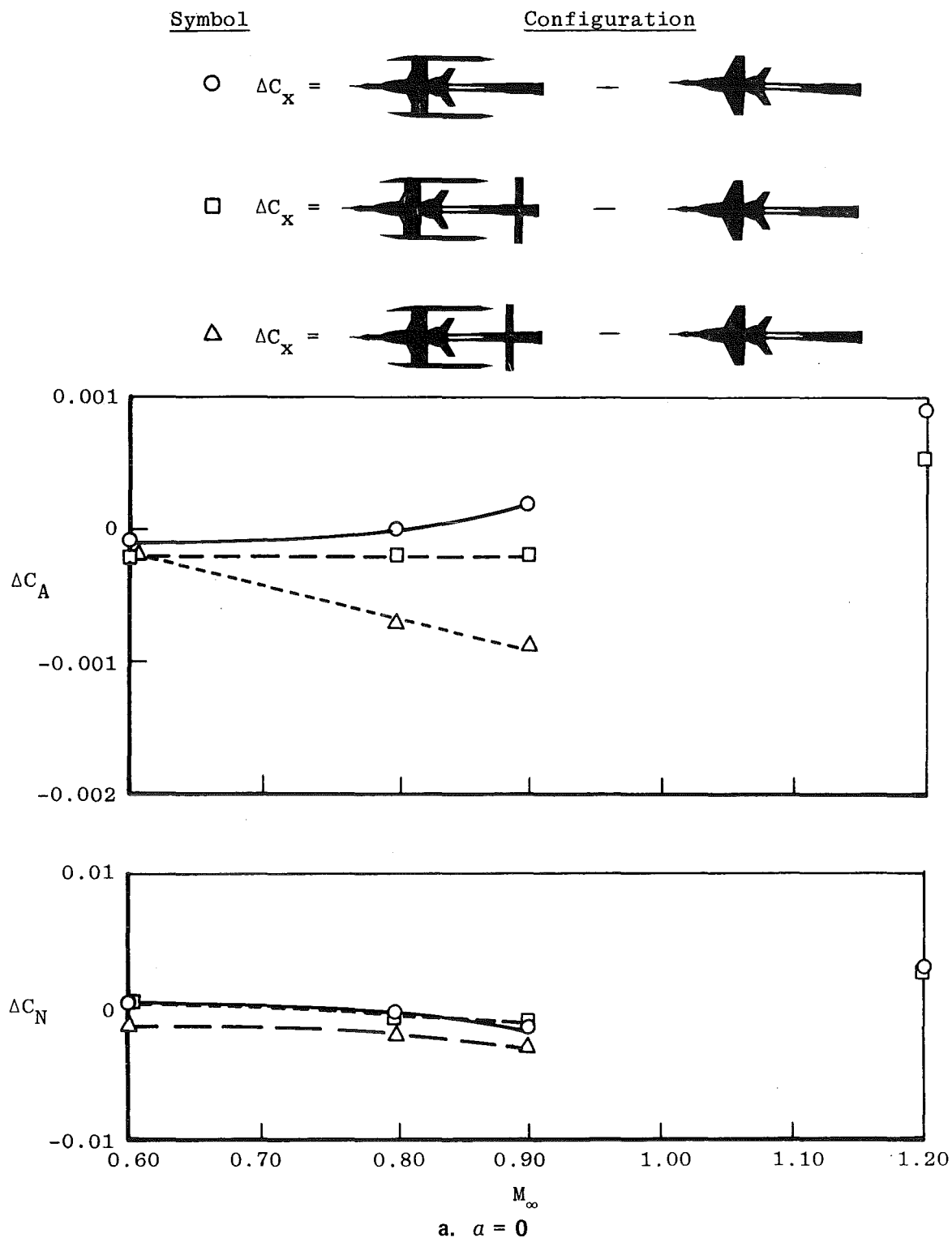
Figure 39. Effect of wing-tip support system components on afterbody force
coefficients for the 0.2-scale YF-17 model cruise nozzle,
NPR = 3.4
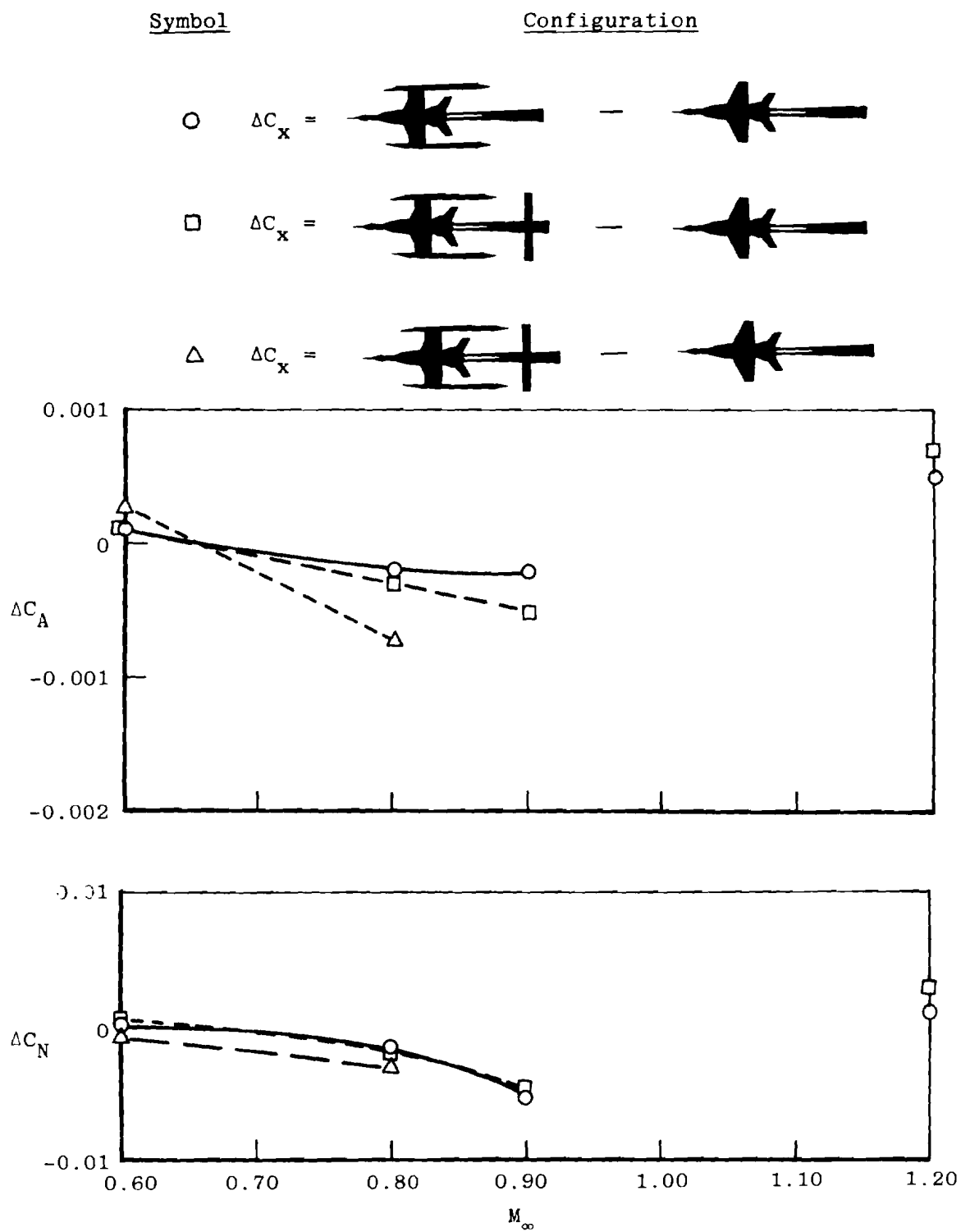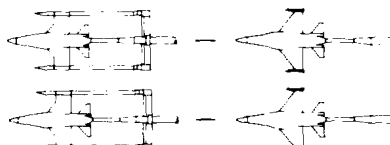
b. a = 4 deg
Figure 39. Concluded.

Sym	Nozzle	NPR			
O	Cruise 3.4	J. Off	ΔC_x		
□	Max A/B 6.6	4.8	ΔC_x		
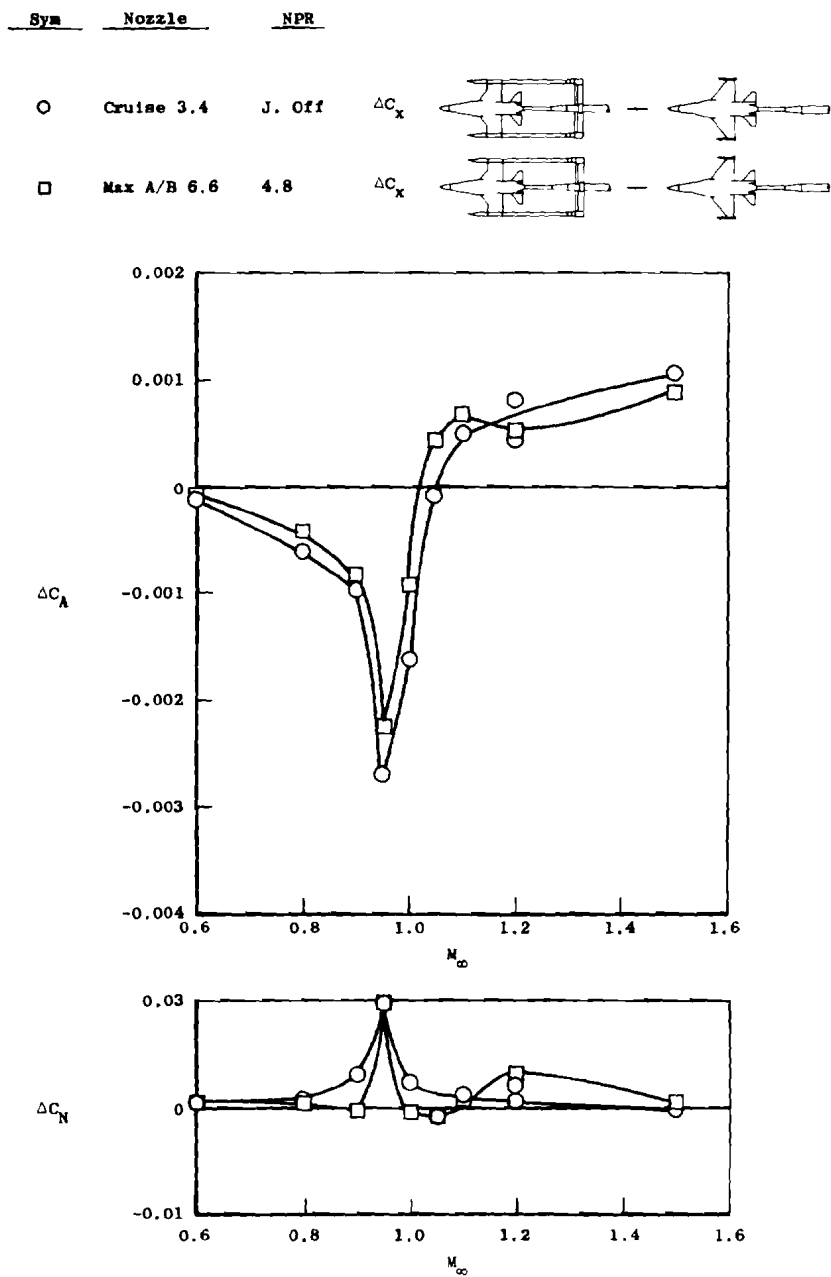
a. $a = 0$ deg

Figure 40. Effect of wing-tip support system on afterbody force
coefficients for the 1/9-scale F-16 model.

Sym	Nozzle	NPR
O	Cruise 3.4	J. Off
□	Max A/B 6.6	4.8
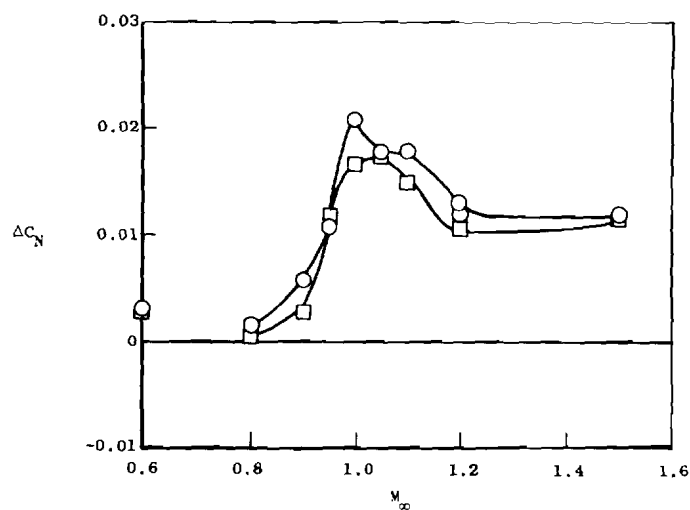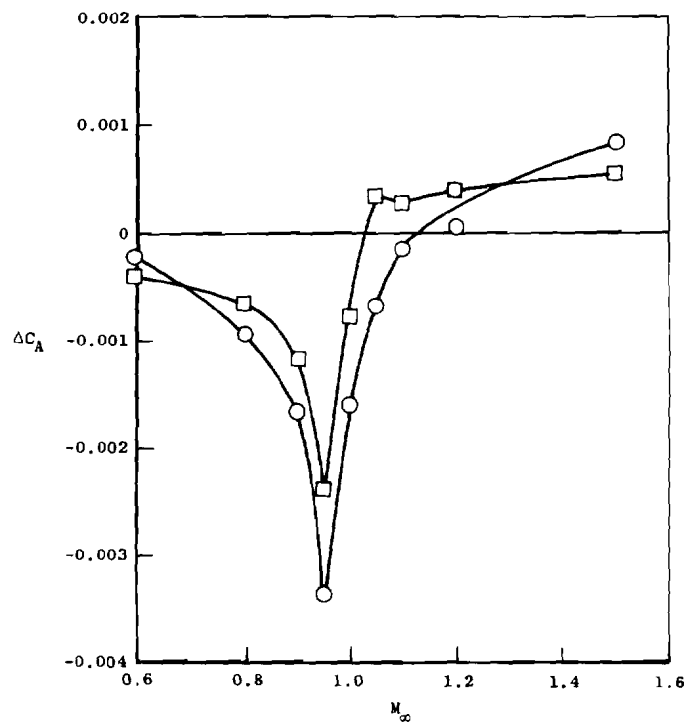
b. a = 7.0 deg

Figure 40. Concluded.

101

Sym	Configurations	Support Systems
O		Sting (Annular Jet)
△		Strut (Dummy Sting and Annular Jet)
□		Wingtip (Dummy Sting and Annular Jet)

a. $a = 0$
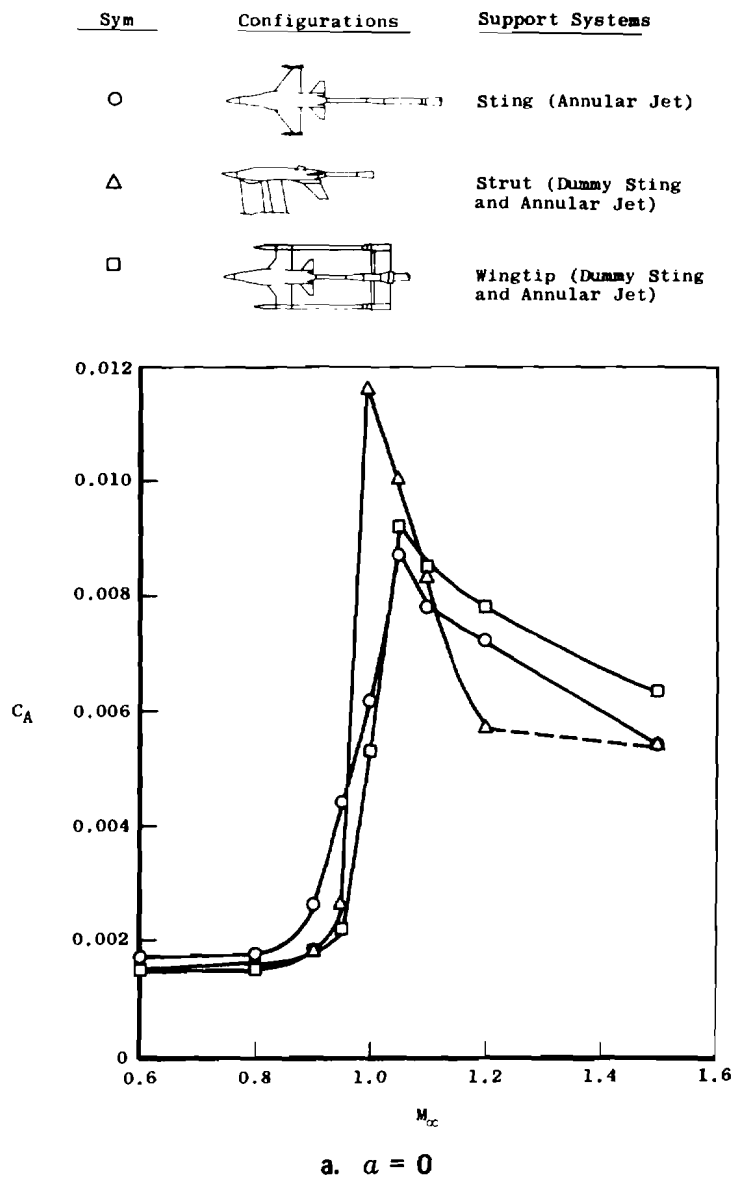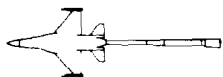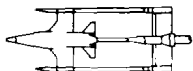
Figure 41. Comparison of afterbody force coefficients determined with sting, strut, and wing-tip support systems (maximum A/B nozzle, NPR = 4.8).

Sym	Configurations	Support Systems
O		Sting (Annular Jet)
△		Strut (Dummy Sting and Annular Jet)
□		Wingtip (Dummy Sting and Annular Jet)

a. Concluded
Figure 41. Continued.

103

Sym	Configurations	Support Systems
O		Sting (Annular Jet)
△		Strut (Dummy Sting and Annular Jet)
□		Wingtip (Dummy Sting and Annular Jet)
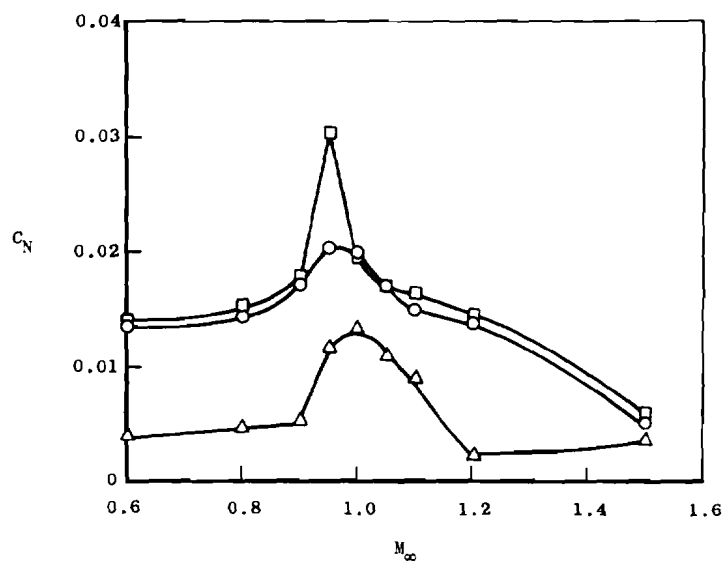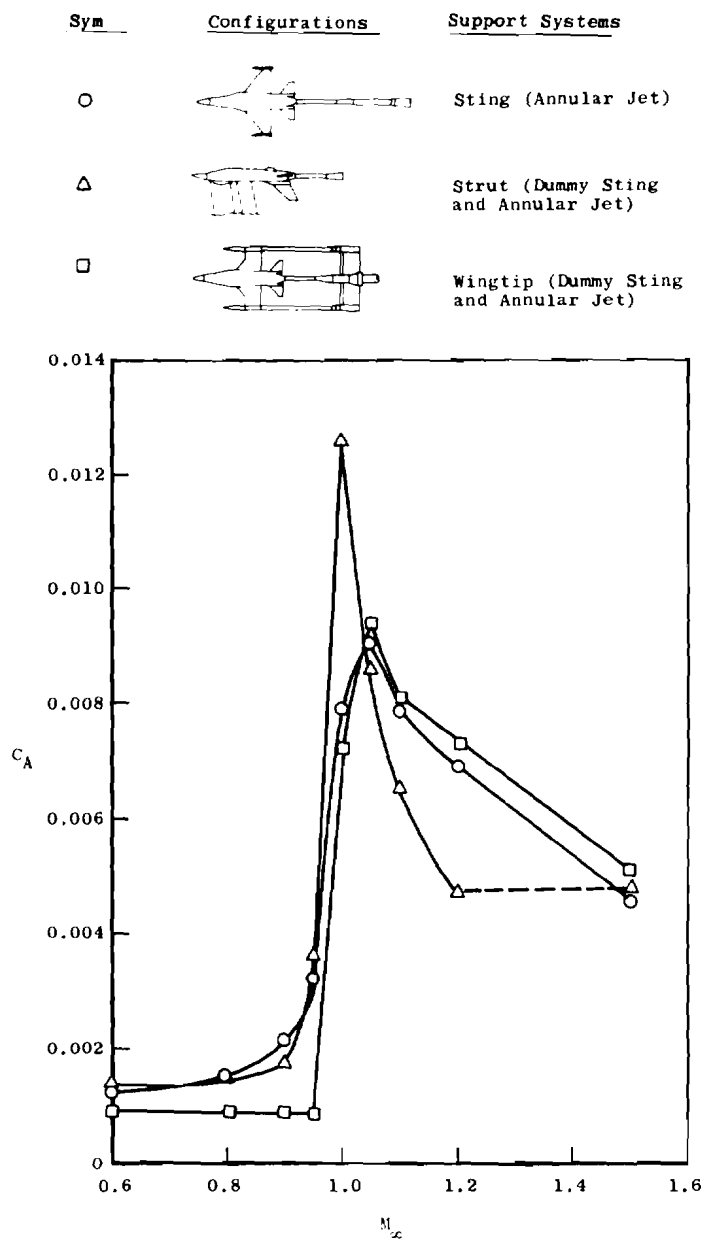
b. a = 7 deg

Figure 41. Continued.
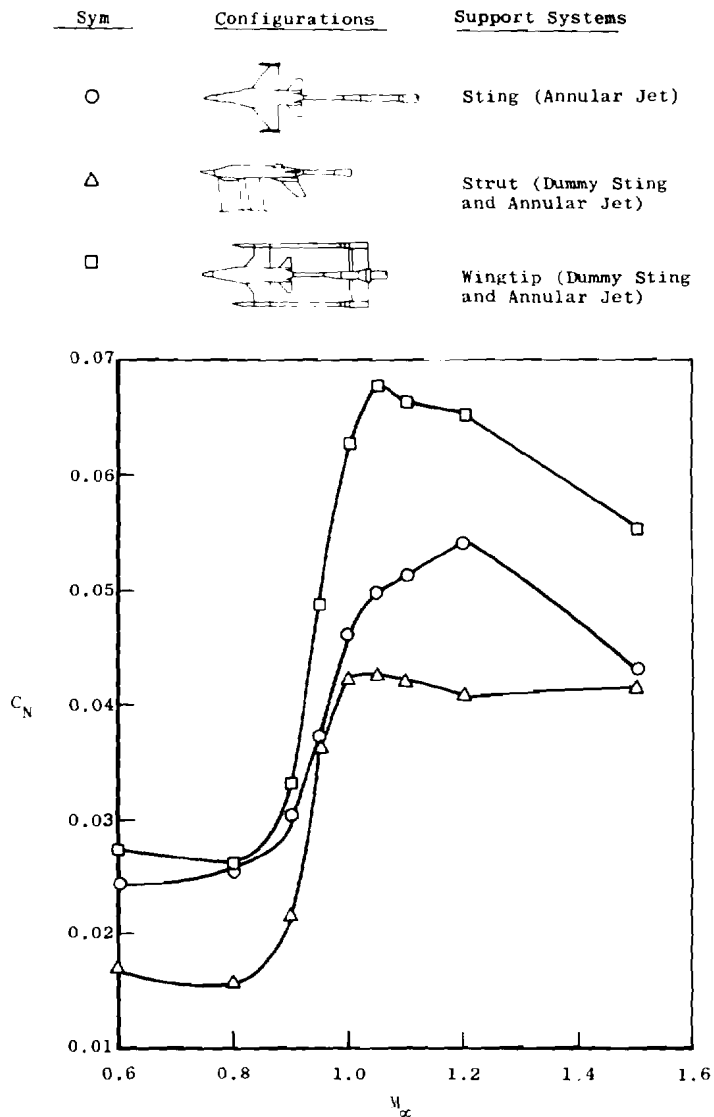
b. Continued
Figure 41. Continued.

Sym	Configurations	Support Systems
O		Sting (Annular Jet)
△		Strut (Dummy Sting and Annular Jet)
□		Wingtip (Dummy Sting and Annular Jet)
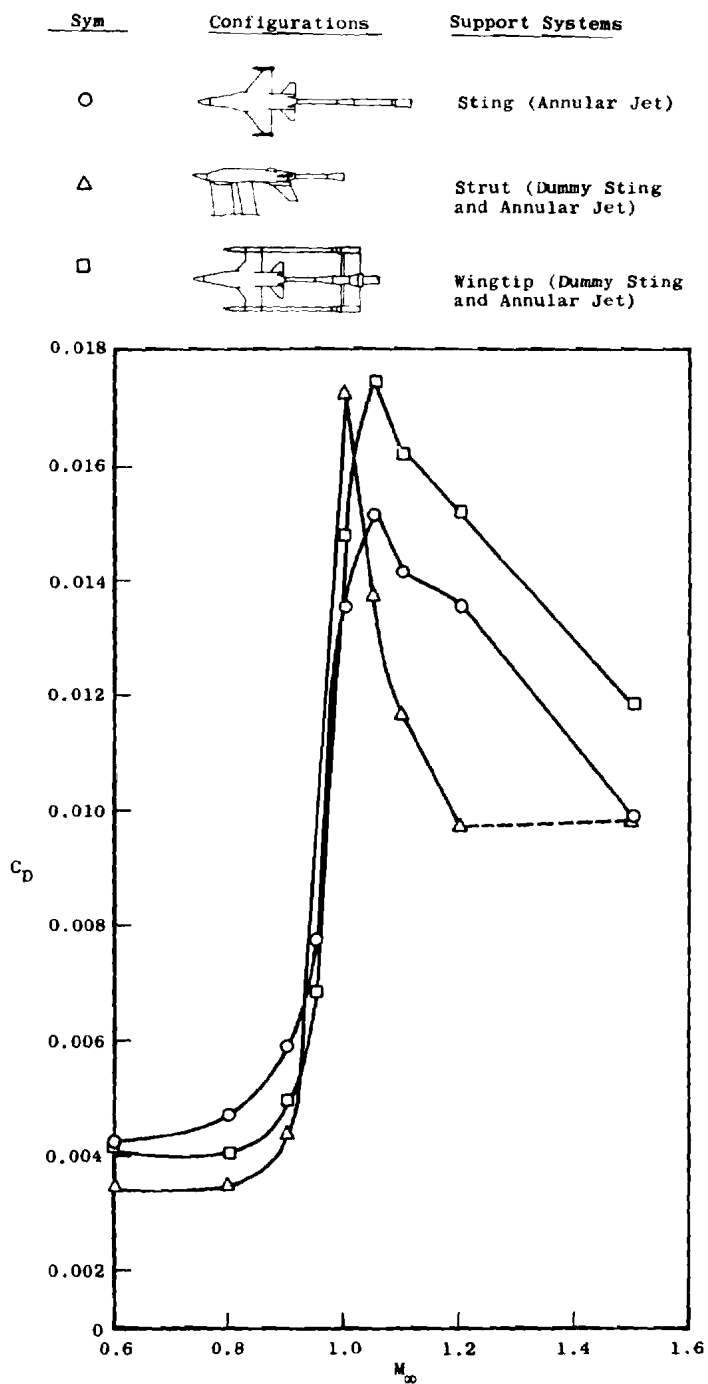
b. Concluded
Figure 41. Concluded.

106
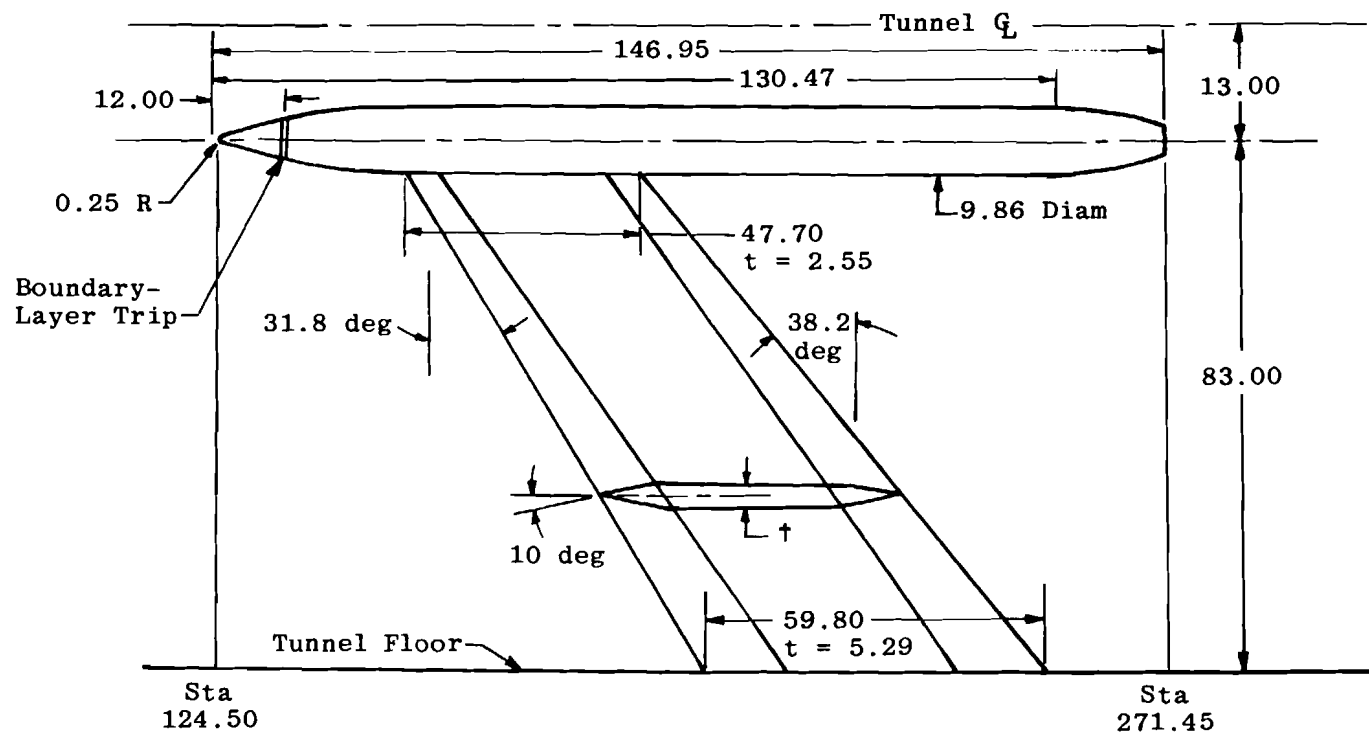
Dimensions in Inches

a. 16T model

Figure 42. Models used for jet simulation investigation.

Stations and Dimensions in Inches
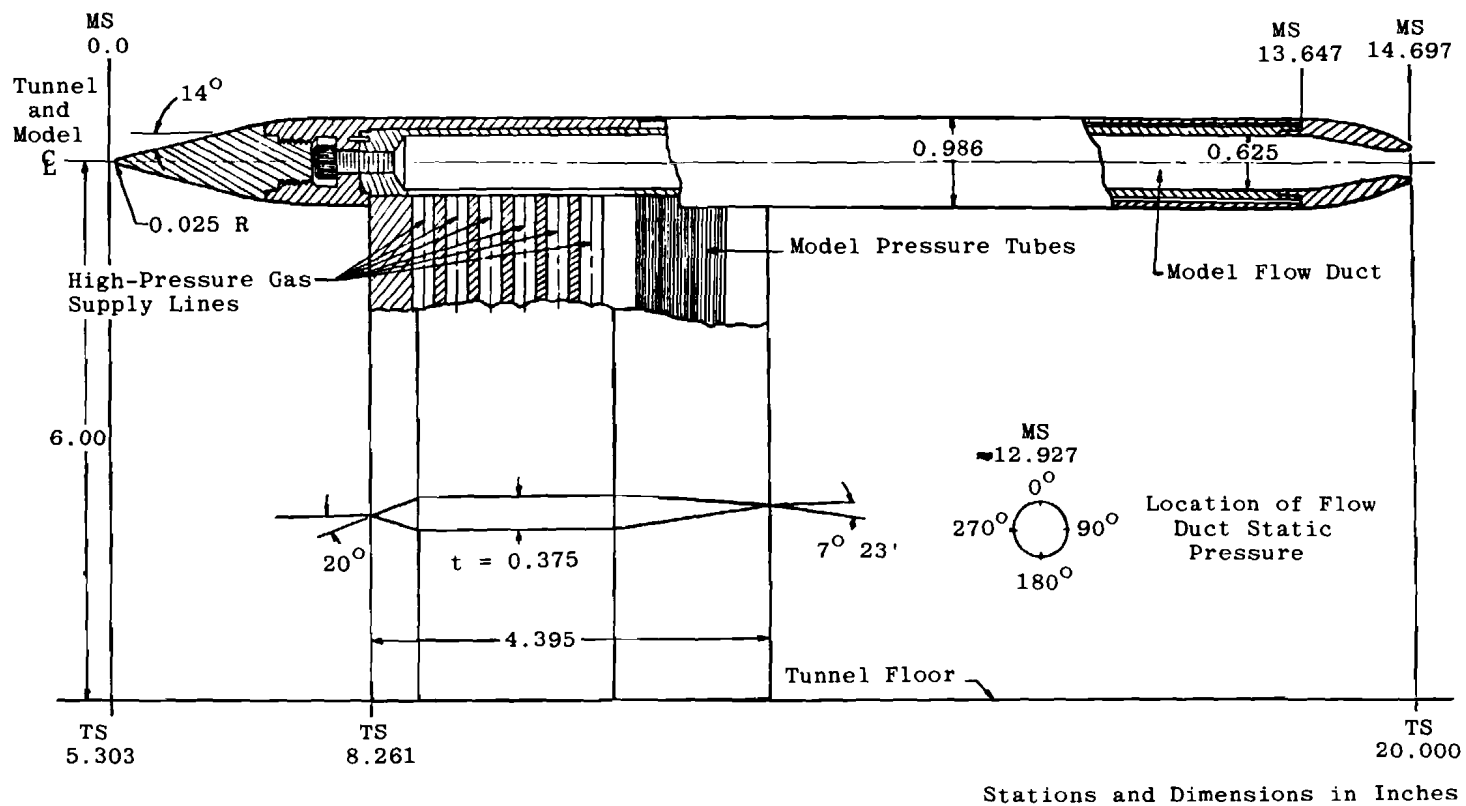
b. 1T model
Figure 42. Concluded.

16.499 (16T)
1.650 (1T)

X

15 deg

Y

Model C$_L$

MS
130.471 (16T)
13.047 (1T)

MS
146.970 (16T)
14.697 (1T)

a. 15-deg boattail

16.499 (16T)
1.650 (1T)

X

Y

Model C$_L$

25 deg

MS
130.471 (16T)
13.047 (1T)

MS
146.970 (16T)
14.697 (1T)
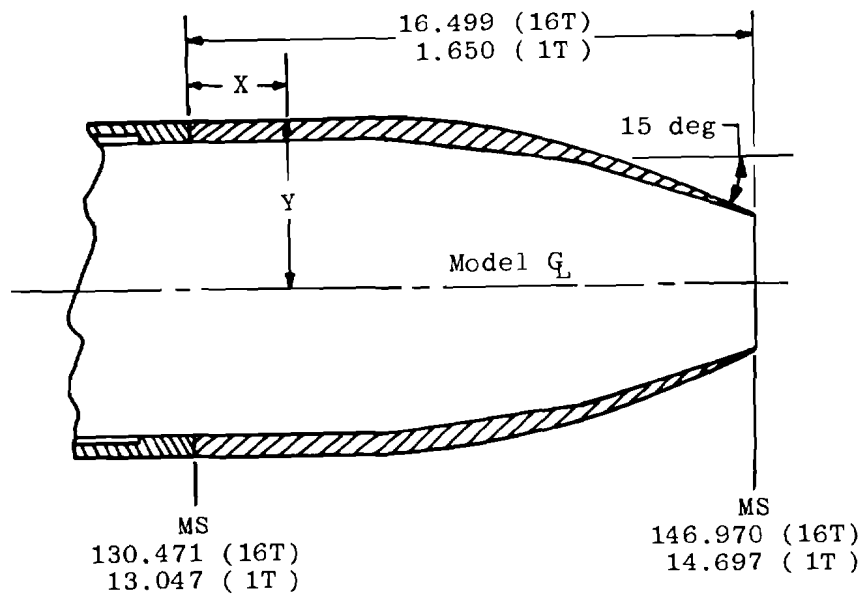
Stations and Dimensions in Inches

b. 25-deg boattail
Figure 43. Boattail configurations used for jet simulation investigations.

109
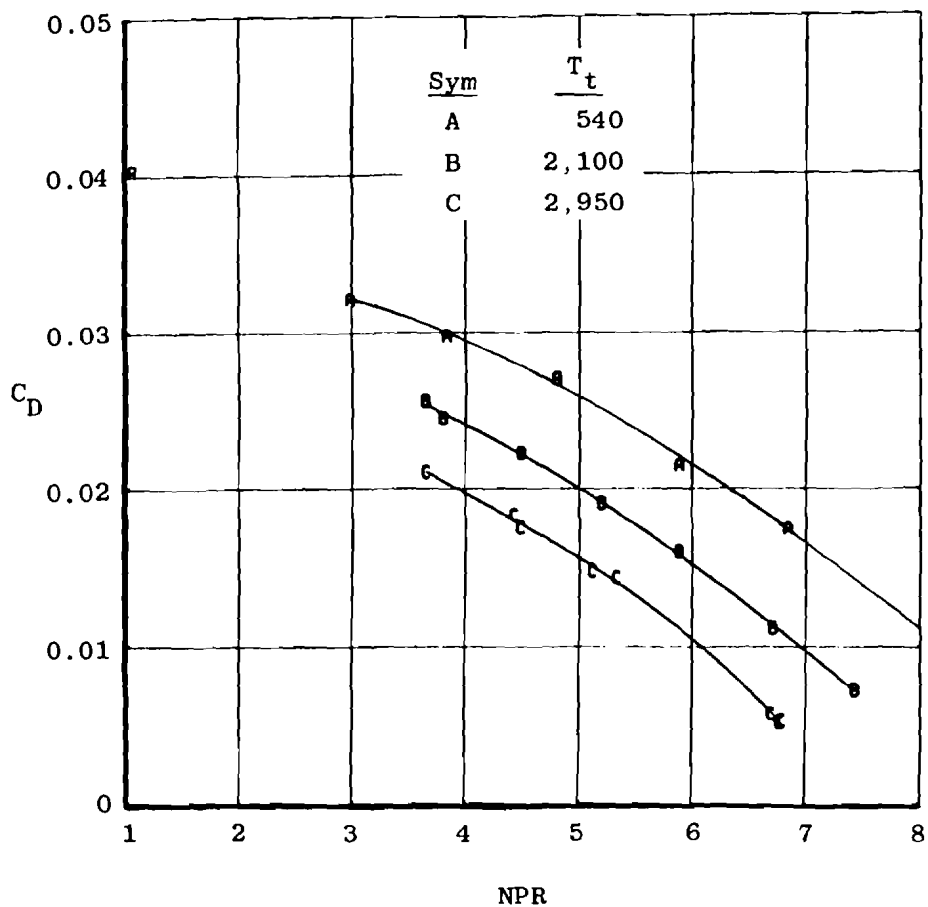
a. $M_\infty = 0.6$
Figure 44. Exhaust plume temperature effects on a 15-deg boattail configuration.
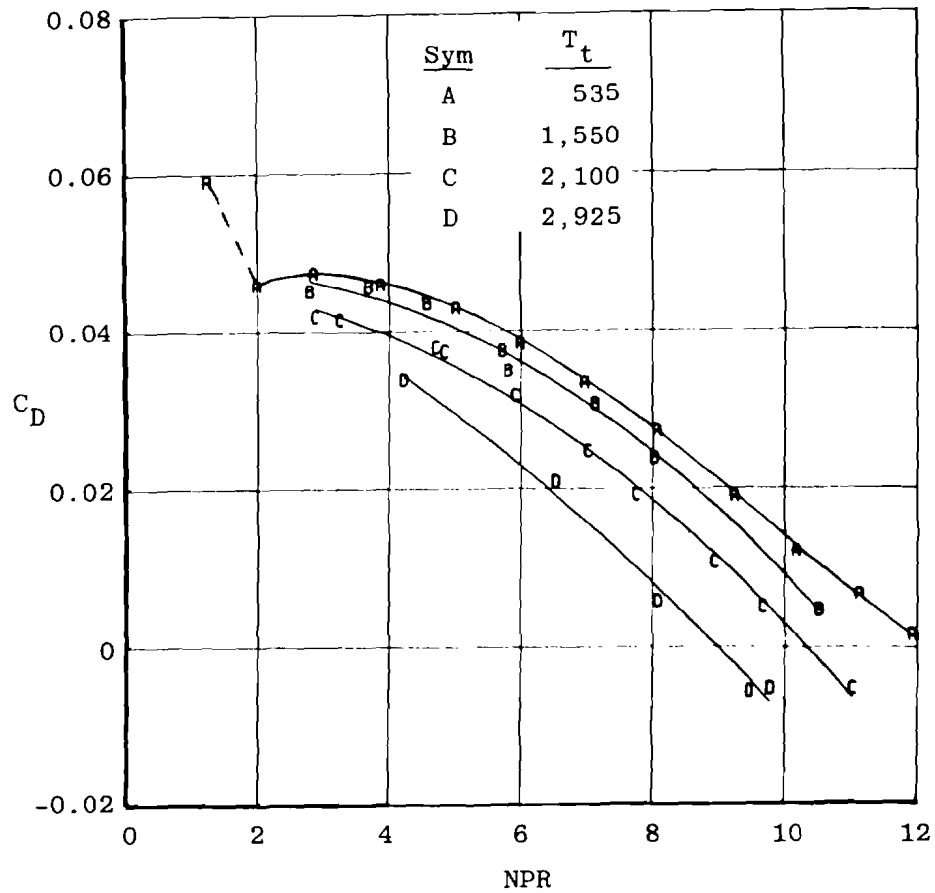
b. $M_\infty = 0.9$
Figure 44. Continued.
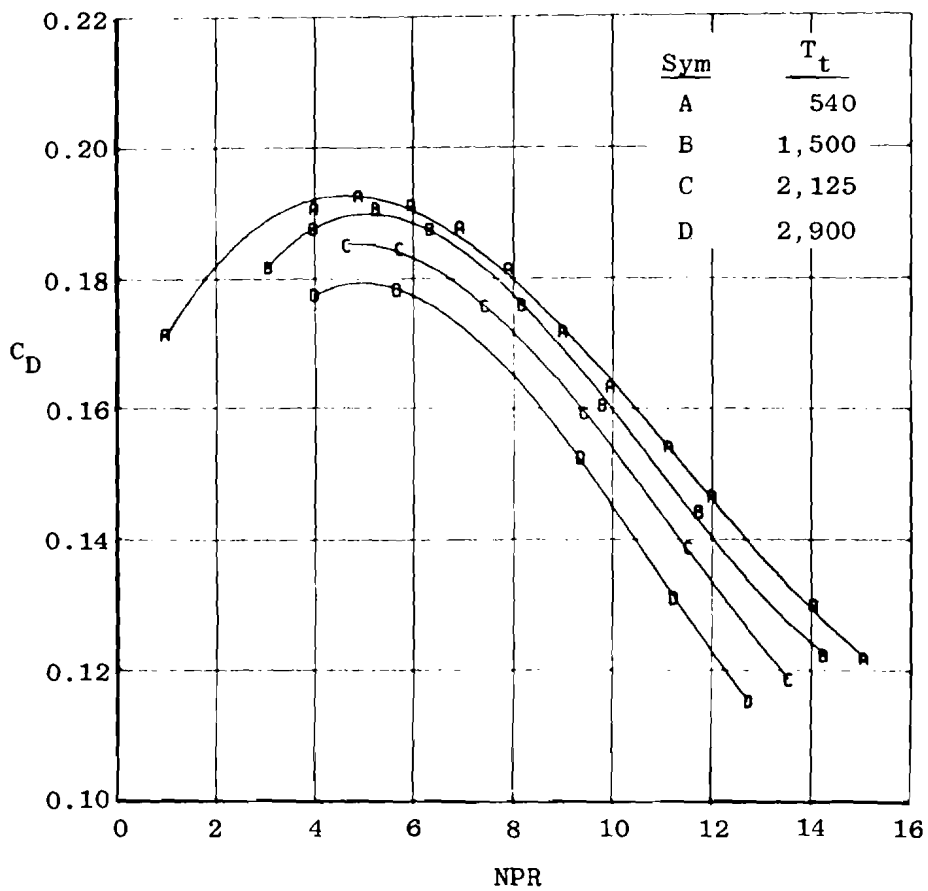
a. $M_\infty = 1.1$
Figure 44. Concluded.
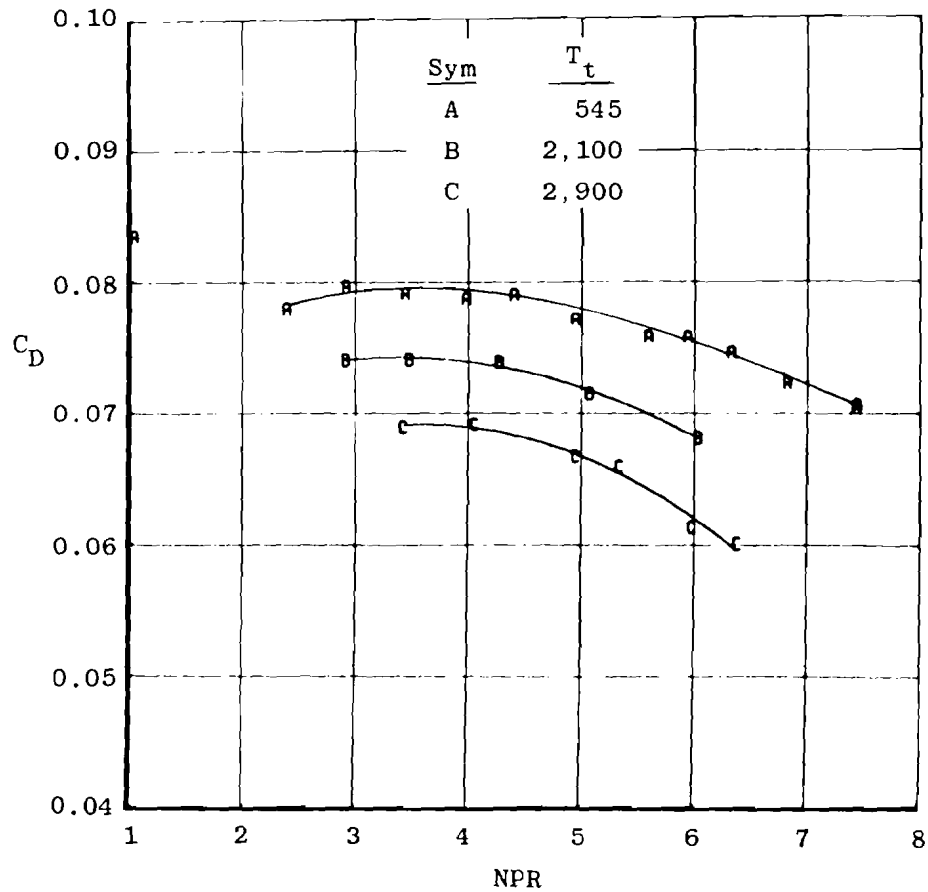
a. $M_\infty = 0.6$

Figure 45. Exhaust plume temperature effects on a 25-deg boattail configuration.
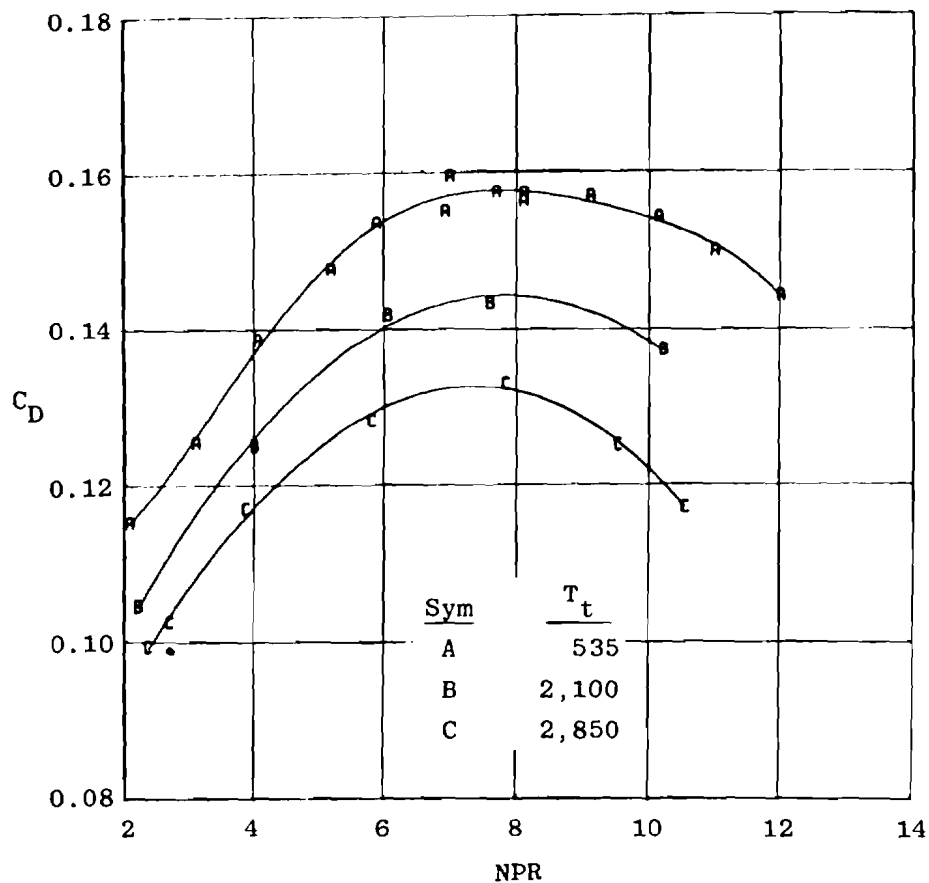
b. $M_\infty = 0.9$
Figure 45. Continued.
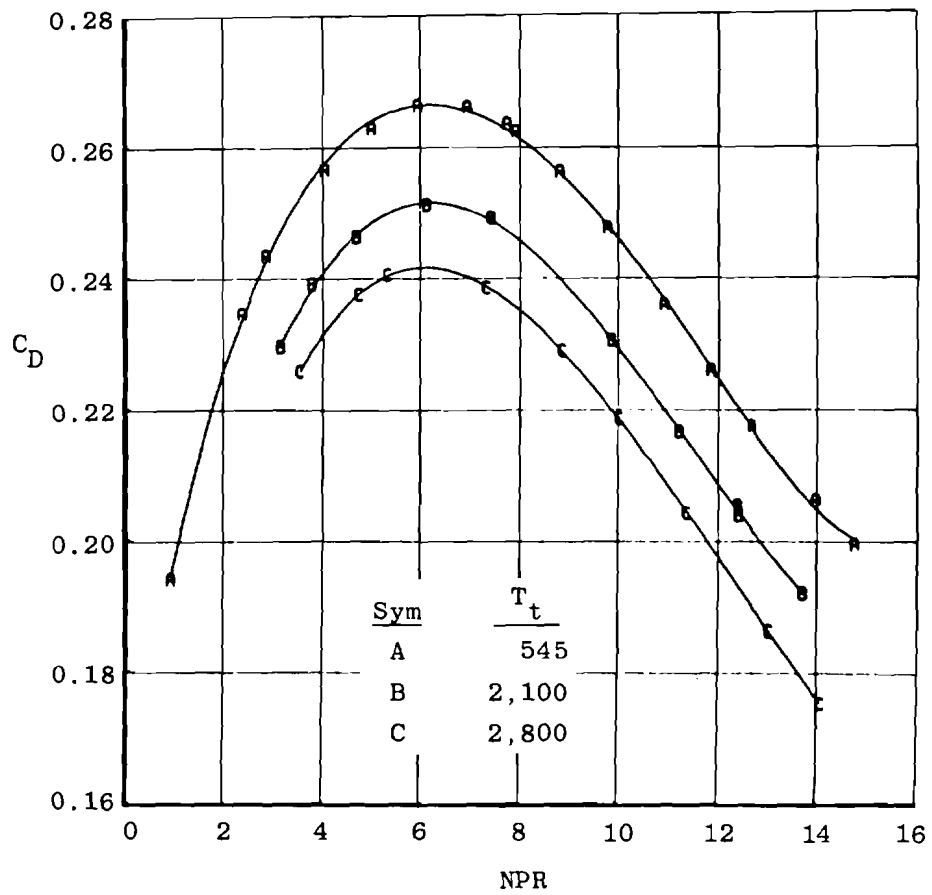
c. $M_\infty = 1.1$
Figure 45. Concluded.
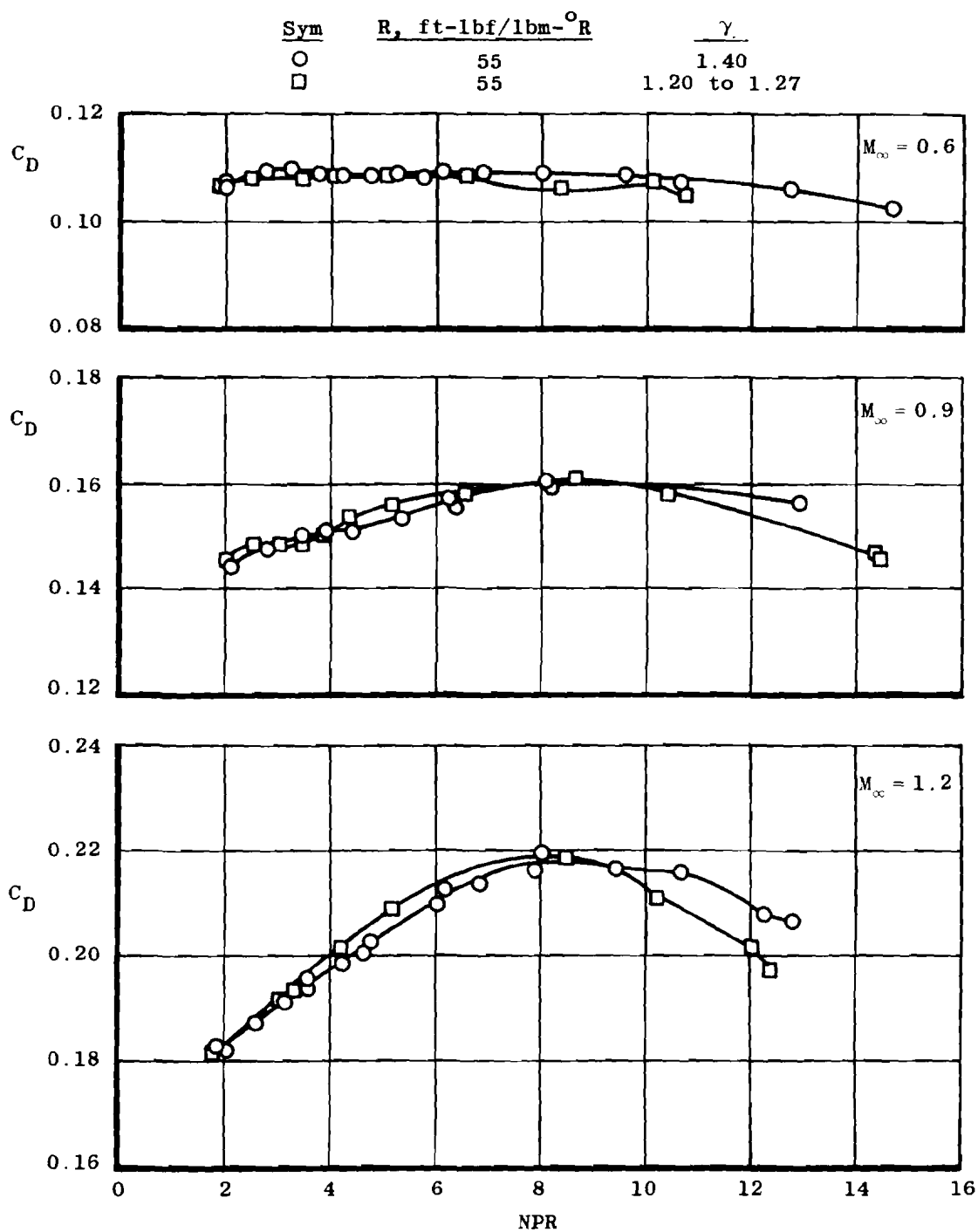
a. 15-deg boattail

Figure 46. Effect of jet specific heat ratio on afterbody pressure drag coefficient.

Sym	R, ft-lbf/lbm-°R	γ
O	55	1.40
□	55	1.20 to 1.27
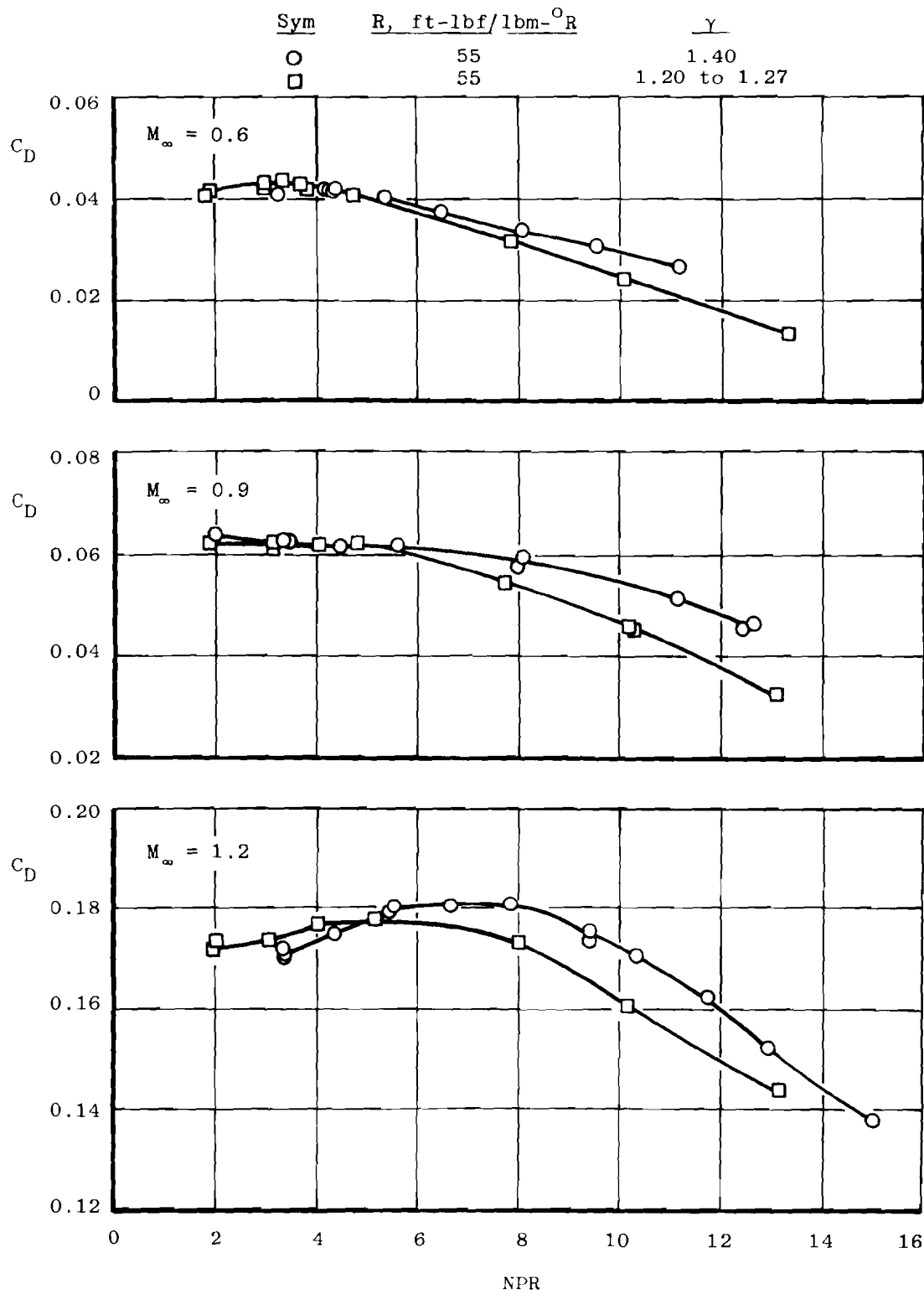
b. 25-deg boattail

Figure 46. Concluded.
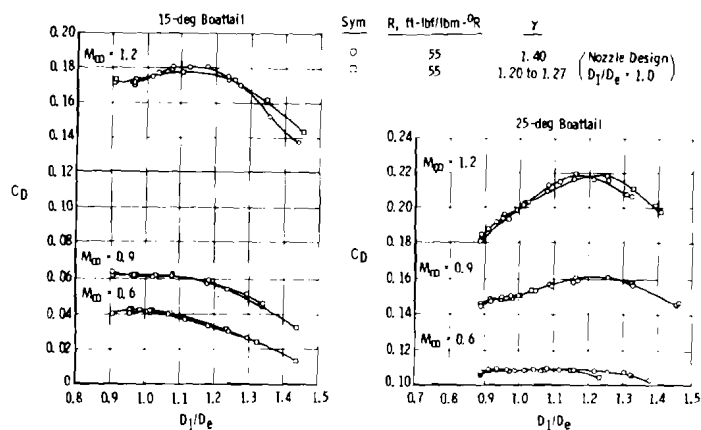
a. Plume-to-nozzle exit diameter ratio
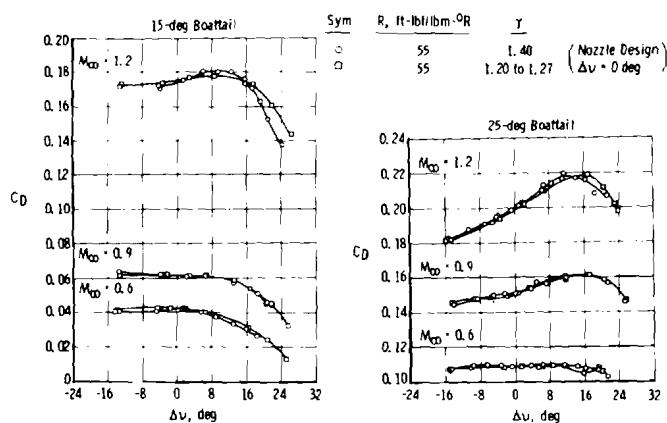
b. Incremental Prandtl-Meyer angle
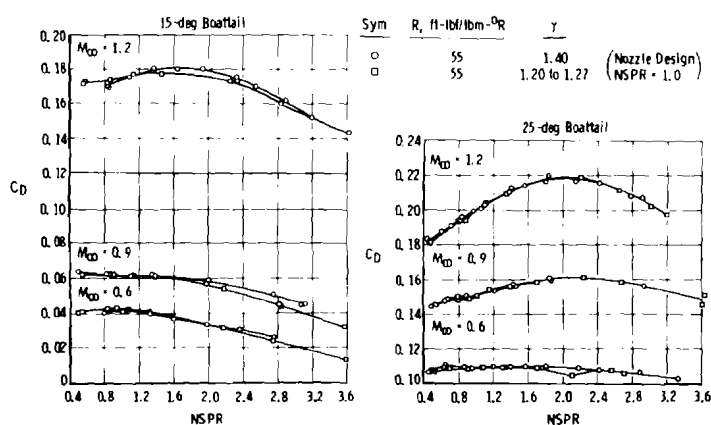
c. Nozzle static pressure ratio

Figure 47. Afterbody drag coefficient correlation with quiescent plume shape parameters for specific heat ratio from 1.2 to 1.4

Sym	R, ft-lbf/lbm-°R	γ
O	55	1.40
△	231	
◇	409	
◁	580	
D	767	
♦	Solid Plume	

a. $M_\infty = 0.6$

b. $M_\infty = 0.9$

c. $M_\infty = 1.2$
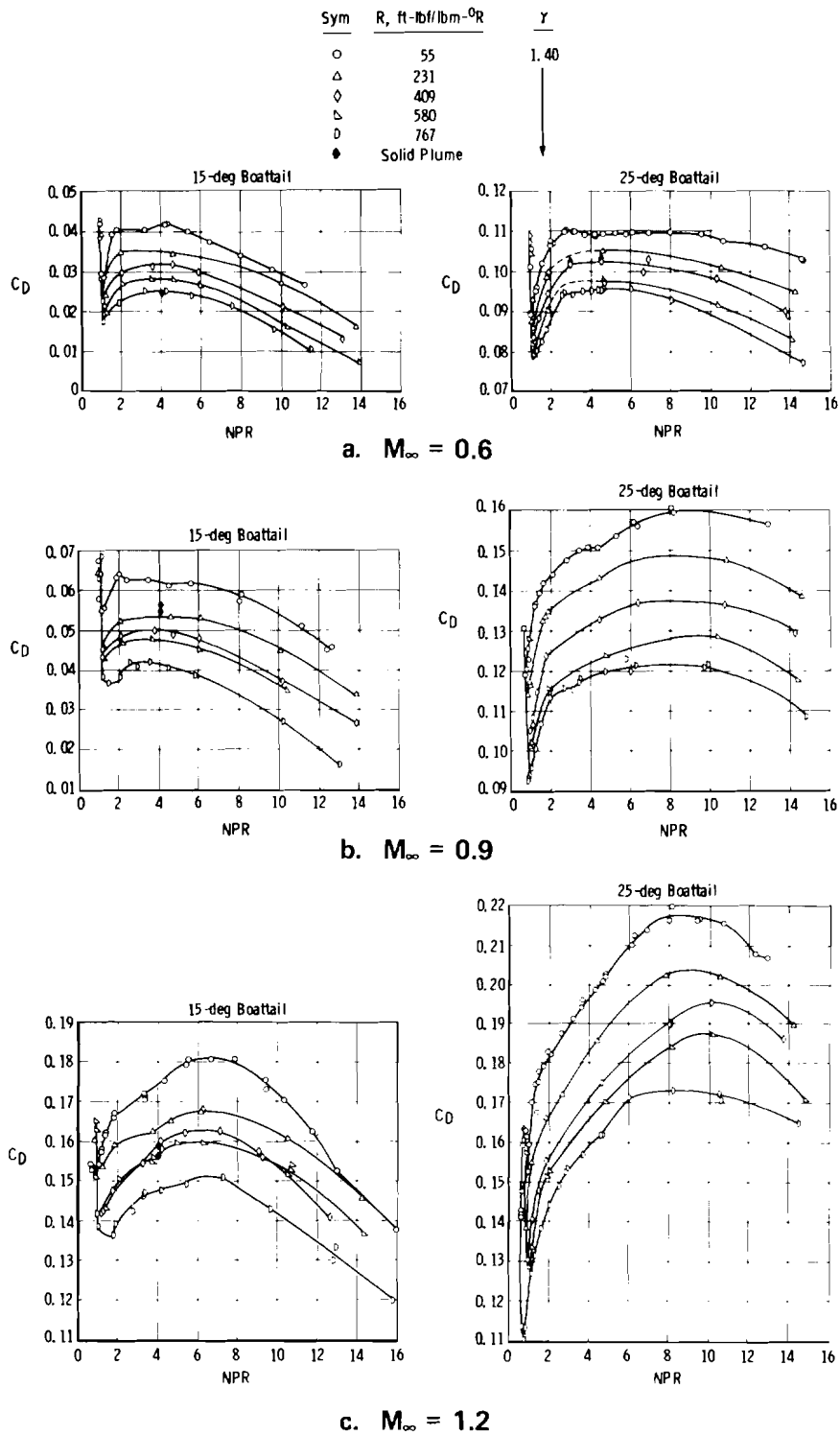
Figure 48. Effect of exhaust gas constant variation on boattail drag coefficient.

119

Afterbody Drag Coefficient

$$\Delta C_D = C_{D_{R_X}} - C_{D_{R_{55}}}$$

where X = 55, 231, 409, 580, or 767

Sym	Nozzle Total Pressure Ratio
O	2
□	6
△	10

15-deg Boattail, M_∞ = 0.6

25-deg Boattail, M_∞ = 0.6

ΔC_D

R, ft-lbf/lbm - $^\circ$R
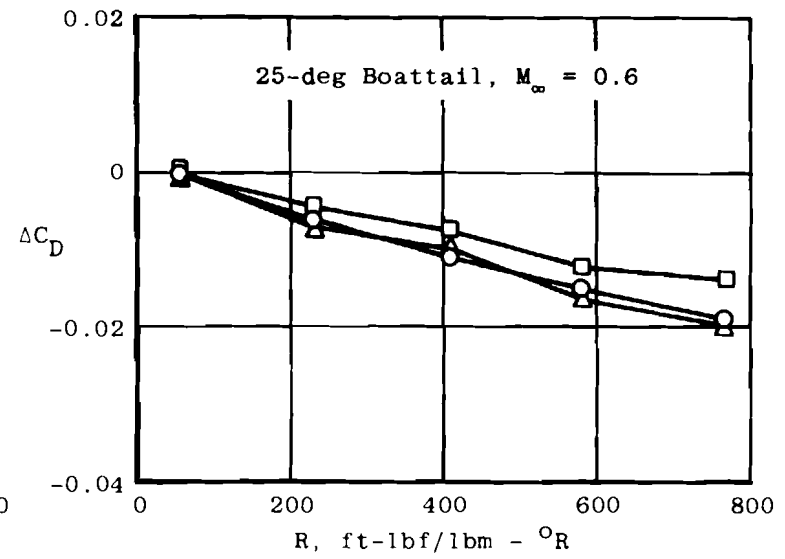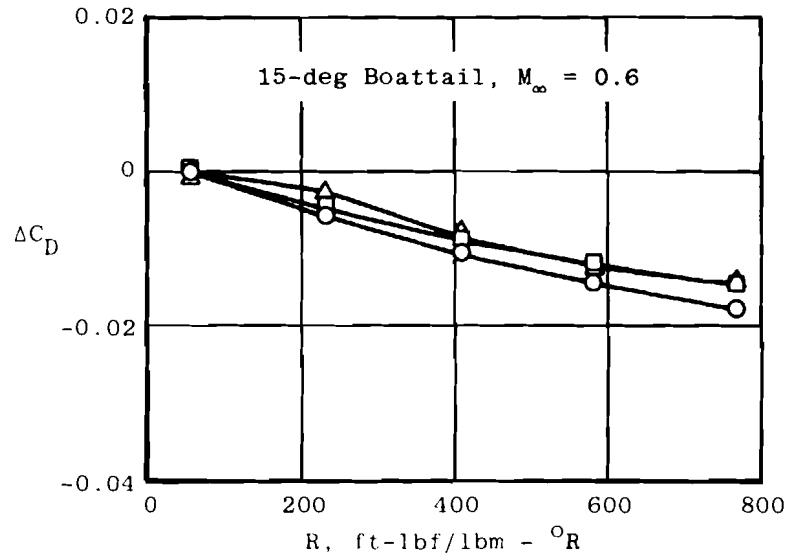
a. M_∞ = 0.6

Figure 49. Change in drag coefficient for various gas mixtures.

Afterbody Drag Coefficient

$$\Delta C_D = C_{D_{R_X}} - C_{D_{R55}}$$

where X = 55, 231, 409, 580, or 767

Sym	Nozzle Total Pressure Ratio
O	2
□	6
△	10

15-deg Boattail, $M_\infty = 0.9$

ΔC_D

R, ft-lbf/lbm - ^{O}R

25-deg Boattail, $M_\infty = 0.9$

ΔC_D

R, ft-lbf/lbm - ^{O}R
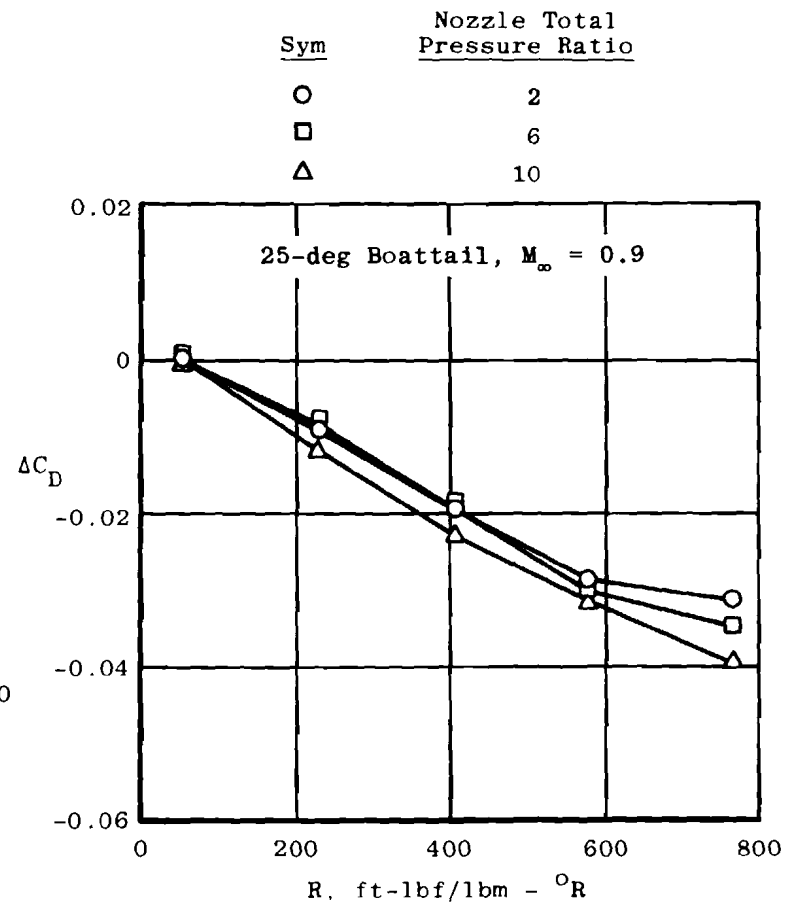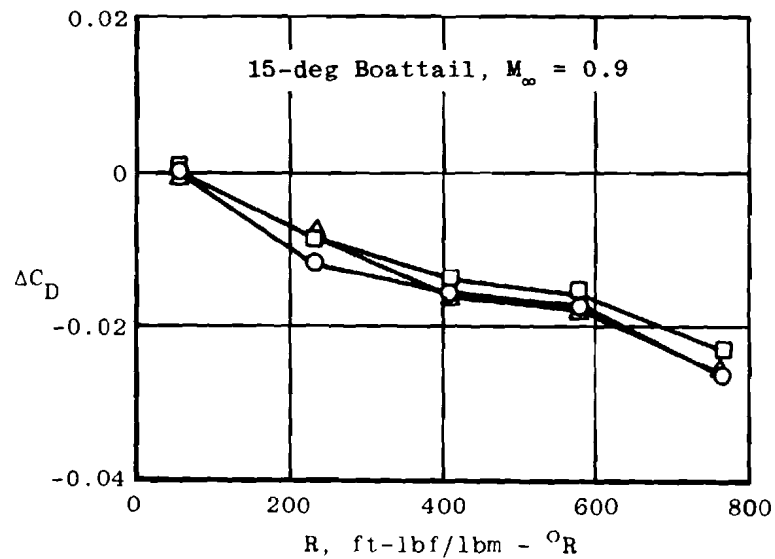
b. $M_\infty = 0.9$
Figure 49. Continued.

121

AEDC-TR-80-8

Afterbody Drag Coefficient

$$\Delta C_D = C_{D_{R_X}} - C_{D_{R_{55}}}$$

Where X = 55, 231, 409, 580, or 767

Sym	Nozzle Total Pressure Ratio
O	2
□	6
△	10

15-deg Boattail, $M_\infty = 1.2$

ΔC_D

R, ft-lbf/lbm-^{O}R

25-deg Boattail, $M_\infty = 1.2$

ΔC_D

R, ft-lbf/lbm-^{O}R
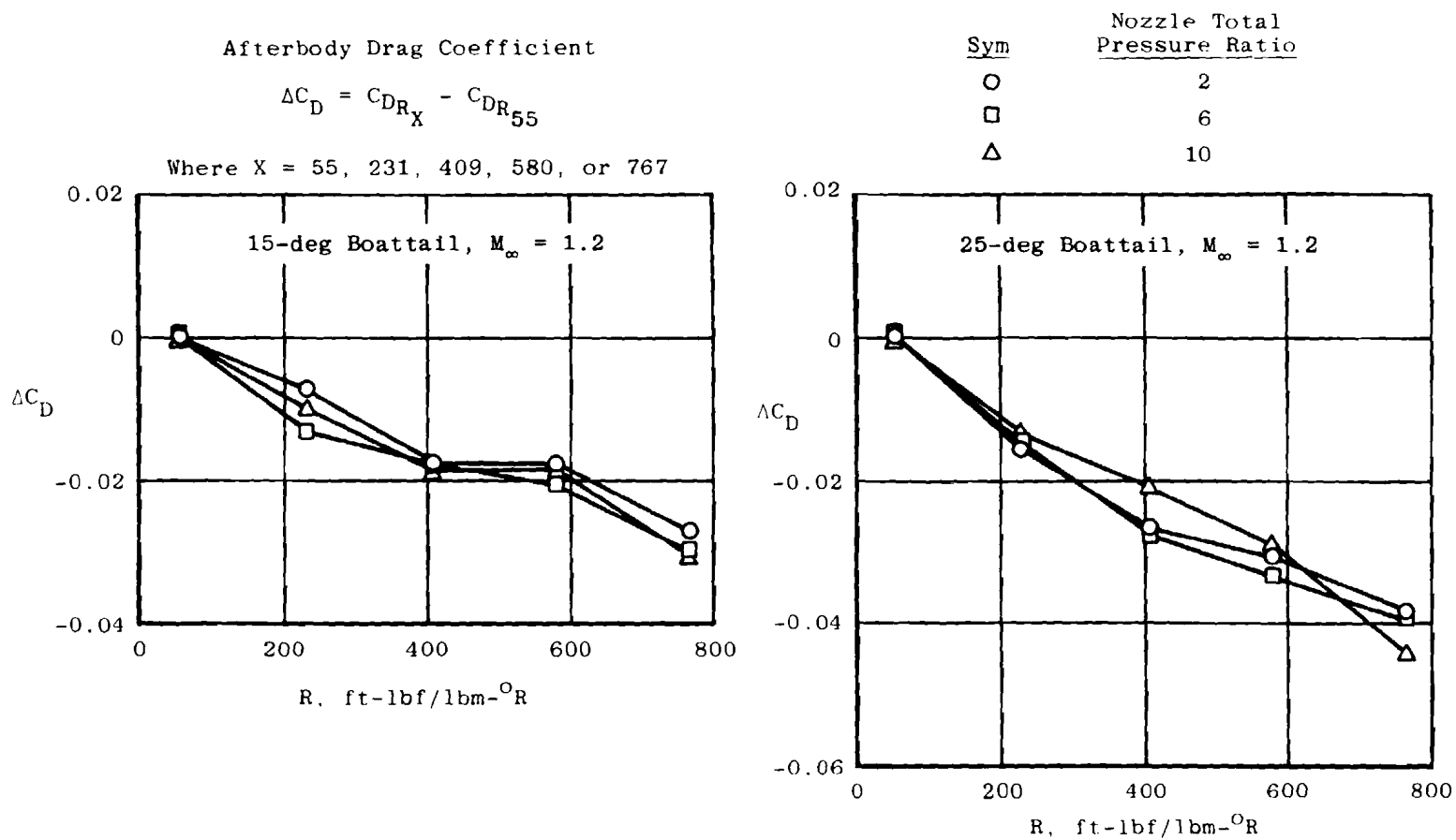
c. $M_\infty = 1.2$

Figure 49. Concluded.

$$\Delta C_D = C_{D_{jet\ on}} - C_{D_{jet\ off}}$$
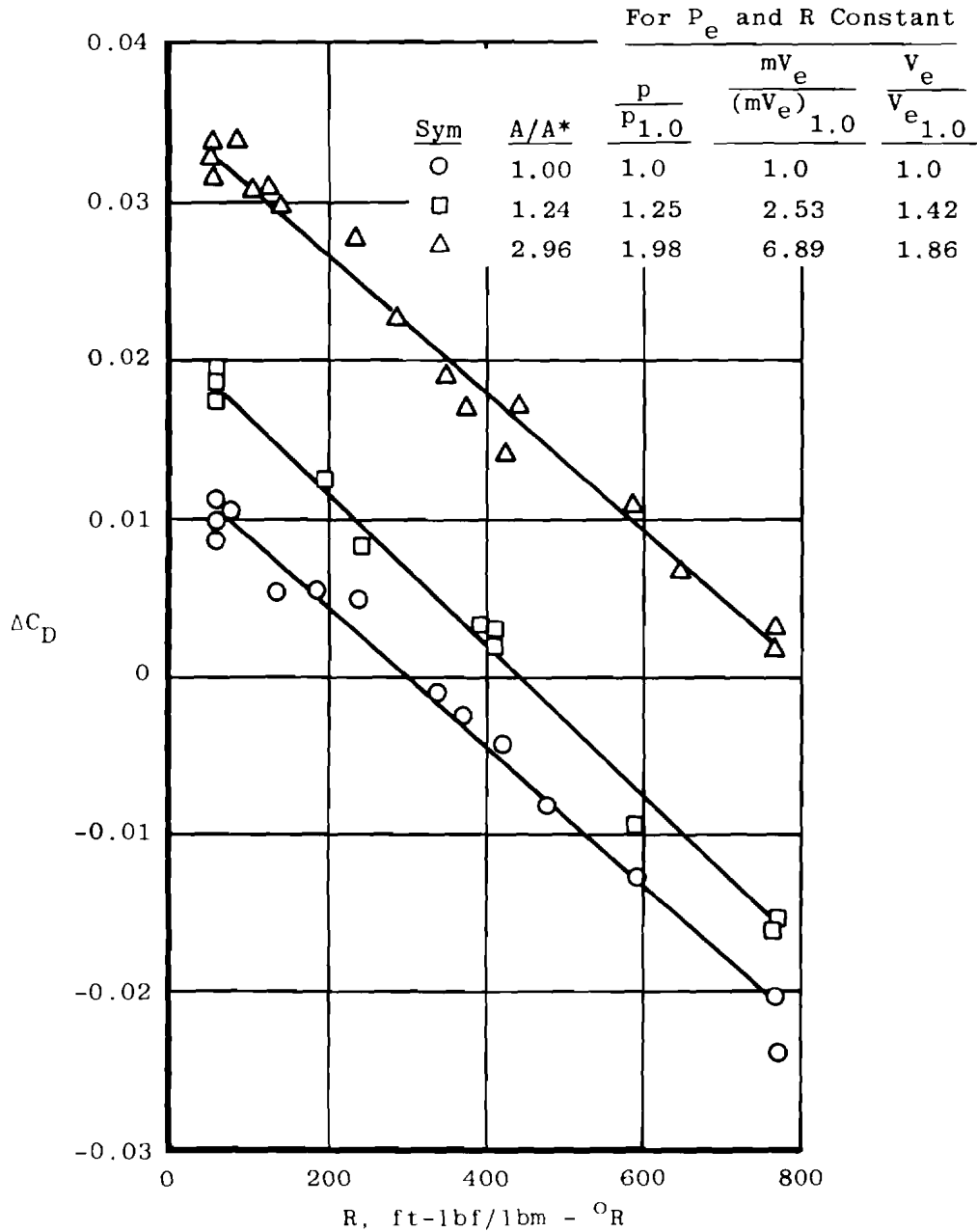
Figure 50. Afterbody drag coefficient for various jet nozzle area ratios as a function of exhaust gas constant at design pressure ratio.

123

$$\Delta C_D = C_{D_{NPR_{design}}} - C_{D_{jet\ off}}$$
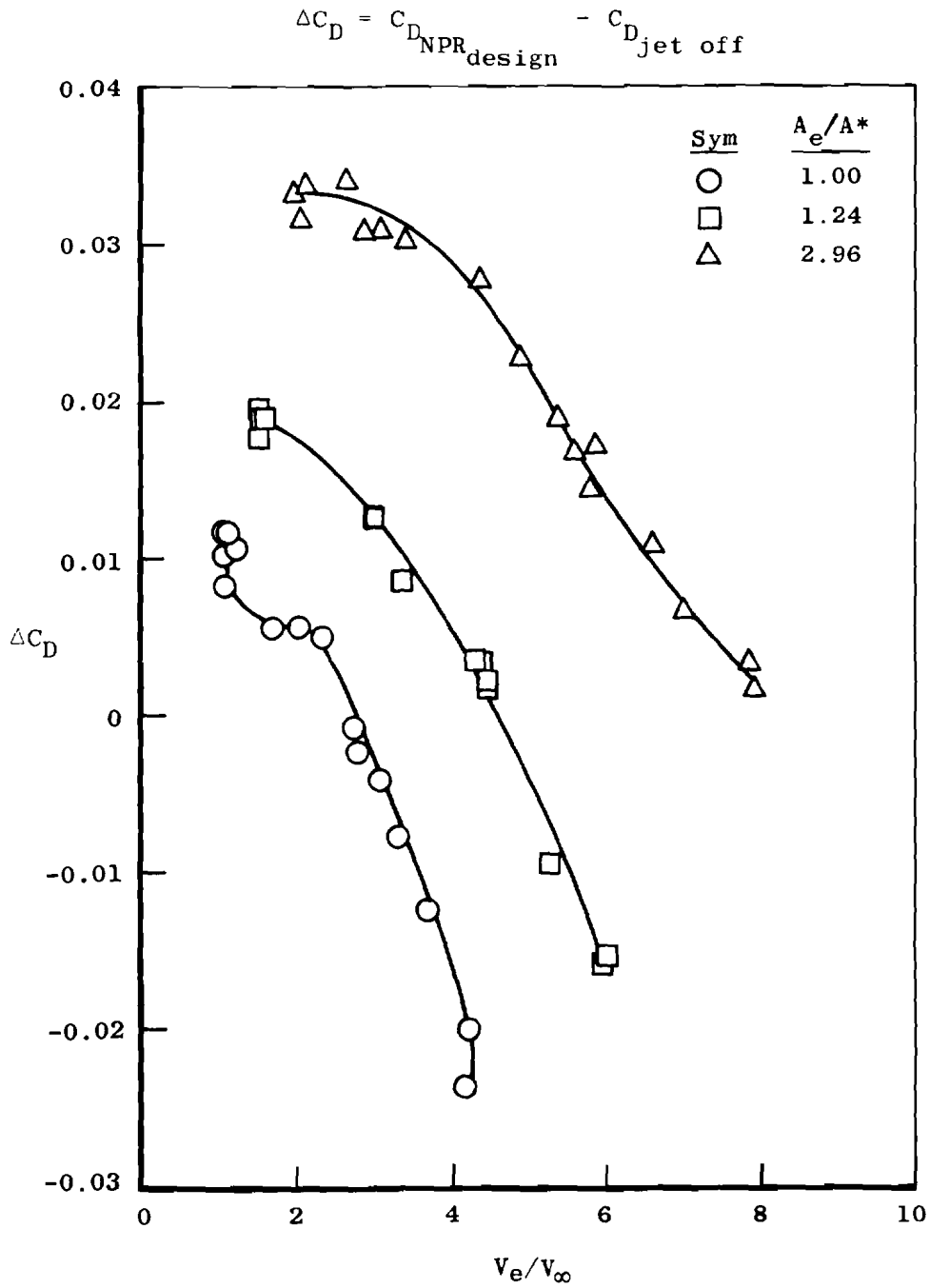
Figure 51. Afterbody drag coefficient for various jet nozzle area ratios as a function of the ratio of jet exit to free-stream velocity.

Sym	Variable	A/A*
O	T_t	1.0
□	R	1.24
△	γ	1.24

$M_\infty = 0.6$

C_D

$M_\infty = 0.9$

C_D

$M_\infty = 1.1$

$M_\infty = 1.2$

C_D

$RT_t \times 10^{-5}$
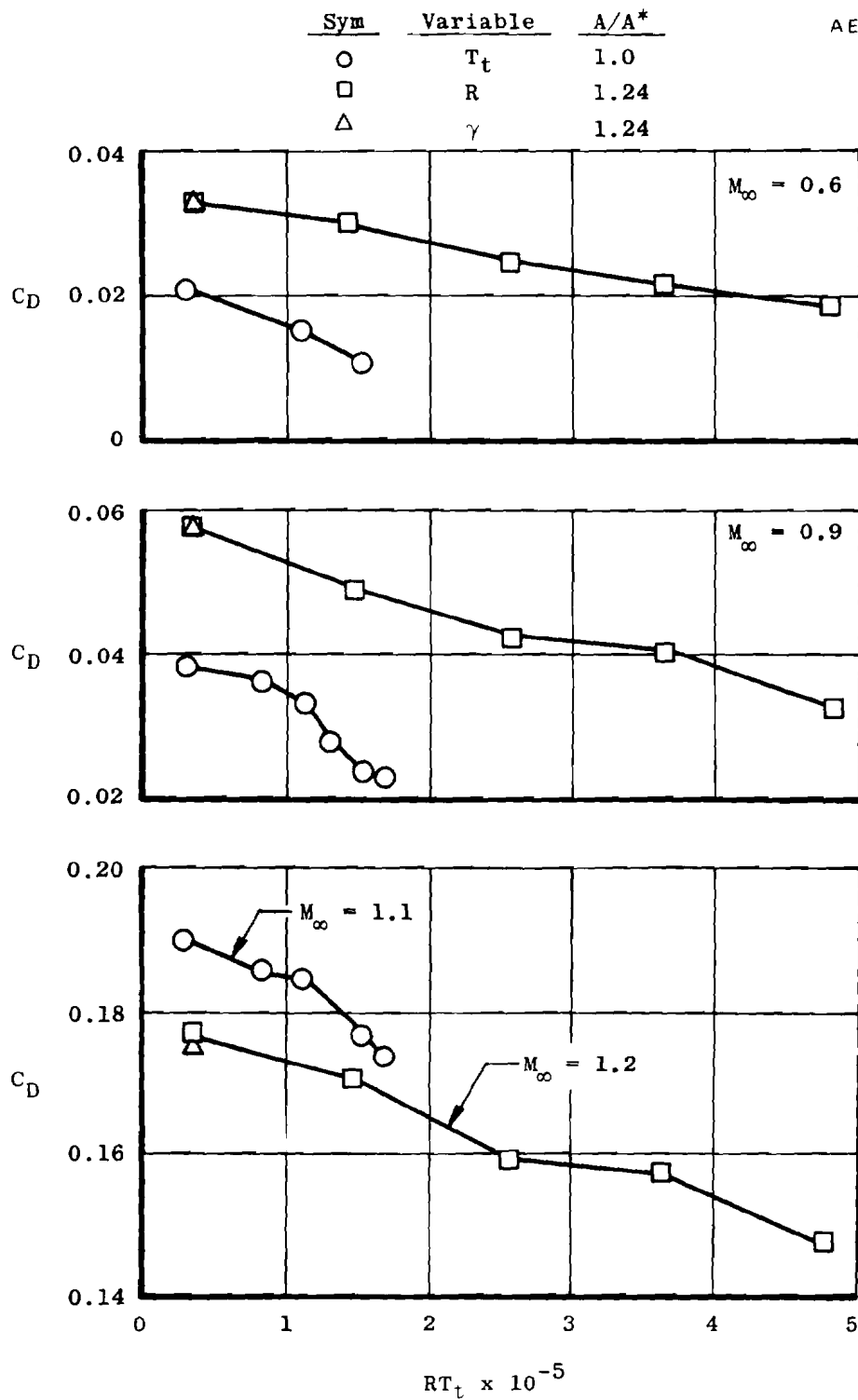
a. 15-deg boattail

Figure 52. Comparison of the effects of temperature and gas constant
on afterbody drag coefficient.

Sym	Variable
O	T_t
□	R
△	γ
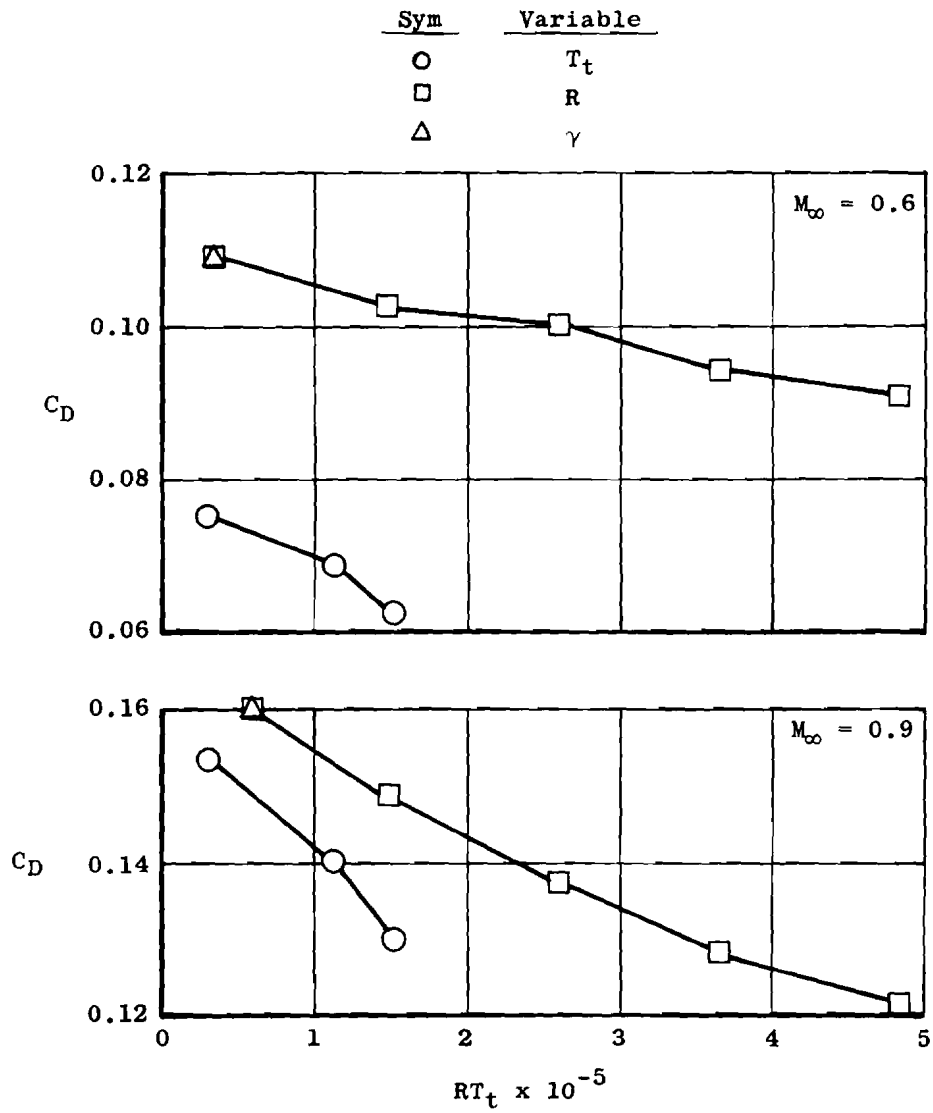
b. 25-deg boattail

Figure 52. Continued.
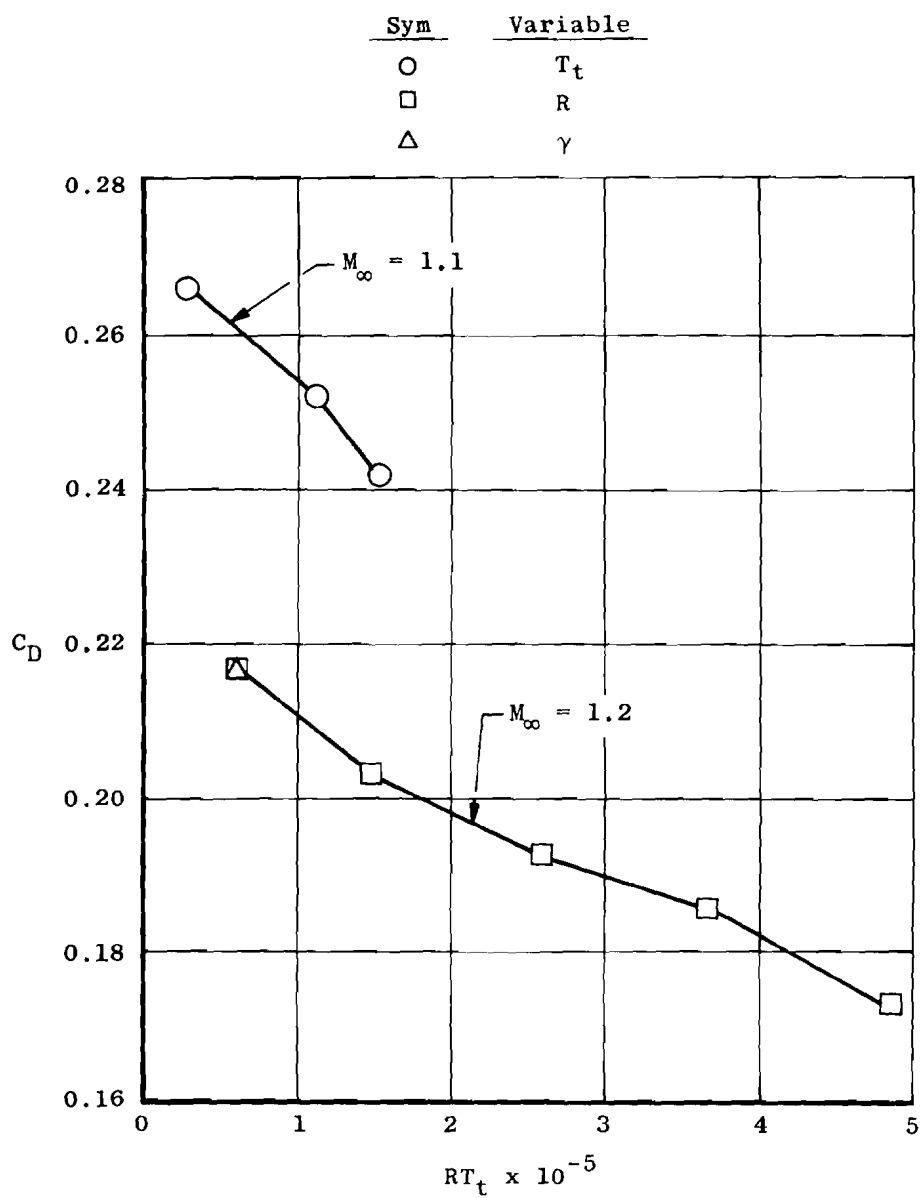
b. Concluded
Figure 52. Concluded.

External Configuration: 15-deg Boattail
Internal Configuration: A/A* = 1.22
Free-Stream Conditions: M_∞ = 0.9, Re = 1.5 x 10^6
                          M_∞ = 1.5, Re = 2.0 x 10^6

Figure 53. Nozzle divergence angle effects on afterbody drag coefficient.

External Configuration: 15-deg Boattail
Internal Configuration: $A/A^* = 1.22$
Free-Stream Conditions: $M_\infty = 0.9$, Re $= 1.5 \times 10^6$
$M_\infty = 1.5$, Re $= 2.0 \times 10^6$
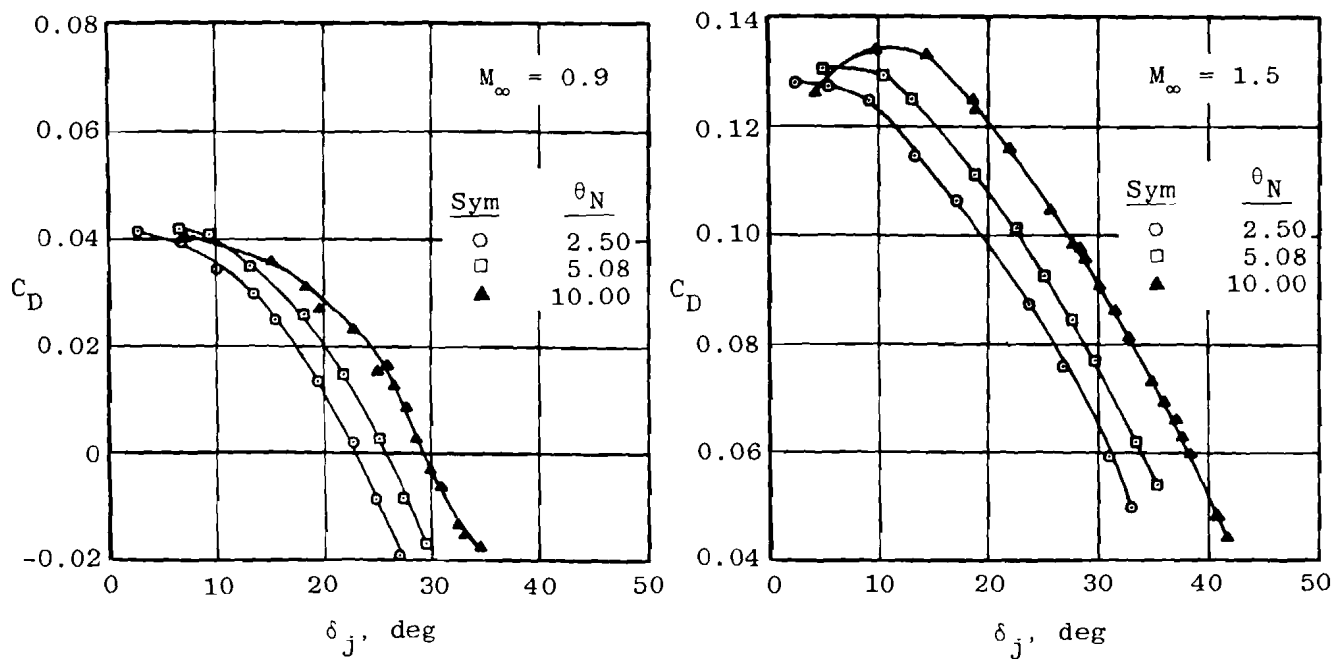
Figure 54. Afterbody drag coefficient as a function of jet inclination angle.

Sym	A/A*
○	1.000
▢	1.134
△	1.221
◇	1.300
✕	1.490
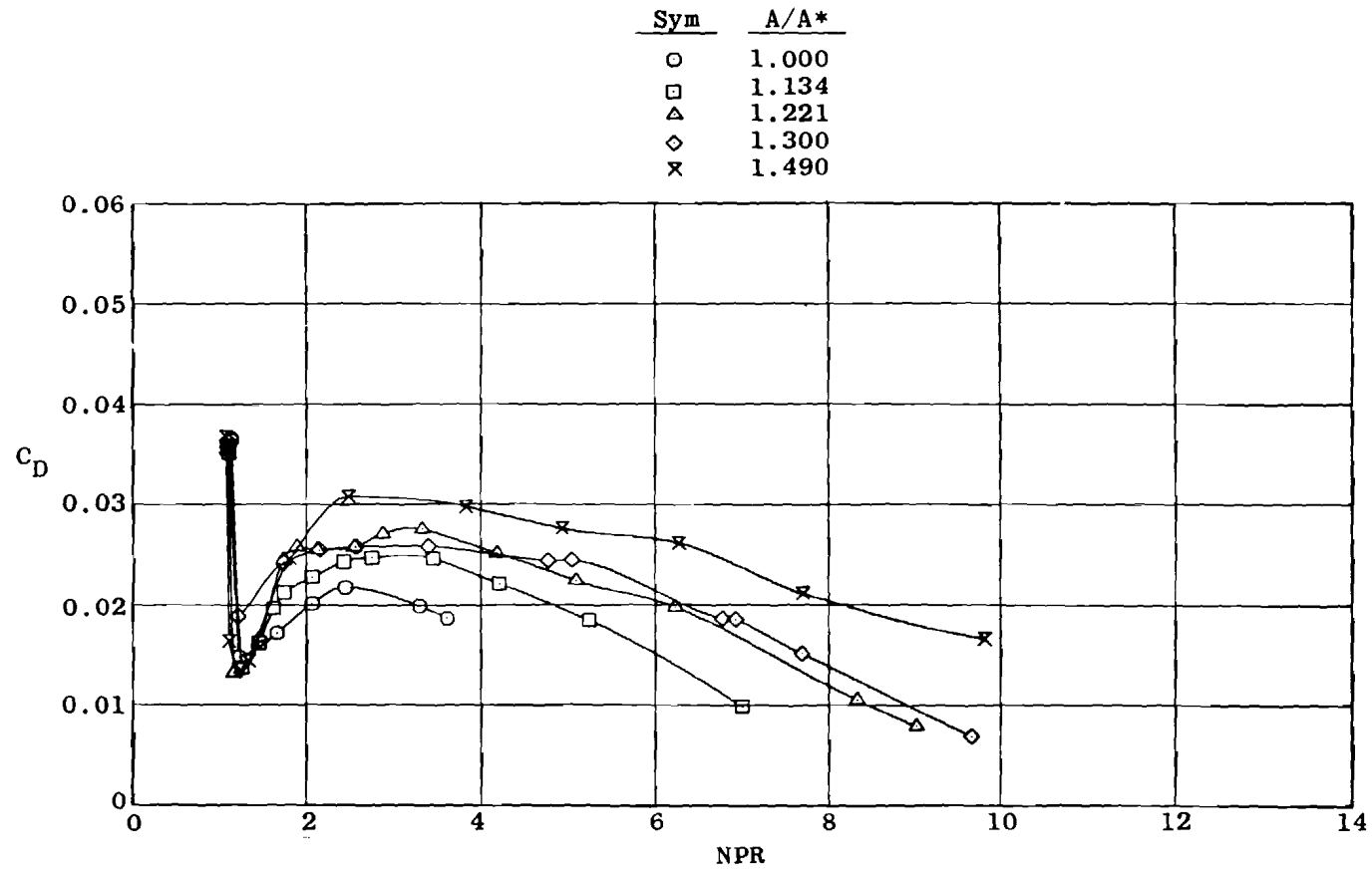
a. $M_\infty = 0.6$

Figure 55. Afterbody drag coefficient for various jet area ratios as a
function of nozzle pressure ratio.

Sym	A/A*
◯	1.000
□	1.134
△	1.221
◇	1.300
✗	1.490
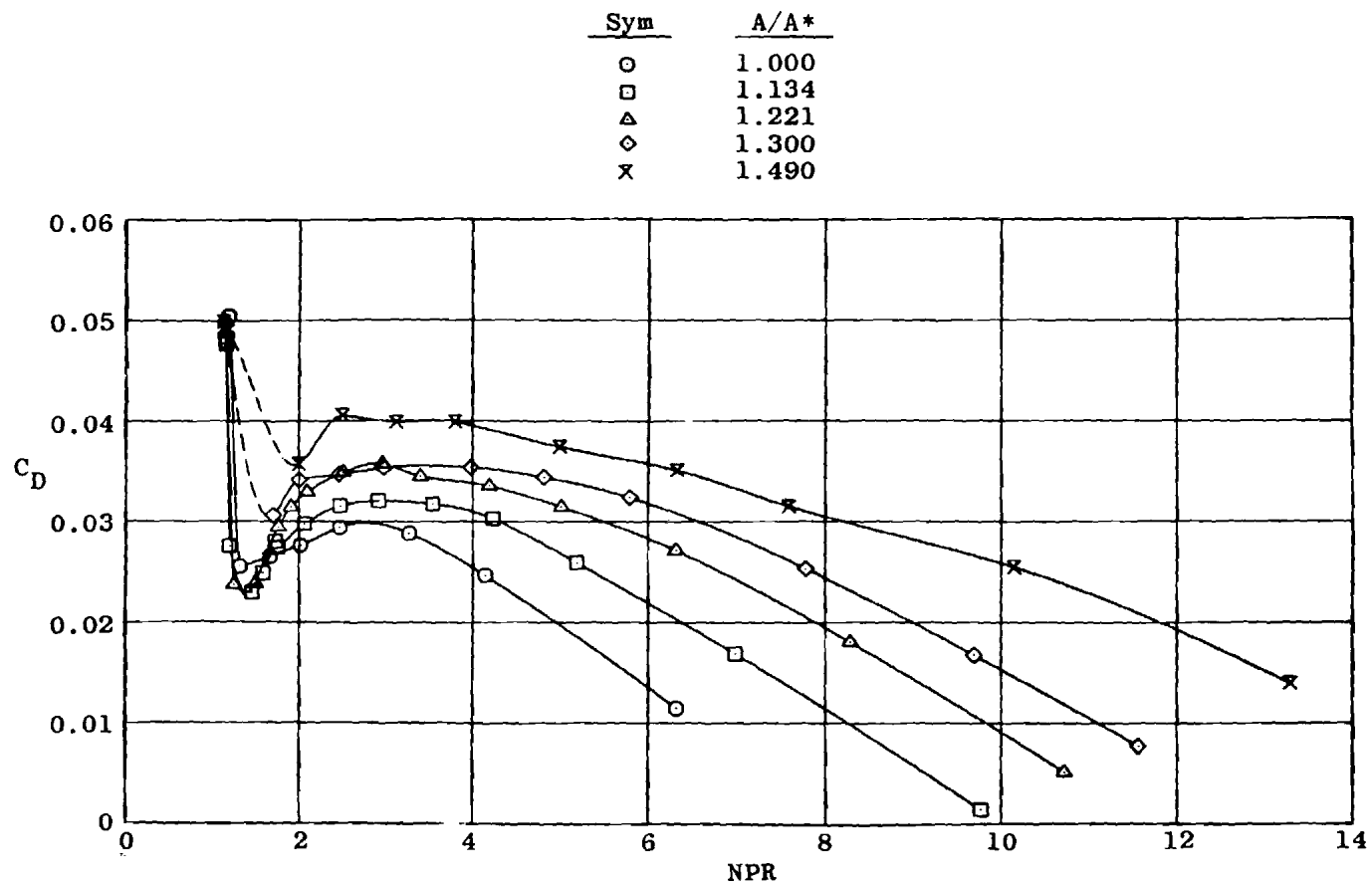
b. $M_\infty = 0.9$

Figure 55. Continued.

Sym	A/A*
□	1.134
△	1.221
◇	1.300
⋈	1.490
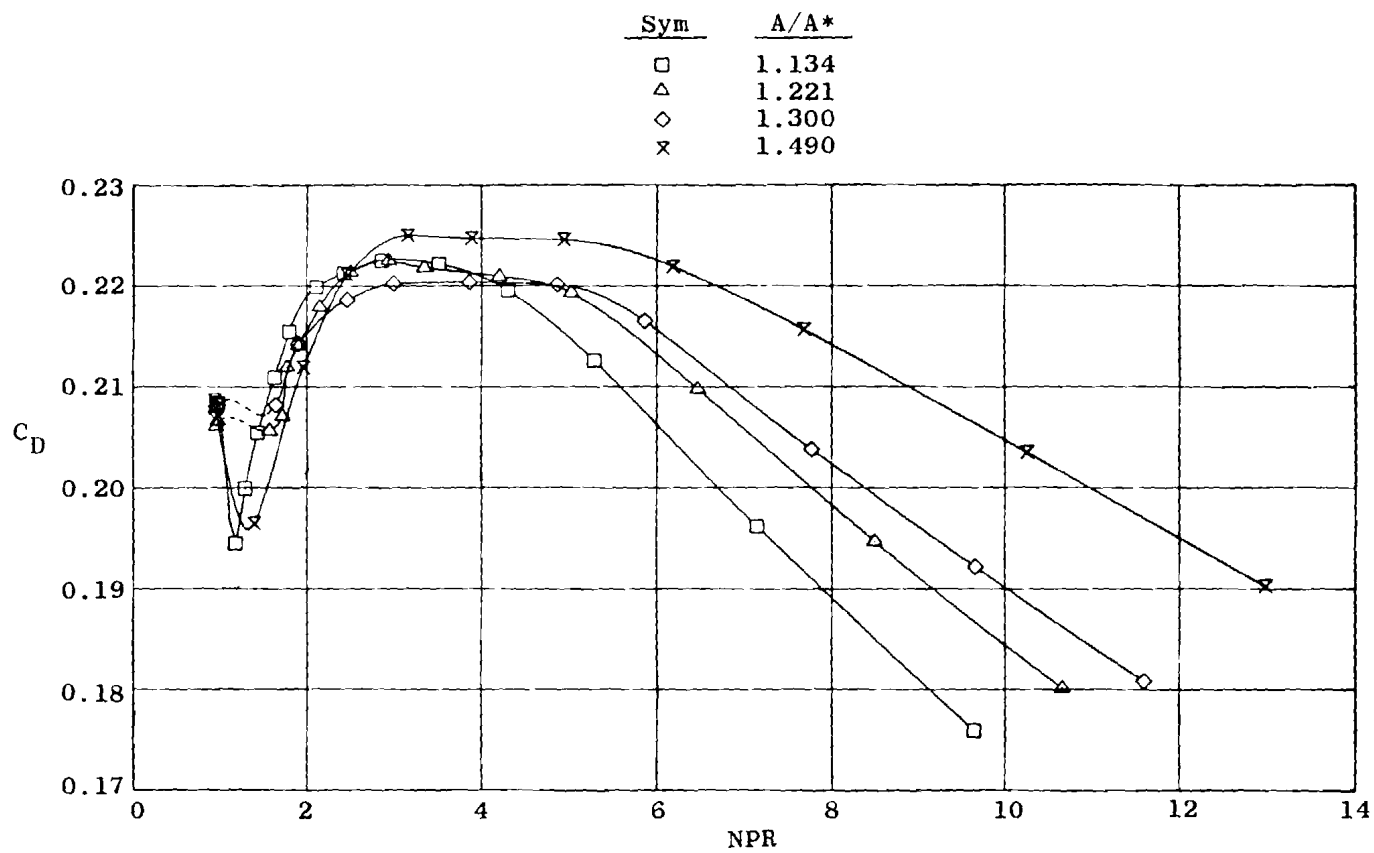
c. $M_\infty = 1.2$

Figure 55. Concluded.
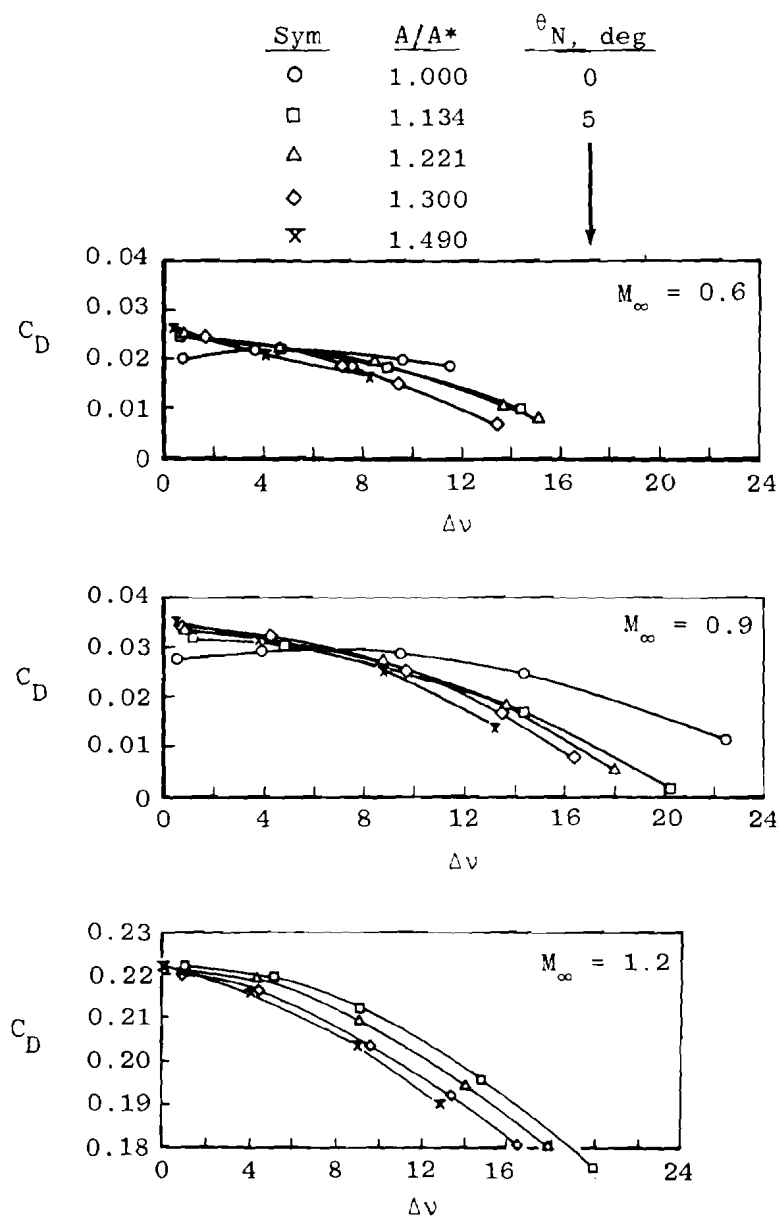
Figure 56. Afterbody drag coefficient for various jet area ratios as a function of incremental Prandtl-Meyer angle.
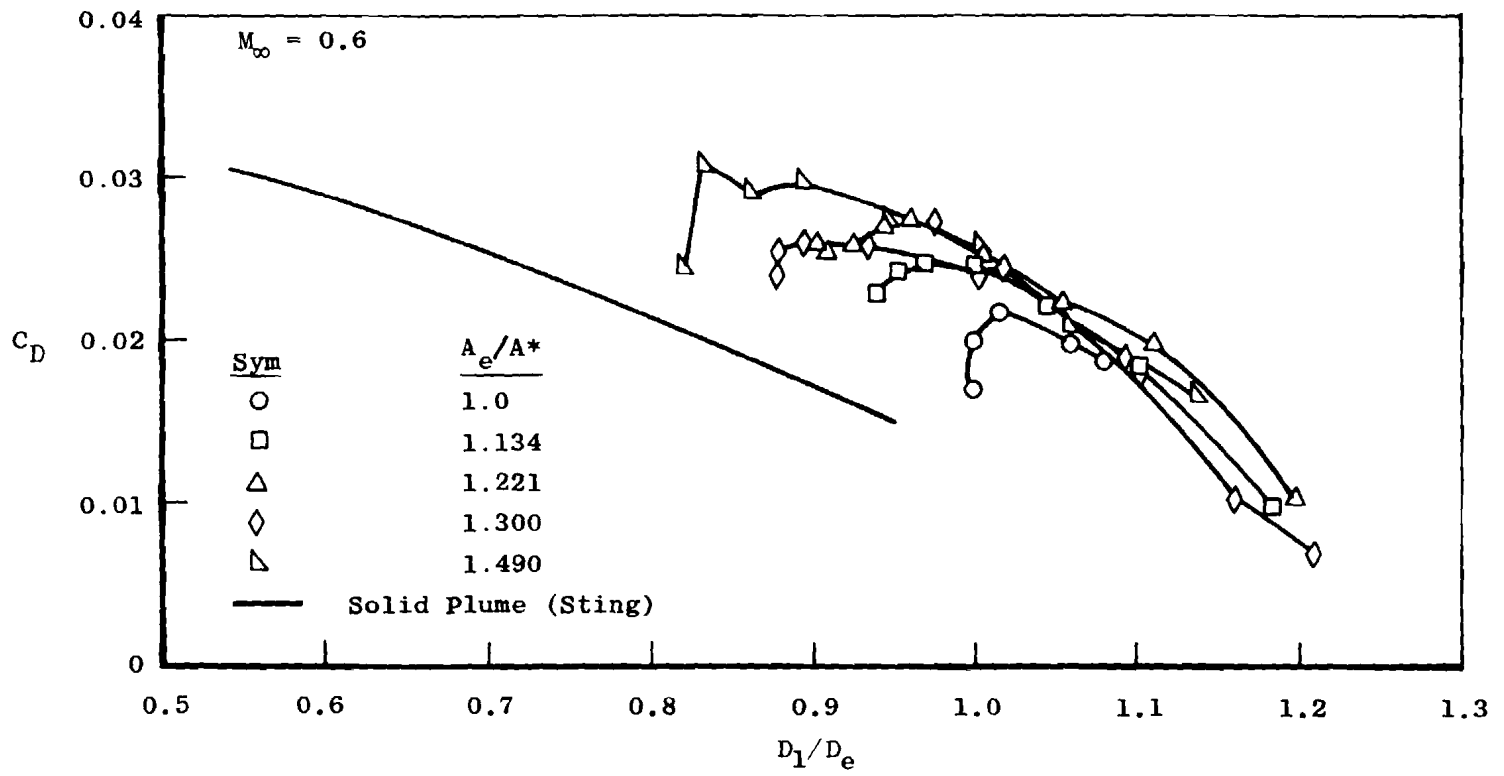
Figure 57. Afterbody drag coefficient for various jet area ratios as a function of jet-to-exit diameter ratio.
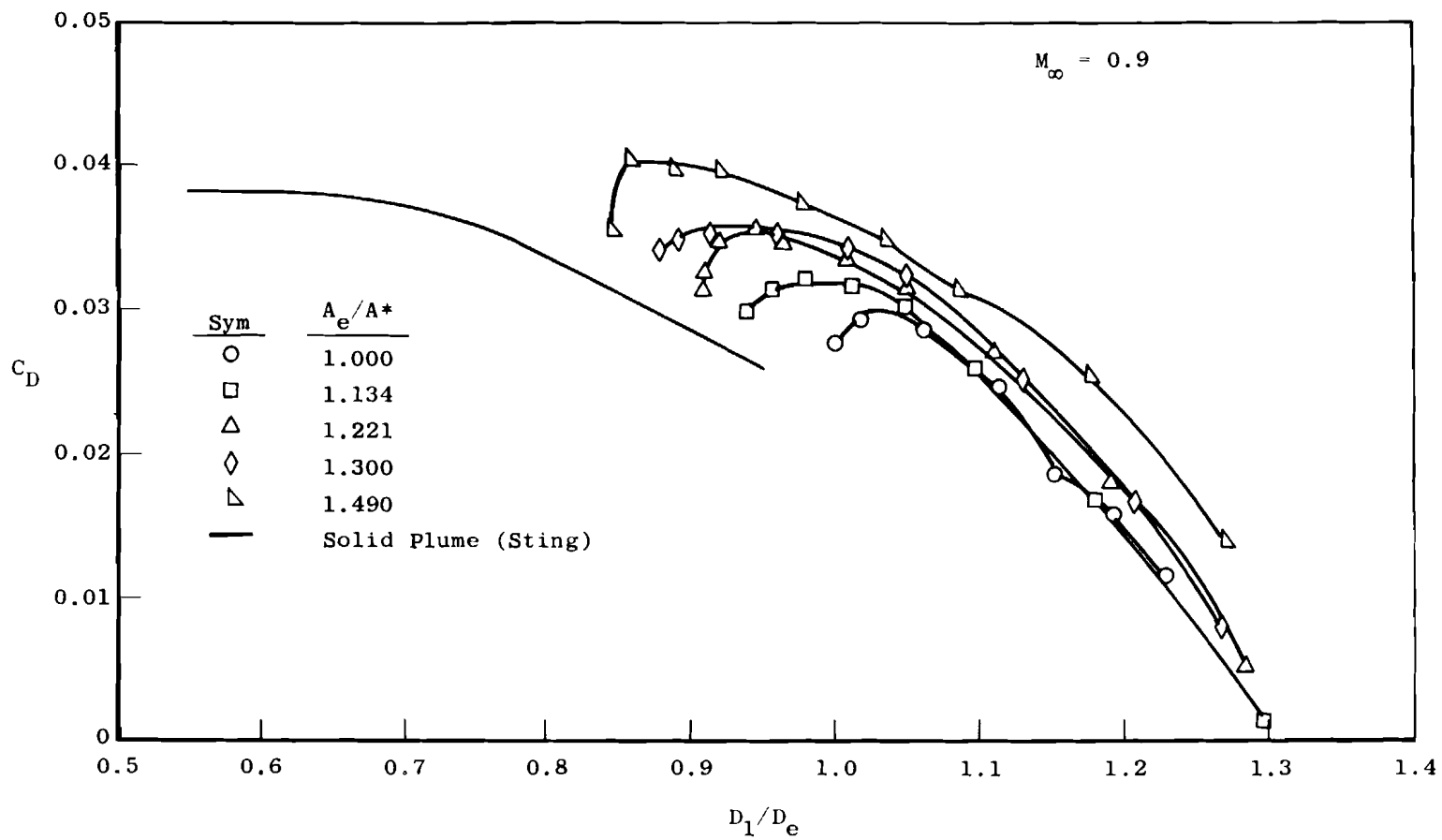
Figure 57. Continued.
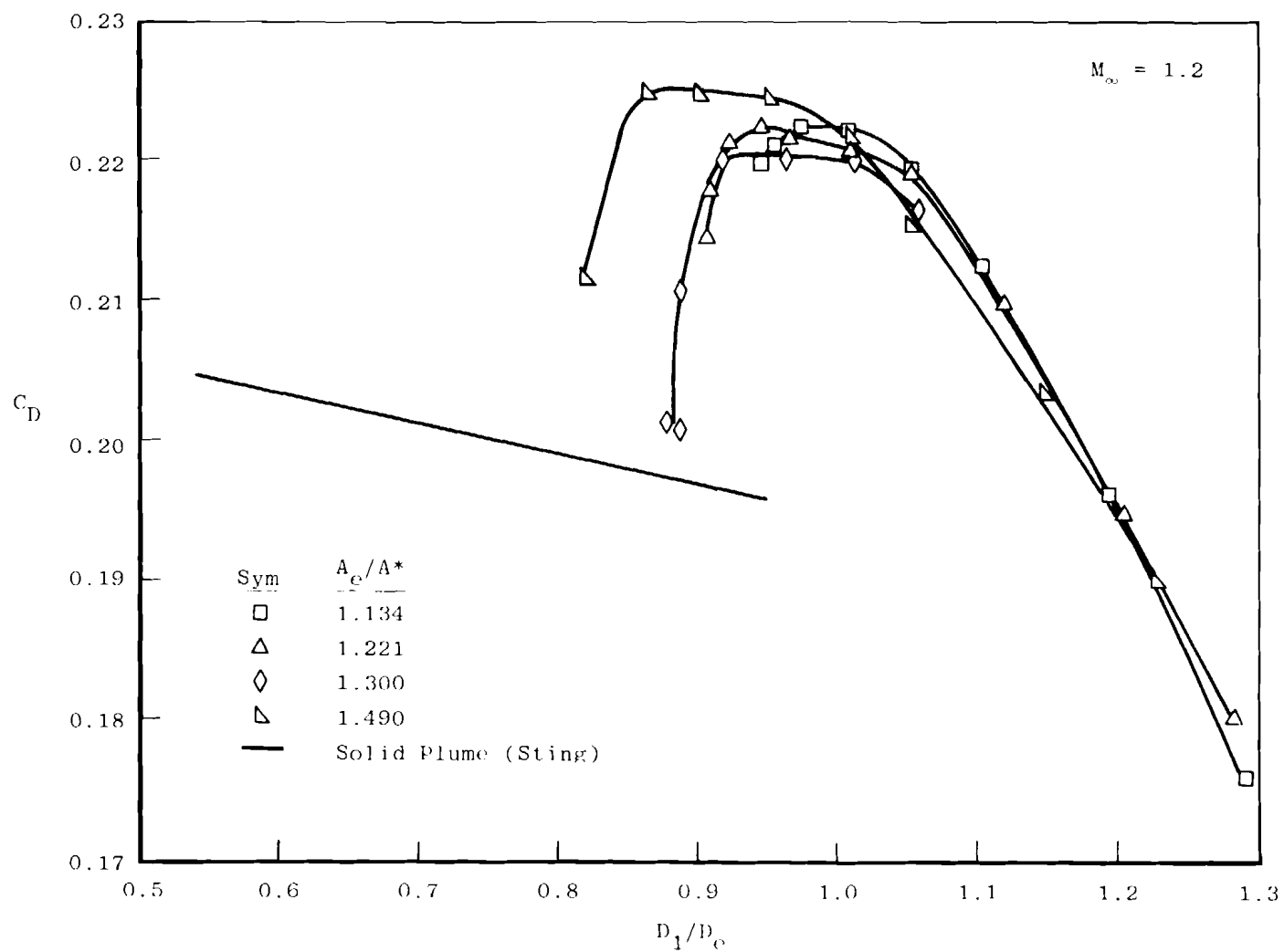
Figure 57. Concluded.
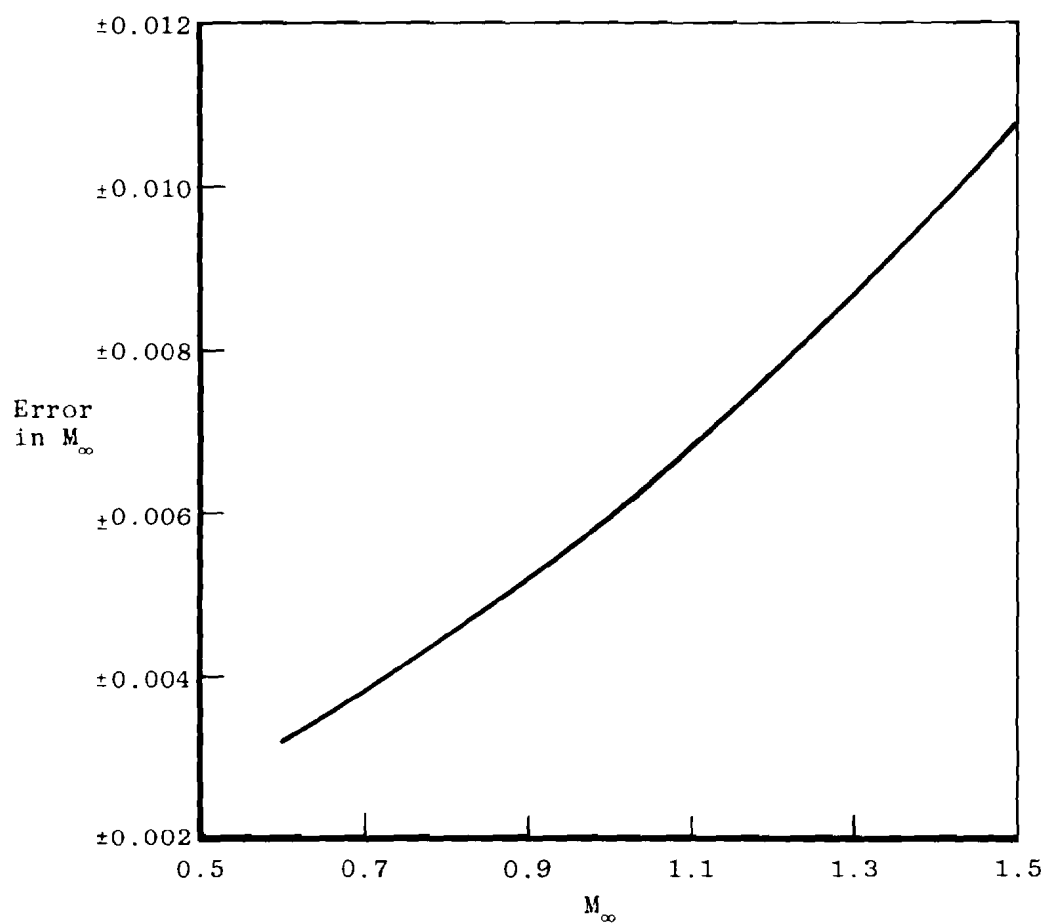
Figure 58. Error in Mach number causing a ±0.01 change in p_∞/q_∞.
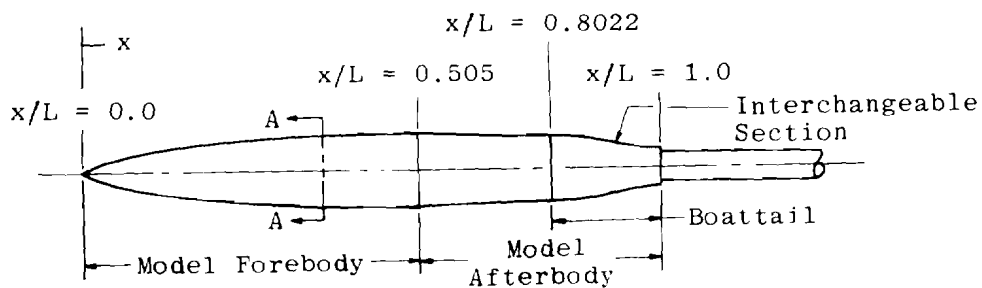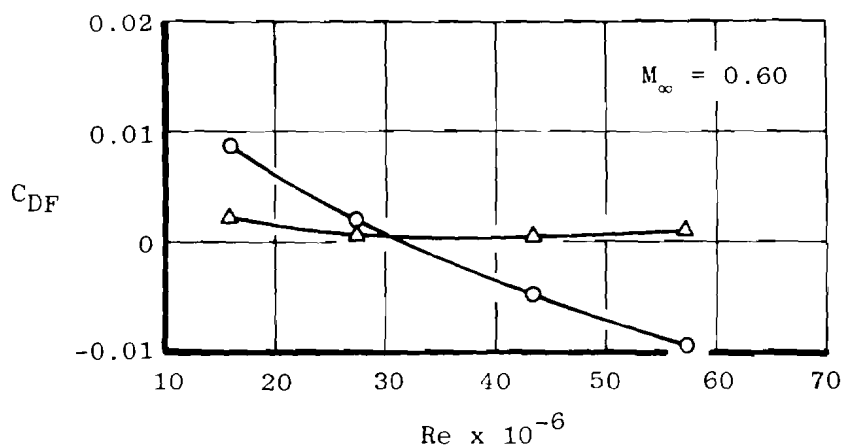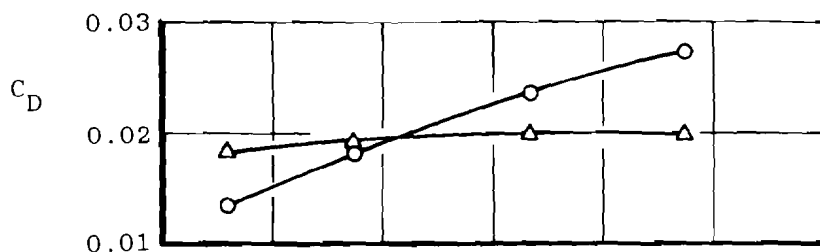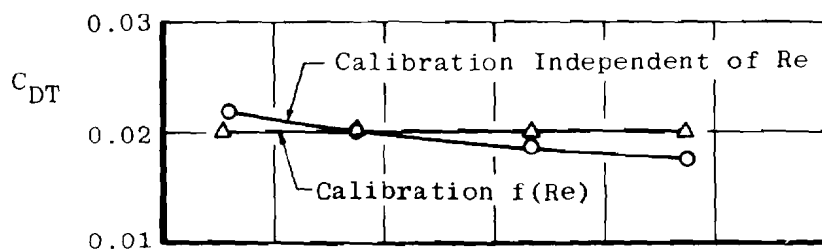
Figure 59. Comparison of pressure drag coefficient for a body of revolution calculated with several tunnel calibrations.
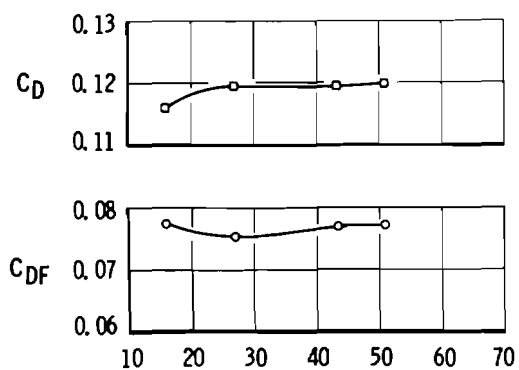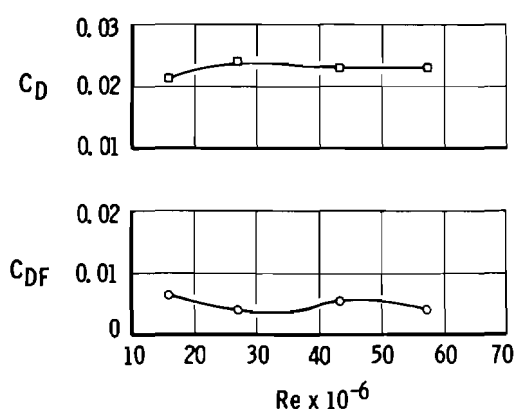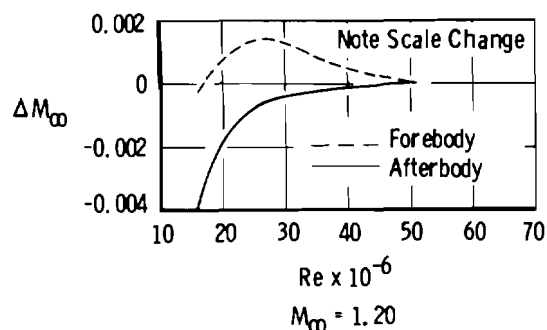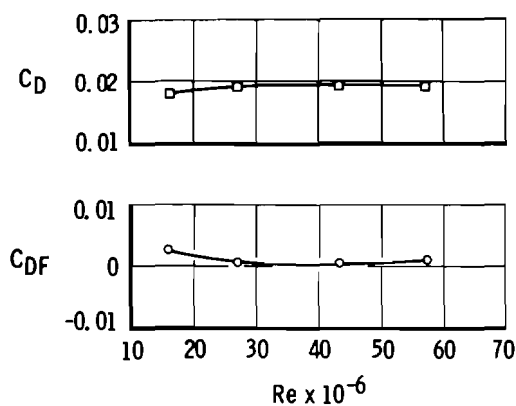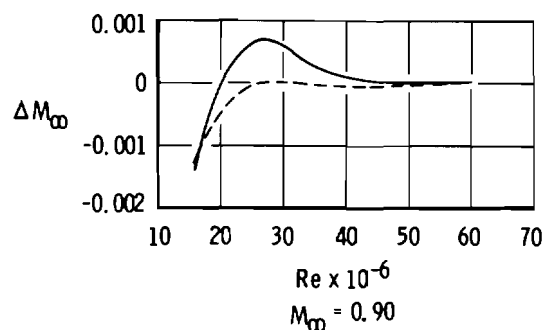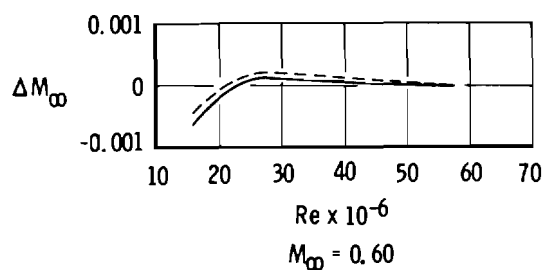
Figure 60. Component drag coefficient for a body of revolution as a function
of Reynolds number and the change in Mach number required for
drag coefficient to be invariant with Reynolds number.

139
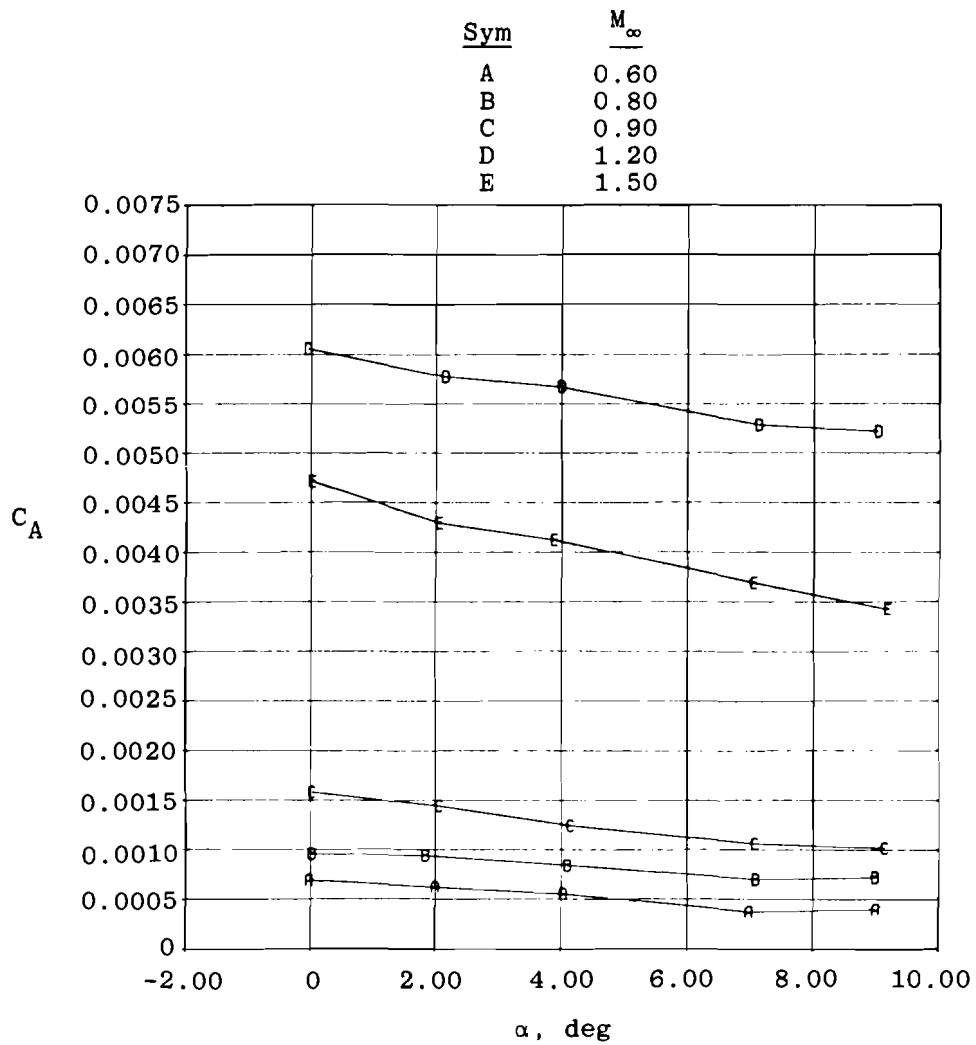
Figure 61. Typical afterbody force coefficient as a function of angle of attack.

Sym	M_∞
A	0.60
B	0.80
C	0.90
D	1.20
E	1.50
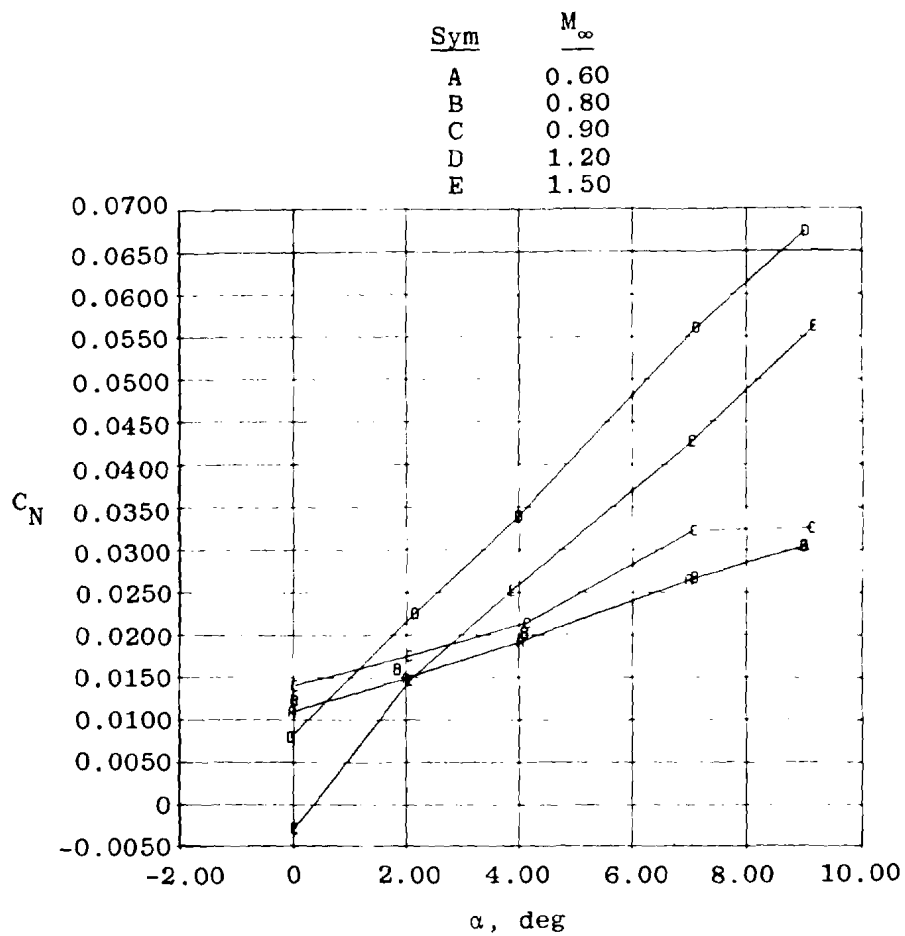
Figure 61. Continued.
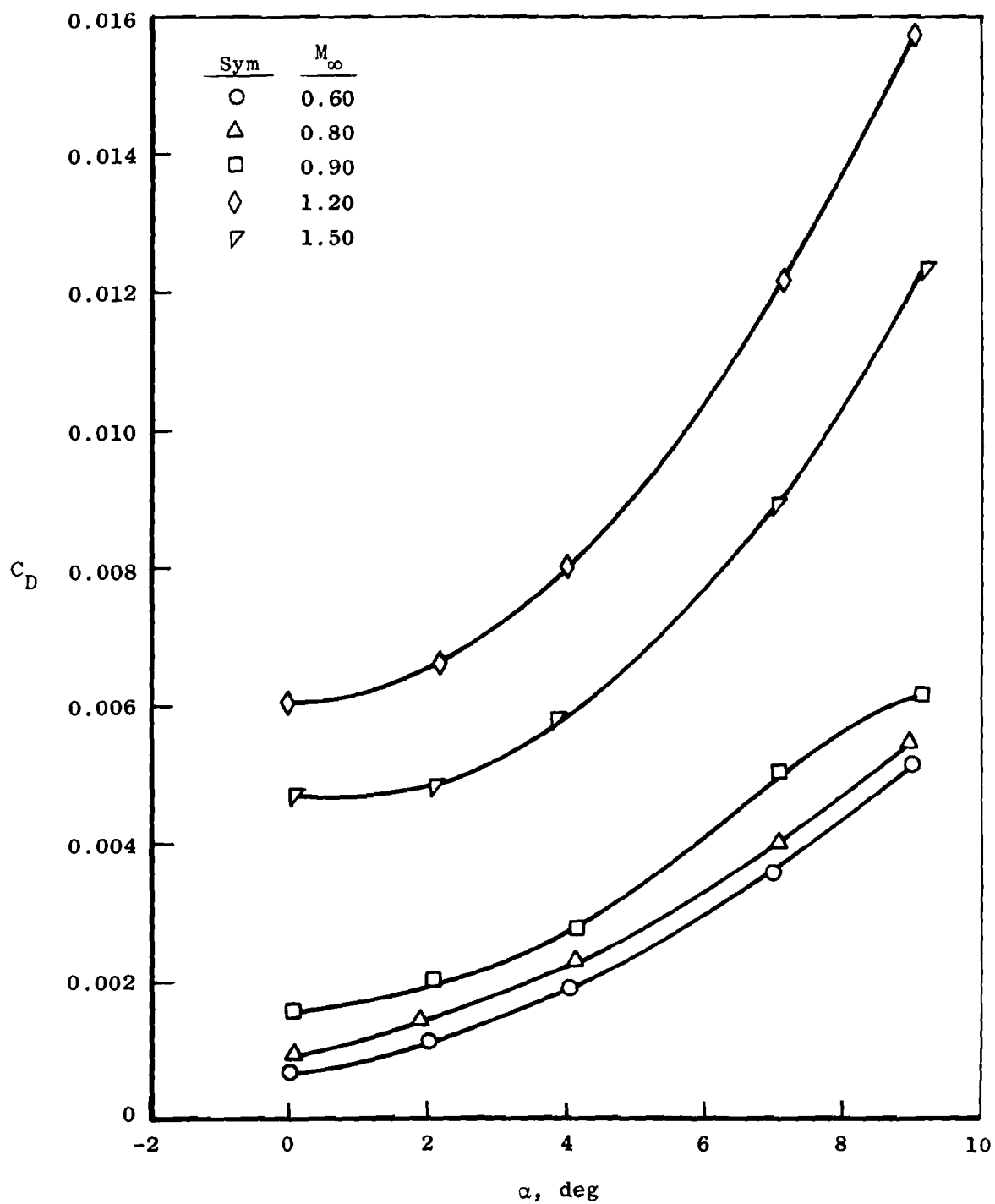
Figure 61. Concluded.
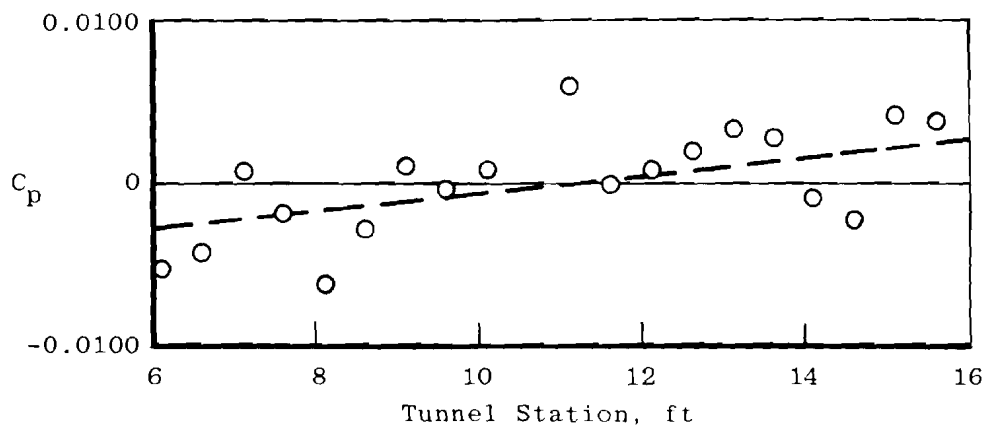
Figure 62. Empty tunnel centerline pressure distribution at M_∞ = 0.8.
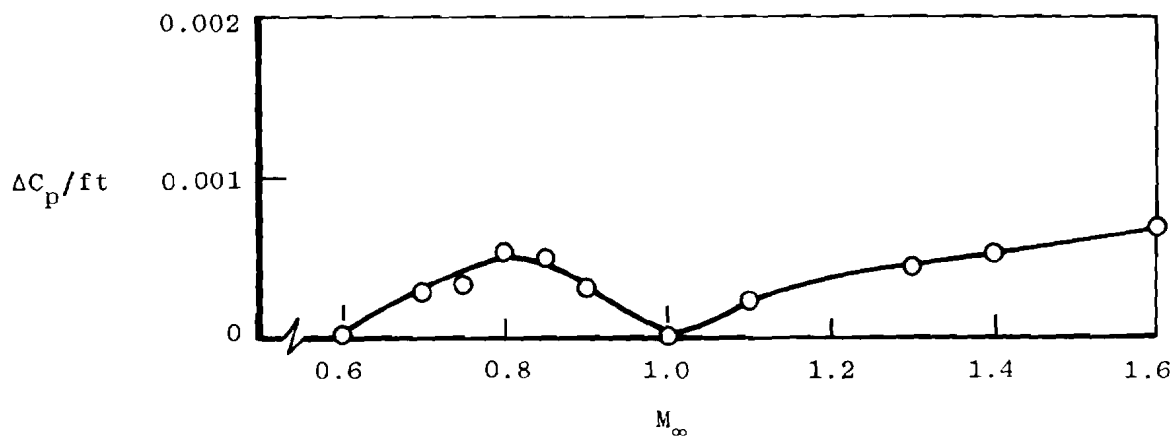
Figure 63. Tunnel 16T test section pressure gradient as a function of Mach number.

143
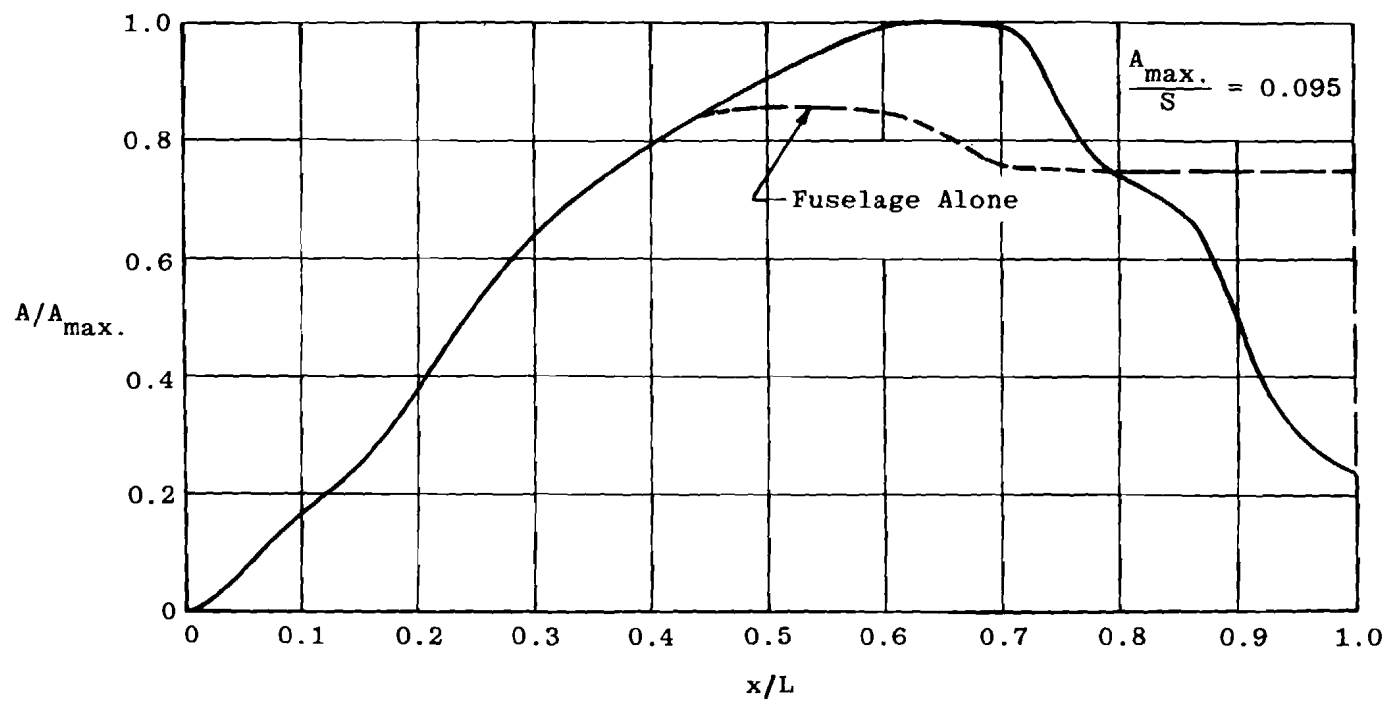
Figure 64. Typical fighter aircraft cross-sectional area distribution.
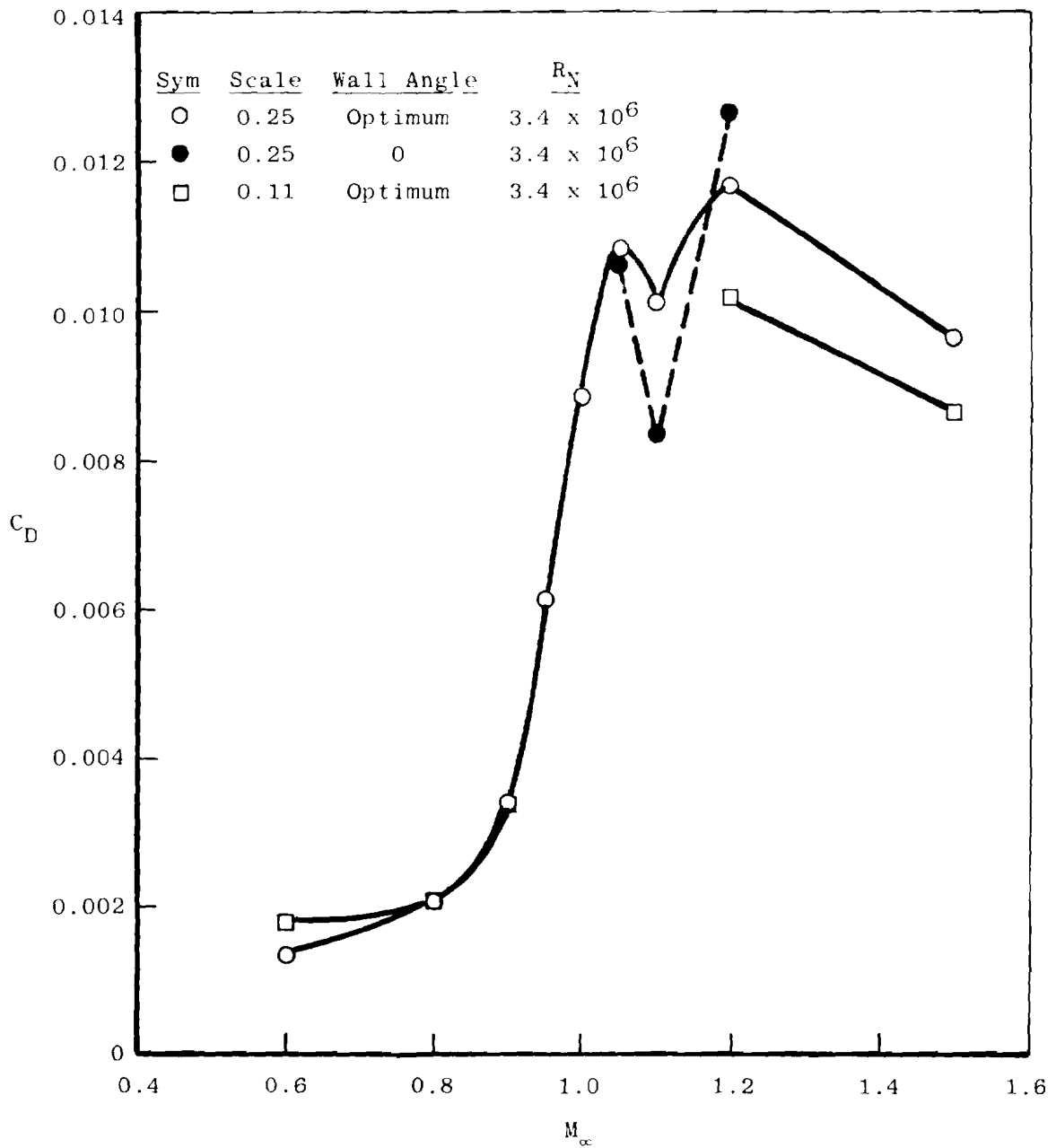
Figure 65. Effect of tunnel wall angle on afterbody drag coefficient for a large sting-mounted model.
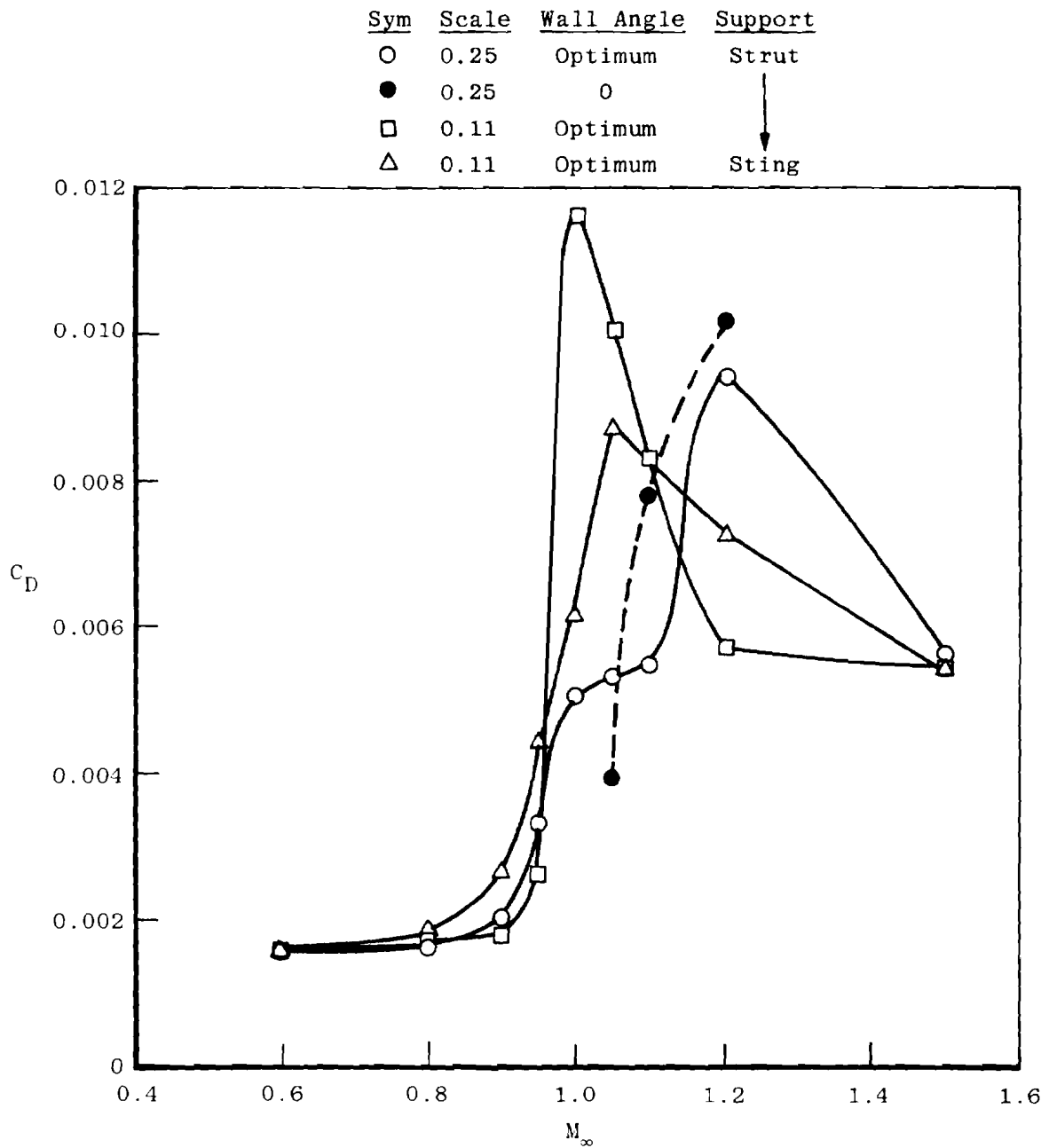
Figure 66. Effect of tunnel wall angle on afterbody drag coefficient for a large strut support model.

$12°$

View A-A

Alternate Wing Configuration
on 4.7- and 17-percent Models

View A-A

Basic Wing Configuration

View B-B

Model Characteristics

Scale	4.7%	13%	17%
Length, in.	35.96	99.45	130.05
Max. Diam, in.	4.47	12.36	16.16
Blockage, $\dfrac{A_{max.}}{A_{tunnel}}$	0.050%	0.381%	0.651%
$\dfrac{Wing\ Span}{Tunnel\ Width}$	0.13	0.35	0.45
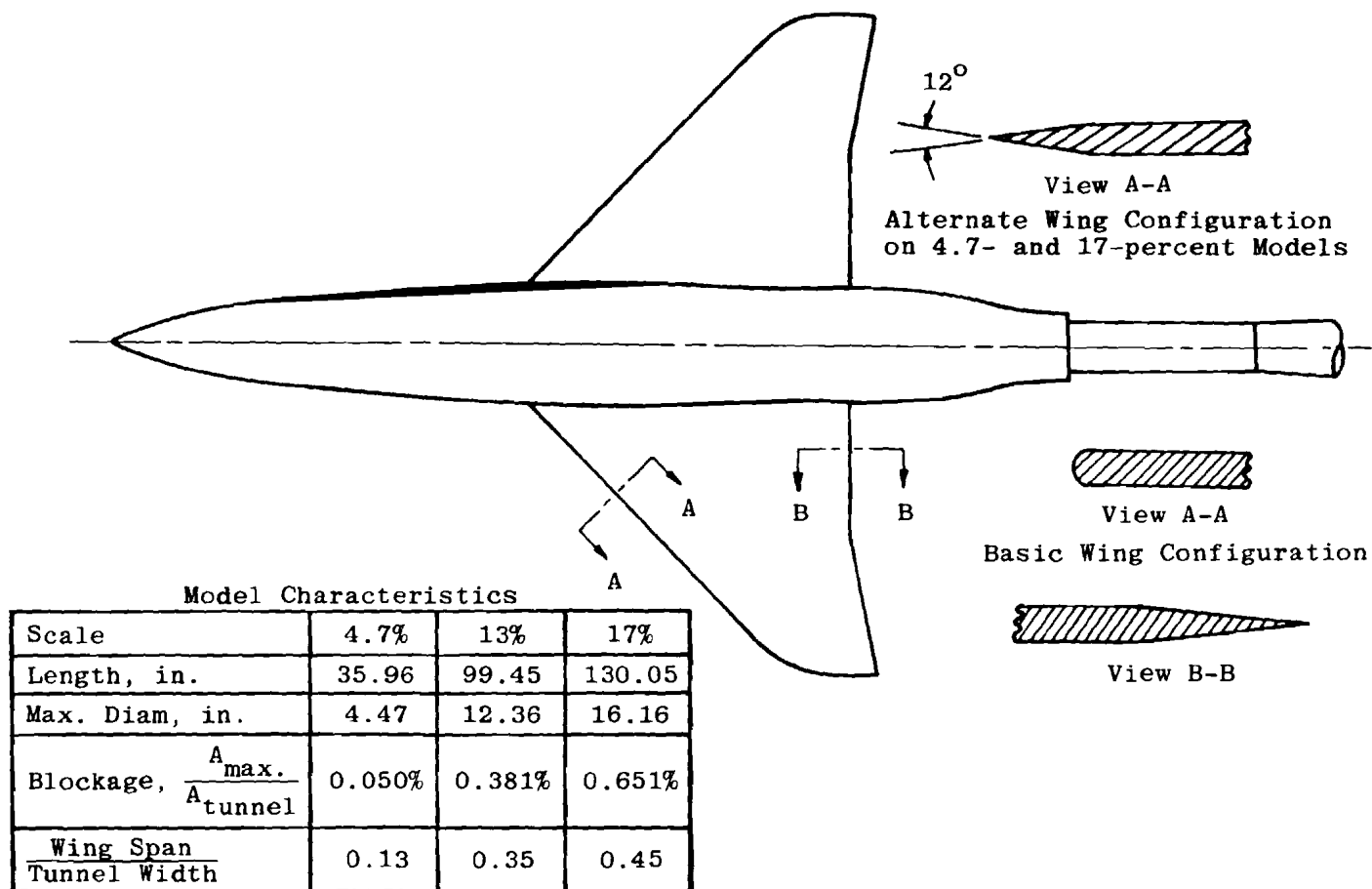
Figure 67.   Characteristics of models used to study effect of model scale.

Sym	Model, percent	Blockage, percent	Length/Width	Span/Width
O	4.7	0.05	0.185	0.13
□	13.0	0.38	0.518	0.35
△	17.0	0.65	0.677	0.45
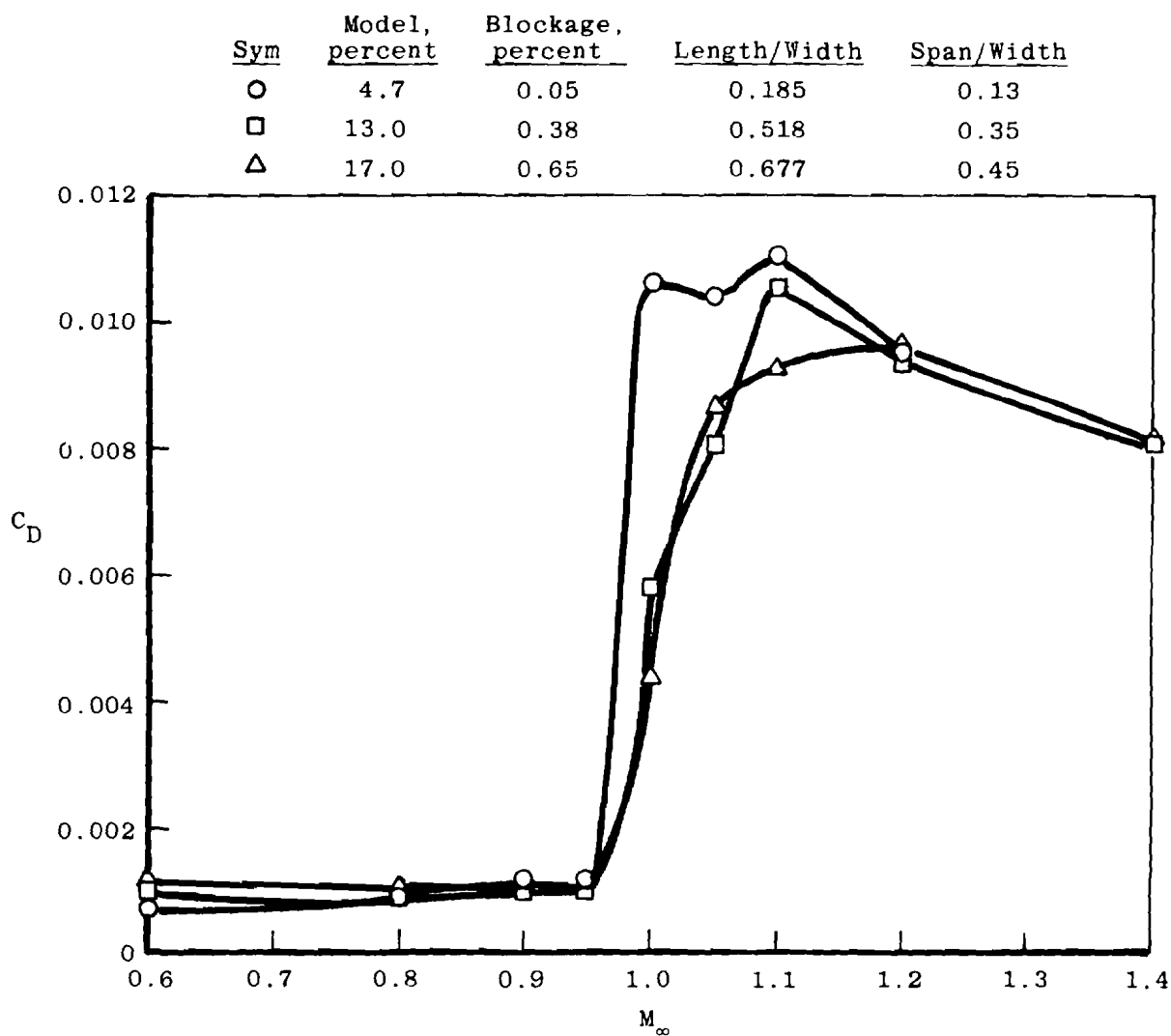
Figure 68. Afterbody drag coefficient as a function of Mach number for various size models.
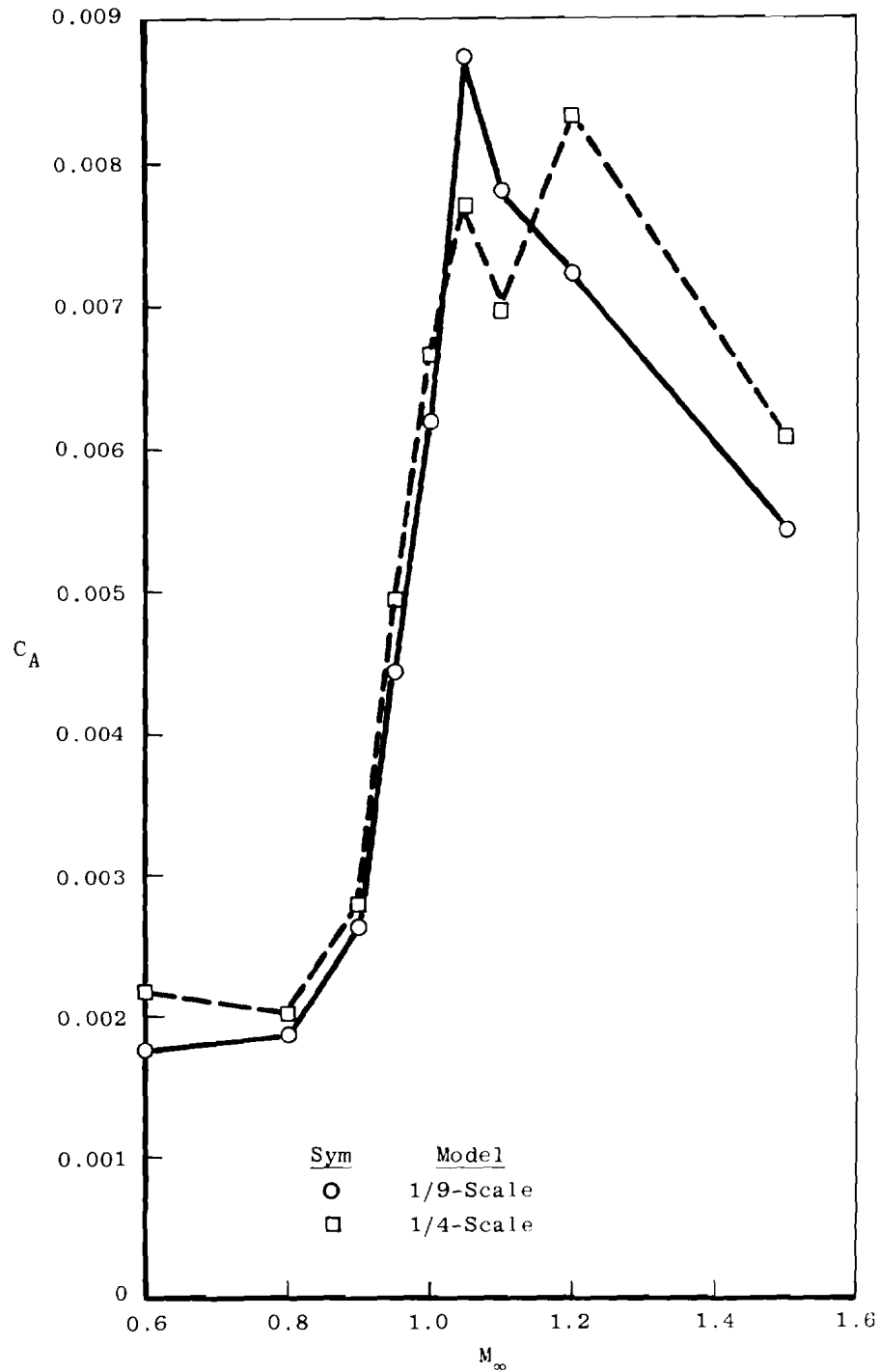
Figure 69. Comparison of afterbody force coefficients for 1/9- and
1/4-scale models at a = 0 deg
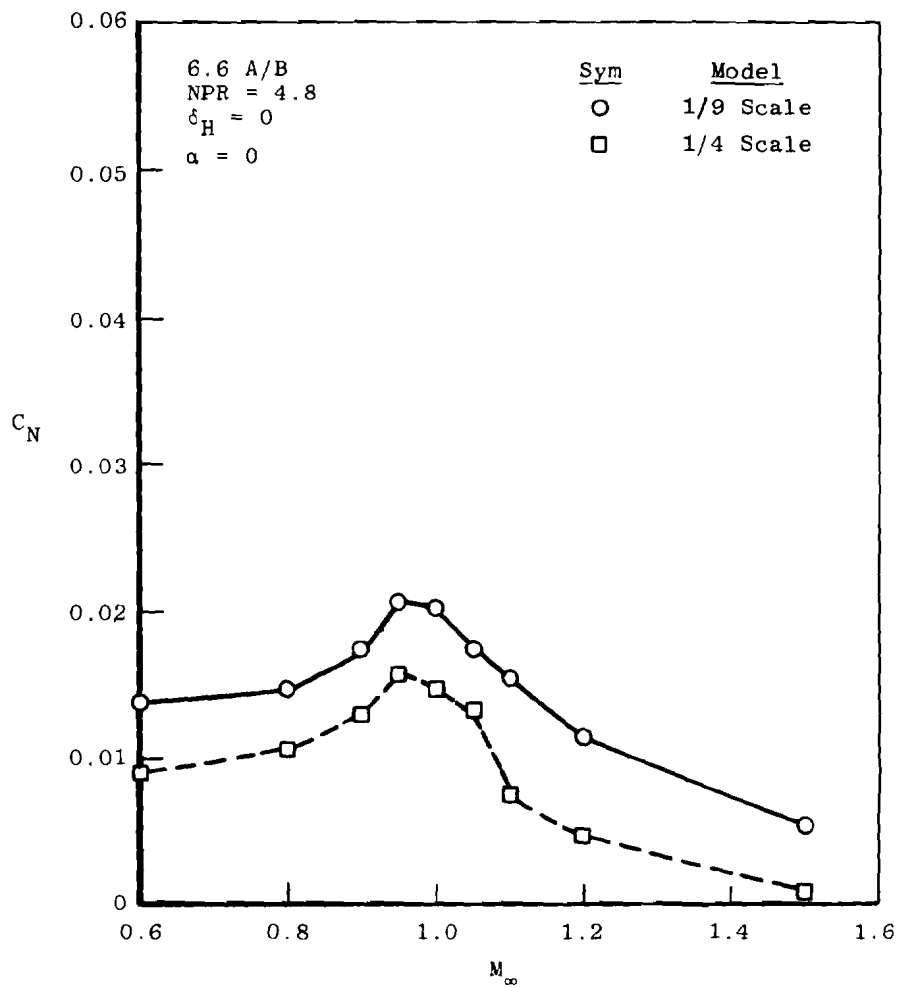
Figure 69. Concluded.
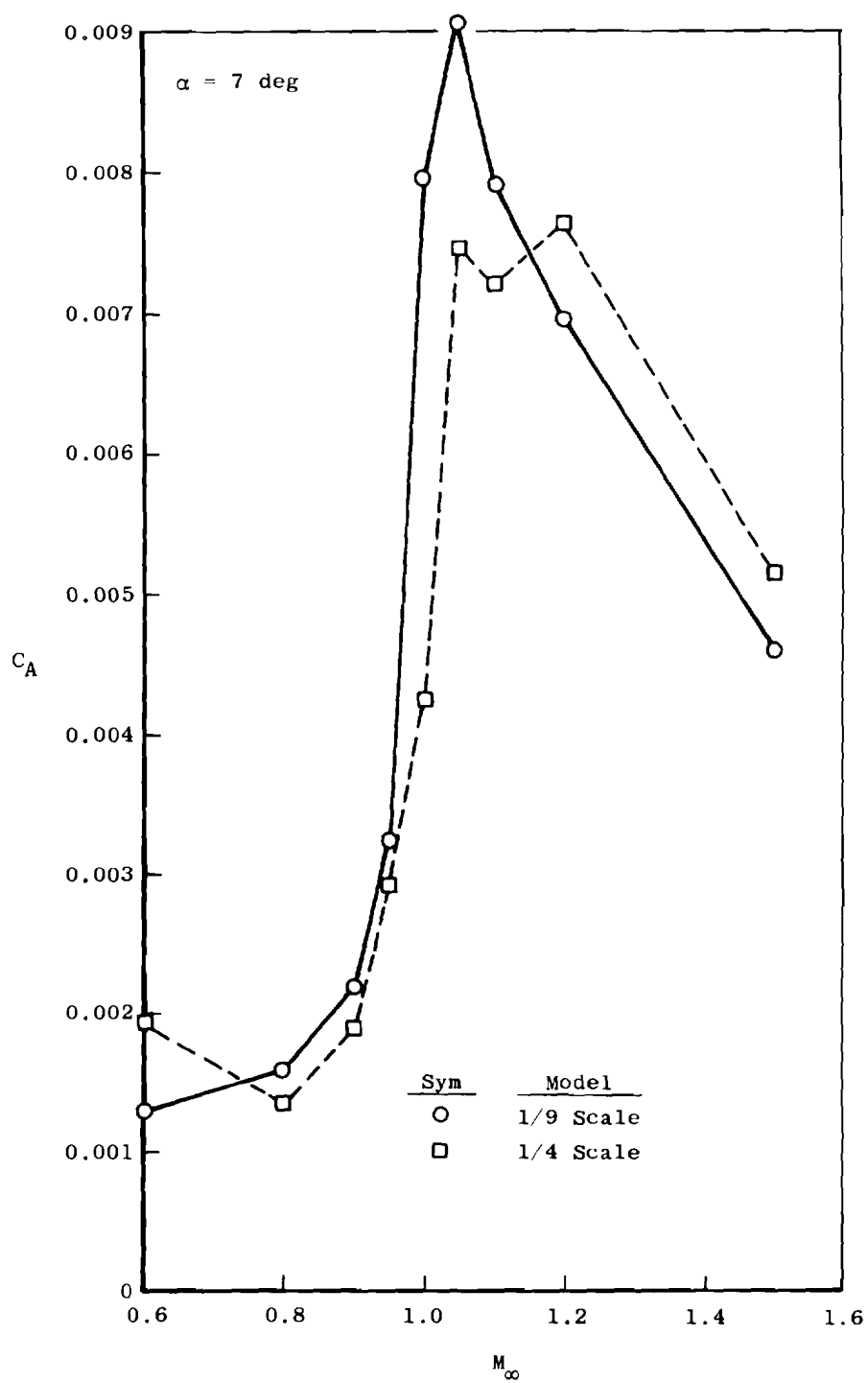
Figure 70. Comparison of afterbody force coefficients for 1/9- and
1/4-scale F-16 models at α = 7 deg

Figure 70. Concluded.

MS
0

MS
65.74

MS
104.331

MS
130.053

A

A

Boattail

Model Forebody

Model Afterbody

MS
104.331

Cylindrical
Boattail

MS
130.053

MS
104.331

MS
130.053

7.5031

15 deg
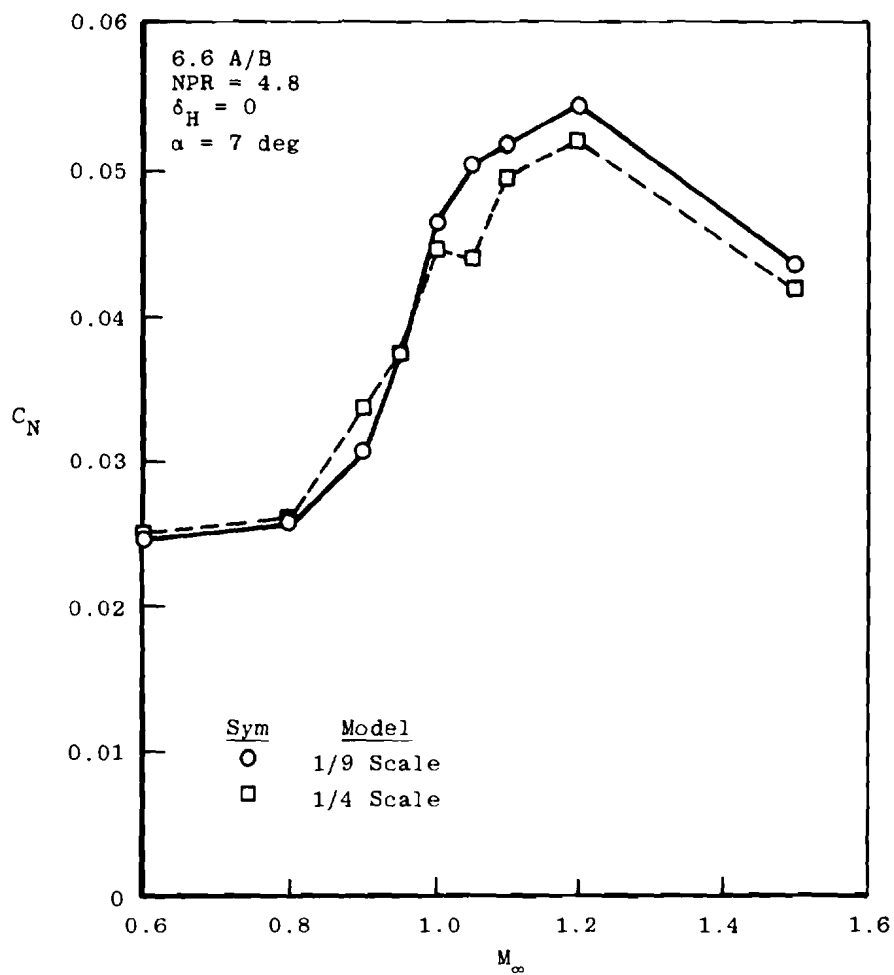
Contoured Boattail
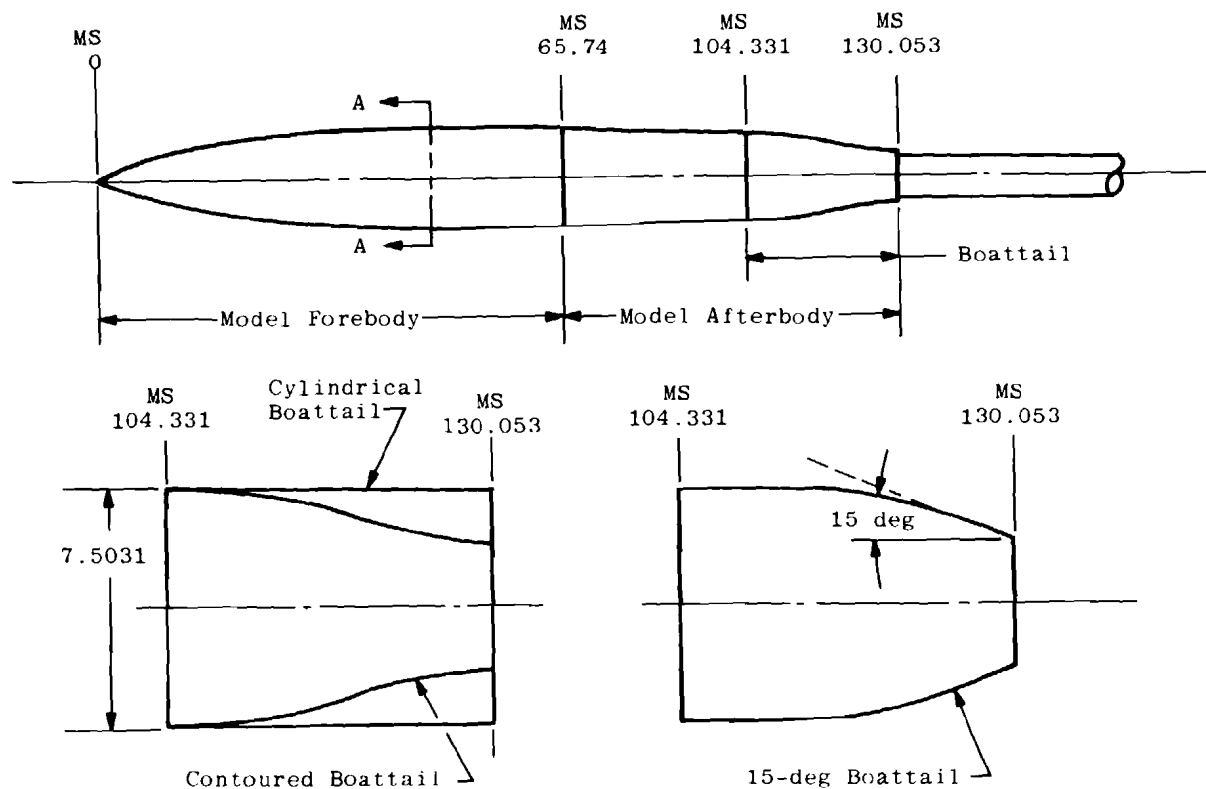
15-deg Boattail

Boattail Characteristics

	Contoured	Cylindrical	15-deg
Length	25.72	25.72	25.72
Exit Radius	4.2678	7.5031	4.2678
Installed Boattail Afterbody Wetted Area, in.^{2}	2870.149	3106.3131	2980.0553

Length = 130.053 in.
Max. Diam = 16.16 in.

Model Stations and Dimensions in Inches

Figure 71. Model and afterbody configurations used to study the effect
of afterbody configuration on forebody drag coefficient.

Sym	Config
O	15-deg Boattail
Δ	Cylindrical Boattail
□	Contoured Boattail
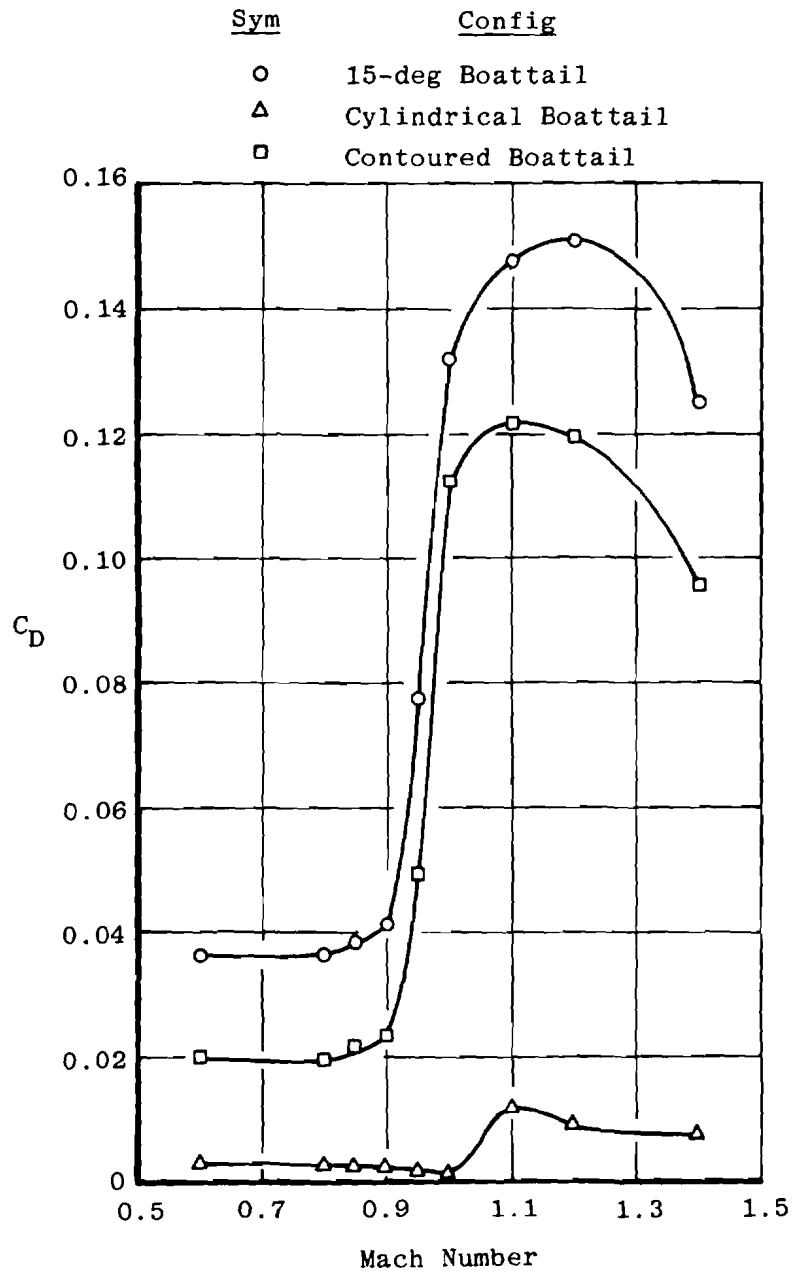
Figure 72. Afterbody drag coefficient for various configurations.
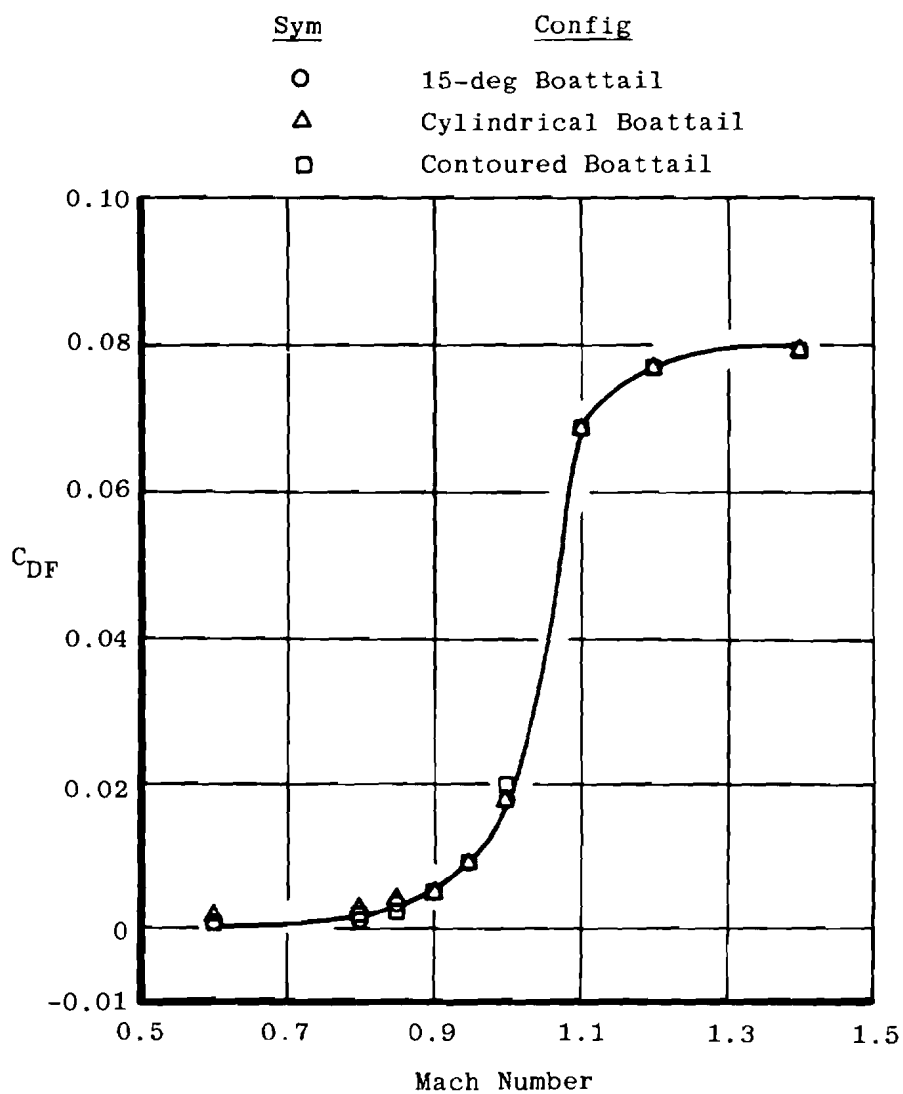
Figure 73. Forebody drag coefficient as a function of Mach number for various afterbody configurations.
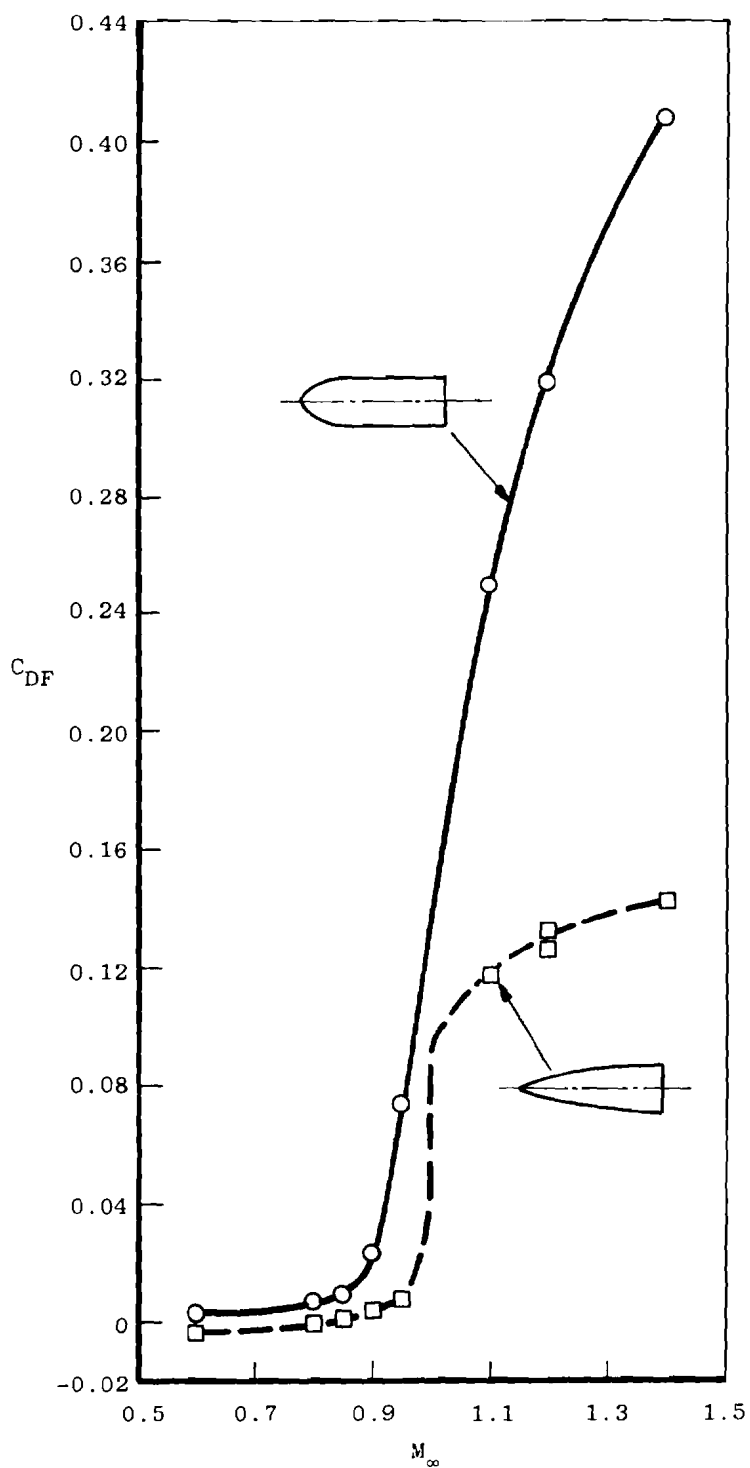
Figure 74. Forebody drag coefficient for blunt and
streamlined configurations.
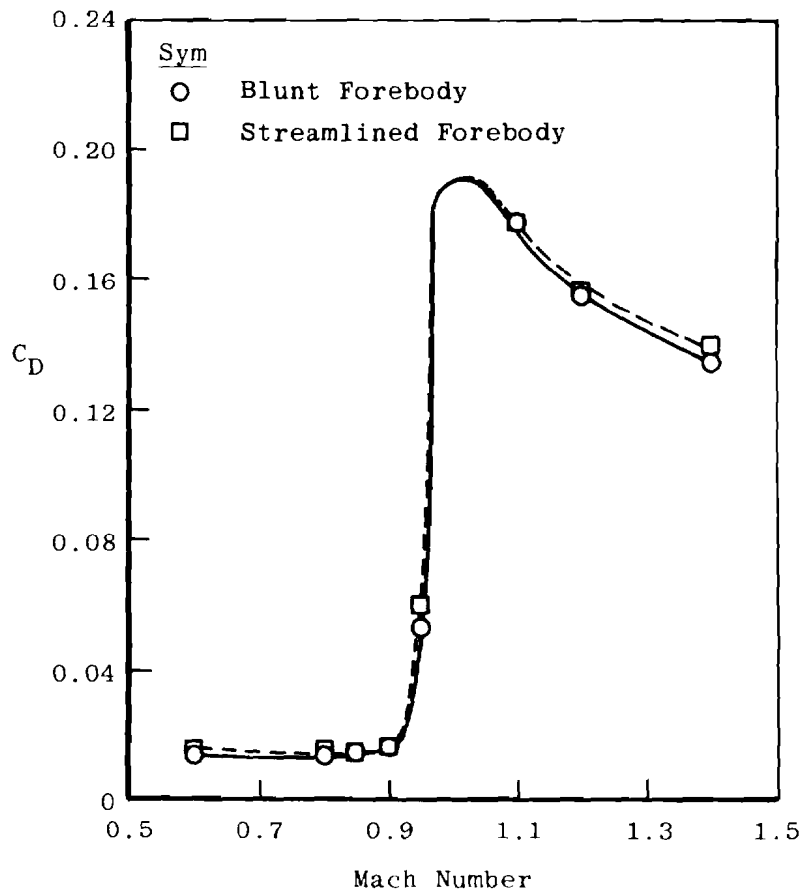
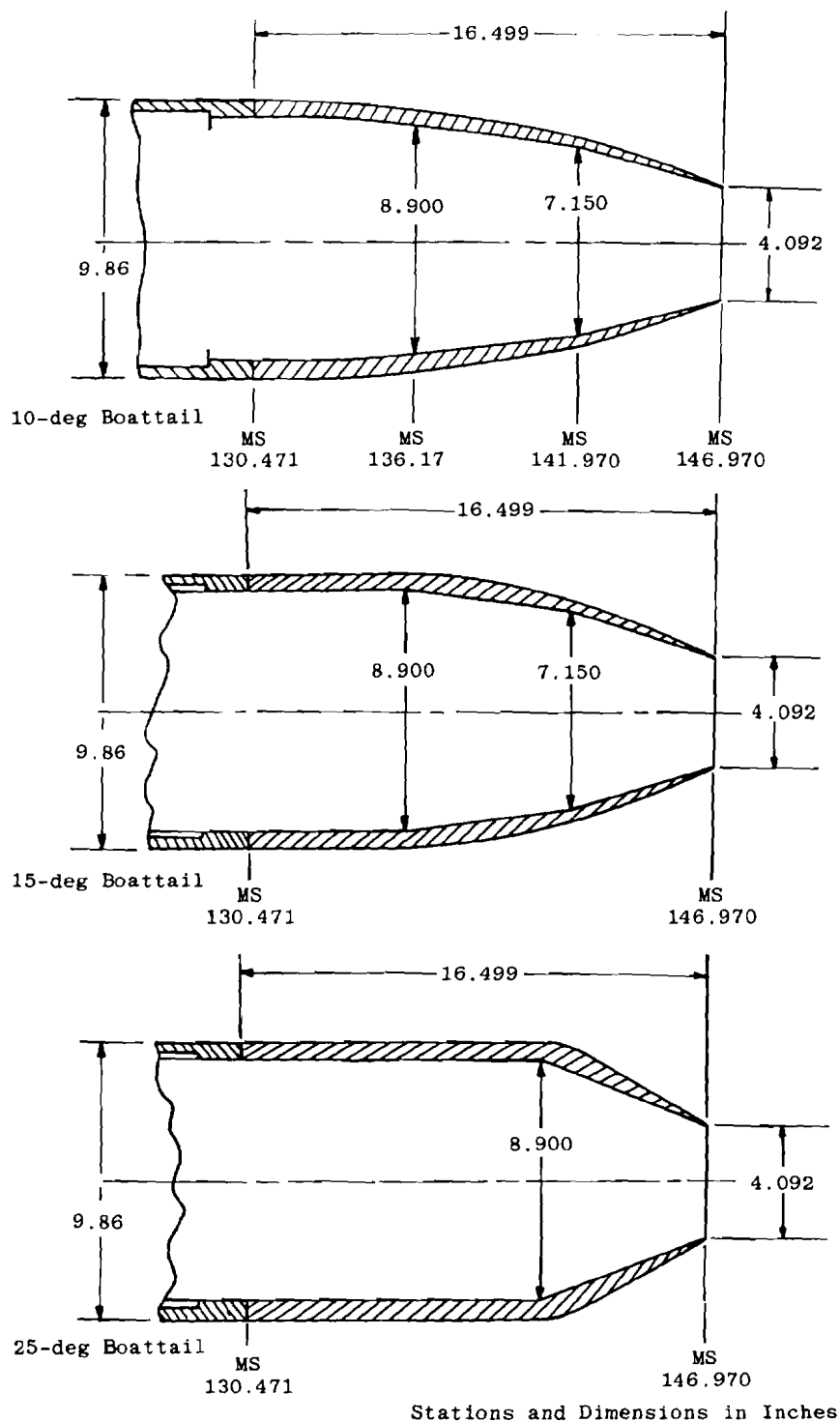Figure 75. Afterbody drag coefficient for blunt and streamlined
forebody configurations.

Figure 76. Configuration details for the 10-, 15-, and
25-deg boattails.
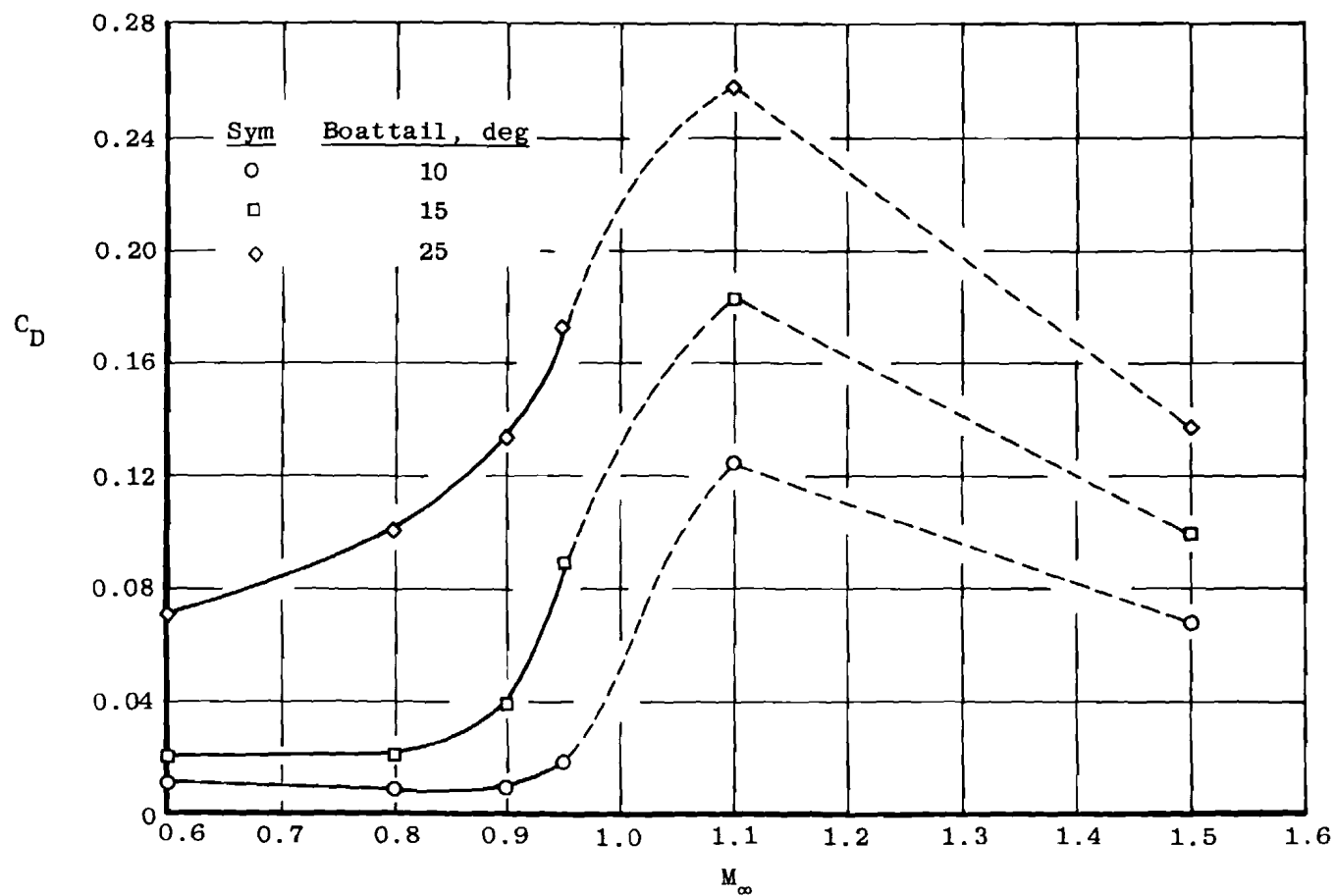
Figure 77. Afterbody drag coefficient for 10-, 15-, and 25-deg
boattails as a function of Mach number.

Sym	Boattail, deg	D_e/D_B
A	15	0.973
B	25	0.973
O	15	0.789
□	25	0.789
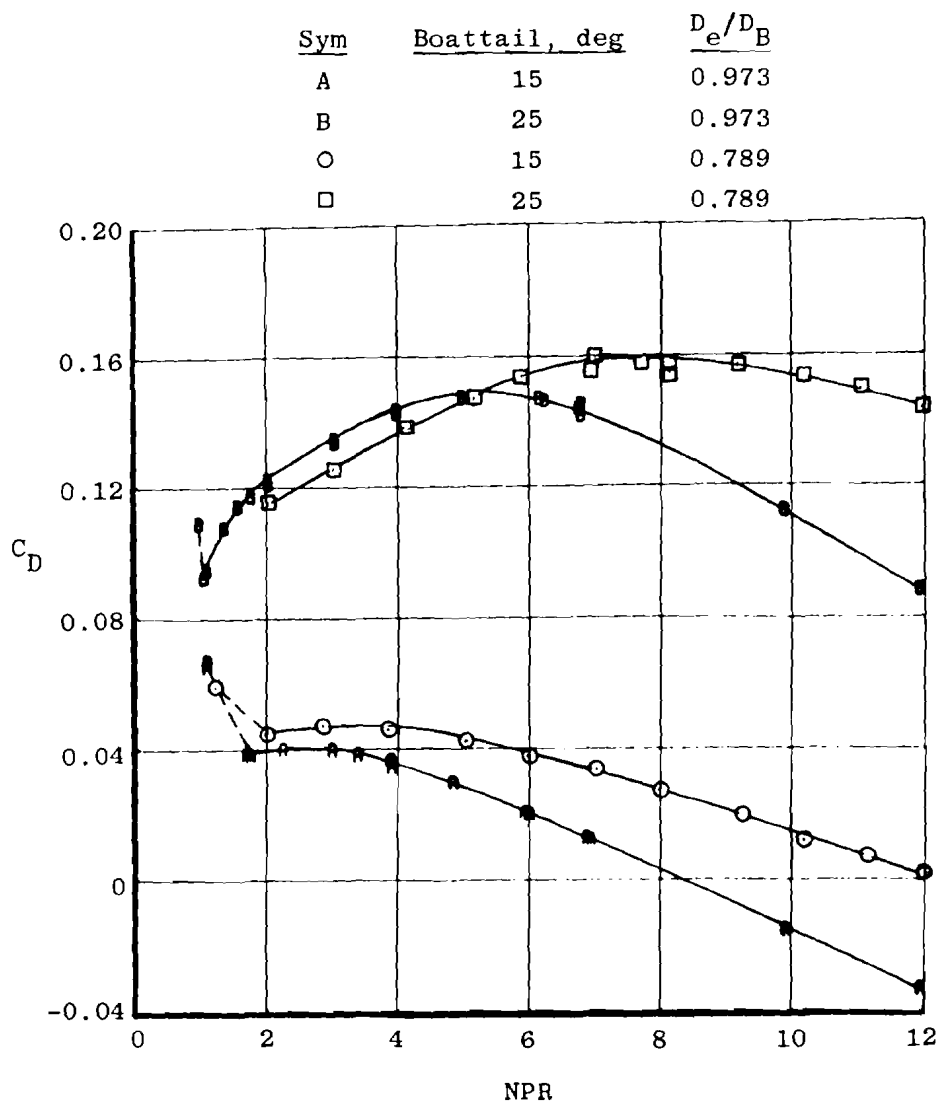
a. $M_\infty = 0.90$

Figure 78. Effect of base area on afterbody drag coefficient.

160

Sym	Boattail, deg	D_e/D_B
A	15	0.973
B	25	0.973
O	15	0.789
□	25	0.789
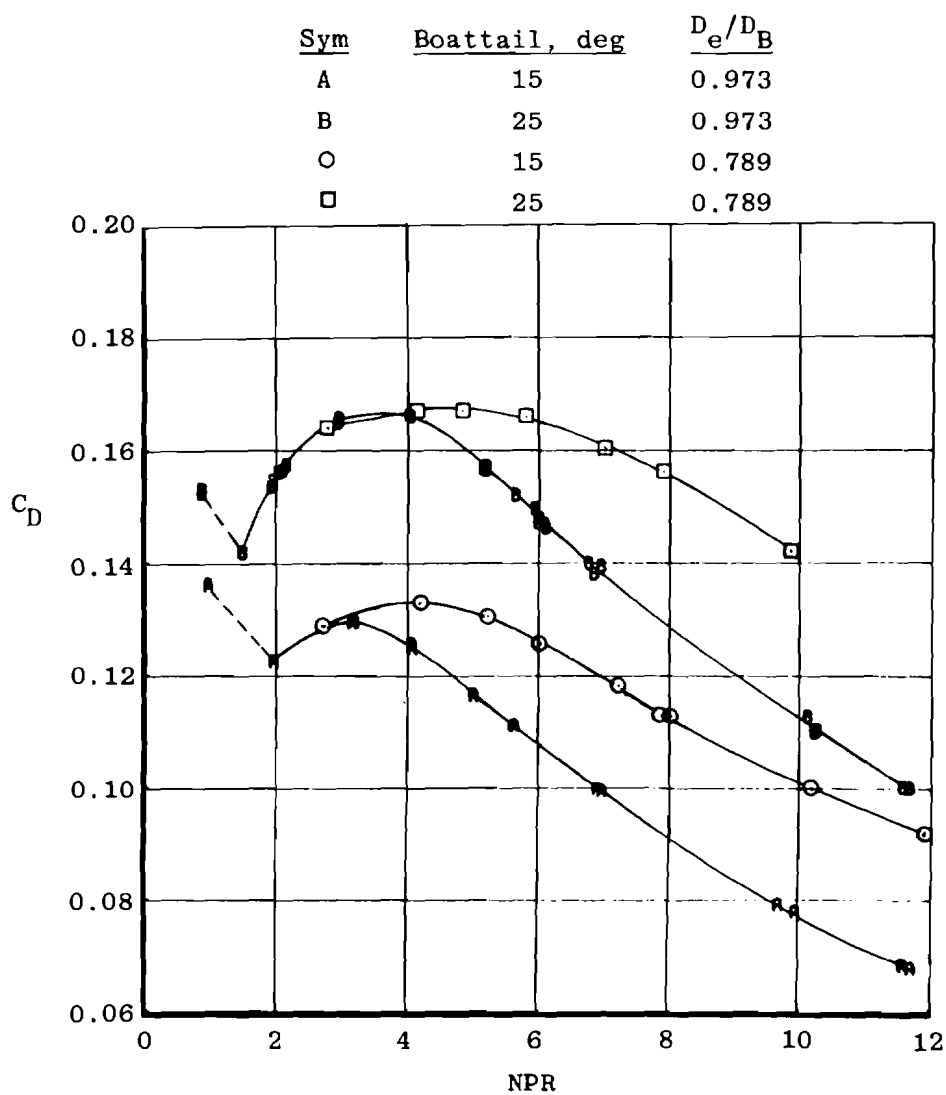
b. $M_\infty = 1.50$
Figure 78. Concluded.

Nozzle

Nozzle
Extension

Inlet Flow Path

Scanivalve
Assembly

4.27 D ⌐Choke
Plate

3.00 D

Aerodynamic
Inlet Fairing

Blunt Inlet Fairing

Strongback Assembly

Duct Total-
Pressure Rake

62.25

12.60

Nozzle Exit
Plane

All Dimensions in Inches
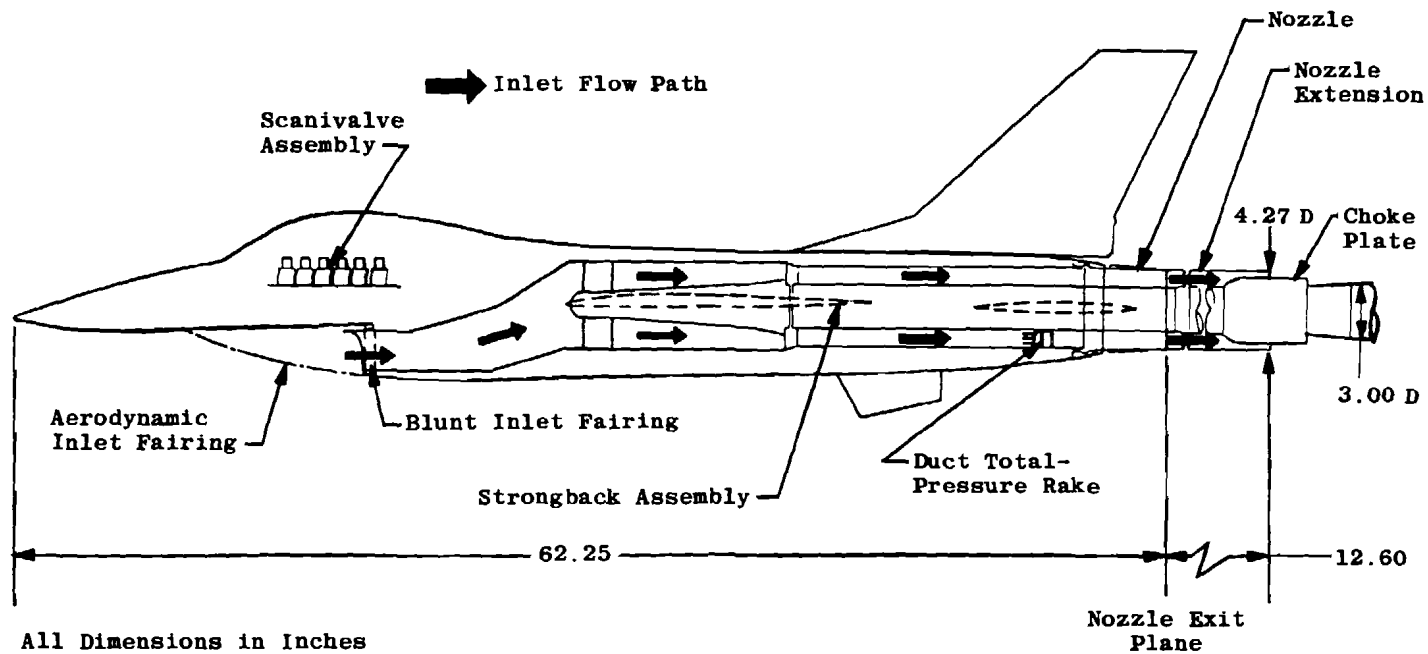
Figure 79. Model configuration used to study inlet fairing effects.
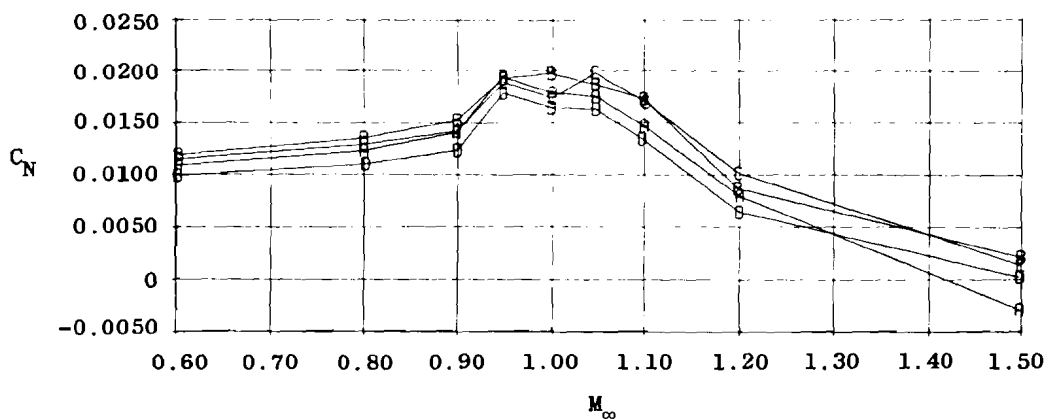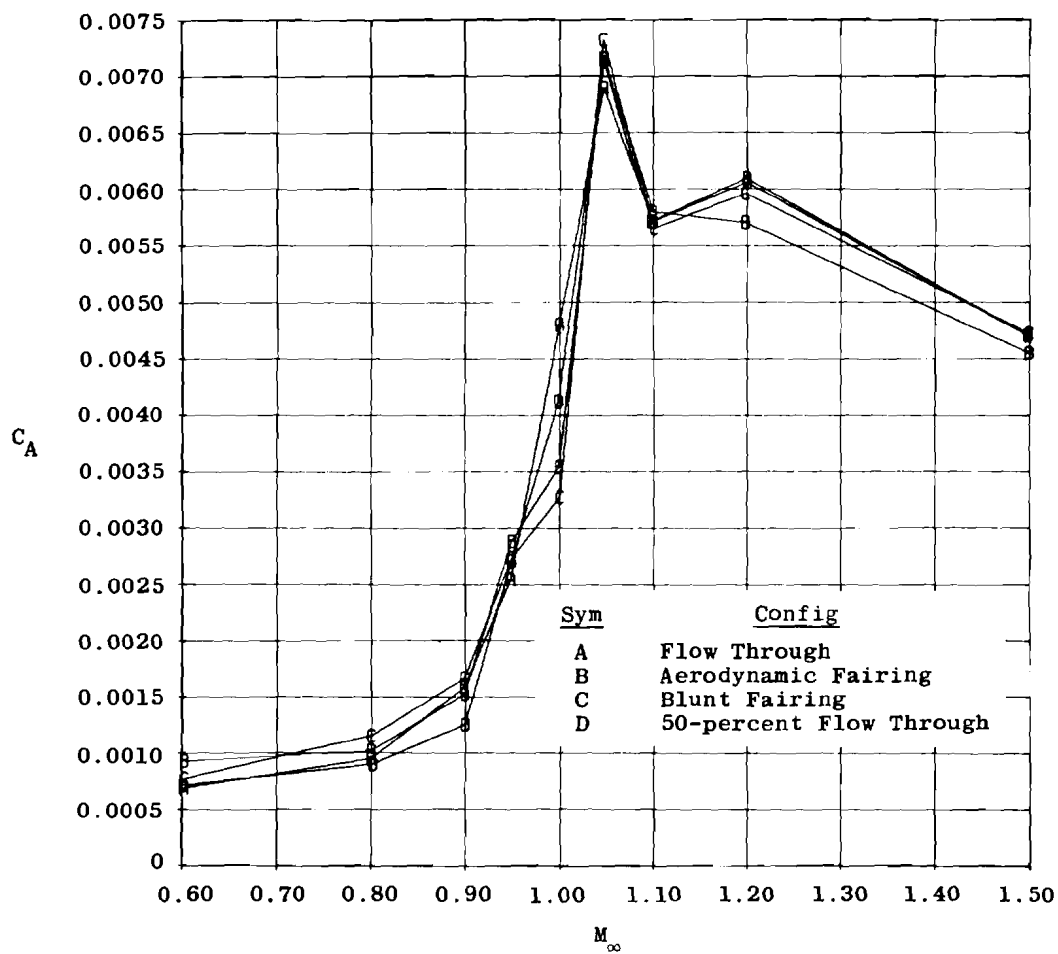
a. $a = 0$

Figure 80. Effect of inlet fairing configurations on afterbody
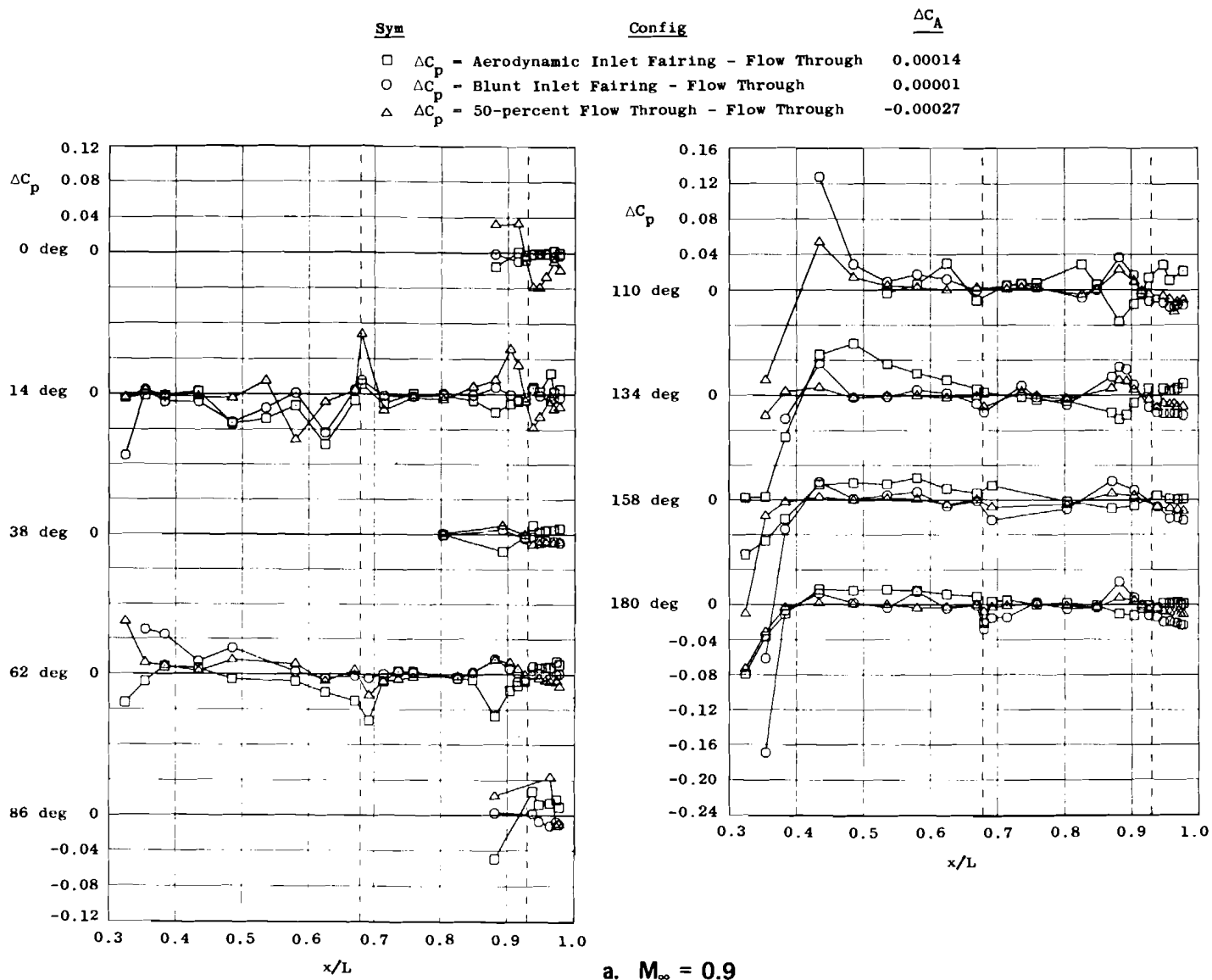force coefficients.

163
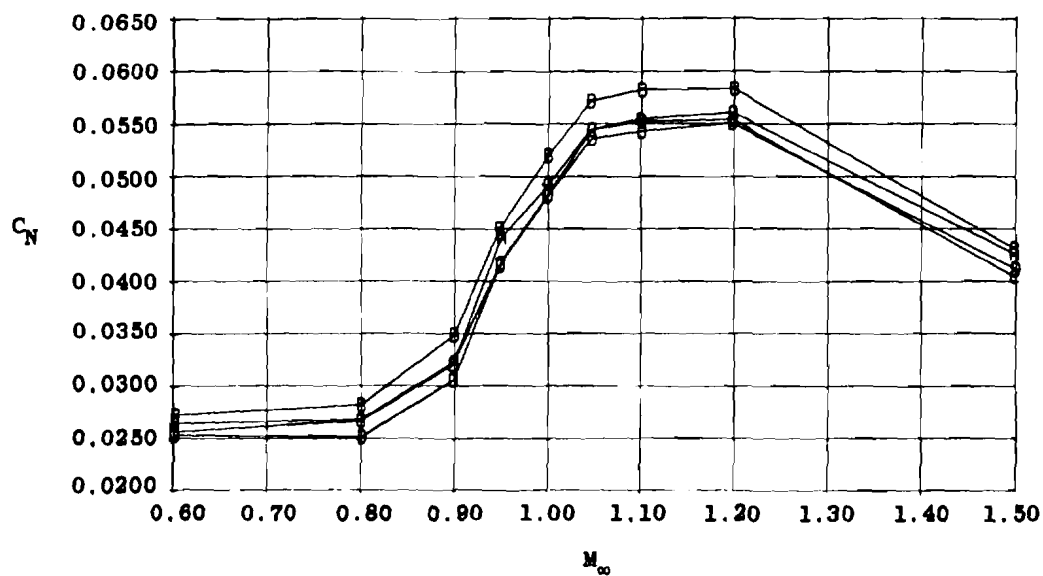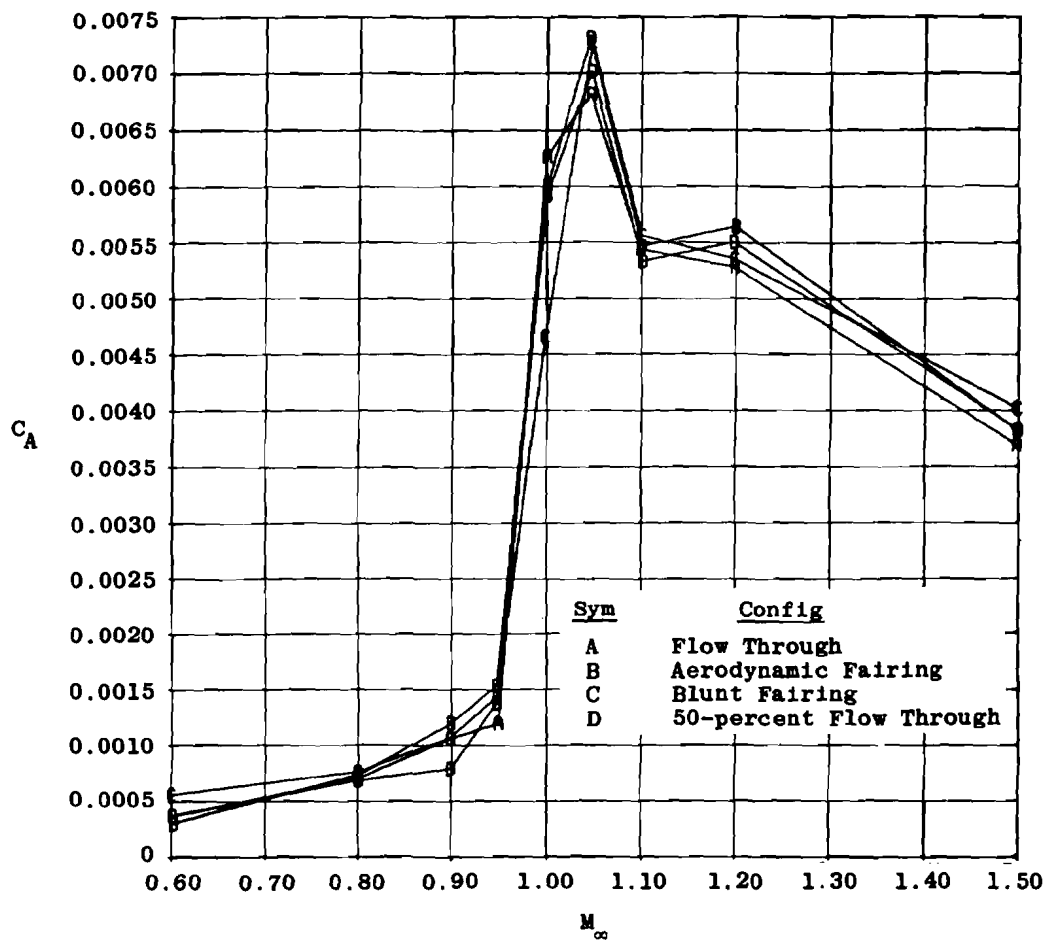
b. $a = 7$ deg
Figure 80. Concluded.

Sym		Config	ΔC_A
□	ΔC_p - Aerodynamic Inlet Fairing - Flow Through		0.00014
O	ΔC_p - Blunt Inlet Fairing - Flow Through		0.00001
△	ΔC_p - 50-percent Flow Through - Flow Through		-0.00027

a. $M_\infty = 0.9$

Figure 81. Change in afterbody pressure distributions for various inlet fairing configurations (reference flow-through).

Sym	Config	ΔC_A
□	ΔC_p = Aerodynamic Inlet Fairing - Flow Through	0.00036
O	ΔC_p = Blunt Inlet Fairing - Flow Through	0.00007
△	ΔC_p = 50-percent Flow Through - Flow Through	0.00022
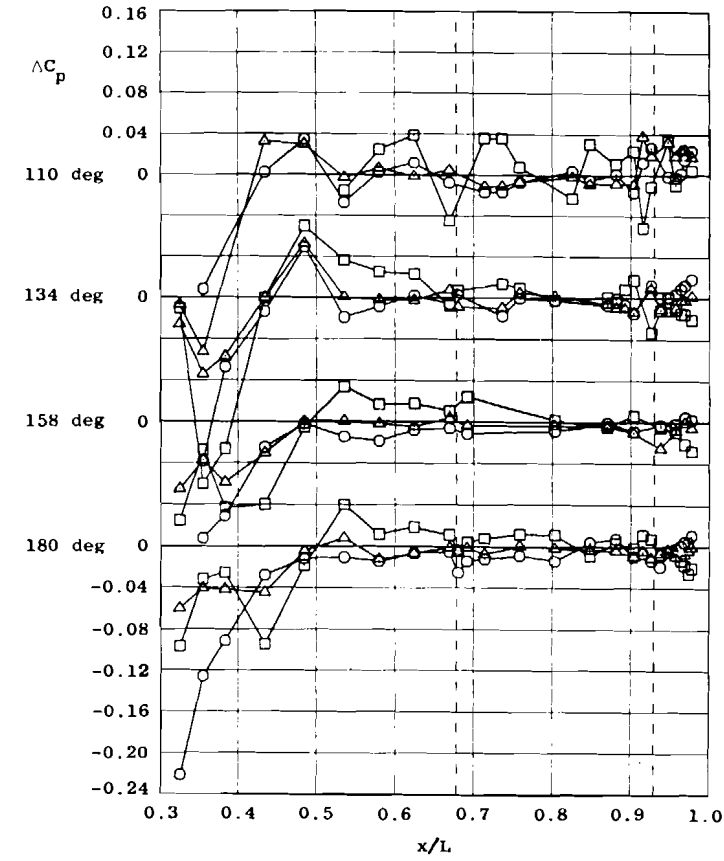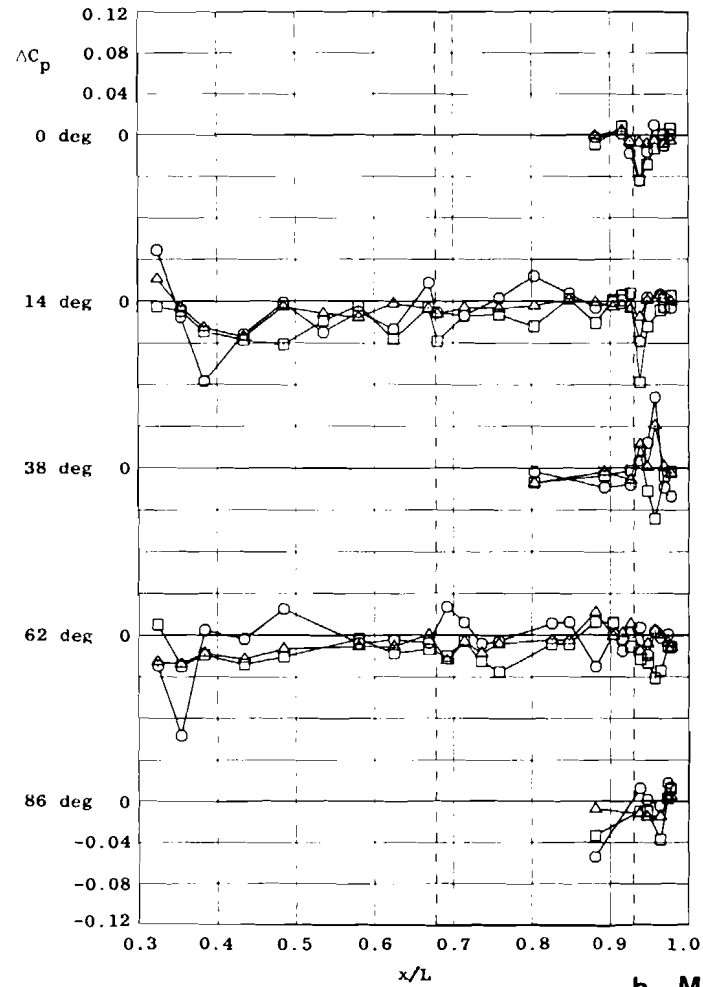
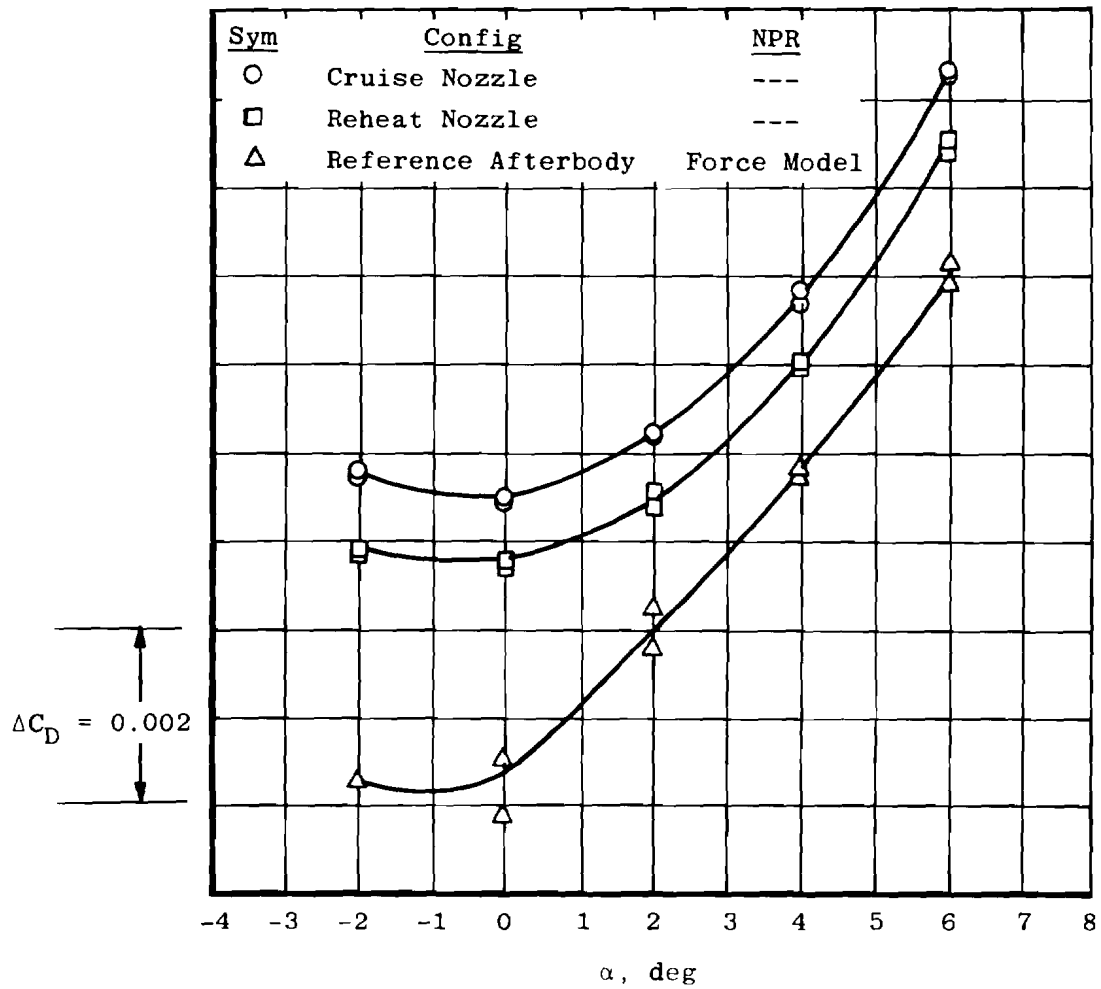
b. M_∞ = 1.2

Figure 81. Concluded.

Figure 82. Angle-of-attack effects on afterbody throttle-dependent aerodynamics.

Bay Purge Exhaust
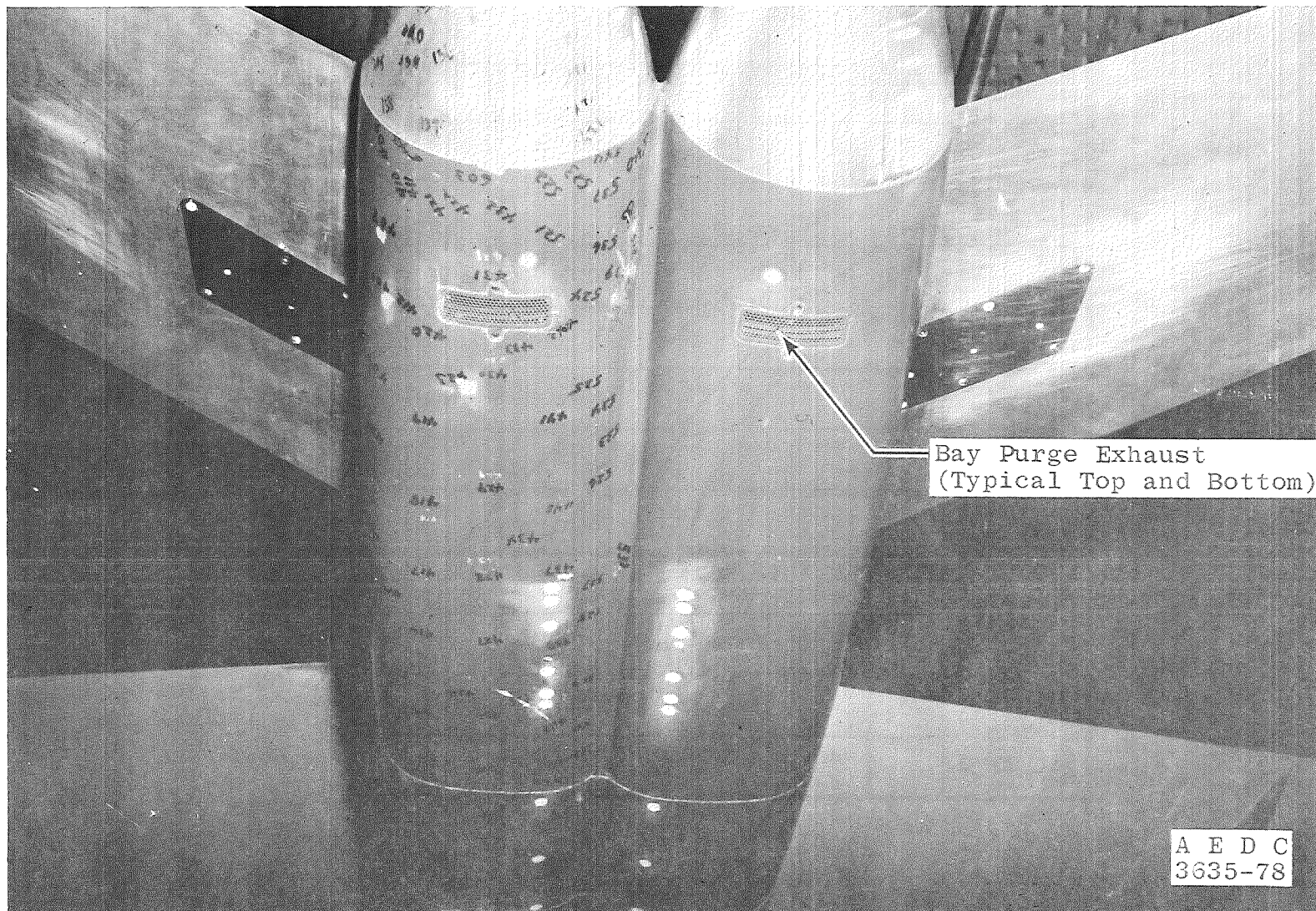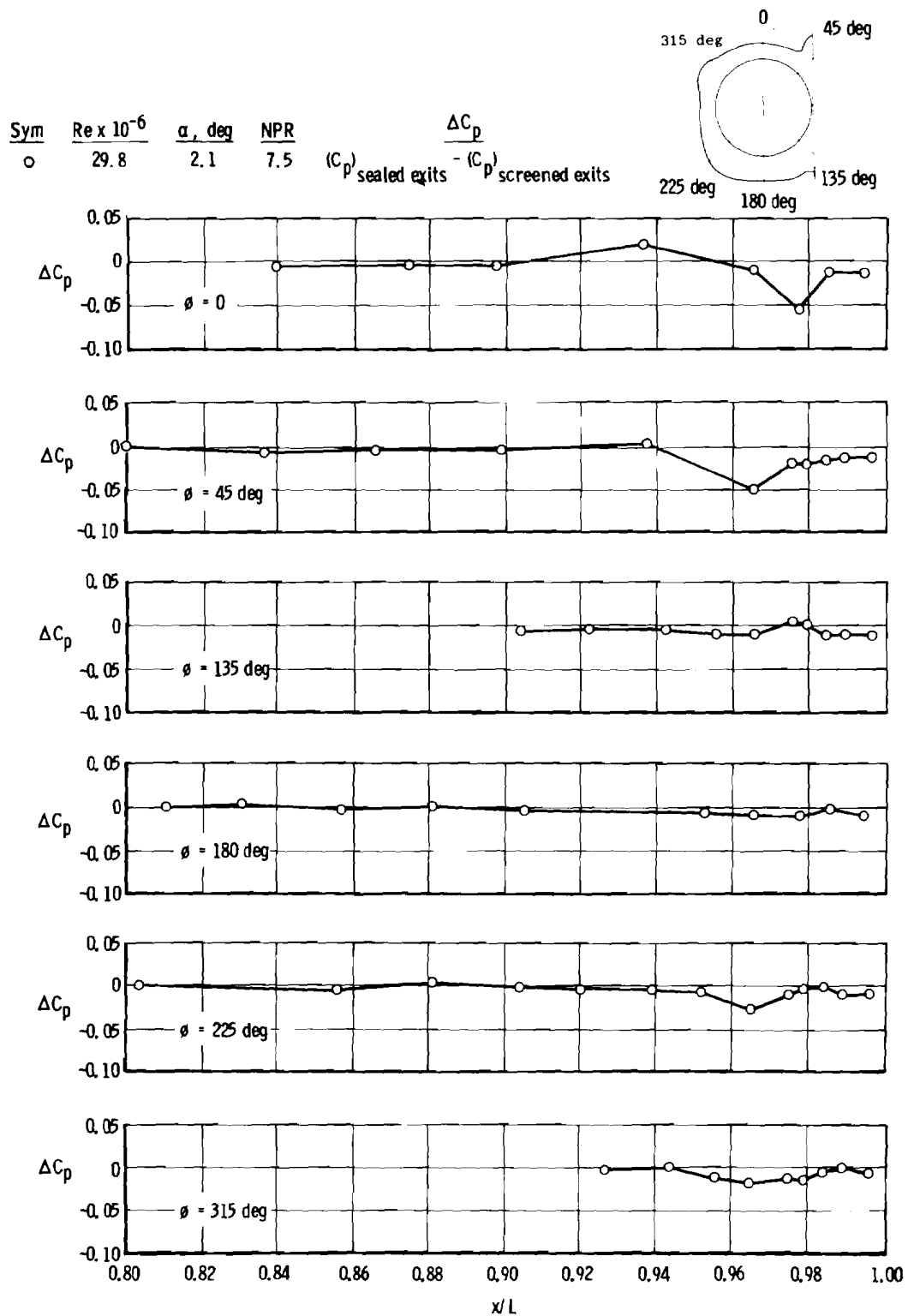(Typical Top and Bottom)

A E D C
3635-78

Figure 83. Bay purge exhaust for the YF-17 model.

Figure 84. Effect of bay purge exhaust on afterbody pressure distribution.

MS
55.01

High-Pressure
Air Inlet

NS
0.900

1.926

Nozzle ₡

0° 48'

Metric Break
NS
17.055

Nozzle ₡

Nacelle
Reference
Plane

2°
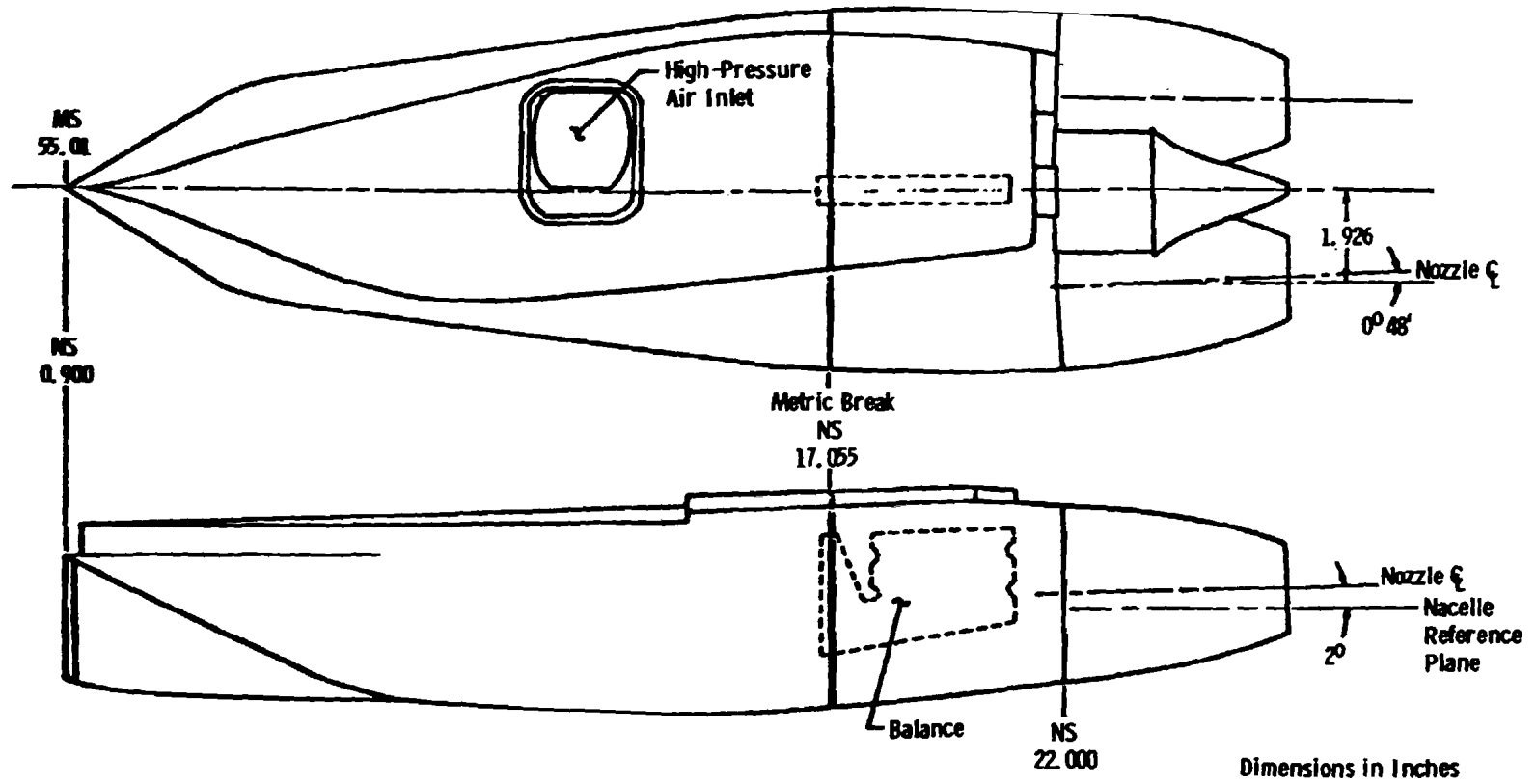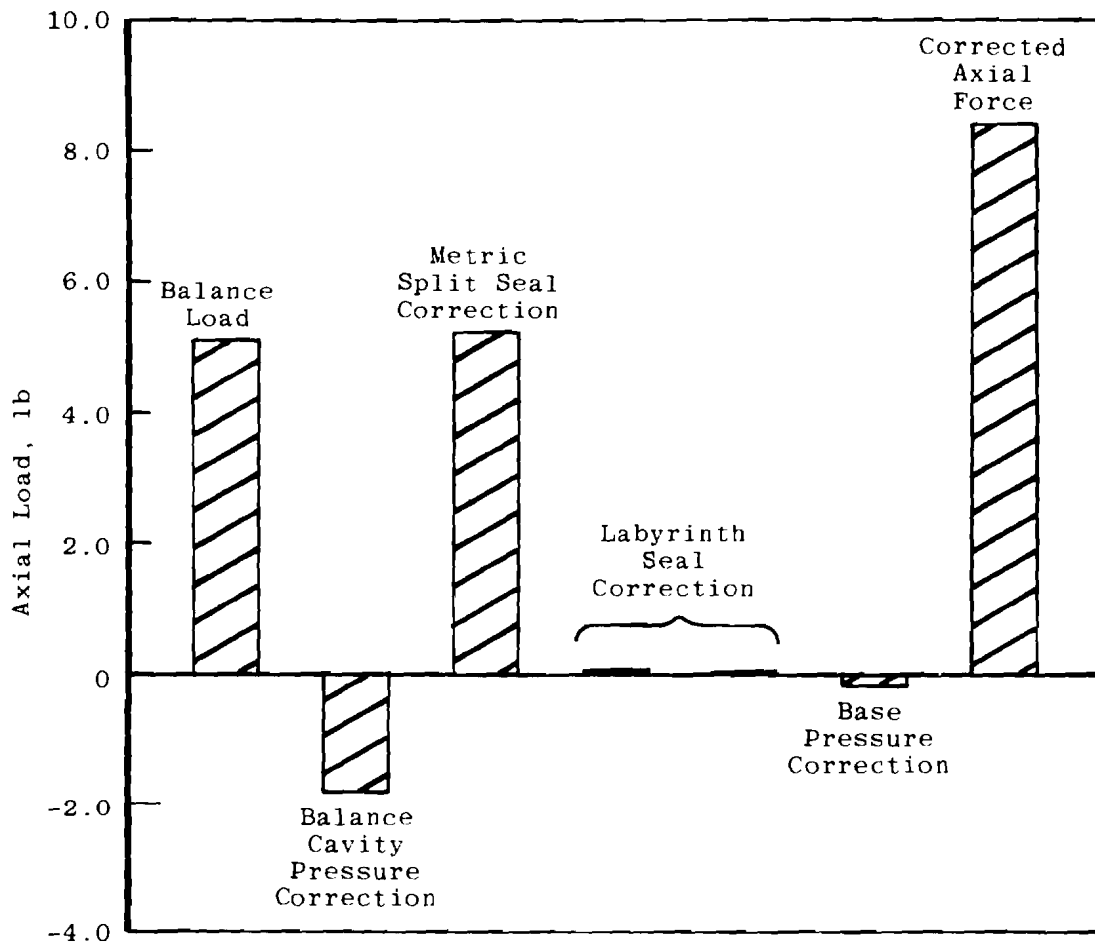
Balance
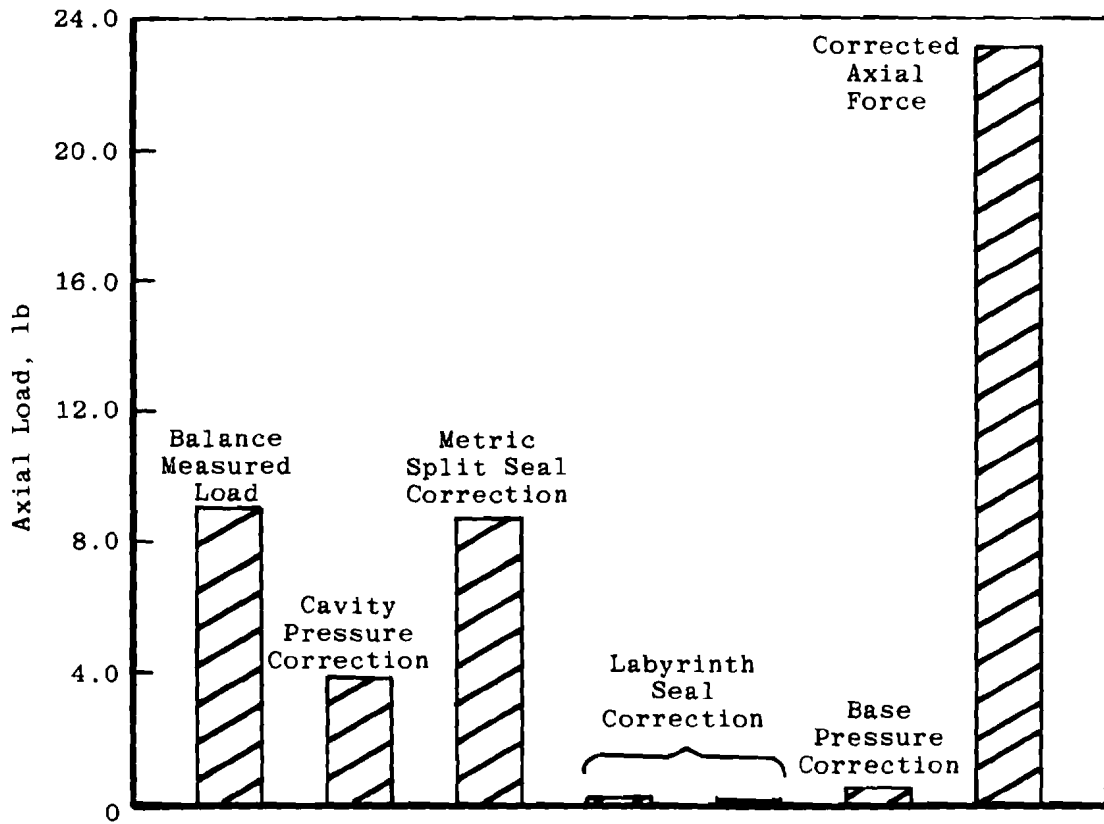
NS
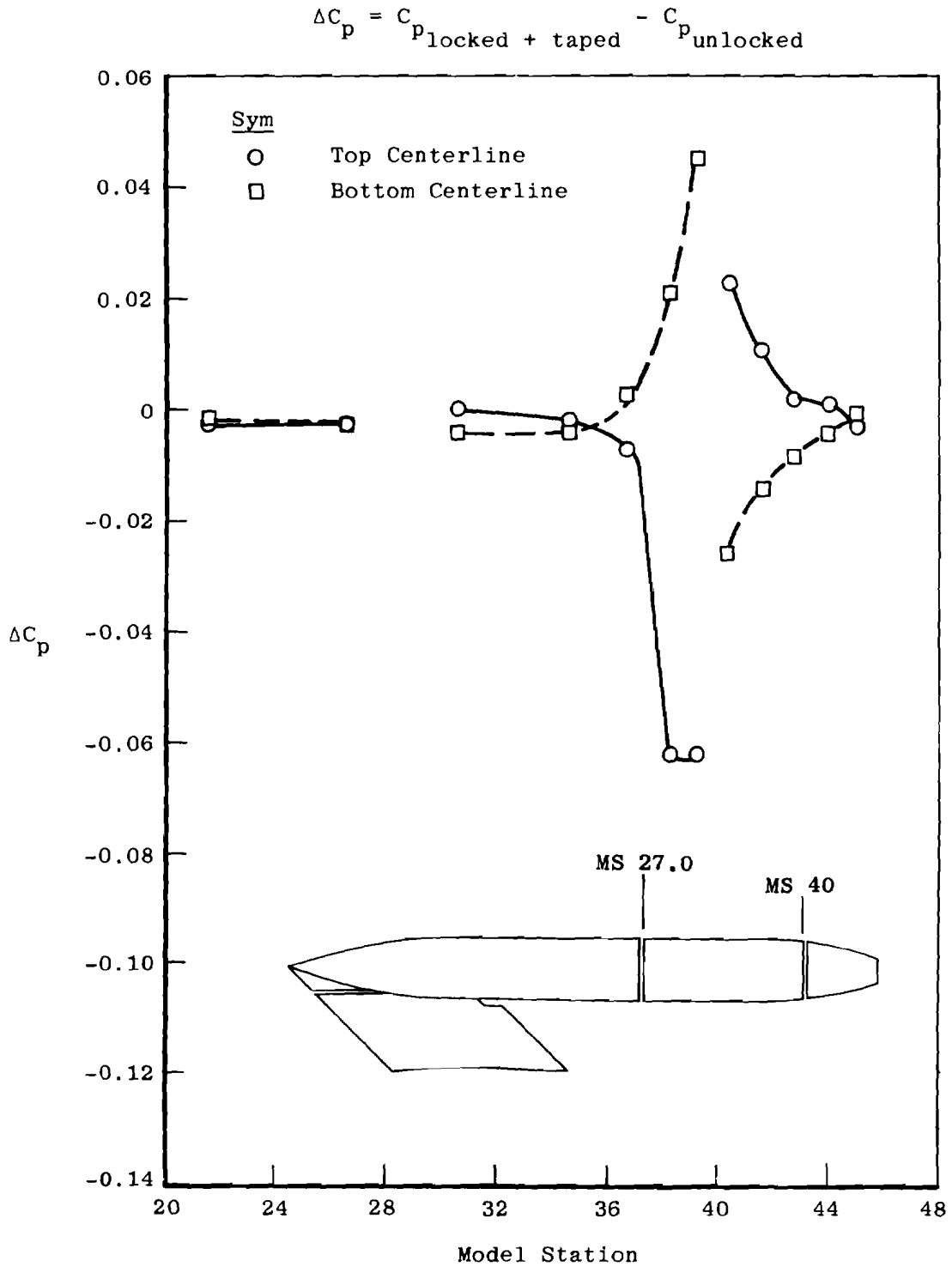22.000

Dimensions in Inches

Figure 85.   Force balance nacelle configuration.

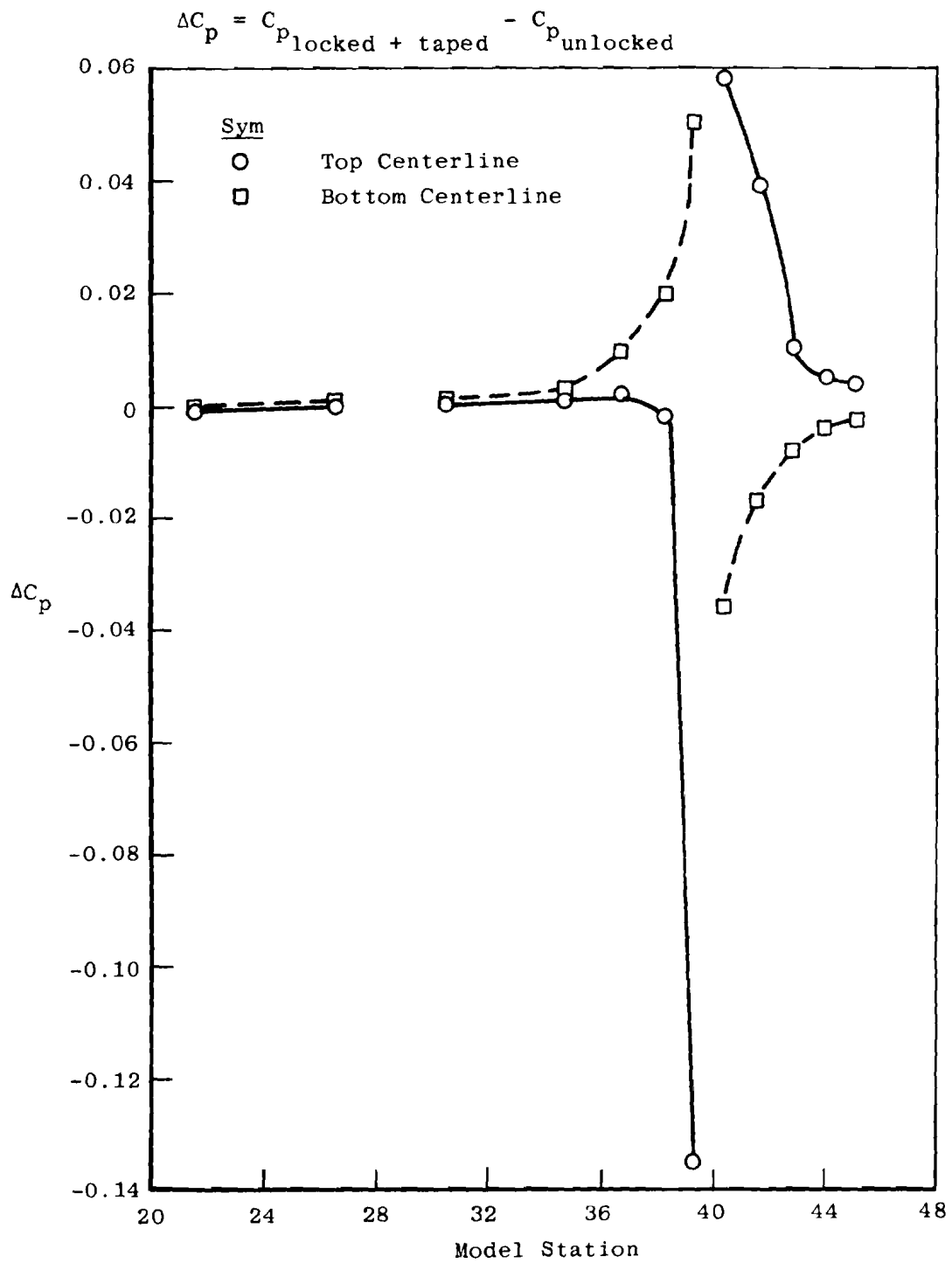a. Subsonic Mach number
Figure 86. Nacelle axial-force components.

b. Supersonic Mach number
Figure 86. Concluded.

$$\Delta C_p = C_{p_{locked + taped}} - C_{p_{unlocked}}$$

a. $a = 0$ deg

Figure 87. Effect of metric break on model pressure distribution.

$$\Delta C_p = C_{p_{\text{locked + taped}}} - C_{p_{\text{unlocked}}}$$

b. $a = 12$ deg
Figure 87. Concluded.

Chamber
Pressure Orifice

12 Equally Spaced Sonic Nozzles

Clearance Holes for Sonic Nozzles

Cavity Vented to Model
Internal Pressures

Supply
Pipe

Airflow

Tailpipe Centerline

Airflow

Nonmetric

Tailpipe

Metric

Flexible Seal
(Metal Bellows)

Inner Sleeve
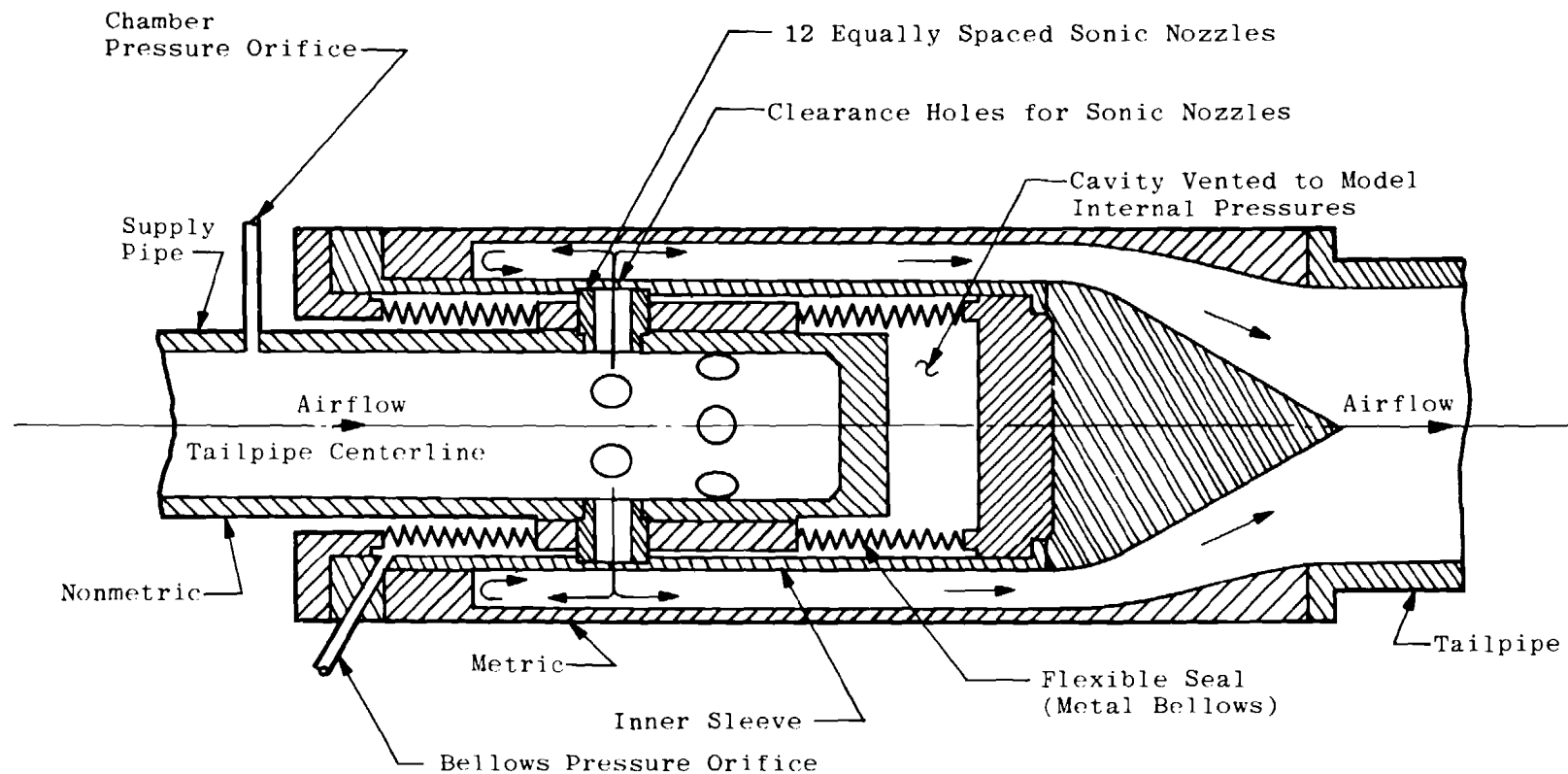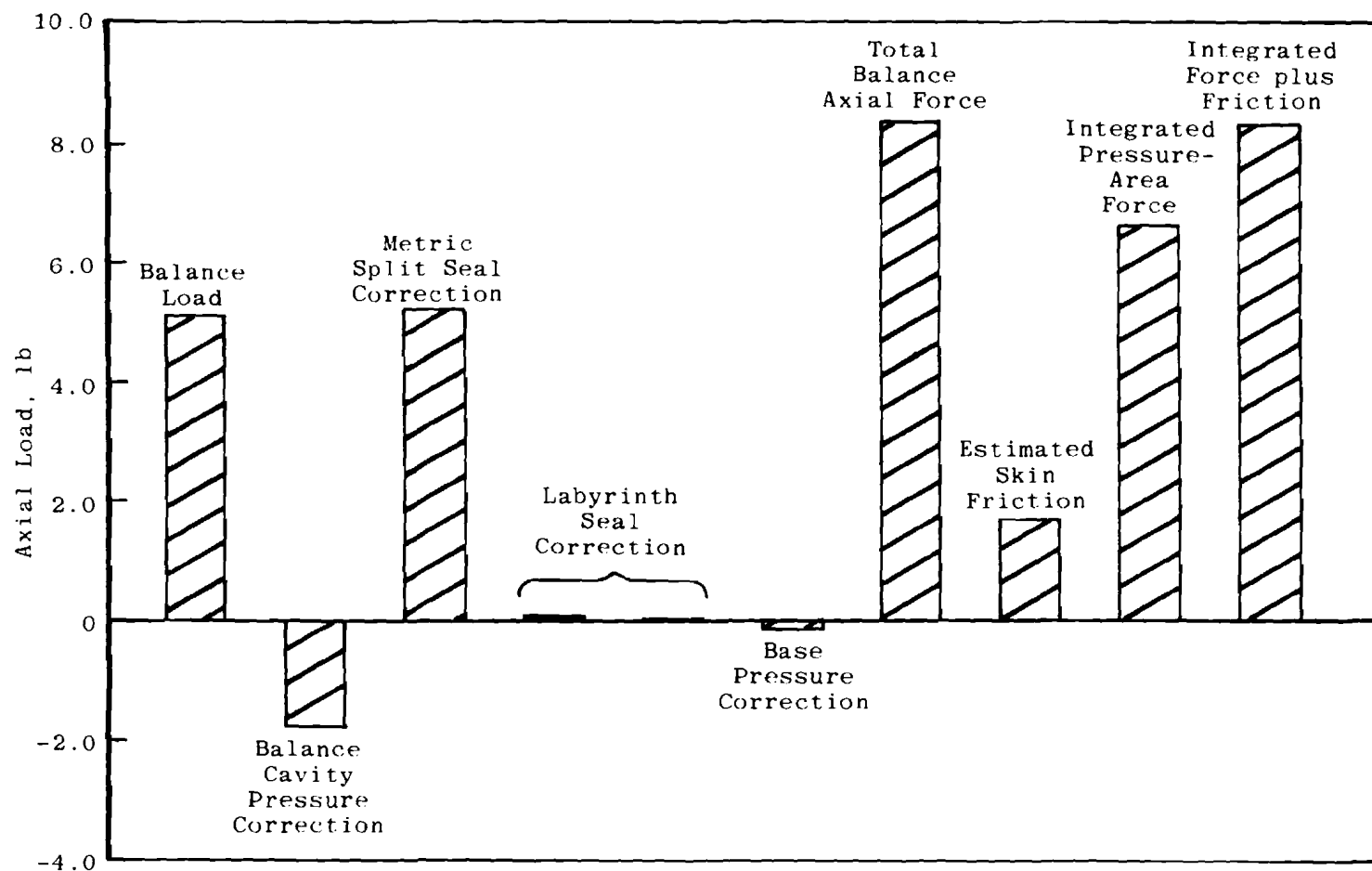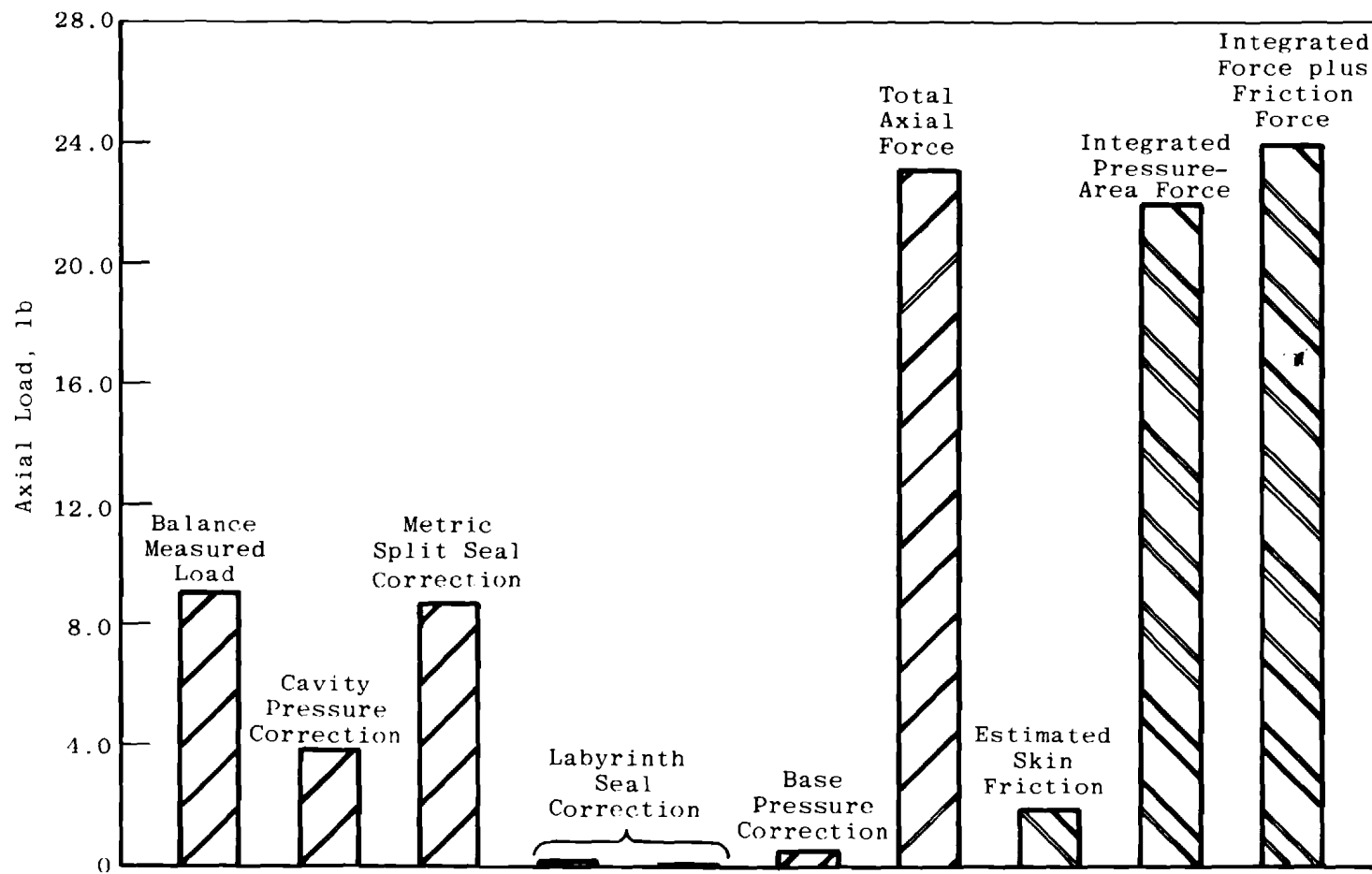
Bellows Pressure Orifice

Figure 88. Typical model bellows configuration.

a. Subsonic Mach number

Figure 89. Comparison of afterbody axial force determined by a force
balance and by integration of pressures.

b. Supersonic Mach number
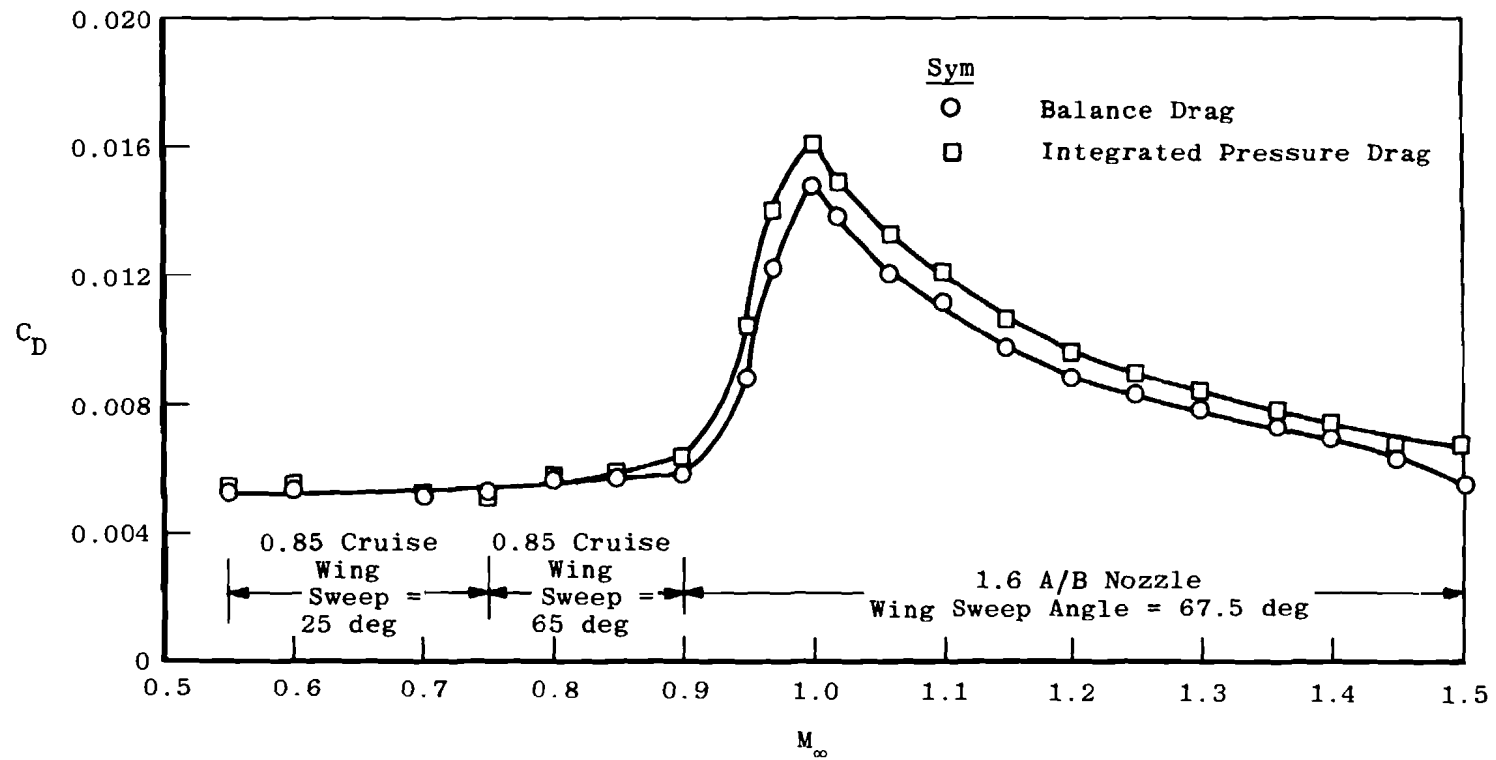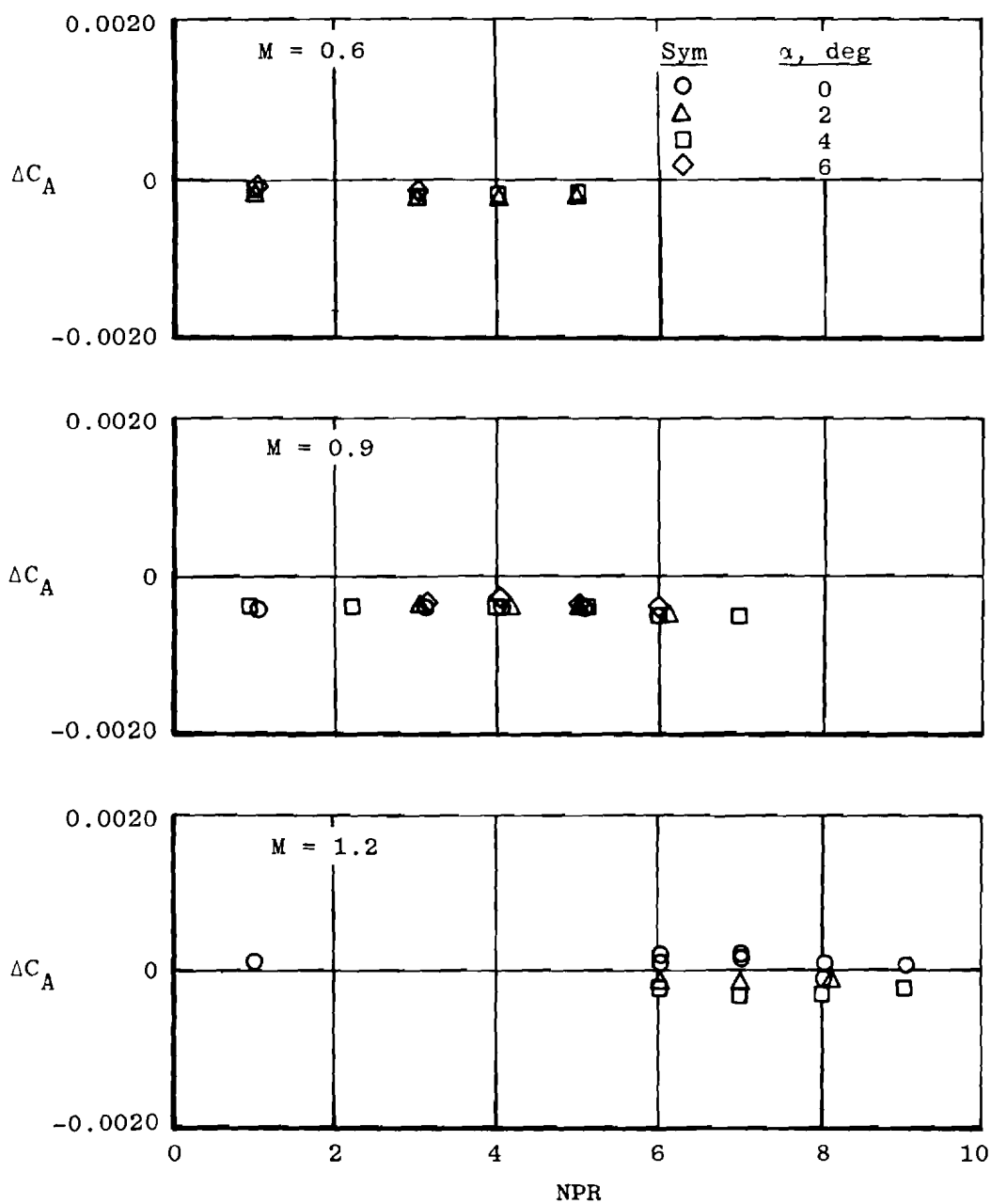Figure 89. Concluded.

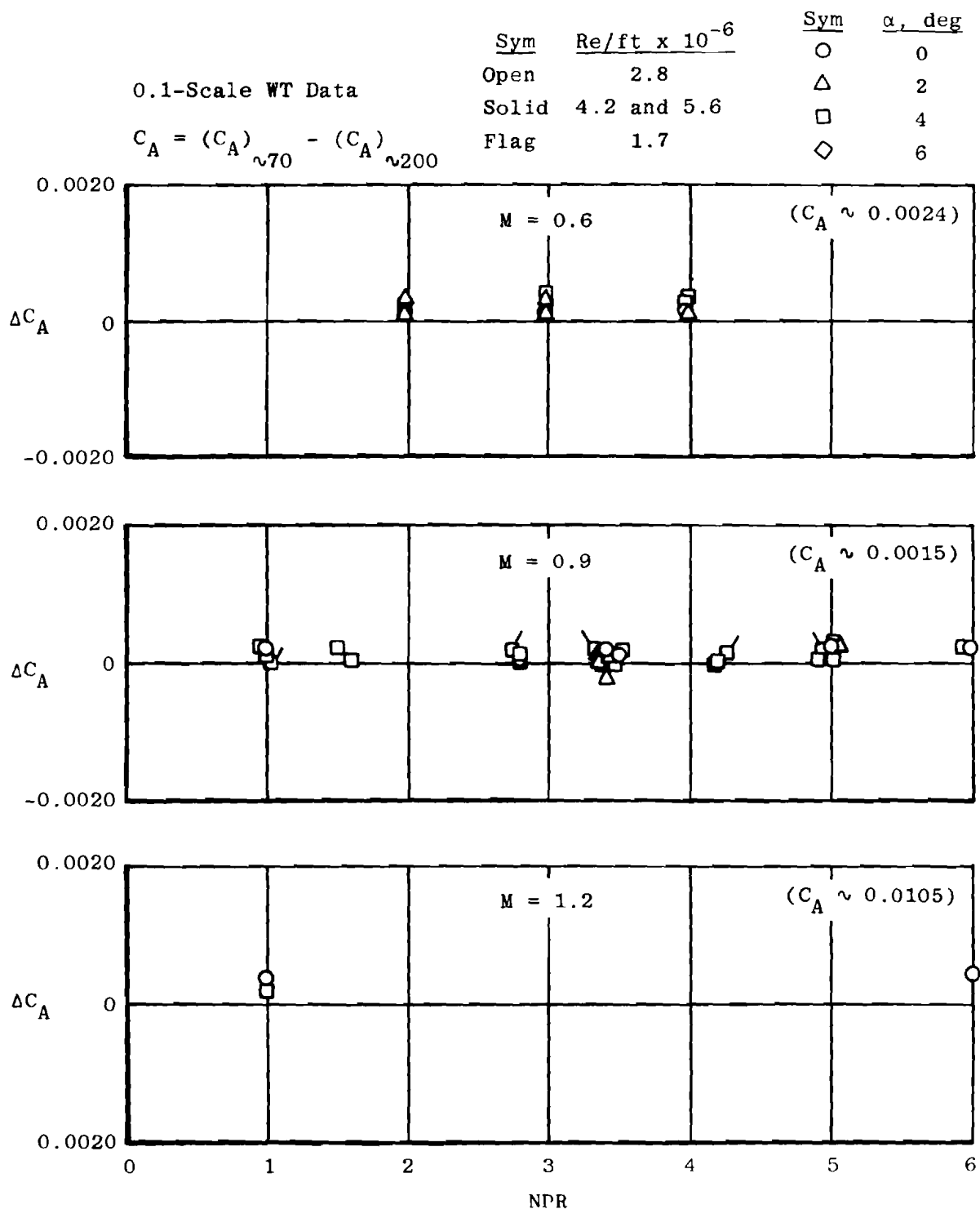Figure 90. Comparison of drag coefficient measurement techniques.

$$\Delta C_A = (C_A)_{70} - (C_A)_{200}$$

a. Cruise nozzle
Figure 91. Effect of number of pressure orifices on afterbody
axial-force coefficient.

179

b. Part AB nozzle
Figure 91. Concluded.

NOMENCLATURE

A	Local cross-sectional area, ft^2
A*	Nozzle throat area, ft^2
A_A	Projected area in the axial direction, ft^2
A_e	Nozzle exit area, ft^2
A_{max}	Maximum cross-sectional area of body of revolution, ft^2
A_N	Projected area normal to the body axis, ft^2
A_{ref}	Reference area, ft^2, A_{max} for bodies of revolution, S for aircraft configurations
C_A	Afterbody axial-force coefficient, force/$q_\infty A_{ref}$
C_{AA}	Aft fuselage axial-force coefficient, (C_A - C_{AN})
C_{AN}	Nozzle axial-force coefficient, force/$q_\infty A_{ref}$
C_D	Afterbody drag coefficient, force/$q_\infty A_{ref}$
C_{DF}	Forebody drag coefficient (force coefficient on the portion of the body ahead of the maximum cross-sectional area), force/$q_\infty A_{ref}$
C_{DT}	Drag coefficient of the complete body, (C_D + C_{DF})
C_N	Afterbody normal-force coefficient, force/$q_\infty A_{ref}$
C_p	Local pressure coefficient, p_ℓ - p_∞/q_∞
C_{p_b}	Base pressure coefficient, p_b - p_∞/q_∞
D	Model diameter, ft
D_1	Quiescent jet diameter when expanded isentropically to free-stream static pressure, ft
D_B	Model base diameter, ft
D_e	Nozzle exit diameter, ft
D_s	Sting diameter, ft
L	Model length, ft

M_∞ Free-stream Mach number

NPR   Nozzle exit total-to-free-stream static pressure ratio

NSPR   Nozzle exit staticto-free-stream static pressure ratio

P_ℓ Local static pressure, psfa

p_∞ Free-stream static pressure, psfa

q_∞ Free-stream dynamic pressure, psf

R   Universal gas constant, ft-lb/lb-°R

Re   Reynolds number based on model length, L

S   Wing area, ft^2

T_t Jet total temperature, °R

t   Strut thickness, ft

V_e Jet exit velocities, ft/sec

V_∞ Free-stream velocity, ft/sec

x   Axial distance, ft

z   Vertical distance, ft

α Angle of attack

γ Gas specific heat ratio

Δ Incremental change in parameter

$\Delta\nu$ Incremental change in Prandtl-Meyer angle from conditions at the nozzle exit-to-free-stream conditions, deg

δ_N Initial jet inclination angle, $(\theta_N + \Delta\nu)$, deg

θ Radial location of orifices, positive clockwise looking upstream, deg

θ_N Nozzle divergence half angle, deg